

# **Design of a Magnetostrictive-Hydraulic Actuator Considering Nonlinear System Dynamics and Fluid-Structure Coupling**

Dissertation

Presented in Partial Fulfillment of the Requirements for the Degree  
Doctor of Philosophy in the Graduate School of The Ohio State  
University

By

John Philip Larson, B.S.

Graduate Program in Mechanical Engineering

The Ohio State University

2014

Dissertation Committee:

Professor Marcelo J. Dapino, Advisor

Professor Ahmet Selamet

Professor Rajendra Singh

Professor Vishnu Baba Sundaresan

© Copyright by  
John Philip Larson  
2014



# Abstract

Smart material electro-hydraulic actuators (EHAs) utilize fluid rectification via one-way check valves to amplify the small, high-frequency vibrations of certain smart materials into large motions of a hydraulic cylinder. Although the concept has been demonstrated in previously, the operating frequency of smart material EHA systems has been limited to a small fraction of the available bandwidth of the driver materials. The focus of this work is to characterize and model the mechanical performance of a magnetostrictive EHA considering key system components: rectification valves, smart material driver, and fluid-system components, leading to an improved actuator design relative to prior work.

The one-way valves were modeled using 3-D finite element analysis, and their behavior was characterized experimentally by static and dynamic experimental measurement. Taking into account the effect of the fluid and mechanical conditions applied to the valves within the pump, the dynamic response of the valve was quantified and applied to determine rectification bandwidth of different valve configurations. A novel miniature reed valve, designed for a frequency response above 10 kHz, was fabricated and tested within a magnetostrictive EHA.

The nonlinear response of the magnetostrictive driver, including saturation and hysteresis effects, was modeled using the Jiles-Atherton approach to calculate the magnetization and the resulting magnetostriction based on the applied field calculated within the rod from Maxwell's equations.

The dynamic pressure response of the fluid system components (pumping chamber, hydraulic cylinder, and connecting passages) was measured over a range of input frequencies. For the magnetostrictive EHA tested, the peak performance frequency was found to be limited by the fluid resonances within the system.

A lumped-parameter modeling approach was applied to model the overall behavior of a magnetostrictive EHA, incorporating models for the reed valve response, nonlinear magnetostrictive behavior, and fluid behavior (including inertia and compliance). This model was validated by experimental study of a magnetostrictive EHA with a reduced volume manifold. The model was subsequently applied to design a compact magnetostrictive EHA for aircraft applications.

Testing of the system shows that the output performance increases with frequency up to a peak unloaded flow rate of  $100 \text{ cm}^3/\text{s}$  ( $6.4 \text{ cu in/s}$ ) at 1200 Hz, which is a 100% to 500% increase over previous state-of-the-art systems. A blocked differential pressure of 12.1 MPa (1750 psi) was measured, resulting in a power capacity of 310 W, more than 100 W higher than previously reported values. The design and modeling approach used to scale up the performance to create a compact aircraft EHA can also be applied to reduce the size and weight of smart material EHAs for lower power level applications.

To my wife and daughter

# Acknowledgments

The work presented in this dissertation would not have been completed without the help and support of many people. I would first like to thank my advisor, Prof. Marcelo Dapino, for initiating this project and allowing me to work on it. I am grateful for the technical and professional advice given throughout the project and for the opportunities to present the research through publications and at conferences. I would also like to thank Prof. Ahmet Selamet, Prof. Rajendra Singh, and Prof. Vishnu Baba Sundaresan for serving on my dissertation committee.

This project was made possible by the Smart Vehicle Concepts Center (SVC), a National Science Foundation Industry/University Cooperative Research Center. I would like to thank the Industrial Advisory Board of the SVC for their continued interest in smart material electro-hydraulic actuators, their feedback on the progress of the project, and support through the SVC fellowship program. I would also especially like to thank Moog, Inc. for initiating and funding this project. I appreciate Tom Greetham, Tom Walters, and Steve Vanda from Moog for their input on the project as mentors.

I would like to thank all of the staff at Ohio State for supporting me during my time at the University. I would like to especially thank the machinists that have helped supply me with the parts needed to conduct experiments: Chad Bivens, Walter Green, and Neil Gardner. This work was also supported in part by an allocation of computing time from the Ohio Supercomputer Center.

The other students in the Smart Materials and Structures Lab at OSU have made working in the lab a great experience. Always having a lot of smart people around to bounce ideas off of has helped to develop the modeling and experimental approaches that I have taken in this work. I have worked with too many other students and post-docs to list here, but I would like to mention Ryan Hanhlen, Gordon Fox, Travis Walker, Suryarghya Chakrabarti, Travis Walker, Philip Evans, Justin Scheidler, Paul Wolcott, Sushma Santapuri, Jungkyu Park, and Leon Headings.

I would not have been able to complete this work without the love and support from my family. I would like to thank my parents for always believing in me and encouraging me to push myself further. I would like to thank my wife, Theresa, for helping me throughout my time at Ohio State. She is always by my side with everything, and I would not have been able to finish this work without her. My daughter, Ariana, has also been a true source of joy and a constant reminder to view the world with the wonder that only a two-year-old can possess.

# Vita

July 31, 1985 ..... Born - Galva, KS

May, 2008 ..... B.S. Mechanical Engineering,  
Magna Cum Laude,  
University of Notre Dame

2008–2014 ..... Distinguished University Fellow,  
NSF I/UCRC Smart Vehicle Concepts  
Center Fellow,  
The Ohio State University

## Publications

J.P. Larson and M.J. Dapino “High-frequency valve development for smart material electro-hydraulic actuators.” *Proceedings of SPIE*, 7979, 79790E, 2011.

J.P. Larson and M.J. Dapino “Design of a smart material electro-hydraulic actuator with improved frequency bandwidth.” *Proceedings of SPIE*, 8343, 83430K, 2012.

J.P. Larson and M.J. Dapino “Reliable, high-frequency miniature valves for smart material electrohydraulic actuators.” *Journal of Intelligent Material Systems and Structures*, 23 (7), 805-813, 2012.

J.P. Larson and M.J. Dapino “Performance Modeling of a Smart Material Hydraulic Actuator.” *ASME 2012 Conference on Smart Materials, Adaptive Structures and Intelligent Systems*, SMASIS2012-8253, pp. 497-503, 2012.

J.P. Larson and M.J. Dapino “Nonlinear dynamic modeling for smart material electro-hydraulic actuator development.” *Proceedings of SPIE*, 8690, 86900I, 2013.

## **Fields of Study**

Major Field: Mechanical Engineering

Studies in:

Smart Materials and Structures

System Dynamics and Vibrations

# Table of Contents

	<b>Page</b>
Abstract . . . . .	ii
Dedication . . . . .	iv
Acknowledgments . . . . .	v
Vita . . . . .	vii
List of Figures . . . . .	xiii
List of Tables . . . . .	xix
List of Symbols . . . . .	xx

## Chapters

<b>1 Introduction . . . . .</b>	<b>1</b>
1.1 Definition of Problem . . . . .	1
1.2 Objectives . . . . .	2
1.3 Research Approach . . . . .	2
1.4 Dissertation Outline . . . . .	3
<b>2 Background Information . . . . .</b>	<b>6</b>
2.1 Motivation . . . . .	6
2.1.1 Aircraft Electrification . . . . .	6
2.1.2 Principle of Operation . . . . .	9
2.2 Magnetostrictive Materials . . . . .	10
2.3 Displacement Amplification . . . . .	14
2.4 Other Smart Materials . . . . .	15
2.5 Smart Material EHA Development . . . . .	16
2.5.1 Performance Summary . . . . .	20
2.5.2 Patents . . . . .	21
2.6 Summary . . . . .	23
<b>3 Miniature Reed Valve Array . . . . .</b>	<b>24</b>
3.1 Introduction . . . . .	24
3.2 Background . . . . .	25



3.3	Design of Miniature Reed Valves . . . . .	27
3.4	Fabrication . . . . .	33
3.5	Finite Element Analysis of Fluid-Structure Interaction . . . . .	33
3.6	Steady-State Flow Testing . . . . .	36
3.7	Actuator Testing of Miniature Reeds . . . . .	37
3.8	Summary . . . . .	39
<b>4</b>	<b>Reduced Volume Manifold EHA Experimental Testing . . . . .</b>	<b>41</b>
4.1	Introduction . . . . .	41
4.2	Background: EHA with External Hydraulic Cylinder . . . . .	41
4.3	Reduced Volume Manifold Smart Material EHA . . . . .	43
4.4	Identification of Losses in Experimental Actuator . . . . .	46
4.4.1	Comparison to External Hydraulic Cylinder Actuator . . . . .	46
4.4.2	Diaphragm Deformation . . . . .	48
4.4.3	Hydraulic Resonances . . . . .	51
4.5	Power & Efficiency Evaluation . . . . .	52
4.5.1	Input frequency sweep at 7.1 A <sub>rms</sub> . . . . .	53
4.5.2	Input Current Variation at 225 Hz Input Frequency . . . . .	55
4.5.3	Higher Current Input Frequency Sweep at 10.6 A <sub>rms</sub> . . . . .	57
4.6	Summary . . . . .	63
<b>5</b>	<b>Reed Valve Development . . . . .</b>	<b>65</b>
5.1	Introduction . . . . .	65
5.2	Background . . . . .	67
5.3	Finite Element Modeling of Steady-State Flow . . . . .	69
5.4	Dynamic Response . . . . .	73
5.4.1	Determination of Reed Valve Natural Frequency . . . . .	73
5.5	Simplified Flow Model . . . . .	77
5.5.1	Effect of Natural Frequency on Fluid Rectification . . . . .	80
5.6	Summary . . . . .	81
<b>6</b>	<b>Performance Modeling . . . . .</b>	<b>83</b>
6.1	Introduction . . . . .	83
6.2	Background . . . . .	84
6.3	Ideal Flow Model . . . . .	86
6.4	Lumped-Parameter Modeling . . . . .	86
6.4.1	Mechanical Subsystem . . . . .	88
6.4.2	Fluid Subsystem . . . . .	89
6.4.3	Passage Compliance . . . . .	93
6.5	Nonlinear Terfenol-D Model Equations . . . . .	93

6.6	Model Results . . . . .	98
6.6.1	No-Valve Modeling . . . . .	98
6.7	Full System Modeling Results with Reeds Installed . . . . .	101
6.7.1	Linear Terfenol-D Model . . . . .	101
6.7.2	AMESim Model . . . . .	103
6.7.3	Nonlinear Terfenol-D Model . . . . .	106
6.8	Summary . . . . .	107
<b>7</b>	<b>Design of a Compact Aircraft EHA . . . . .</b>	<b>109</b>
7.1	Introduction . . . . .	109
7.2	Design Requirements . . . . .	110
7.3	Preliminary Design . . . . .	112
7.3.1	Power Analysis and Losses . . . . .	115
7.4	Detailed Design . . . . .	119
7.4.1	Magnetic Circuit Design . . . . .	119
7.4.2	Solid Model . . . . .	124
7.4.3	Finite-Element Modeling . . . . .	126
7.4.4	Pumping Chamber Modeling . . . . .	126
7.4.5	Reed Valve Modeling . . . . .	130
7.5	System-Level Modeling . . . . .	132
7.5.1	No-Reed Dynamic Model . . . . .	132
7.5.2	Full System Model . . . . .	136
7.5.3	Linear Terfenol-D Model . . . . .	137
7.5.4	Nonlinear Terfenol-D Model . . . . .	140
7.6	Summary . . . . .	142
<b>8</b>	<b>Compact Aircraft EHA Testing . . . . .</b>	<b>144</b>
8.1	Introduction . . . . .	144
8.2	Coil Fabrication . . . . .	144
8.3	Experimental Setup . . . . .	147
8.4	Performance . . . . .	148
8.5	Summary . . . . .	154
<b>9</b>	<b>Contributions and Future Work . . . . .</b>	<b>157</b>
9.1	Summary of Findings . . . . .	157
9.2	Research Contributions . . . . .	160
9.3	Future Work . . . . .	163

## Appendices

<b>A</b>	<b>Allowable Stress Calculation for Valve Design . . . . .</b>	<b>166</b>
----------	--	------------

<b>B</b>	<b>Calculation of Reed Valve Opening Area Factor</b>	<b>168</b>
<b>C</b>	<b>Actuator Parameters</b>	<b>170</b>
C.1	Reduced Volume EHA Parameters	170
C.2	Compact Aircraft EHA Parameters	174
C.3	Jiles-Atherton Model Parameters	176
C.4	Fluid Viscosity Comparison	177
<b>D</b>	<b>Design Drawings for Compact Aircraft EHA</b>	<b>179</b>
D.1	Solid Model Exploded Views	179
D.2	Detailed Design Drawings	185
	<b>Bibliography</b>	<b>202</b>

# List of Figures

Figure		Page
2.1	Comparison of secondary power systems in a conventional commercial aircraft and the “more-electrical” aircraft design. . . . .	7
2.2	Summary of the actuator types used for flight control and other aircraft applications. . . . .	8
2.3	Principle of operation for a smart material electro-hydraulic actuator.	10
2.4	A simplified representation of the process of magnetostriction. . . . .	11
2.5	Magnetostrictive strain vs. applied field for Terfenol-D for a range of preload stress values. . . . .	13
3.1	Magnetostrictive electro-hydraulic actuator used to evaluate the dynamic performance of the miniature reed valve arrays. . . . .	28
3.2	Valve port geometry for the the magnetostrictive hydraulic pump used to evaluate the miniature reed valve array performance. . . . .	29
3.3	Design of the miniature reed valve array layers. . . . .	30
3.4	Design stress in fully-open miniature reed (25 $\mu\text{m}$ displacement) calculated using a COMSOL finite element model. . . . .	31
3.5	Design stress in the miniature reed valve while closed, supporting a 10 MPa (1500 psi) pressure. . . . .	32
3.6	Calculated mode shapes for miniature reed design. . . . .	32
3.7	Comparison of the miniature reed valves both as-received and after polishing. . . . .	34
3.8	Geometry used for finite-element modeling using COMSOL. . . . .	35
3.9	Comparison of steady-state testing results to finite-element model results. . . . .	36
3.10	Unloaded velocity performance comparison between the single reed valves and the miniature reed valve array. . . . .	38

4.1	Exploded view of the pump assembly with a detailed view of the pumping chamber. . . . .	42
4.2	Experimental setup for previous magnetostrictive EHA configuration. . . . .	43
4.3	Test configuration for reduced-volume manifold magnetostrictive EHA pump. . . . .	45
4.4	Unloaded flow rate for the pump connected to an external hydraulic cylinder and using the reduced volume manifold. . . . .	47
4.5	The application and removal of the preload procedure caused a plastic deformation of the piston seal diaphragm. . . . .	49
4.6	Replacing the diaphragm and adjusting the preload sequence improved pump flow performance significantly. . . . .	50
4.7	Compression test setup for measuring the pump diaphragm stiffness. . . . .	50
4.8	A needle valve was added to the system to close off pressure sensor passage. . . . .	51
4.9	Removing the extra fluid volume associated with the output pressure sensor improved the pump frequency bandwidth and performance. . . . .	52
4.10	Experimental output cylinder flow rate vs. input frequency with a 7.1 A <sub>rms</sub> sinusoidal input current applied over the frequency range. . . . .	53
4.11	Output force vs. velocity measured at 225 Hz input frequency. . . . .	54
4.12	Testing of the experimental actuator at 225 Hz with a 220 N load applied over a range of input frequencies. . . . .	56
4.13	Experimental output cylinder velocity rate vs. input frequency. . . . .	57
4.14	Output power vs. input frequency for a range of applied mass loads. . . . .	59
4.15	Efficiency vs. input frequency for a range of applied mass loads . . . . .	60
4.16	Input power vs. input frequency for a range of applied mass loads. . . . .	61
4.17	Force vs. velocity curves for a range of input frequencies. . . . .	62
5.1	Velocity field for a 0.13 mm thick reed valve calculated by Chaudhuri, Yoo, and Wereley (2009) . . . . .	68
5.2	Single reed valve dimensions used within the reduced volume manifold EHA. . . . .	69
5.3	The geometry used for finite-element modeling of the reeds. . . . .	70
5.4	A typical velocity field calculated by applying a differential pressure across the inlet and outlet passages to the reed valves. . . . .	70
5.5	Two-dimensional representation of the reed valve solution geometry demonstrating improvement in element quality using a prescribed mesh displacement. . . . .	71
5.6	Reed valve flow resistance compared to tip displacement comparing experimental results with COMSOL calculations. . . . .	72
5.7	Illustration of reed valve dynamic test configuration. . . . .	74
5.8	Test setup for evaluating the natural frequency of the reed valves. . . . .	75
5.9	Reed valve dynamic experimental results compared with theoretical calculation of the natural frequency based on the length of the valve. . . . .	76

5.10	Calculation of the applied pressure area for the reed valves. . . . .	78
5.11	First bending mode of the reed valve, calculated using COMSOL. . .	79
5.12	Comparison between the steady-state flow measurements and calculating the of the flow rate using the orifice flow equation. . . . .	79
5.13	Normalized flow response over the reed valves for a sinusoidal pressure distribution over a range of frequencies. . . . .	80
6.1	Ideal (loss-less) flow estimate from the linear piezomagnetic equations compared to the experimental results. . . . .	87
6.2	Mechanical model of the pumping piston. . . . .	88
6.3	System model diagram showing the layout of the fluid passages. . . .	90
6.4	Each section of the fluid passages is modeled using one or more lumped-parameter nodes incorporating the equivalent resistance, inertia, and compliance of the fluid in the section. . . . .	90
6.5	Variation of the effective bulk modulus of the fluid within the pump due to pressure changes and entrained air based on (6.9). . . . .	92
6.6	Effect of mechanical stiffness on the effective compliance of a fluid passage. . . . .	94
6.7	Layout of the hydraulic system model for the experimental system without the reed valves installed. . . . .	99
6.8	Experimental results of measuring the pressure amplitude generated within the system for a constant current input over the frequency range.	99
6.9	Model results of for the pressure amplitude generated within the system for a constant current input over the frequency range. . . . .	100
6.10	Model results for applying the linear Terfenol-D model for a $7.1 A_{rms}$ input current over the frequency range. . . . .	102
6.11	AMESim implementation of lumped parameter model utilizing the linear magnetostrictive model . . . . .	103
6.12	Comparison of the system response calculated with AMESim with experimental data. . . . .	105
6.13	Comparison of the measured unloaded velocity with the calculation using the nonlinear Jiles-Atherton model for the Terfenol-D rod for a $7.1 A_{rms}$ constant input current over the frequency range. . . . .	106
7.1	Commercial hydraulic actuator (Moog, Inc.) used for the design of a high-power magnetostrictive EHA. . . . .	111
7.2	Allowable piston diameter for each available size Terfenol-D rod. . . .	113
7.3	Unloaded flow rate vs. frequency for a combination of driver lengths and piston diameters. . . . .	114
7.4	Estimated output power based on a quasi-static analysis for the preliminary pump design. . . . .	117
7.5	Results of applying the quasi-static power calculation to the previous, reduced-volume-manifold EHA. . . . .	118

7.6	Geometry of magnetic circuit FE model, including the rod, flux return, coil, and surrounding air. . . . .	122
7.7	Comparison of the field distribution (Oe) using a 18 cm and a 15 cm long coil. . . . .	123
7.8	Magnetic field distribution (Oe) for FE model of final magnetic circuit design. . . . .	124
7.9	CAD rendering of high-power magnetostrictive EHA design with cross-section. . . . .	125
7.10	Displacement ( $\mu\text{m}$ ) of the pump flux return when subject to a 13 kN (3000 lb <sub>f</sub> ) load. . . . .	127
7.11	Calculated stress in MPa on the flux return when subjected to a 13 kN load (3000 lb <sub>f</sub> ), which corresponds to a pump pressure of 22 MPa (3100 psi). . . . .	127
7.12	Geometry of the finite element model used to evaluate the stress due to the applied pressure within the hydraulic manifold. . . . .	128
7.13	Stress from a 22 MPa (3100 psi) applied pressure on the internal flow passages of the hydraulic cylinder manifold. . . . .	128
7.14	Velocity field calculated within the pumping chamber from an axis-symmetric model (m/s). . . . .	129
7.15	Pressure distribution within the pumping chamber (psi). . . . .	130
7.16	Bending stress (MPa) calculated for the reed valve in the while opening. . . . .	131
7.17	Axi-symmetric calculation of the stress (MPa) in the portion of the valve covering the inlet hole for a blocked pressure of 22 MPa (3100 psi). . . . .	131
7.18	Schematic representation of the no-reed dynamic model used to determine the response of the fluid system components of the high-power EHA actuator design. . . . .	133
7.19	Modeled pressure amplitude response for a sinusoidal input current applied at each frequency. . . . .	134
7.20	Time traces of the pressure amplitudes for the no-reed model at the frequency peaks. . . . .	135
7.21	Typical unloaded displacement results for the full system model. . . . .	138
7.22	Predicted output velocity for a range of input frequencies with a constant current applied at each frequency. . . . .	138
7.23	Eddy currents reduce the field in the Terfenol-D rod at high currents. . . . .	140
7.24	Nonlinear strain vs. field model results at 450 Hz. . . . .	141
7.25	Typical unloaded displacement results for the system model including nonlinear Terfenol-D effects. . . . .	141
7.26	Predicted velocity response for a constant current amplitude frequency sweep using a nonlinear magnetostrictive model. . . . .	142
8.1	Assembled compact aircraft electro-hydraulic actuator. . . . .	145
8.2	View of the partially assembled magnetostrictive pump showing the coil and laminated Terfenol-D rod. . . . .	146

8.3	Experimental test setup for unloaded and blocked force testing of the high-power EHA system. . . . .	147
8.4	Unloaded velocity vs. frequency test results for the high power EHA design. . . . .	149
8.5	Input current and voltage for the unloaded velocity tests conducted at a 8.8 A <sub>rms</sub> input current over the frequency range. . . . .	150
8.6	Input power applied over the frequency range tested for the 8.8 A <sub>rms</sub> input current input tests with the 0.51 mm (0.02") reed valves installed. . . . .	152
8.7	The piston seal diaphragm in the compact aircraft EHA was found to be deformed when the actuator was disassembled after testing. . . . .	153
8.8	Unloaded velocity vs. frequency comparison between two different reed thicknesses. . . . .	155
C.1	System model diagram showing the layout of the fluid passages. . . . .	170
C.2	Cut-away drawing of the reduced-volume manifold. . . . .	173
C.3	Viscosity comparison between Royco 756 and Mobil DTE-24 hydraulic fluids. . . . .	178
C.4	Calculation of hydraulic fluid viscosity at room temperature. . . . .	178
D.1	Overall assembly for the high power EHA design. . . . .	180
D.2	Cross section view of the high-power EHA design. . . . .	181
D.3	Cross section of the adapter plate, which connects the magnetostrictive pump with the hydraulic cylinder. . . . .	182
D.4	Bill of material for the magnetostrictive pump portion of the high-power EHA design. . . . .	183
D.5	Exploded view of the EHA actuator assembly, showing the placement of the rectification reed valves. . . . .	184
D.6	Detailed drawing of the manifold to interface with the hydraulic actuator centerline. . . . .	185
D.7	Hole details for the actuator manifold. . . . .	186
D.8	Internal geometry of the actuator manifold. . . . .	187
D.9	Adapter plate used to connect the pump portion of the actuator with the hydraulic cylinder manifold. . . . .	188
D.10	Details for the return valve passages within the adapter plate. . . . .	189
D.11	Surface details for the adapter plate. . . . .	190
D.12	Reed valve dimensional drawing. . . . .	191
D.13	Spacer dimensions used to clamp down valves thinner than 0.51 mm . . . . .	192
D.14	Pump head design drawing. . . . .	193
D.15	Cut-away view of pump head. . . . .	194
D.16	Upper half of pumping piston. . . . .	195
D.17	Pumping chamber seal diaphragm design drawing. . . . .	196
D.18	Lower half of pumping chamber design. . . . .	197



D.19 Guide ring used to align flux return with pumping piston and to complete the magnetic circuit. . . . .	198
D.20 Flux return and pump body. . . . .	199
D.21 Modified screw for preload adjustment. . . . .	200
D.22 Sketch of coil dimensions provided for reference. . . . .	201

# List of Tables

Table		Page
2.1	Properties of various magnetostrictive materials. . . . .	12
2.2	Performance comparison of smart material electro-hydraulic actuators. . . . .	20
2.3	Commercial smart material pump developments . . . . .	21
3.1	Area comparison for miniature reed valve design. . . . .	34
4.1	Comparison of the output velocity with applied load for two different input current levels. . . . .	58
4.2	Summary of experimental tests applied to the reduced volume mani- fold EHA. . . . .	64
5.1	Reed natural frequency testing results. . . . .	75
6.1	Performance comparison of smart material electro-hydraulic actuators. . . . .	85
6.2	Summary of the no-reed model results. . . . .	101
7.1	Performance goals for the high-power smart material EHA design. . . . .	110
7.2	Design requirements applying the hydraulic cylinder area to the overall actuator performance goals. . . . .	111
7.3	Terfenol-D properties used for initial design of magnetostrictive EHA . . . . .	112
7.4	Preliminary Design Parameters . . . . .	119
C.1	Fluid passage dimensions for the reduced-volume-manifold EHA. . . . .	171
C.2	Magnetostrictive driver, piston, and output hydraulic cylinder prop- erties for the reduced-volume-manifold EHA. . . . .	172
C.3	Fluid passage dimensions for the compact aircraft EHA. . . . .	174
C.4	Magnetostrictive driver, piston, and output hydraulic cylinder prop- erties for the compact aircraft EHA. . . . .	175
C.5	Parameter values used for the Jiles-Atherton model applied to model the nonlinear behavior of the Terfenol-D rod. . . . .	176

# List of Symbols

Symbol	Description
$\alpha$	Piezomagnetic coupling coefficient, JA model parameter
$\beta$	Effective fluid bulk modulus
$\gamma$	Correction factor for added mass
$\delta$	Displacement
$\epsilon$	Strain
$\epsilon_0$	Permittivity of free space
$\lambda_r$	Valve area factor
$\lambda$	Magnetostriction
$\lambda_s$	Saturation magnetostriction
$\mu$	Fluid absolute viscosity
$\omega$	Angular frequency
$\rho$	Fluid density
$\sigma$	Stress
$a$	Shape parameter for JA model
$A$	Area
$b$	Damping factor
$c$	Reversibility parameter
$C_d$	Orifice flow coefficient
$C$	Fluid compliance
$d$	Fluid passage diameter
$E$	Electric field
$f$	Frequency
$F$	Force
$J$	Current density
$k$	Stiffness, JA model parameter
$H$	Magnetic field
$l$	Length
$L$	Fluid inertia, Length
$m$	Mass
mmf	Magnetomotive force

Symbol	Description
$M$	Magnetization
$N_R$	Reynold's number
$P$	Pressure
$Q$	Volumetric flow rate
$r$	Radius
$R$	Flow resistance, Outer radius
$t$	Time
$V$	Volume, Velocity
$w$	Width
$W$	Work
$x$	Position

Subscript	Description
acc	Accumulator
avg	Average
A-H	Fluid passages in hydraulic manifold
bias	Relating to the applied bias pressure
ch	Pumping chamber
out	Output hydraulic cylinder
f	Friction force
ext	External load force
hs	High-pressure side of the output hydraulic cylinder
ls	Low-pressure side of the output hydraulic cylinder
p	Pumping piston
ri	Inlet reed valve from pumping chamber
ro	Outlet reed valve from pumping chamber
TD	Terfenol-D drive rod
v	Valve

# Chapter 1

## Introduction

### 1.1 Definition of Problem

The high energy density of certain smart materials such as magnetostrictives and piezoelectrics makes them attractive for aerospace actuator applications where size and weight are critical design considerations [1]. However, the relatively small motions available from these materials means that some form of displacement amplification is necessary. Smart material electro-hydraulic actuators (EHAs) use fluid rectification via one-way valves to convert the high-frequency, high-force vibrations of the material into large motions of a hydraulic cylinder. The result is a compact, power-by-wire system that can offer an alternative to conventional hydraulic systems. By eliminating the need for large, centralized hydraulic pumps and the associated fluid lines, weight and maintenance requirements can be reduced while improving reliability.

The rectification approach leverages the high-frequency bandwidth of the materials to produce high-pressure fluid flow, resulting in actuator motion. The output performance of these systems can be improved increasing the drive frequency; for a given piston stroke, more rapid pumping cycles means more fluid flow. The smart materials used for these devices are capable operating frequencies in the kHz range; however, the peak system performance has typically been restricted to using input frequencies of a few hundred hertz.

## 1.2 Objectives

The research objectives for this work are as follows:

1. Increase the overall power output of a smart material EHA
2. Develop a system-level modeling framework to understand the behavior of smart material EHA systems, including nonlinear system dynamics and fluid-structure coupling
3. Apply the system-level model to design a magnetostrictive EHA with an improved frequency bandwidth for aircraft applications

## 1.3 Research Approach

Factors which have prevented previous EHA systems from fully utilizing the drive materials include the dynamic response of the one-way rectification valves, fluid-system losses (inertia and resonance effects), and smart material driver nonlinearities. The approach taken in this work is to develop an understanding each of these effects individually via experimental study and modeling. The component-level models are then combined into a system-level modeling framework, which is used to describe the overall response of a smart material EHA system and to design scaled-up actuator for aircraft applications.

The main drawbacks of using smart materials are the added cost and need to account for the complex, nonlinear material behavior in the design. The currently limited use of the magnetostrictive material Terfenol-D for actuator applications means that each actuator is relatively expensive. By developing a modeling approach which can be used to scale smart material EHA systems for specific applications, this work

has the potential to lead to more widespread commercial adoption of magnetostrictive systems. The goal for designing a compact aircraft EHA is to scale up the power capacity, but the same the approach can also be used to design smaller and lighter actuators at other power levels. These applications include vehicle systems where hydraulics are currently being used, such as active suspension components, engine mounts, and automatic transmissions. Additionally, smart material EHAs can be used for other novel applications where there is a need for small, lightweight, high-power actuators such as robotics and biomechanics.

## 1.4 Dissertation Outline

Chapter 2 outlines background information for using magnetostrictive-hydraulic actuators as an alternative to conventional hydraulic systems. The motivation for using smart materials to develop power-by-wire systems in aircraft is presented along with a comparison of the relative merits of applying other materials and displacement amplification techniques. A literature survey of previous efforts to develop EHA actuators to amplify motion of smart materials is presented, including a summary of the output performance results. While there is a general trend of increasing the available power along with the frequency at which the peak performance occurs, the relatively low frequency of operation relative to the available bandwidth of the materials prevents the systems from realizing their potential to form high energy density actuators.

Chapter 3 presents the design and experimental testing of a miniature valve array, which was designed to enable the rectification of fluid at very high frequencies ( $>10$  kHz). The one-way check valves used to transform the high frequency oscillations into a one-directional flow of fluid have been identified as a limiting factor in the performance of smart material EHA systems. By using an array of miniature valves, each valve can be designed to have a low mass with a high stiffness to improve

the frequency response, while the pressure drop over the combined flow area remains relatively low. The miniature array was demonstrated to successfully rectify flow and survive within a high-pressure pump environment; however, the experimental magnetostrictive EHA used to evaluate the valves remained limited to a peak performance frequency of 225 Hz.

Chapter 4 shows an experimental study of the performance of a magnetostrictive electro-hydraulic actuator designed with a reduced-volume manifold. This study was used to identify the sources of loss in a magnetostrictive EHA system and to validate the models used for designing the high-power system. The performance was evaluated over a range of test conditions, including measurement of the dynamic response without the reed valves installed, to determine the contribution of the fluid-system components on the range of input frequencies over which the system can operate. Modification of the system to eliminate unnecessary fluid volumes was shown to have an effect on the dynamic response of the system.

Chapter 5 presents the modeling and experimental testing applied to characterize the single reed-type valves used for rectifying fluid within the experimental magnetostrictive EHA. A 3-D finite element model was developed to quantify fluid-structure interaction between the reed valves and hydraulic fluid, including the valve deflection to an applied pressure differential and the resulting amount of fluid flow. Steady-state flow experiments were used to validate the model performance. Additional experimental testing was conducted to determine the dynamic response of the valves, including the effect of the mass loading from the hydraulic fluid and the boundary conditions of the valve seat. A set of simplified equations suitable for calculating the reed valve performance in a system-level model were proposed and compared to the experimental data.



Chapter 6 develops an overall modeling framework for the system using a lumped parameter approach. Model equations describing the behavior of the mechanical, electrical, and fluid aspects of the system are presented; the results of the model are compared to the measured output performance of a magnetostrictive EHA. The model includes the nonlinear response of the magnetostrictive driver to applied magnetic field, which was modeled using Maxwell's equations for magnetic diffusion along with the Jiles-Atherton model to calculate the magnetization of the material and the resulting magnetostriction. An additional implementation of the model using the commercial 1-D modeling software AMESim is demonstrated as well.

Chapter 7 presents the design process for a compact aircraft magnetostrictive electro-hydraulic actuator. This actuator is designed to utilize a higher input frequency than previous smart material EHA designs in order to demonstrate an output capacity that is relevant to aerospace applications. Design targets for the system are identified, and an initial set of system parameters is developed based on quasi-static calculations of the blocked-force and unloaded-velocity capacity of the available Terfenol-D rods. The detailed system model developed in previous chapters is then applied to refine the design and predict the output performance over a range of input frequencies.

Chapter 8 shows the assembly and testing of the high-power, compact aircraft EHA system. The system is evaluated according to its unloaded velocity and blocked pressure performance over a range of input frequencies. Testing was also conducted using two different thicknesses of reed valves.

Chapter 9 summarizes the contributions of this dissertation to the current state-of-the-art smart material EHA performance and outlines potential future directions for applying the results of this work.

# Chapter 2

## Background Information

### 2.1 Motivation

Smart material electro-hydraulic actuators (EHAs) use hydraulic rectification to take advantage of the high force and fast frequency response of smart materials such as piezoelectrics and magnetostrictives. The small, high-frequency pulses of fluid produced by a pump piston driven by the material are collected with one-way valves. A hydraulic cylinder is integrated with the pump to form a compact, lightweight actuator. Electro-hydrostatic actuators offer an alternative to conventional hydraulic systems in aerospace, automotive, and robotic applications where size and weight are of concern [2–4]. Cost and complexity can be drawbacks of EHAs.

#### 2.1.1 Aircraft Electrification

A long-standing trend in aerospace industry and a research initiative by the U.S. Air Force is the “More-Electric Aircraft” (MEA) in which the electrical, hydraulic, and pneumatic secondary power systems are combined into a single, electrical system [5]. Eliminating the need to generate and distribute hydraulic and pneumatic power reduces weight and maintenance requirements while improving reliability (Figure 2.1) [6, 7]. To realize these improvements, there is a need to develop new actuators to replace the function of centralized hydraulic components. Smart material EHAs

can fill the role of replacing the functionality of conventional hydraulic components where other approaches have been unsuccessful.

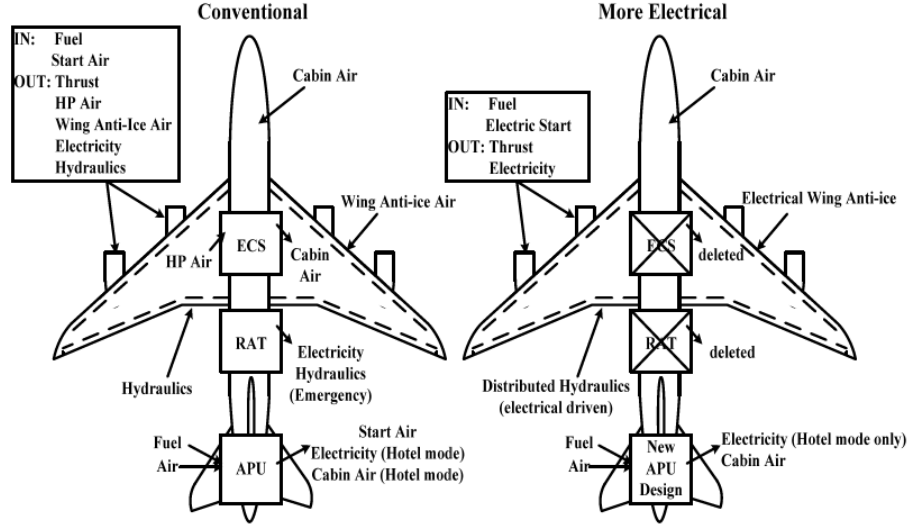


Figure 2.1: Comparison of secondary power systems in a conventional commercial aircraft and the “more-electrical” aircraft design (Reproduced from [6]).

Approaches for powered flight control can be generally categorized as hydraulic, electric, or electro-hydraulic (Figure 2.2). Electromechanical actuators (EMAs) are an alternative approach to EHA systems that can be practical for some applications; these actuators generally consist of an electric motor driving a ball-screw shaft. One of the key concerns for EMAs is the potential for failure in a locked state, which could freeze the flight control surface in an unfavorable position [2, 8]. Hydraulic systems have a more graceful failure mode; a loss of pressure causes them to act simply as a damper, either allowing a backup system to actuate the surface or returning to a neutral position due to aerodynamic loading. Another concern for consistent operation is that wear of the mechanical components may introduce free play (e.g. gear backlash) or other nonlinear behavior to the actuator response [9]. Additionally,

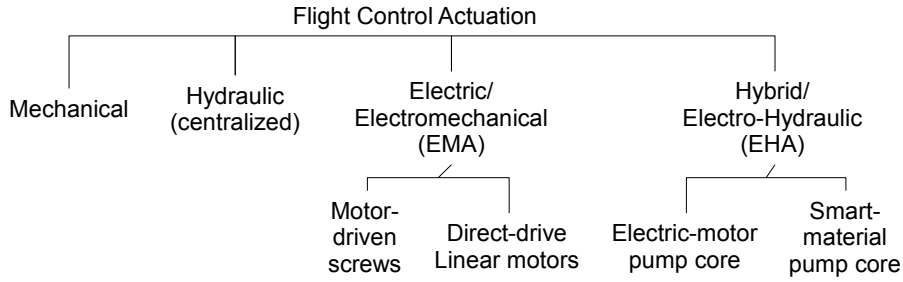


Figure 2.2: Summary of the actuator types used for flight control and other aircraft applications (Reproduced from [2]).

the high angular momentum of the EMA motors limits the bandwidth of operation [2].

Electro-hydraulic actuators address the limitations of both conventional hydraulic and electromechanical actuation. In an EHA, the output hydraulic cylinder is co-located with its supply pump to create a compact, power-by-wire system. The system is a self-contained unit, thus eliminating the weight and associated maintenance requirements of a centralized hydraulic pump, fluid lines, and control valves [8]. The hydraulic output cylinder retains the failure-mode and wear advantages of a hydraulic system. EHA systems are in use in both commercial and military aircraft applications, notably the Airbus A380 and the F-35 Joint Strike Fighter [9]. These systems typically use high-speed, multi-piston, brush-less DC motor pumps operating at speeds up to 20,000 RPM [8]. While these systems function well at high power levels, there is difficulty in scaling them down for applications below 4 kW (5 HP) due to manufacturing tolerances resulting in unacceptably high leakage flows [8]. There is a growing need for better actuators for aircraft at relatively low power levels for applications such as distributed structural control (morphing wings) and smaller aircraft such as UAVs [2, 8, 10].

Smart material electro-hydraulic actuators are a subset of EHAs that utilize a piston pump driven by an active material instead of an electric motor. The result is a nearly solid-state system with no rotating components and almost no moving parts. The high energy density of the materials allows for the creation efficient actuators at smaller scales than can be achieved with electric motor driven EHA pump systems.

### **2.1.2 Principle of Operation**

A smart material EHA consists of a pump driven by a smart material (typically a magnetostrictive rod or piezoelectric stack), which is directly connected to a hydraulic cylinder that is used to drive a load. The actuator principle of operation is shown in Figure 2.3. An applied field, typically sinusoidal, causes the smart material to alternatively extend and contract. The extension stroke compresses hydraulic fluid in the pump chamber; the pressure in the pumping chamber increases until the outlet check valve opens to allow fluid to flow and causes the output hydraulic cylinder to move. During the return stroke, the driver contracts to return the piston to its initial position. The outlet check valve maintains the high-side hydraulic cylinder pressure by preventing backflow while the pumping chamber expands. The pressure in the pumping chamber continues to decrease until it is below the low-pressure side of the hydraulic cylinder. Then, the inlet check valve opens to draw fluid into the pumping chamber to refill for the next compression stroke. Although not shown in Figure 2.3, motion reversal is possible through the addition of a four-way directional control valve. Terfenol-D is a brittle material that is weak in tension, so an accumulator on the low-pressure side of the hydraulic cylinder maintains a bias pressure to keep the smart material driver in compression during operation and to prevent fluid cavitation.

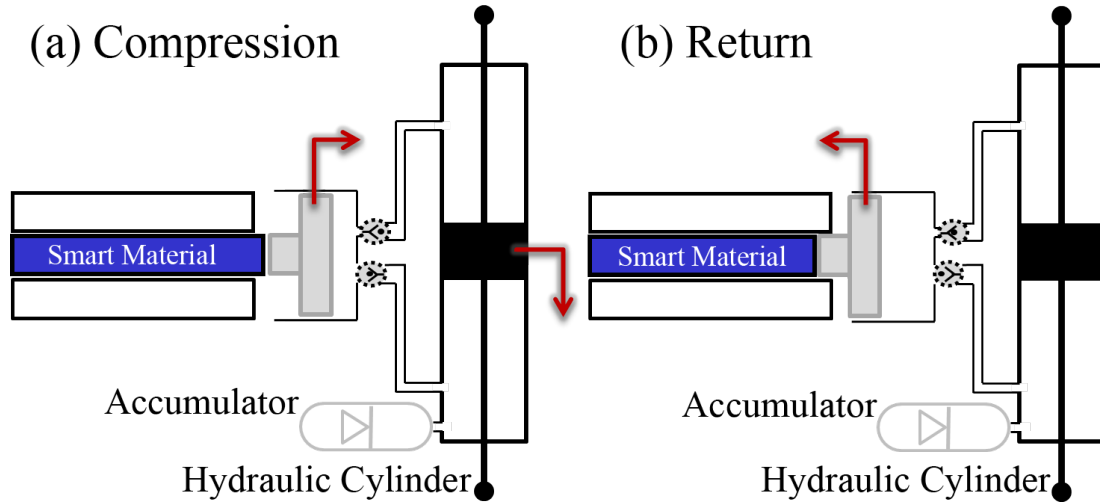


Figure 2.3: The principle of operation for a smart material electro-hydraulic actuator consists of alternating compression (a) and return (b) strokes of the smart material driver resulting in motion of the hydraulic cylinder.

## 2.2 Magnetostrictive Materials

Magnetostriction is the strain response of a material due to changes in magnetic fields. An externally applied magnetic field causes the rotation and realignment, which causes internal strains within the material. Figure 2.4 shows a simplified illustration of the magnetostrictive effect. Magnetostriction was first measured in iron by James Joule in 1842. While the effect can be observed in many magnetic materials, certain compounds containing iron and rare earths known as giant magnetostrictive materials, are capable of producing strains over 1000 ppm. This is several orders of magnitude higher than other materials (Table 2.1). The low Curie temperature of most of the giant magnetostrictive materials make them suitable for only cryogenic applications, but two alloys have been developed with a combination of high Curie temperature and saturation strain: Terfenol-D and Galfenol.

Terfenol-D an acronym for an alloy of terbium “Te”, iron “Fe”, and dysprosium “D” developed by the Naval Ordnance Laboratory “NOL”; the high magnetostriction

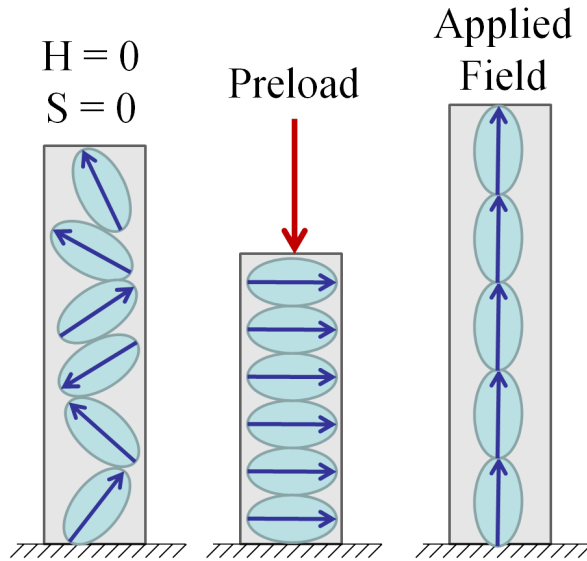


Figure 2.4: A simplified representation of the process of magnetostriction. In the absence of an applied field  $H$  or stress  $S$ , the magnetic domains within the material are aligned randomly (left). Application of a magnetic field aligns the domains with the field direction, causing the material to lengthen (right). Application of a compressive force aligns the domains perpendicularly, increasing the potential magnetostriction, since the the domains have more potential to rotate on average (center).

potential (2000 ppm) makes it useful for high-power actuator applications. Galfenol is an alloy of gallium and iron developed more recently [11]. It has superior mechanical properties than other giant magnetostrictive materials, which allows it to function in tension and be incorporated into the structural components of devices. However, the limited strain potential of Galfenol (approximately 1/4 of Terfenol-D) makes it less suitable for high-power smart material pump development.

Table 2.1: Properties of various magnetostrictive materials [12].

Material	Saturation Strain (ppm)	Curie Temperature (K)
Ni	-50	630
Fe	-14	1040
Fe <sub>3</sub> O <sub>4</sub>	60	860
Tb <sub>0.5</sub> Zn <sub>0.5</sub>	5500	180
Tb <sub>0.5</sub> Dy <sub>x</sub> Zn	5000	200
Terfenol-D	2000	650
Galfenol	300	950

The response of Terfenol-D is nonlinear, depending on many factors including the amount of preload, the temperature, and the operating frequency. Figure 2.5 shows a series of typical response curves for the material over a range of applied stress and input field values. For low drive levels, the response can be approximated by linearizing the stiffness (Young's modulus) and piezomagnetic coupling terms about the operating point. For higher drive levels, the response is very nonlinear as the output strain approaches saturation. An appropriate level of preload stress can increase the strain realized from the material as it aligns the magnetic domains perpendicular to the preload direction enabling a larger motion when field is applied. However, additional



preload reduces the material response, since the applied stress must be overcome to produce motion. The magnetostrictive response acts to extend the length of the rod along the axis of the applied field for both positive and negative fields.

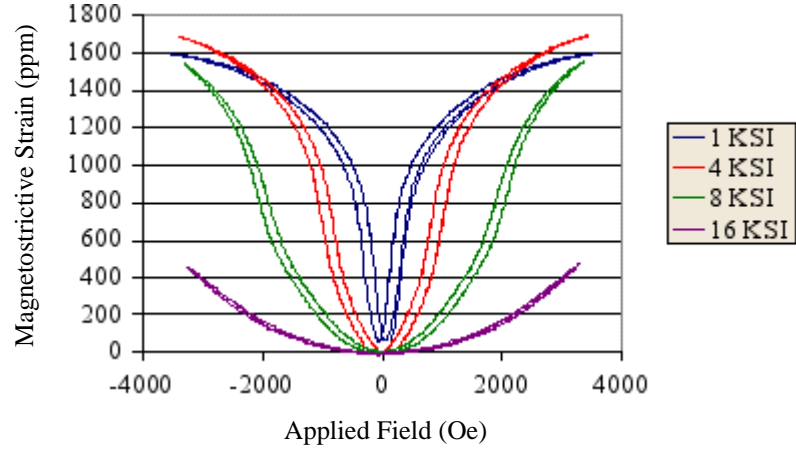


Figure 2.5: Magnetostrictive strain vs. applied field for Terfenol-D for a range of preload stress values (Reproduced from [1]).

Typically, a biased magnetic field is supplied using either permanent magnets or a DC current to a coil to select an operating region for the material at a point where the slope of the magnetostrictive strain vs. field curve is highest for a given load condition, also known as the “burst” region (Figure 2.5). Unbiased operation about the zero applied field point reduces the magnetostrictive response and results in frequency doubling, where the output response frequency is double the input frequency because the maximum positive strain is reached at both the positive and negative peaks of a given cycle.

## 2.3 Displacement Amplification

In order to utilize the small, high-frequency oscillations that can be produced from magnetostrictive materials, some form of amplification is generally required. The methods for increasing the output stroke of magnetostrictive materials can be classified into two categories: direct and rectification.

Direct amplification methods use a mechanism, such as a lever, to multiply the motion that is generated from each material activation. There is a one-to-one correspondence between the motion of the driving material and the output of the mechanism; therefore, the output vibrations of the mechanism are at the same frequency as the driving material activations [13, 14]. A hydraulic version of this approach uses the area ratio between two connected pistons to amplify the motion generated by the smart material [15]. While there are applications where direct amplifications are useful, the the main drawback of this approach is that the force available from the material is decreased by the amplification ratio.

Rectification methods transform the small, high-frequency vibrations generated by the magnetostrictive material into large, lower-frequency displacements of an actuator [7, 13, 16]. These methods are fundamentally different from direct methods because the output motion is no longer directly linked to the material activation frequency.

Smart Material EHAs are one type of step-and-repeat motion amplification device that can be used to increase the displacement obtained from a magnetostrictive material. Fluid rectification via one-way check valves is used to transform the high-frequency vibrations of a smart material into large motions of a hydraulic cylinder. This approach differs from other step-and-repeat or inchworm-type amplification methods, which use friction to collect the vibrations of the material [13]. Friction

based approaches can have problems with either wear or load capacity, especially when high force output is desired.

## 2.4 Other Smart Materials

Piezoelectric materials are ceramic material which demonstrate a strain response to applied electric fields. They have a high-force, low-displacement actuator output profile similar to magnetostrictives and have been demonstrated favorably as drive materials for frequency-rectification hydraulic pumps. This dissertation focuses on the development of actuators utilizing magnetostrictive drivers; the design objective of a high-power EHA for aircraft applications was the reason for using a magnetostrictive driver.

Aerospace applications place a very high priority on reliability considerations, which favors magnetostrictives. One key difference between magnetostrictives and piezoelectrics is that the strain response to an applied field is an inherent material property in the case of magnetostrictives but not in piezoelectrics. Piezoelectric actuators must be polarized to give a strain response. If the piezoelectric is subjected to high temperatures or stress, it may become “de-poled” over time and cease to function [17, 18]. This is not an issue with magnetostrictive materials, which do not lose performance even when subject to high temperatures or stress levels over long periods of time. (Note that performance of magnetostrictives will decrease as temperatures are increased up to the Curie temperature, where no magnetostriction will occur, but the performance will recover when the temperature decreases.) Temperature considerations are a key concern for military aircraft applications, which may be designed for an operating range of  $-54^{\circ}\text{ C}$  to  $130^{\circ}\text{ C}$  [8, 18]. High temperatures can also damage the insulating materials between layers of a piezoelectric stack actuator [19].

Other applications may favor other materials. For instance, it may be beneficial to use a piezoelectric material in a smaller actuator where forces are lower or for more compact packaging, since there is no need for a coil to supply a magnetic field as in the case of magnetostrictives. The model framework presented in this dissertation is general and can be applied to both magnetostrictive and piezoelectric systems. Using piezoelectric materials could potentially simplify the modeling in many cases, as piezoelectric materials tend to have a more linear response than magnetostrictives, especially when operated over a limited input voltage range due to fatigue concerns.

Additional types of smart materials can be used for developing hydraulic actuators. For example, Shin et al. (2002) describes the development of a shape memory actuators (SMA) based pump [20]. However, the benefits and drawbacks of different materials may be quite different, requiring different actuator architectures and corresponding system models. In the case of SMAs, these materials provide much higher displacements (up to 7% strain) but at much lower frequencies (approximately 1-10 Hz) due the time required to heat and cool the thermally activated system. The actuator and corresponding modeling approaches described in this dissertation are suitable only for high-force, high-frequency response materials.

## 2.5 Smart Material EHA Development

The development of smart material EHAs has been an ongoing process. One of the first magnetostrictive pumps described in the literature was a water pump developed by Gerver et al. (1998) [17]. It was designed to replace the conventional water pumps used for life support systems in space suits; with virtually no moving parts, it was could be designed for operation over long durations without maintenance [17]. Metal flaps supported by a springs were used for rectification valves, and the system performance peaked at a 35 Hz input frequency. In an attempt to achieve higher flows

despite the severe frequency restriction, a bellows-type displacement amplification system was used to increase the piston stroke.

Mauck and Lynch (2000) tested a piezoelectric actuator at frequencies up to 60 Hz and demonstrated that using a lower viscosity fluid and applying a higher bias pressure on the system increased the output performance. Further testing up to 100 Hz (Oates and Lynch, 2001) showed a drop in the blocked pressure and a leveling-off in the flow rate at frequencies above 60-80 Hz, which was attributed to the bandwidth limitations of the commercial, ball-spring check valves used [21]. The system included a 4-way valve for bi-directional operation, but the reported output performance was limited to unidirectional results.

Kinetic Ceramics (2002) developed a commercial piezoelectric hydraulic pump with disc-type valves, which has been applied in diesel fuel injector applications [22–24]. Lee et al. (2004) tested a version of these pumps, replacing the passive valve with an active piezoelectric disc valve [23]. Additionally, finite element analysis was applied to predict the flow within the pumping chamber at different frequencies and to propose an optimized housing design [23].

Sirohi and Chopra (2003) compared the use of commercial ball-type valves with reed valves and showed that the reed valves performed better at higher frequencies [25]. Bi-directional motion of the output hydraulic cylinder was demonstrated, but leakage within the 4-way valve used for bidirectional operation reduced the performance compared to unidirectional testing [25].

Bridger et al. (Active Signal, 2004) compared strut-based and inertial designs for smart material pumps [10]. A typical magnetostrictive or piezoelectric actuator design uses a rigid anchor to keep the non-active end of the actuator (tail) from moving. Any compliance in the connecting struts results in less motion as measured at the active end of the actuator (head/piston). An inertial design uses a tuned-mass resonator as

the tail, which amplifies the motion and potential output of the pump piston, similar to the tonpliz designs often used for sonar applications. The inertial mass design was shown to be capable of generating very high pressures, up to 21 MPa (3000 psi); however, the authors were unable to demonstrate fluid rectification at the required high frequency for the inertial mass (2.4 kHz), so the system could not function as an actuator.

Keller (2004) attempted to utilize fluid resonances to design systems to operate at 20 kHz and 1 kHz, but was unsuccessful due to reed valve bandwidth limitations. However, the reed valves were applied successfully in a non-resonant design [22]. Chapman et al. (2005) demonstrated the potential for miniaturizing smart material hydraulic systems by creating a piezoelectric pump approximately the size of a AA battery, capable of producing a flow rate of  $0.8 \text{ cm}^3/\text{s}$  and a pressure up to 4 MPa at a 60 Hz drive frequency [26].

Rupinsky and Dapino (2006) designed an EHA using the magnetostrictive material, Terfenol-D [27]. This system produced a blocked pressure of 7.6 MPa and a flow rate of  $2.2 \text{ cm}^3/\text{s}$  at 160 Hz; a high amount of friction within the tested hydraulic cylinder limited the overall performance. Nosse and Dapino (2007) developed an active valve concept for smart material pumps using magnetorheological (MR) fluids [28]. The change in fluid viscosity with magnetic field is used to direct the flow through the system. While a proof-of-concept pump was able to demonstrate that the system could rectify flow, the pump frequency was limited due to a combination of a low frequency conventional inlet valve and the high viscosity of the MR fluid [29].

Sneed et al. (CSA Engineering, 2006) developed a high power hydraulic pump driven by a Terfenol-D rod for aircraft morphing wing applications. An output power of 150 W was reported at 200 Hz with an input frequency of 200 Hz [30]. The authors

also compared different input waveforms, finding that similar or slightly higher performance was attained by using a square-wave input rather than a sinusoid. A later study (2007) showed that two pumps could be combined in series to generate higher pressures or in parallel to generate higher flow rates [31].

Four different active materials, Lead-Zirconate-Titanate(PZT), Lead-Magnesium-Niobate (PMN), Terfenol-D, and Galfenol, were compared within an actuator tested by John et al.; the PMN and Terfenol-D systems were found to have the highest output power capacity (2.5 W), but the PMN system was found to be significantly more efficient (7% vs. 0.5%) [32]. The strain from the Galfenol driver was too small to produce a positive flow rate. Chaudhuri et al. (2009) compared two different lengths of Terfenol-D rod (51 mm and 102 mm) within an actuator system and reported similar performance results for both [33]. Computational fluid dynamics (CFD) modeling showed that the reed valves used within the system had a significant effect on the performance [33]. John et al. (2009) also used CFD to model the flow of fluid out of the pumping chamber; it was determined that the force required to move fluid in and out of the chamber at high frequencies approached the blocking force of the piezoelectric, limiting the flow [34]. Previous analysis by John et al. showed that the calculated pressure vs. flow rate were highly dependent on the pump geometry [35], including chamfers or fillets on the entrance/exit to the pumping chamber [36].

Chaudhuri and Wereley (2012) also completed a review of smart material EHAs [37]. Factors that limit smart material EHA performance were identified as the rectification valves, fluid inertia and compressibility, drive circuit bandwidth, and actuator material stiffness.

### 2.5.1 Performance Summary

Table 2.2 summarizes the performance of smart material EHAs published in the literature. Where applicable, the results have been converted from force to pressure and from velocity to flow rate using the area of the output cylinder to give a meaningful comparison. Where not reported separately, the power output was estimated by one forth of the unloaded flow rate times the blocked differential pressure (7.1). The results show a general trend of increasing the performance output by increasing the actuation frequency, with input frequencies going from 30-60 Hz up to 600 Hz.

Table 2.2: Performance comparison of smart material electro-hydraulic actuators.

Blocked Pressure [kPa]	No-Load Flow Rate [cm <sup>3</sup> /s]	Power Output [W]	Input Freq. [Hz]	Authors	Year
34	30	0.3	35	Gerver et al. [17]	1998
3800*	5.2*	4.9**	60	Mauck and Lynch [19]	2000
4000	4.2	4.2**	80	Oates and Lynch [21]	2001
1600*	3.0*	1.2**	300	Sirohi and Chopra [25]	2003
8300	0.34	0.7**	100	Lee et al. [23]	2004
2000*	3.7*	3.6	140	Tan et al. [38]	2005
7600	2.2*	4.2**	160	Rupinsky and Dapino [27]	2006
610*	26*	2.5	400	John et al. (PMN) [32]	2007
470*	24*	2.5	600	John et al. (Terfenol-D) [32]	2007
350*	25	3	275	Chaudhuri et al. (51 mm) [33]	2009
350*	23	2.7	475	Chaudhuri et al. (102 mm) [33]	2009
550	19	2.6	200	Kim and Wang [39]	2010
490*	43*	3.6	400	Chaudhuri and Wereley [40]	2010
4500*	17*	18.4	225	Larson and Dapino [41]	2012

\*Value calculated based on the reported blocked-force or no-load velocity values and the output cylinder area. \*\*Estimate of power output based on the no-load flow rate and blocked pressure.



Table 2.3 include several additional efforts by commercial companies developing smart material pumps. The commercial sources are clearly targeting higher power applications by building systems with reported performance values over 150 W. Where reported, the input frequencies remain around 200 Hz, which indicates that the increase in performance is due to the use of larger drive materials and higher input fields compared to the sources listed in Table 2.2. The exception is Bridger et al. (Active Signal), which demonstrated the generation of very high pressures at 2400 Hz by using an resonating mass design; however, fluid rectification was not demonstrated so the pump could not actually produce a positive flow [10].

Table 2.3: Commercial smart material pump developments

Blocked Pressure [MPa]	No-Load Flow Rate [cm <sup>3</sup> /s]	Power Output [W]	Input Freq. [Hz]	Company	Year
10	4	10**	—	Kinetic Ceramics [22]	2002
21	—	—	2400	Bridger et al. [10]	2004
12	25	150	200	CSA Engineering, Inc. [30]	2006
12	21	180	200	CSA [31] (single pump)	2007
22	21	300	200	CSA [31] (two in series)	2007
17	38	160	—	Kinetic Ceramics [24]	2009

\*\*Estimate of power output based on the no-load flow rate and blocked pressure.  
 —Indicates that item was not reported

## 2.5.2 Patents

Several patents have been issued that relate to smart material hydraulic pumps. Stevens (1958) filed an early patent on the topic of smart material pumps; a magnetostrictive or piezoelectric material was used to drive a diaphragm-type pump with

the goal of using for precise metering in a fuel injection application [42]. Stec (1964) described another type of piezoelectric pump, which relied on the volume change of a piezoelectric material to create the pumping action with check valves installed to direct the flow [43]. Designs for miniature piezoelectric pumps were given in two patents by Beckman and Blickstein (1985), which recognized that the piezoelectric driver can also be used to sense the load on the pump with appropriate electrical circuitry [44, 45]. Hansen et al. (1998) used active valves based on magnetostrictive materials [46]. Sager and Matice (1998) designed several pumps using mechanically-amplified piezoelectric bender actuators in different configurations [47]. Other variations on piezoelectric diaphragm pumps, including versions with check valves are described by Bishop (2000) [48].

More recent patents include combining a smart material pump with an hydraulic cylinder to form a complete actuator system. Cusack (1988) proposed magnetostrictive pumps using conventional ball-spring check valves [49] and novel, magnetically-activated reversible shuttle valves [50]. An additional patent described how the magnetically-activated reversible valves could be applied to make a very compact actuator [51]. Engdahl et al. (1990) filed a patent on several configurations of Terfenol-D based pumps for undersea oil and gas production applications; the systems included pumps utilizing multiple Terfenol-D rods to increase the flow rate, using a dual-chamber pump with double-acting piston [52]. Bridger et al. (2004) filed for a patent on a smart material pump using a novel rotating valve design and another system using passive flow geometry to achieve rectification (i.e. a fluid “diode” with no moving parts) [8]. Burkart et al. (2008) received a patent on applying a piezoelectric EHA to an automotive transmission shifting application [53]. O’Neill (2009) published several designs developed by Kinetic Ceramics Inc., featuring disc-type and miniature valves applied to a piezoelectric pump [54].

## 2.6 Summary

In aircraft, there is a general trend in replacing the current hydraulic and pneumatic secondary power systems with power-by-wire devices. A factor driving this trend is the desire to reduce weight and maintenance requirements by eliminating the lines and control valves required to distribute fluid power throughout an aircraft. Electro-hydraulic actuators combine a hydraulic pump directly with a hydraulic cylinder actuator to create a compact, electrically-driven actuator system. Smart material EHAs use fluid rectification via one-way check valves to convert the high-frequency vibrations of certain high-energy-density smart materials (specifically magnetostrictives and piezoelectrics) into large output motions of a hydraulic cylinder.

The concept of using the magnetostrictive effect for pumping fluid dates back to before 1958 [42]. Subsequent development has led to the creation of increasingly high power actuators. However, the peak operating frequency of these systems has been limited to a few hundred hertz, despite the high-frequency capabilities of the smart materials drivers, which have a bandwidth over 1 kHz. A factor that has been identified as a limitation on the frequency response of these devices is the check valves used for fluid rectification. Chapter 3 presents the development and testing of a valve configuration designed to have a very-high frequency dynamic response by utilizing an array of miniature valves.

# Chapter 3

## Miniature Reed Valve Array

### 3.1 Introduction

The basic concept of a smart material electro-hydraulic actuator (EHA) is to use fluid rectification to convert the high-frequency vibrations of a material into large motions of an output actuator. The fluid valves that perform the rectification are a critical system component. Since the volume of fluid that is pumped by each activation cycle of the material is relatively small, any losses during the rectification process have a direct impact on the overall performance of the actuator. Additionally, to create fluid flow, the valves must have a dynamic response high enough to be able to open and close at the appropriate points of the pump piston stroke.

This chapter presents the design and experimental testing of an array of miniature valves. Making the valves smaller is one way to increase the frequency bandwidth over which the valves can rectify fluid flow. By miniaturizing the valves, a smaller (less mass) and stiffer valve can be used to increase the natural frequency of the valve, resulting in a higher operating bandwidth. A summary of work from the literature on high-frequency valve development is presented, which was used to guide the development of a reliable, miniature valve array for use in a smart material pump. Computational Fluid Dynamics (CFD) modeling was used to study the fluid-structure interaction to determine the response of the valve to applied fluid pressure, and the

modeling results are compared with experimental flow testing on the valves. The dynamic performance of the miniature reed array is evaluated by experimental testing within a magnetostrictive hydraulic actuator.

While the valve development and test results presented in this chapter are focused on developing high-frequency valves for smart material EHA pumps, the valves and models presented here may have other applications in high-frequency hydraulics or simply in miniaturization of fluid systems.

## 3.2 Background

The theoretical power output from a smart material pump is directly proportional to the frequency of operation. Both piezoelectrics and magnetostrictives are capable of operating at high frequencies; however, designing check valves to perform the fluid rectification above 1 kHz has proven difficult. Early smart material pumps used either commercially available ball-spring valves or custom disc-spring valves, which limited the pumping frequency for peak performance to below 100 Hz [17, 19, 21, 52]. Later designs used valves consisting of a thin metal reed covering an inlet hole [25, 27, 40]. Using reed valves enabled the performance of smart material electro-hydraulic actuators to improve, but the pumping frequency for peak performance has typically been limited to several hundred hertz.

Single reed-style valves have been the subject of much study for improving the performance of smart material electro-hydraulic actuators. Keller calculated the natural frequency of a reed valve by approximating it as a cantilever beam; however, the effect of the added fluid mass and damping was not considered [22]. Chaudhuri et al. considered the coupling between fluid flow and valve displacement in a 2-D finite element analysis of reed valves [33]. Walters presented flow resistance calculations

based on 3-D computational fluid dynamics (CFD) model which considered a static reed geometry at several points of deflection [55].

One variation of the reed valve concept is a disc-type valve, which have been utilized in the pumps designed by Kinetic Ceramics [56]. Stiffening the reeds to increase the frequency response reduces the flow area (i.e. stiffer reeds open less for a given pressure); to compensate, the reed area is increased, which naturally leads to utilizing the whole opening radius in as disc-type design.

Active valves have been considered as well for extending the frequency response. However, in practice these valves either have the same frequency limitations as passive reeds or significantly restrict flow. They also come at a cost of added complexity; with additional circuitry required to both power the active valves and synchronize the motion with the pump piston driver. High frequency valves based on smart materials have also been proposed using magnetostrictives [57] and MR fluids [28]; however these device concepts have not been incorporated with a pump and hydraulic cylinder to create full actuator systems. Active valves have a potential advantage over passive valves in that the duty cycle (percent of pumping cycle that the valve is open) can be adjusted to optimize performance [38]. Also with active valves, it may be possible to adjust the pump/valve phase to achieve bi-directional motion of an output cylinder without an additional directional control valve.

An approach to developing check valves with increased rectification bandwidth is to use an array of miniature valves. Decreasing the size (mass) of each valve while maintaining the stiffness improves the frequency response, while using many valves in an array can maintain the flow rate of a larger, single-reed design. Previous attempts to develop miniature valve arrays for hydraulic actuators include silicon valves, nickel valves on a silicon substrate, and all-nickel valves [58–60]. These valve designs were manufactured using MEMS processes to selectively add and remove

material to fabricate the different valve layers. The miniature valve array concept was proven to be promising; a pump using the silicon and nickel-silicon valves successfully generated a differential pressure at frequencies above 10 kHz [54, 56, 59]. However, the silicon valves were found to quickly fail when tested at pump pressures, and the nickel valves produced unacceptably high reverse flows because of fabrication defect [56]. Seong et al. used Nitinol to design a miniature valve array with large valve openings by taking advantage of the high strains (up to 10%) available due to the pseudoelastic effect [61]. Testing was limited to static flow conditions; fatigue life considerations may limit the available strains from the Nitinol for high frequency pump applications [62]. No miniature valve array has been demonstrated to reliably rectify flow in the high-pressure, high-frequency environment of smart pumps.

### **3.3 Design of Miniature Reed Valves**

To address the fatigue issues present in previously published miniature reed valve designs; a novel valve design was developed and tested [63]. By decreasing the size (mass) while increasing the stiffness, the dynamic response of these check valves is improved in comparison to the larger single-reed design used for other experimental testing. To maintain a similar level of flow, several of these smaller valves were placed in an array.

Stainless steel was chosen for the valve material due to its corrosion resistance and well-known fatigue behavior. Unlike materials used in previous miniature reed designs (such as silicon and nickel), the fatigue strength for austenitic stainless steel is nearly constant above  $10^6$  cycles [64, 65]. This allows for an endurance limit to be used to design the valves to survive the high-frequency cycles of pressure generated by the pump.

The miniature reed valve array was designed to fit within the valve port of an existing magnetostrictive electro-hydrostatic actuator to facilitate testing (Figure 3.1). An adapter plate was added to the system to maximize the available area to use for

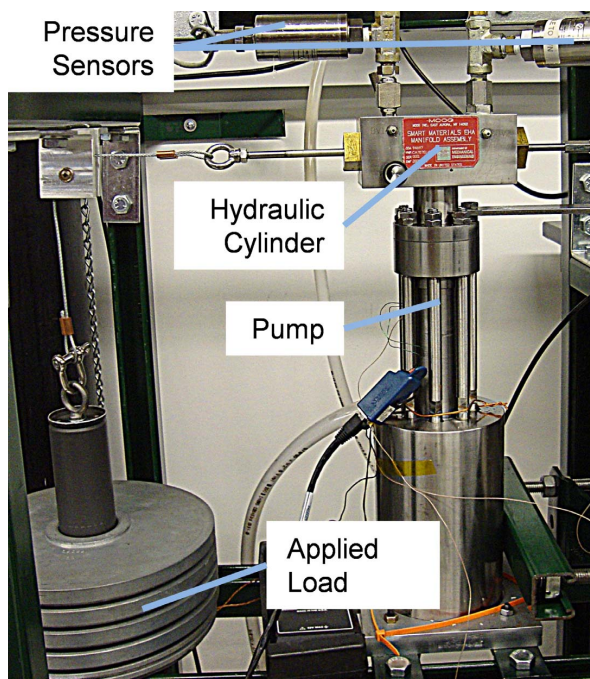


Figure 3.1: Magnetostrictive electro-hydraulic actuator used to evaluate the dynamic performance of the miniature reed valve arrays.

the miniature reeds (Figure 3.2); however, the valve port size constrained the overall diameter of the reed valve array to 6.4 mm (0.25 in). This diameter limited the number of valves that could be used in the array to 21.

The valve design consists of four layers: inlet, valve, spacer, and outlet (Figure 3.3). The valve layer contains the valve flaps, which cover holes in the inlet layer. The outlet layer contains both the fluid flow path and stops to limit the travel of the valves. The maximum distance that the valves can open is determined by the



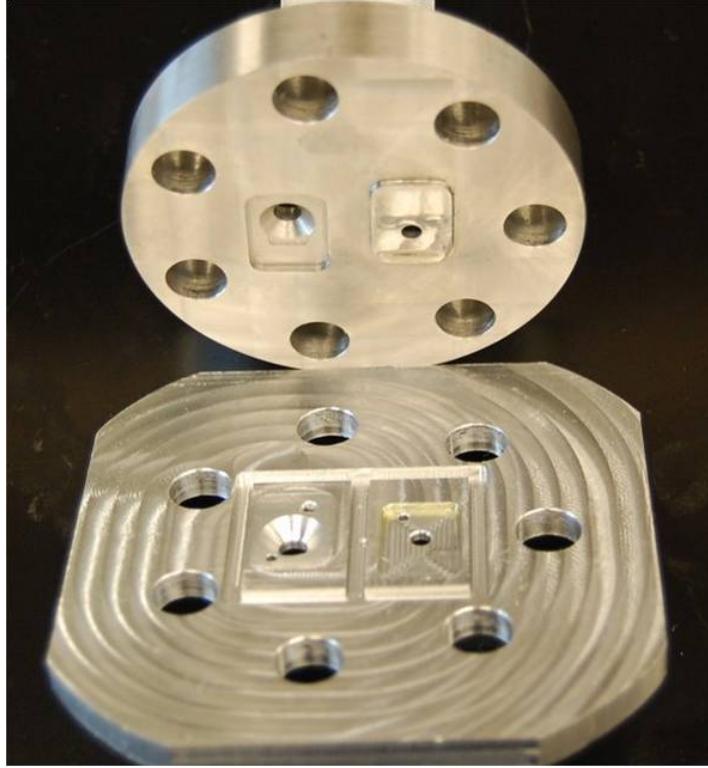


Figure 3.2: Valve port geometry for the the magnetostrictive hydraulic pump used to evaluate the miniature reed valve array performance. While an adapter plate (lower) was used to maximize the size of the array based on the ports in the existing pump head (upper), the array was still limited to using only a small part of the pumping chamber area. The opening for the outlet valve array is shown on the left, the inlet reed array fits on the bottom side of the adapter plate (not shown). See Figure 4.8 for a view of the adapter plate installed in the system.

thickness of a spacer layer between the valve layer and the outlet layer. Limiting the opening distance is necessary to keep the stress in the valve below allowable levels. Alignment holes are provided to keep the different layers aligned with pins.

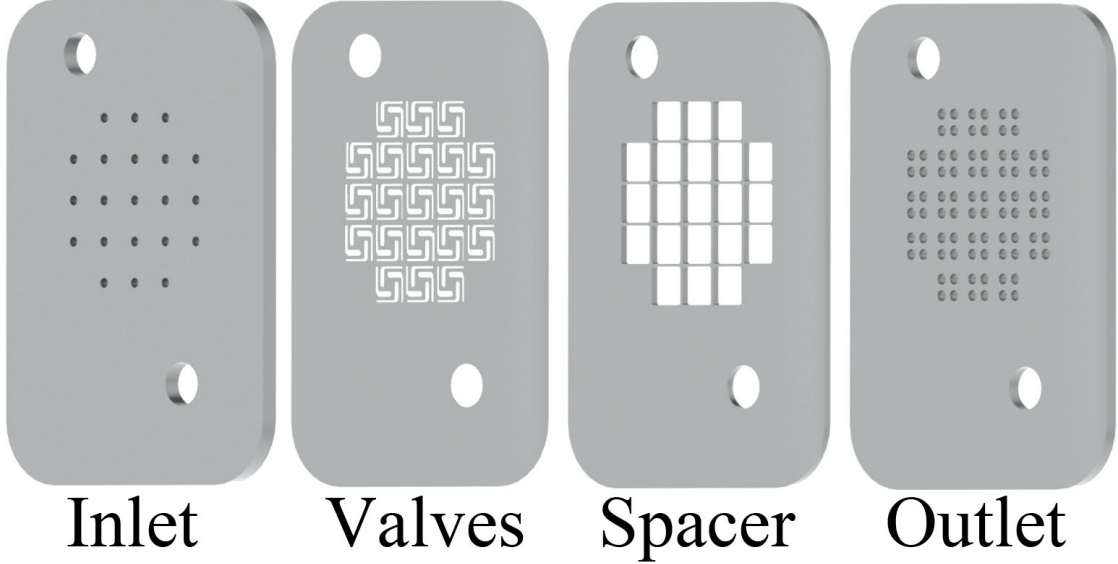


Figure 3.3: Design of the miniature reed valve array layers: outlet layer, spacer layer, valve layer, and inlet layer (left to right). Two large holes are provided on each part for alignment pins.

For reliable operation at frequencies at high frequencies, design for infinite fatigue life was applied for the high-pressure environment in the pump. An allowable stress of 390 MPa (56 ksi) was calculated for the 301 fully-hardened stainless steel used in the design (Appendix A). Two extreme cases were considered for the analysis: full valve displacement and blocked pump pressure. The displacement is limited by the designed thickness of the spacer layer (25  $\mu\text{m}$ ), and the maximum blocked pressure capability of the pump was determined in previous experiments to be approximately 10 MPa (1500 psi). A finite element model was developed using COMSOL to analyze

the stress in each of these cases; the design dimensions were optimized to reduce the stress to allowable levels. The maximum stress was calculated to be 374 MPa for the fully-open case and 368 MPa for the maximum pump pressure level (Figures 3.4 and 3.5).

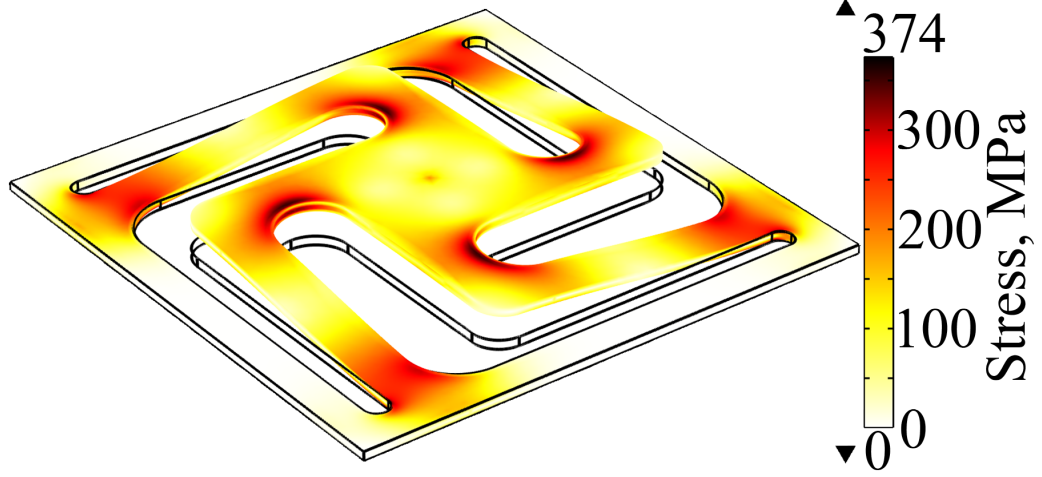


Figure 3.4: Design stress in fully-open miniature reed ( $25\ \mu\text{m}$  displacement) calculated using a COMSOL finite element model.

For successful performance in the EHA pump at frequencies over 1 kHz, it is desired for the valve natural frequency to be well above this value. The first natural frequency of the valve design was calculated as 20.7 kHz in vacuum using COMSOL (Figure 3.6). During operation, the hydraulic fluid effectively adds mass to the valve, decreasing frequency response. The decreased first natural frequency in the fluid,  $f_{\text{fluid}}$ , compared to the natural frequency in vacuum,  $f_{\text{vacuum}}$ , is then

$$\frac{f_{\text{fluid}}}{f_{\text{vacuum}}} = \left(1 + \frac{m_{\text{add}}}{m_{\text{p}}}\right)^{-1/2}, \quad (3.1)$$

where  $m_{\text{p}}$  is the mass of the plate and  $m_{\text{add}}$  is the added mass [66]. The miniature valve geometry can be approximated by a square plate to give  $m_{\text{add}} = 0.455\rho l^3$ , where

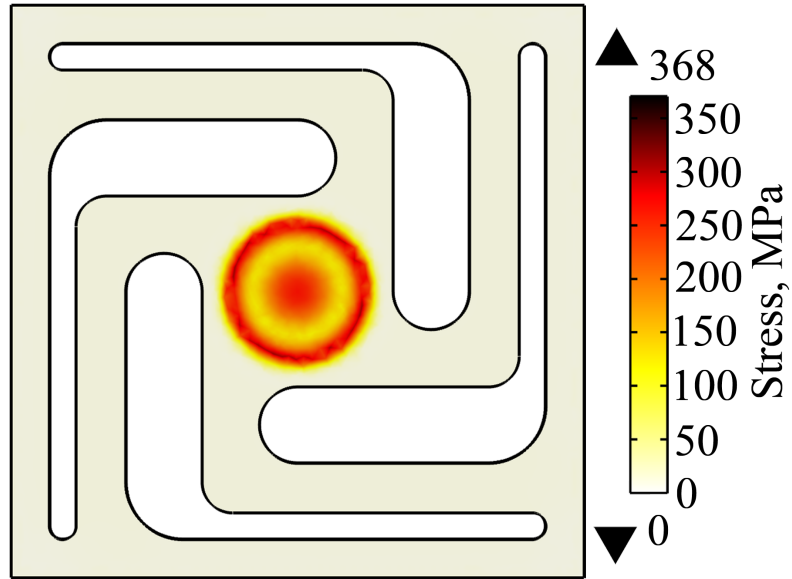


Figure 3.5: Design stress in the miniature reed valve while closed, supporting a 10 MPa (1500 psi) pressure.

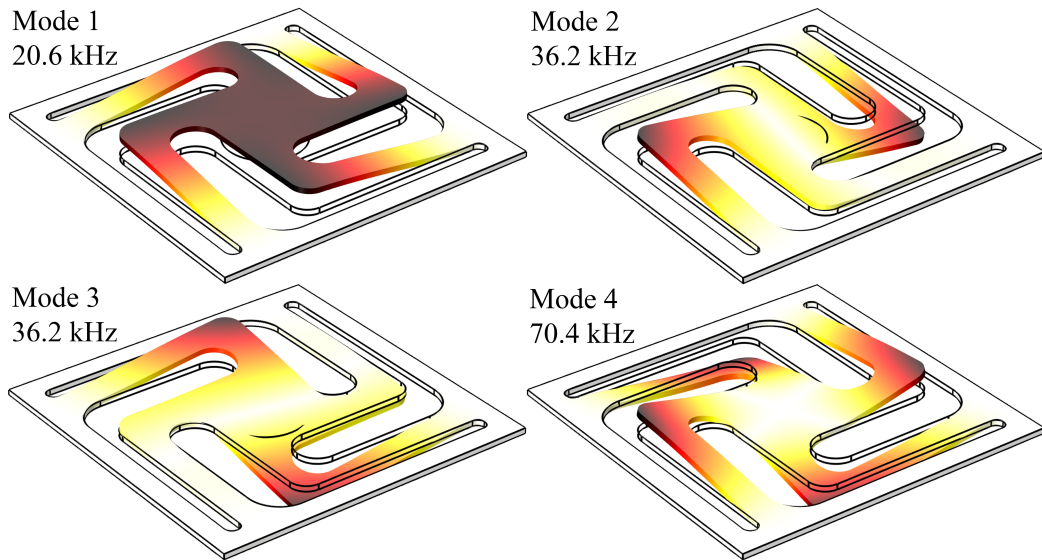


Figure 3.6: First four mode shapes calculated for the miniature reed valve design; the first mode is calculated at 20.7 kHz in vacuum.

$\rho$  is the density of the fluid and  $l$  is the length of one of the sides. Equation (3.1) predicts that the miniature reed design has a first natural frequency of 14.7 kHz in hydraulic fluid (Mobil DTE 24).

### 3.4 Fabrication

As designed, the reed valves consist of 500  $\mu\text{m}$  square flaps with four spring arms. These flaps each cover a 360  $\mu\text{m}$  diameter hole in the inlet valve layer. The valve and spacer layers were laser cut from 25  $\mu\text{m}$  thick stock. The thicker inlet (700  $\mu\text{m}$ ) and outlet (300  $\mu\text{m}$ ) layers were fabricated with micromachining processes.

The laser cutting process was found to leave a large amount of oxidation on the valves. In initial tests on the valves in the as-received condition, the oxidation effectively reduced the spacing distance, which limited the amount that the valves could open and decreased the flow performance. Additionally, the layer of oxidation interfered with the seal between the valve and valve seat to cause an increase leakage flow under reverse pressure. Polishing removed much of the oxidation to allow the valves to function as designed (Figure 3.7).

The stiffness of the miniature reed valves is calculated to be 8.55 N/mm using the 3-D finite element structural mechanics model. The model geometry was adjusted according to measurements of the reeds to account for fabrication tolerances and material removal from polishing.

### 3.5 Finite Element Analysis of Fluid-Structure Interaction

To calculate the expected flow performance of the miniature reed valves, the multiphysics software COMSOL was used. A fluid-structure interaction model was developed based on the geometry of the reed valves. The fluid pressure and the flow distribution along with the resulting valve deformation were solved simultaneously.

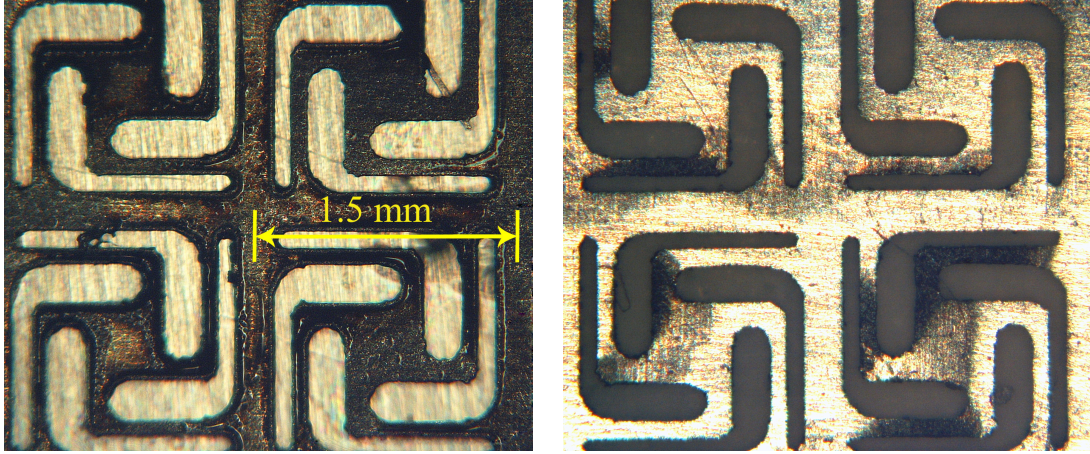


Figure 3.7: The as-received condition of the miniature reeds had a large amount of oxidation remaining from the laser cutting process (left). A polishing step removed much of this oxidation (right).

Figure 3.8 shows the geometry for modeling the flow through one of the valves in the array. A 2-D axi-symmetric model was used to efficiently predict the flow characteristics of the valve. The 2-D approximation of the valve as a disc is suitable because the majority of the pressure drop in the valve takes place underneath the valve seat.

Table 3.1: Area comparison for miniature reed valve design; the area at the interface between the valve and inlet passage is much smaller than the inlet and outlet passages, which makes a 2-D axisymmetric model appropriate for calculating the pressure drop across the valve array.

Region	Area [mm <sup>2</sup> ]
Valve/Inlet Interface, Fully Open Valve	0.03
Inlet Passage	0.10
Outlet Passages	0.40

The stiffness of the valve was calculated using a 3-D structural mechanics model (Figure 3.4) and applied to the valve disc as an additional load. A constant pressure differential was applied between the inlet and outlet, and a no-slip condition was applied to the walls. To keep the fluid domain continuous, an offset is needed between the

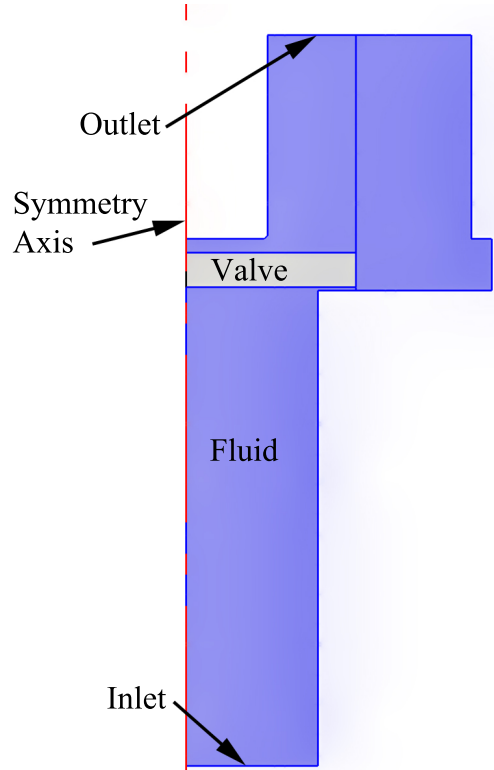


Figure 3.8: Geometry used for finite-element modeling using COMSOL.

valve and valve seat in the initial geometry. This offset was kept small to minimize its effect on the solution. An arbitrary Lagrangian-Eulerian (ALE) finite element formulation was used to deform the mesh and track the motion of the valve with applied pressure. The finite element modeling results were validated based on static testing of the reed valve.

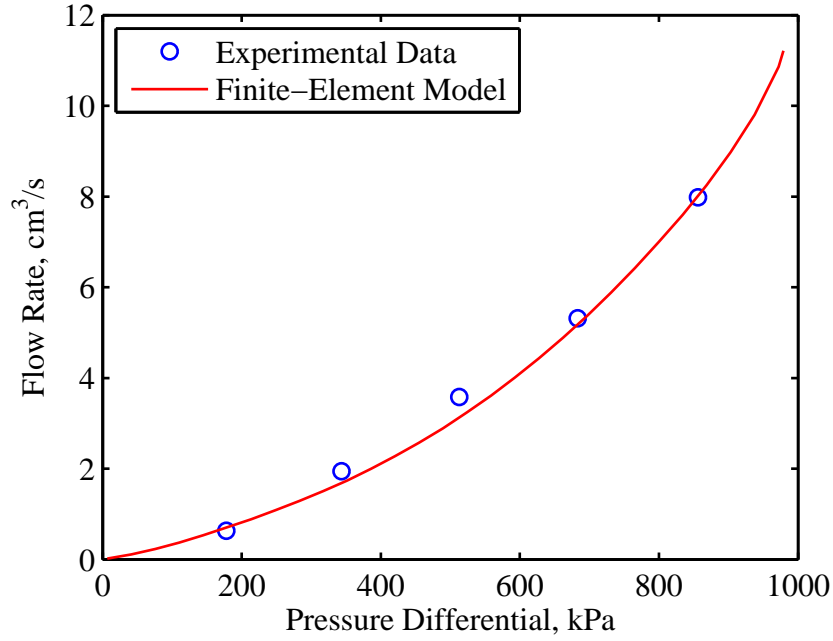


Figure 3.9: Comparison of steady-state testing results to finite-element model results.

### 3.6 Steady-State Flow Testing

A steady-state flow test was conducted to determine the flow resistance of the valve and validate the finite-element model results. A valve holder was fabricated for the test to match the geometry of the valve port in the pump. A fluid reservoir supplied Mobil DTE 24 hydraulic fluid at a constant pressure, maintained by a compressed nitrogen cylinder and regulator. The mass flow rate of the fluid was measured with a precision scale and the pressure differential across the valve was measured using two Sensotec 7351-02 pressure sensors. Testing was conducted up to 900 kPa; the results are compared with the COMSOL finite-element model predictions (Figure 3.9).

To test for the one-way performance, a set of tests was conducted with the direction of applied pressure reversed. A small amount of leakage was observed, measuring approximately  $0.5 \text{ cm}^3/\text{s}$  over the full range of pressures tested (0 – 1.4 MPa). The



leakage may be attributed to the valves not sealing fully because of oxidation remaining from the laser cutting process (Figure 3.7). Misalignment between the valve flaps and inlet holes may be an additional source of leakage.

### 3.7 Actuator Testing of Miniature Reeds

Dynamic testing of the miniature reeds was conducted using an experimental magnetostrictive electro-hydraulic actuator (Figure 3.1). For comparison, the system was also tested using large single-reed valve for fluid rectification and with the same test conditions. A constant sinusoidal current ( $3.5 A_{\text{rms}}$ ) was applied over a range of frequencies; the resulting displacement of the hydraulic cylinder was measured. A bias pressure of 2.6 MPa (375 psi) was used for all tests, resulting in a pre-load of 10.3 MPa (1.5 ksi) on the Terfenol-D driver due to the area ratio between the 13 mm diameter rod and 25 mm diameter pumping piston. (See Chapter 4 for a detailed description of the reduced-volume-manifold magnetostrictive electro-hydraulic actuator used to evaluate the miniature reed array.)

While the miniature reeds were demonstrated to survive the high-pressure, high-frequency environment within the pump, the frequency bandwidth of the actuator did not change (Figure 3.10). This indicates that other factors, such as the fluid passage dynamics, limit the frequency response of the experimental system. The flow rate in the system with the miniature reeds was also significantly reduced when using the miniature reeds, but this reduction was a consequence of designing the miniature reed array to fit in the same valve port as the single-reeds (to enable comparison testing). This artificially limited the number of valves that could be used in the array; a pump head made specifically for the miniature reeds could have incorporated at least 4 times as many valves without an increase in overall size.

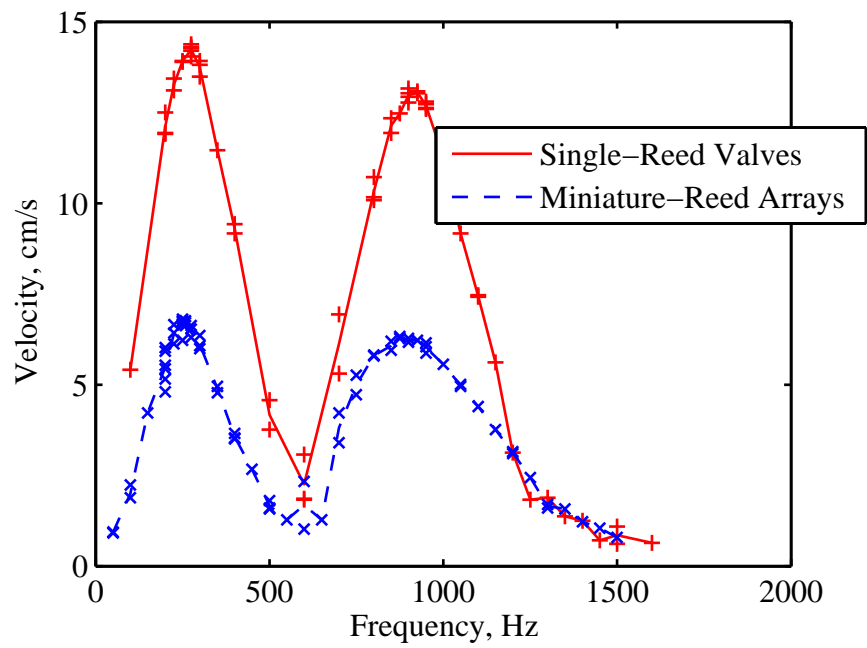


Figure 3.10: Unloaded velocity performance comparison between the single reed valves and the miniature reed valve array tested in an experimental actuator with constant applied current over the frequency range.

### 3.8 Summary

The novel design for miniature reed valves, with each layer machined separately using micromachining processes, successfully rectified fluid flow. The design was proven to be robust, successfully surviving operation at high-pressure and high-frequency inside the pump. The measured flow rates from the miniature reed valves are lower than the flow rates for the single-reed valves, but this is expected because the miniature-reed array design utilizes the existing valve ports at a penalty of greatly reduced available flow area. The flow restriction of the valves could be reduced simply by using a larger number of valves in the array. The area of the pump piston is approximately eight times the area of the inlet and outlet reeds combined ( $507 \text{ mm}^2$  vs.  $63 \text{ mm}^2$ ), so a pump designed specifically for a miniature-reed array could utilize significantly more valves without increasing the overall size of the system.

A fluid-structure interaction model for valve flow resistance has been established and the results verified by steady-state measurement of the flow through the valve array. Additionally, the natural frequencies of the valves were calculated using finite element analysis, and the effect of the added mass of the hydraulic fluid was calculated. These calculations show that the miniature reed valves should be capable of rectification of fluid flows at frequencies well over 1 kHz, even though testing was limited by the experimental smart material pump used.

The valves used within the reduced-volume EHA experimental system were shown to not be a contributing factor in the frequency bandwidth of the system. Instead, the frequency response of the hydraulic components, i.e. passages and flow volumes within the pump and manifold, determined the system response. This means that the dynamic response of the fluid system, including any connected actuators, must be taken into account during the design process of the system. Optimizing the manifold

passage geometry to support high-frequency fluid flow is necessary to fully utilize the miniature-reed valve design to improve the performance of smart actuators.

# Chapter 4

## Reduced Volume Manifold EHA Experimental Testing

### 4.1 Introduction

This chapter presents the experimental results for the performance of a magnetostrictive electro-hydraulic actuator (EHA) designed with a reduced-volume manifold. The system was tested in several configurations over a range of input conditions in order to quantify the performance of the system and to identify the limitations on the system frequency bandwidth. Additionally, this system was used to evaluate a novel design for a miniature reed valve array (Chapter 3) and to validate a general modeling framework for smart material EHAs (Chapter 6).

### 4.2 Background: EHA with External Hydraulic Cylinder

The reduced volume manifold EHA presented in this dissertation utilizes a magnetostrictive pump that was developed previously. Rupinsky (2006) and Walters (2008) designed, fabricated, and tested the pump section of the actuator, utilizing an external hydraulic cylinder connected with hydraulic tubing to form a complete EHA [27, 55, 67]. The reduced volume manifold replaces the top plate of the pump, which had contained the input and output ports (Figure 4.1). Design calculations and detailed

design drawings for the pump components were published previously by Rupinsky (2006) [67].

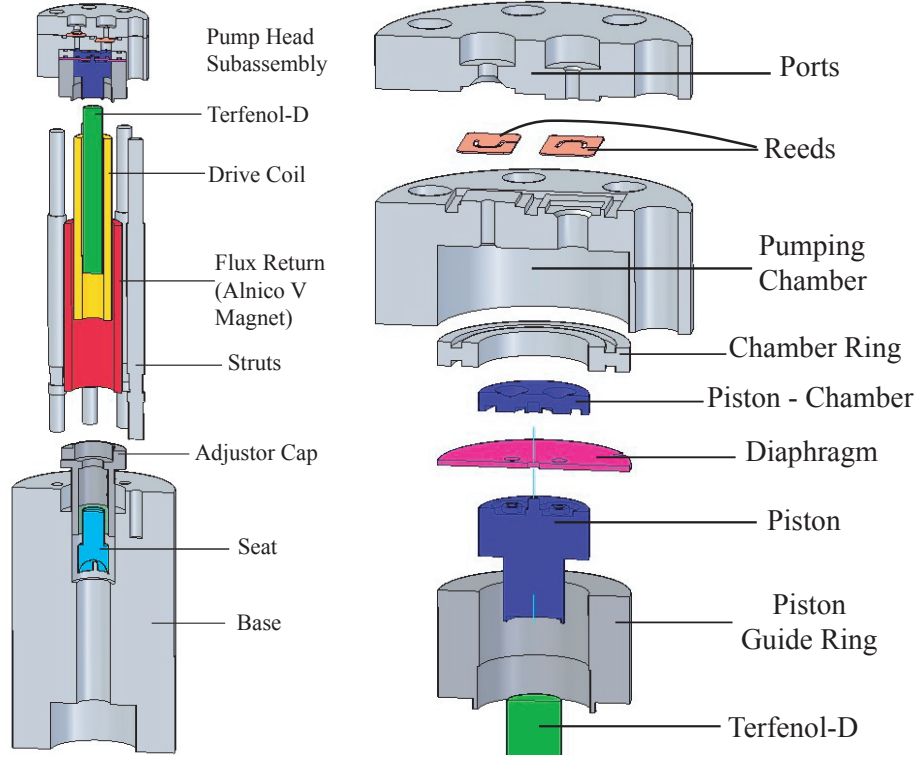


Figure 4.1: Exploded view of the pump assembly with a detailed view of the pumping chamber (Reproduced from [67]).

The pump has a piston diameter of 25.4 mm and is driven by a 114 mm long, 12 mm diameter solid Terfenol-D rod (Figure 4.2). For testing, pump was connected to a commercial hydraulic cylinder with a 25 mm bore and 18 mm rod (Vickers TV25BE7N3KA102HR). The frequency response of the system was limited, with a peak unloaded velocity of 0.93 cm/s at 165 Hz [67]. The relatively low bandwidth of the pump actuator was attributed to the high amount of friction present in the hydraulic cylinder [27]. The blocked pressure capacity was measured to decrease as

the input frequency was increased, making the system unable to move the hydraulic cylinder at frequencies above 165 Hz. Additionally, the pressure drop due the relatively long sections of tubing used to connect the pump with the output cylinder would have contributed to reduced the performance of the system, especially at higher frequencies due to the inertia of the fluid.

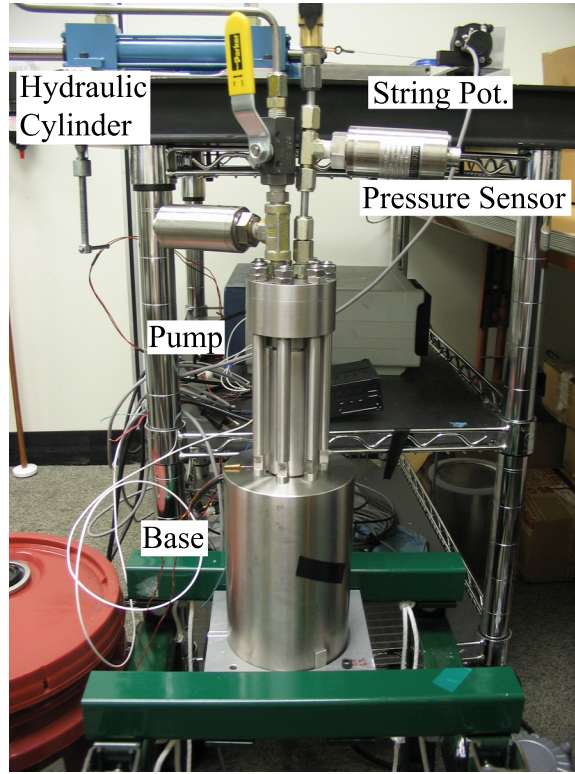


Figure 4.2: Experimental setup for previous magnetostrictive EHA configuration used by Rupinsky (2006) [27, 67] and Walters (2008) [55] (Reproduced from [67]).

### 4.3 Reduced Volume Manifold Smart Material EHA

To address the limitations of the external hydraulic cylinder EHA configuration presented in the previous section, a new manifold was created for the system. The

manifold contains the output hydraulic cylinder and associated flow passages, and it bolts directly onto the pump to create a self-contained, compact actuator. Integrating the hydraulic passages into a manifold with the output cylinder reduces the volume of the system compared to using discrete hydraulic tubing; hence the system is referred to as the “Reduced Volume Manifold EHA” in this dissertation.

The test configuration for the system is shown in Figure 4.3. A sinusoidal current was applied to drive the rod at over a range of input frequencies, with a bias DC current applied to prevent frequency doubling by the magnetostrictive material. A bias pressure was applied using a nitrogen-charged accumulator keeps the Terfenol-D rod in compression during operation and to favorably align the magnetic domains of the material for peak performance, as shown in Figure 2.5. The hydraulic fluid used was Mobil DTE-24, which has a density of  $871 \text{ kg/m}^3$  at a viscosity of 80 cSt at room temperature (See Section C.4).

An AE Techron LVC 5050 linear amplifier was used to apply the input current to the system, and the displacement of the output cylinder was measured using a string potentiometer. A strain gage was used to measure the strain of the Terfenol-D rod during testing. Two thermocouples were used to measure the temperature of the rod and input coil, which was restricted to between 21 and 26 degrees C to avoid variation in the actuator performance due to temperature. Two Sensotec TJE-5000 pressure sensors were provided to measure the pressure at the high-pressure and low-pressure sides of the output cylinder. A National Instruments cDAQ-9178 was used to collect the sensor data from the experimental system and to generate the sinusoidal input signal with DC bias applied to the drive coil.



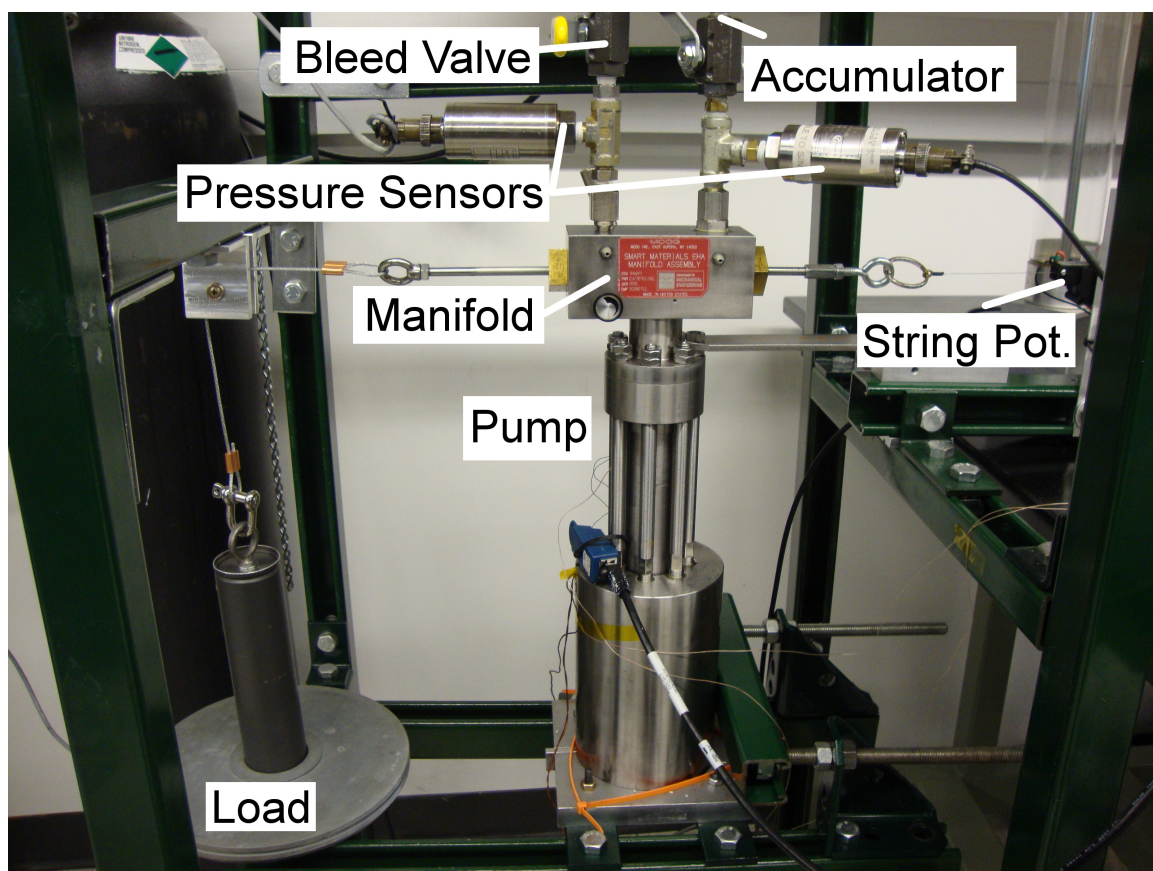


Figure 4.3: Test configuration for reduced-volume manifold magnetostriuctive EHA pump; the system was tested over a range of loads using the weight and pulley system shown.

## 4.4 Identification of Losses in Experimental Actuator

Initial testing of the reduced volume manifold EHA system was conducted to identify sources of loss, which could be controlled or eliminated to improve the performance of the system. The system response was compared to previous testing using an external hydraulic cylinder. The effects of diaphragm deformation and an unfavorable resonance due to an extra volume associated with a pressure sensor on the high-pressure side of the hydraulic cylinder were also considered.

### 4.4.1 Comparison to External Hydraulic Cylinder Actuator

The effect of combining the hydraulic cylinder with the pump using a reduced volume manifold was evaluated using the same test conditions applied previously to the system with an external hydraulic cylinder. A biased sinusoidal current of  $3.5 A_{\text{rms}}$  was applied and the output cylinder velocity was measured for a range of input frequencies [27, 67]. The measured velocity was converted to flow rate according to the output cylinder area for comparison to previous testing, since previous hydraulic cylinder had a different internal area. A bias pressure of 1.7 MPa (250 psi), which corresponds to a preload stress of 7 MPa (1 ksi), was applied to the Terfenol-D rod.

The reduced volume manifold system showed a dramatic increase in performance over the previous system, both in the increased flow (from  $2 \text{ cm}^3/\text{s}$  to  $7.5 \text{ cm}^3/\text{s}$ ) and the expanded input frequency bandwidth over which the system operates (165 Hz to 300 Hz). This increase can be attributed to the reduction in flow losses by using shorter flow passages and the decrease in output cylinder friction.

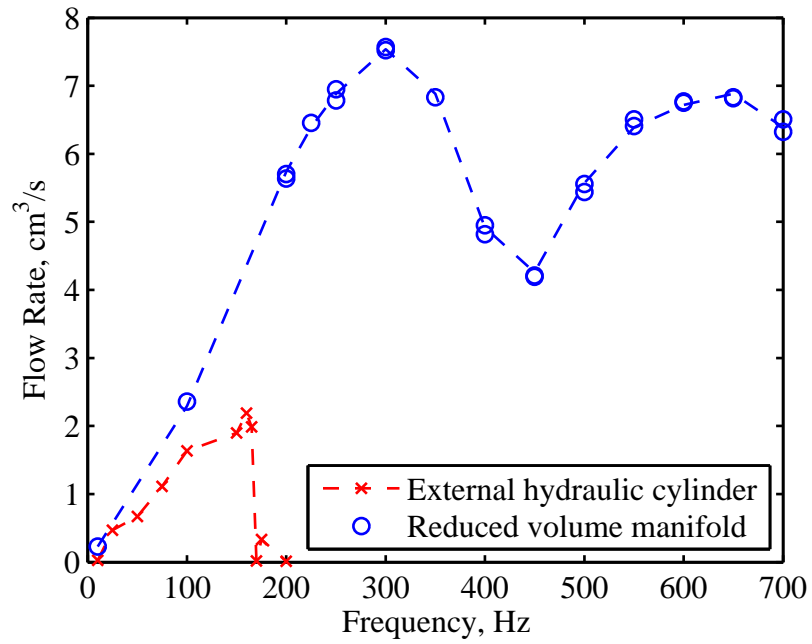


Figure 4.4: Unloaded flow rate for the magnetostrictive pump connected to an external hydraulic cylinder (Figure 4.2) and using the reduced volume manifold (Figure 4.3). Each circle represents an individual test result; the dashed lines indicate the average flow rate at each frequency.

#### 4.4.2 Diaphragm Deformation

Further testing of the system revealed that the diaphragm used to seal the pumping chamber was getting deformed during testing, most likely during the application/removal of the bias pressure during assembly/disassembly (Figure 4.5). The bias pressure is necessary to prevent prevent cavitation and apply a mechanical preload to the Terfenol-D rod. Terfenol-D is a relatively brittle material, so it is critical to maintain a mechanical preload to ensure that the material operate in compression; this preload also improves the output strain of the material by aligning the magnetic domains perpendicular to the rod axis before a field is applied (Figure 2.5).

In the experimental system, the preload is provided by a bias pressure maintained by a nitrogen-charged accumulator. After the system is assembled, filled with fluid, and purged to remove any entrained air bubbles; the bias pressure is applied in progressive intervals, up to a predetermined value. After each pressure addition, the preload bolt within the pump base is adjusted to keep the diaphragm flat within the pumping chamber (i.e. the “seat” in Figure 4.1 is adjusted to compensate for the compression of the Terfenol-D rod with applied pressure). To prevent deformation of the diaphragm during pump assembly, the pressure addition interval was decreased from 200 kPa (30 psi) to 100 kPa (15 psi). Removal of the bias pressure was conducted in a similar fashion; however, since it is more difficult to remove pressure from the system in small intervals, a new diaphragm was installed during each assembly of the pump. Note that in normal operation, the bias pressure would be applied during initial assembly and would be maintained for the lifetime of the system; in this research actuator, more frequent assembly/disassembly was necessary to test the system in different configurations.

A bias pressure of 2.6 MPa (375 psi) was used for all testing subsequent to the initial set of test data (Figure 4.4), which was conducted at a lower bias pressure

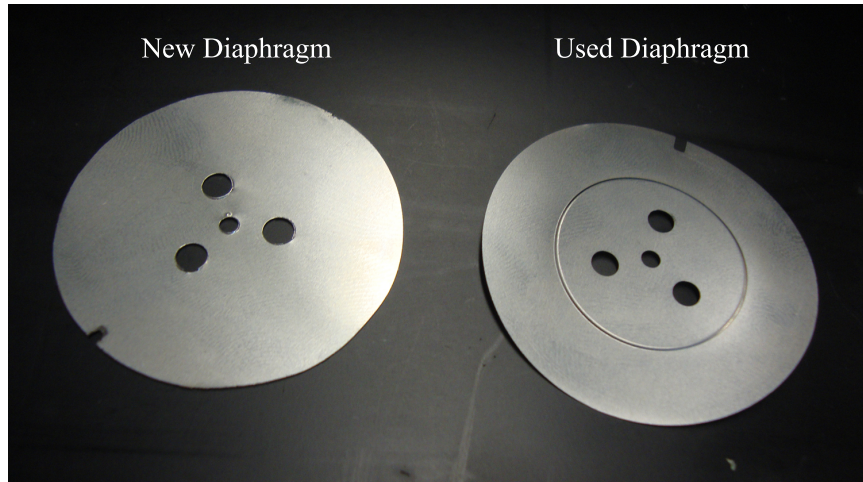


Figure 4.5: The application and removal of the preload procedure caused a plastic deformation of the piston seal diaphragm.

to match experimental conditions used for the external hydraulic cylinder actuator. Using a new piston seal diaphragm and the revised procedure for applying the bias pressure increased the output velocity of the output cylinder significantly (Figure 4.6). The frequencies at which peak performance occurred remained the same.

Plastic deformation causes the diaphragm stiffness to be increased due to strain hardening of the stainless steel shim stock used; an increase in the stiffness of the diaphragm results in less displacement of the magnetostrictive rod during each pumping cycle, decreasing the flow rate. To quantify this effect, several diaphragms in both new and deformed condition were tested in compression using a mechanical testing machine (Test Resources model 131R500). The diaphragm was tested in the exact configuration used within the EHA pump, using the piston and pumping chamber from the pump itself. The stiffness of the “deformed” diaphragm taken out of the pump was 1500 N/mm, which was much higher than the 160 N/mm stiffness measured for a “new” diaphragm.

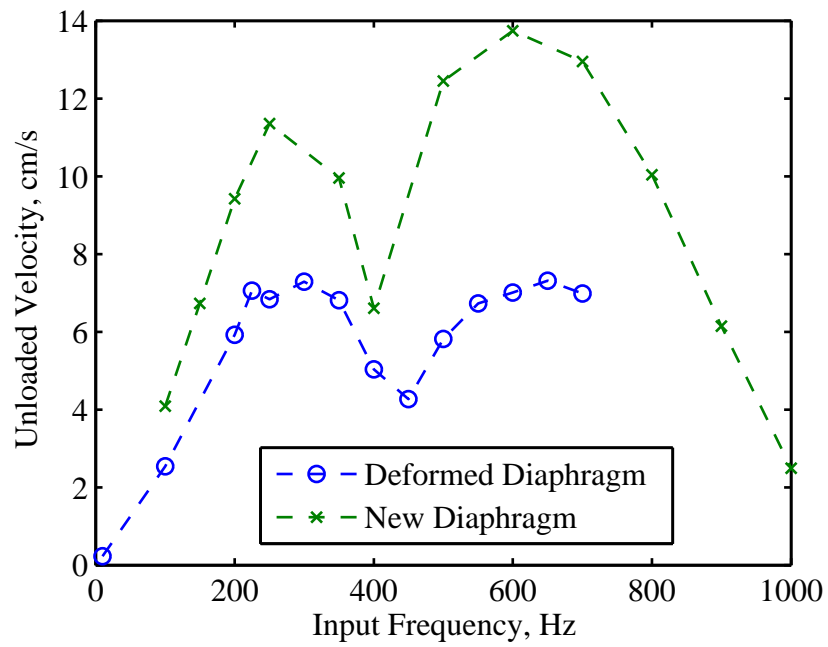


Figure 4.6: Replacing the diaphragm and adjusting the preload sequence improved pump flow performance significantly.

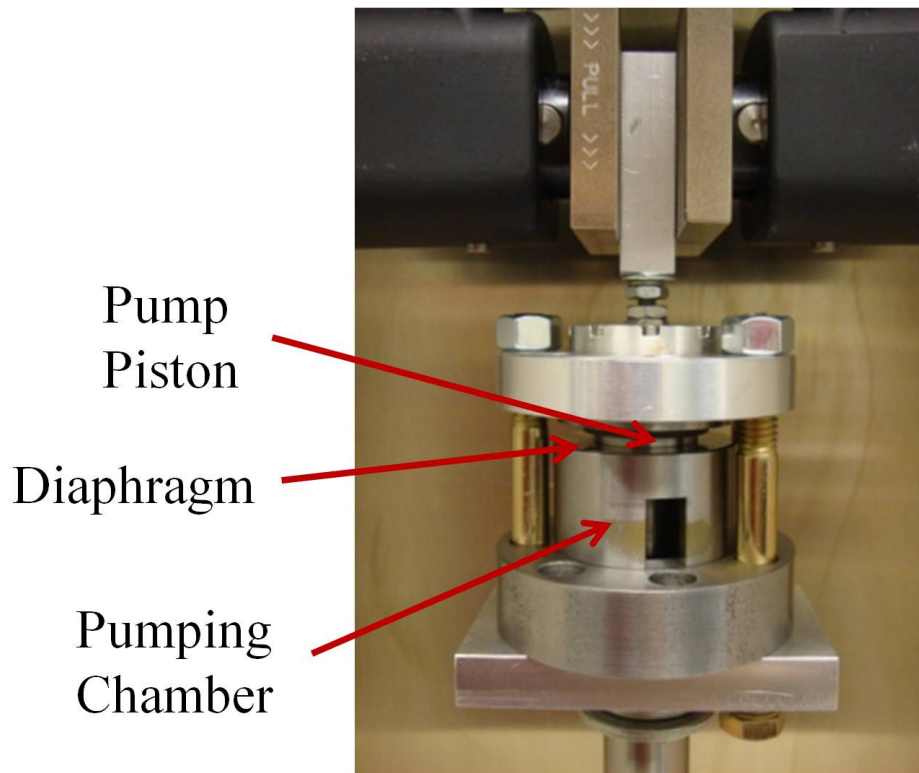


Figure 4.7: Compression test setup for measuring the pump diaphragm stiffness.

### 4.4.3 Hydraulic Resonances

Modeling of the system showed that the extra volume associated with a passage connecting a sensor measuring the pressure at the high-side of the output cylinder added a significant compliance to the system [41]. The total volume added is approximately  $10 \text{ cm}^3$  (0.6 cu. in.); the output hydraulic cylinder for comparison has a volume of 1.7–6.5  $\text{cm}^3$  (0.1–0.4 cu. in.), depending on the cylinder position. (Refer to Appendix C for detailed system dimensions.) A needle valve was added to cut off the extra volume for testing, while allowing for purging of entrained air during pump assembly and connection to a pressure sensor for blocked-pressure measurements (Figure 4.8).

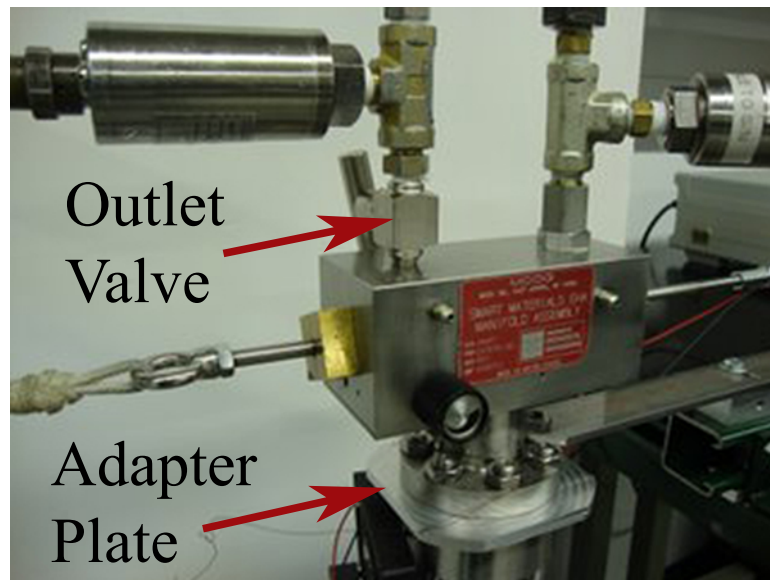


Figure 4.8: A needle valve was added to the system to close off pressure sensor passage to determine the effect on the system performance. Also shown is the adapter plate used for miniature reed array testing (Figure 3.10).



Closing off the extra volume with a valve improved the output performance and bandwidth of operation (Figure 4.9). The maximum unloaded velocity was increased from 10.4 cm/s to 14.3 cm/s, using the same 3.5 A<sub>rms</sub> sinusoidal input current with DC bias applied at each frequency. The frequencies at which peak performance occurred also increased by closing off the extra volume, from 200 Hz to 275 Hz for the first velocity peak and from 550 Hz to 925 Hz for the second peak.

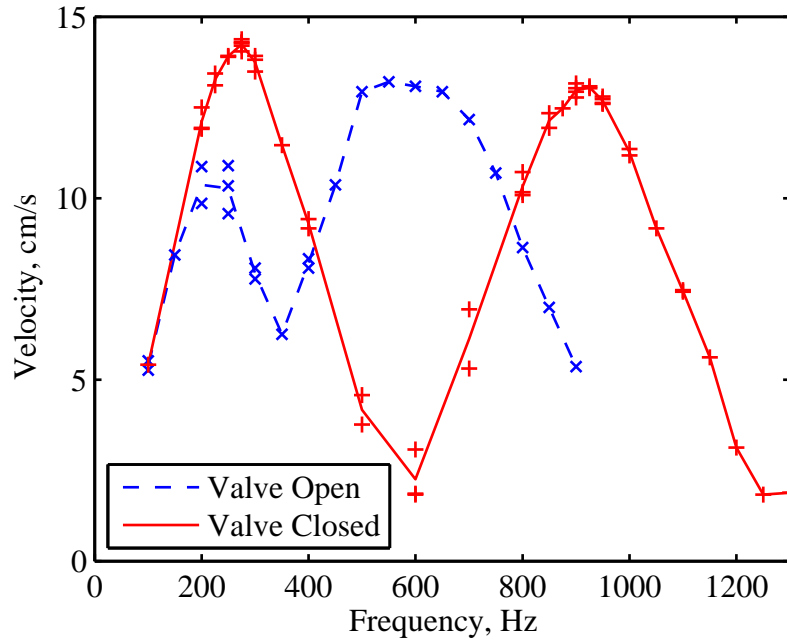


Figure 4.9: Removing the extra fluid volume associated with the output pressure sensor improved the pump frequency bandwidth and performance. A sinusoidal current of 3.5 A<sub>rms</sub> was applied at each frequency.

## 4.5 Power & Efficiency Evaluation

After removing the unnecessary source of loss from system by using a reduced-volume manifold, correcting the seal diaphragm deformation, and removing the extraneous



sensor volume, a series of tests were conducted to quantify the performance of the system. A sinusoidal current was applied to the system at discrete frequency points over a range of frequencies (100 Hz to 1200 Hz) with a DC bias current to keep the applied field in a one direction. Testing over the frequency range was repeated with for a range of applied loads, implemented by hanging weights on a pulley connected to the hydraulic cylinder. The velocity of the output hydraulic cylinder was measured at each frequency. Frequency sweeps were conducted at two current levels:  $7.1 \text{ A}_{\text{rms}}$  and  $10.6 \text{ A}_{\text{rms}}$ . Additional testing was conducted to vary the input current while holding the applied input frequency and load constant.

#### 4.5.1 Input frequency sweep at $7.1 \text{ A}_{\text{rms}}$

Figure 4.10 shows the measured velocity resulting from an input current of  $7.1 \text{ A}_{\text{rms}}$  applied at each frequency point for a range of applied loads from 0 N to 310 N. The

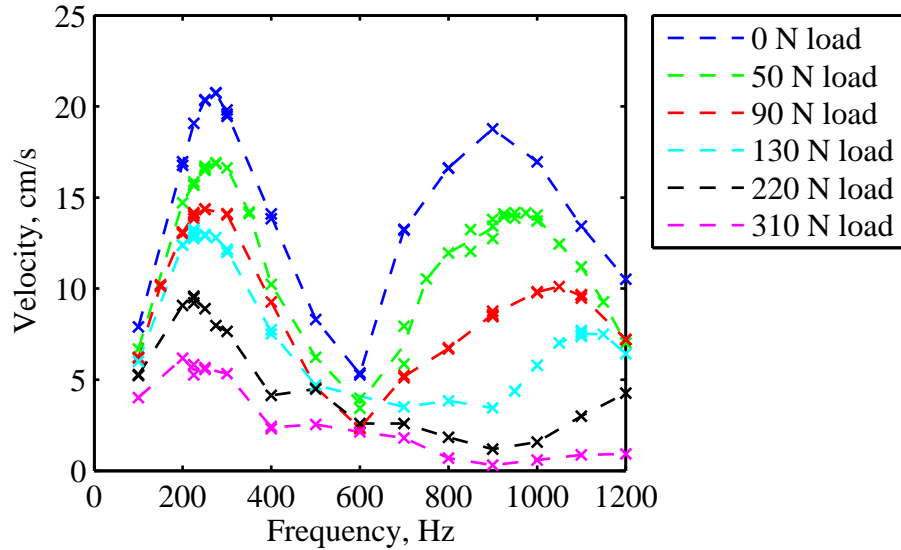


Figure 4.10: Experimental output cylinder flow rate vs. input frequency with a  $7.1 \text{ A}_{\text{rms}}$  sinusoidal input current applied over the frequency range.

results show a double-peaked output profile with peaks at approximately 225 Hz and 900 Hz. Two interesting features of the output response are the approximately linear response with input frequency below 200 Hz and the high frequency peak, which shows an increase in the location of the peak as the load is increased.

Figure 4.11 shows the output behavior over a larger range of loads at 225 Hz; the response shows a peak no-load velocity of 19 cm/s and a blocked force value of approximately 500 N with a nearly linear response in between. The peak output power of 21 W was measured at 220 N.

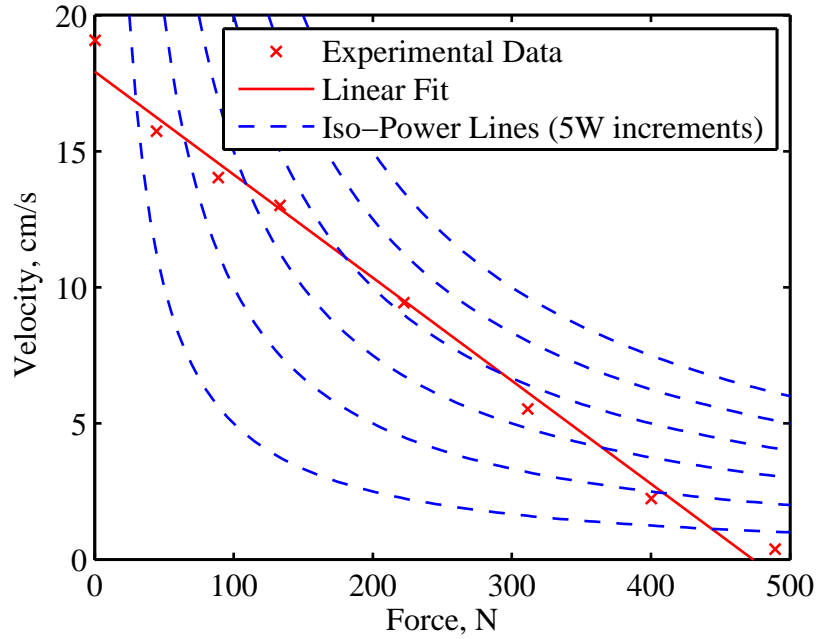


Figure 4.11: Output force vs. velocity measured at 225 Hz input frequency; the peak output power is 21 W which occurs at a 220 N load. Input current level is 7.1 A<sub>rms</sub>.

### 4.5.2 Input Current Variation at 225 Hz Input Frequency

Additional tests were conducted at the peak power conditions (225 Hz, 220 N load) using a higher range of input currents (Figure 4.12). Increasing the input current to 12.4 A<sub>rms</sub> increased the output velocity up to 17 cm/s, which corresponds to an output power of 37 W. There is a decrease in efficiency with the increased input current from 12% in the 7.1 A<sub>rms</sub> input case to approximately 5% with a 12.4 A<sub>rms</sub> input. The decrease in efficiency is due to the Terfenol-D driver approaching saturation, where the amount of strain output for a given applied field decreases. The blocked pressure differential produced by the pump at the 12.4 A<sub>rms</sub> current level was also measured at 12.5 MPa.

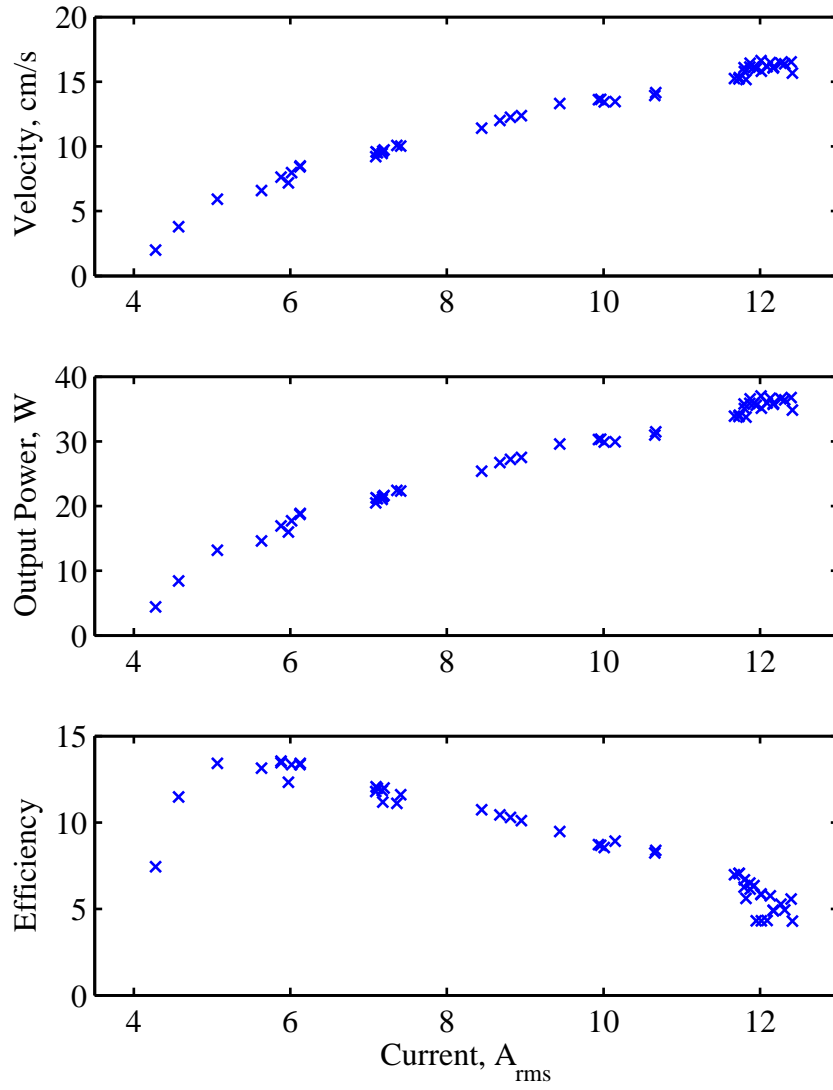


Figure 4.12: Testing of the experimental actuator at 225 Hz with a 220 N load applied over a range of input frequencies.

### 4.5.3 Higher Current Input Frequency Sweep at 10.6 $A_{\text{rms}}$

An additional set of testing was conducted at a higher current of 10.6  $A_{\text{rms}}$ . This current level was applied over a smaller frequency range (up to 700 Hz) due to limitations of the Techron LVC 5050 drive amplifier. The general trends of the measured velocity curves are similar to the lower input current levels, with a velocity peak at approximately 250 Hz and an increasing velocity at higher frequencies towards another peak at 900 Hz (not measured in this test). Since the applied current is higher, the magnitude of the velocity is higher, especially for cases with an applied load.

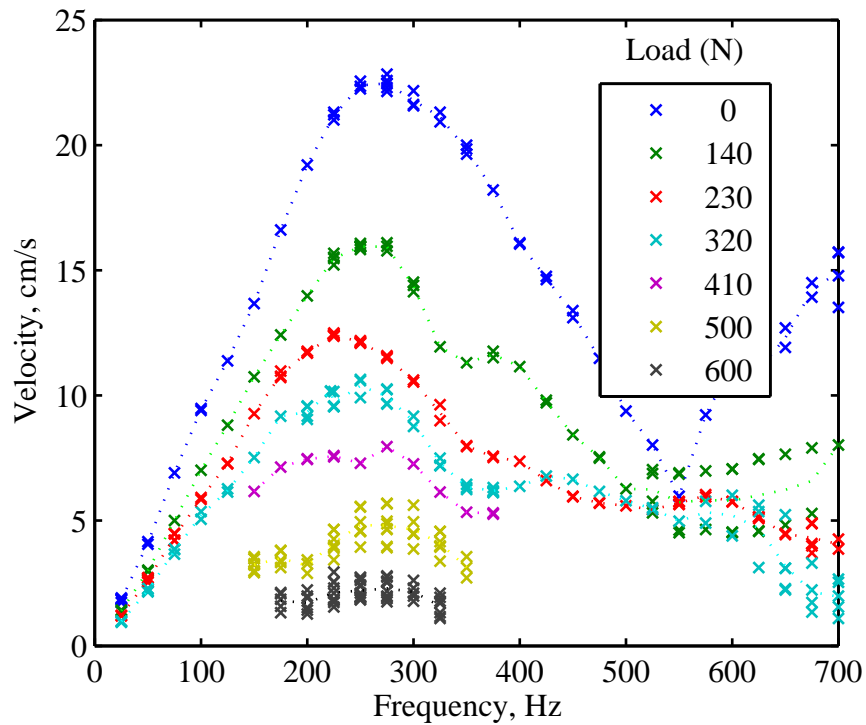


Figure 4.13: Experimental output cylinder velocity rate vs. input frequency with a 10.6  $A_{\text{rms}}$  sinusoidal input current applied over the frequency range.

The increase in output velocity for the higher current test conditions is more significant at higher levels of applied load (Table 4.1). The difference is small for the unloaded case, approximately 8%. However, when significant loads are applied the the 50% increase in applied current (from 7.1 A<sub>rms</sub> to 10.6 A<sub>rms</sub>) resulted in a 51%-83% increase in output velocity. The difference is due to the operation of the magnetostrictive rod driving the system. With no load applied to the system, the driving rod only has to overcome hydraulic losses and the hydraulic cylinder friction. Thus the rod would be expected to be operating near its saturation limit in both cases; Terfenol-D has a relatively slow approach to saturation, so higher applied fields will give a higher magnetostriction, even if the increase is small relative to the increase in field. The applied load reduces the amount of magnetostriction resulting from a given field, so increases in the field will increase the strain output of the rod proportionally.

Table 4.1: Comparison of the output velocity with applied load for two different input current levels. While the difference is small for the unloaded case due to saturation of the magnetostrictive rod, there is a significant increase in the velocity and consequently the output power at higher applied loads.

7.1 A <sub>rms</sub> Data			10.6 A <sub>rms</sub> Data			Velocity Increase
Load [N]	Peak Freq. [Hz]	Velocity [cm/s]	Load [N]	Peak Freq. [Hz]	Velocity [cm/s]	
0	275	21	0	275	23	8%
130	250	13	140	250	16	23%
220	225	9.2	230	225	12	34%
310	200	6.2	320	200	9.3	51%
310	250	5.7	320	250	10	83%

Figure 4.14 summarizes the performance of the system in terms of the output power, calculated from the velocity times applied load force. The peak power output

for the  $10.6 \text{ A}_{\text{rms}}$  input current testing was  $33.5 \text{ W}$  measured at  $250 \text{ Hz}$  with a  $320 \text{ N}$  applied load. There was significant scattering in the output velocity data for testing at

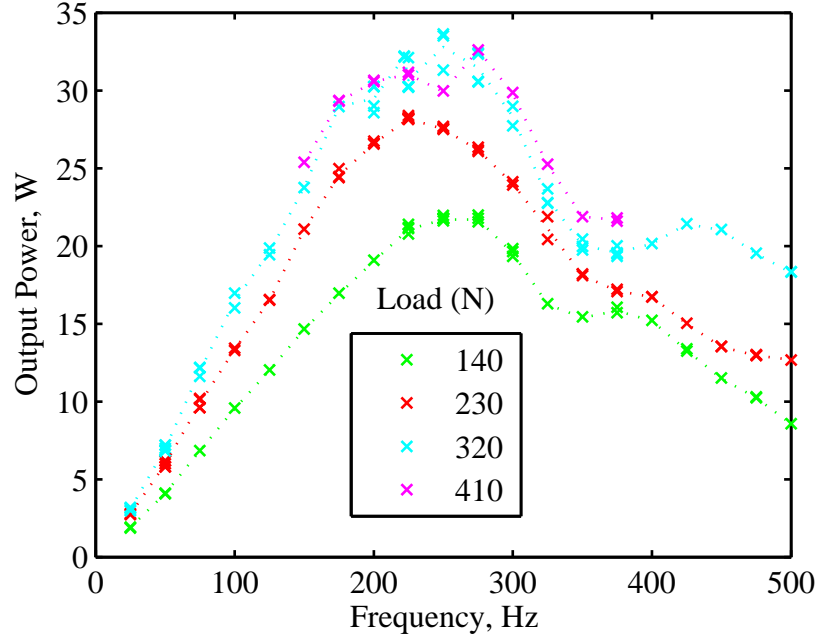


Figure 4.14: Output power vs. input frequency for a range of applied mass loads with a  $10.6 \text{ A}_{\text{rms}}$  sinusoidal input current applied over the frequency range.

very high loads ( $500\text{--}600 \text{ N}$ ), so these test results were not included in the calculations of output power and efficiency. These high output load levels were approaching the capacity of the pulley system used to apply the load to the actuator, so some side loading to the output cylinder may have affected the results.

The efficiency was calculated at each data point by dividing the measured output power by the AC component of the input power. As shown in Figure 4.15, the efficiency trends correspond to with the measure velocity; the peak power output conditions result in a measured efficiency of  $8.3\%$ . Characterizing the actuator

efficiency by the AC component of the input power alone is appropriate since a permanent magnet could be used to supply the bias magnetic field to avoid these efficiency losses. Additionally, even using a DC current to supply the magnetic bias, the losses are resistive and can be reduced by using larger diameter wire within the coil (refer to the test result presented in Chapter 8). Including the DC bias, the overall system efficiency is 6%, which is still significantly higher than the previously reported efficiency value for a magnetostrictive EHA of 0.5% [32].

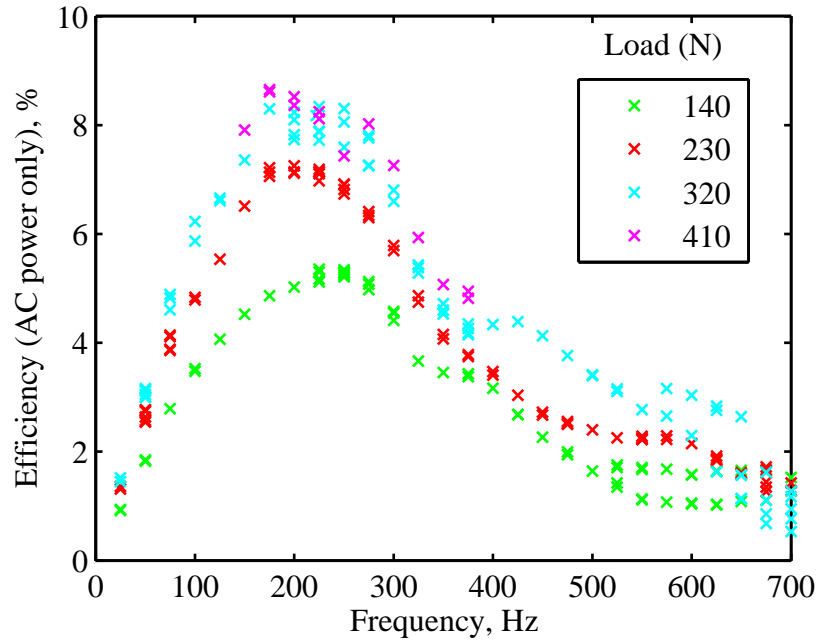


Figure 4.15: Efficiency vs. input frequency for a range of applied mass loads, neglecting the DC bias component of the input power (A sinusoidal input current of  $10.6 A_{\text{rms}}$  applied over the frequency range).

The input power for each test point is given in Figure 4.16. The AC component of the input power increased with frequency, as higher voltage were required to maintain the constant level of applied current for this inductive system. The DC component



of the input power, used to supply a bias magnetic field was fairly constant over the applied frequency range at approximately 150 W. Some variation was observed, which is likely due to resistivity changes due to heating of the coil during operation.

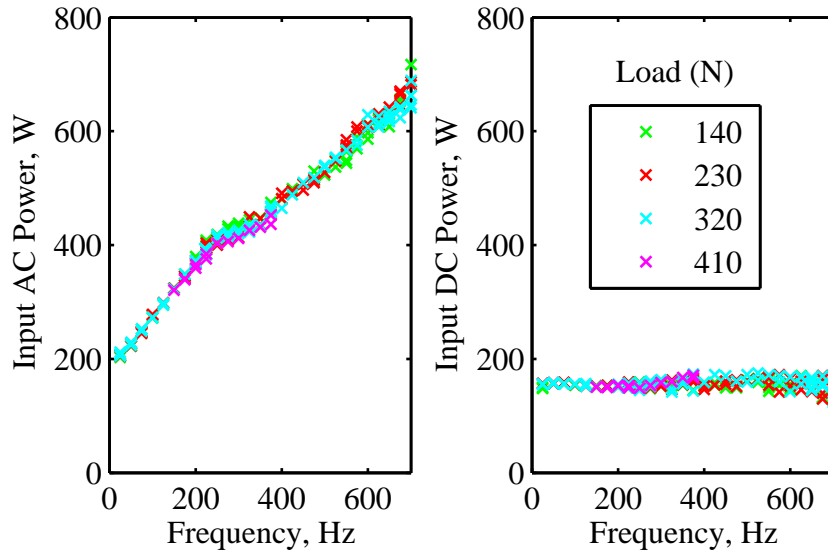


Figure 4.16: Input power vs. input frequency for a range of applied mass loads with a  $10.6 A_{\text{rms}}$  sinusoidal input current applied over the frequency range. The overall input power is divided the sinusoidal AC component (left) and the DC bias field component (right).

For comparison to other smart material electro-hydraulic actuator systems, it is useful to consider the results in terms of the Force-Velocity curves (Figure 4.17). A linear fit of the 250 Hz data projects a blocked force value of 630 N and an unloaded velocity of 21 cm/s; based on the cylinder area ( $0.95 \text{ cm}^2$ ), this corresponds to a blocked pressure differential of 6.7 MPa and an unloaded flow rate of  $20 \text{ cm}^3$  for the  $10.6 A_{\text{rms}}$  input current tests.

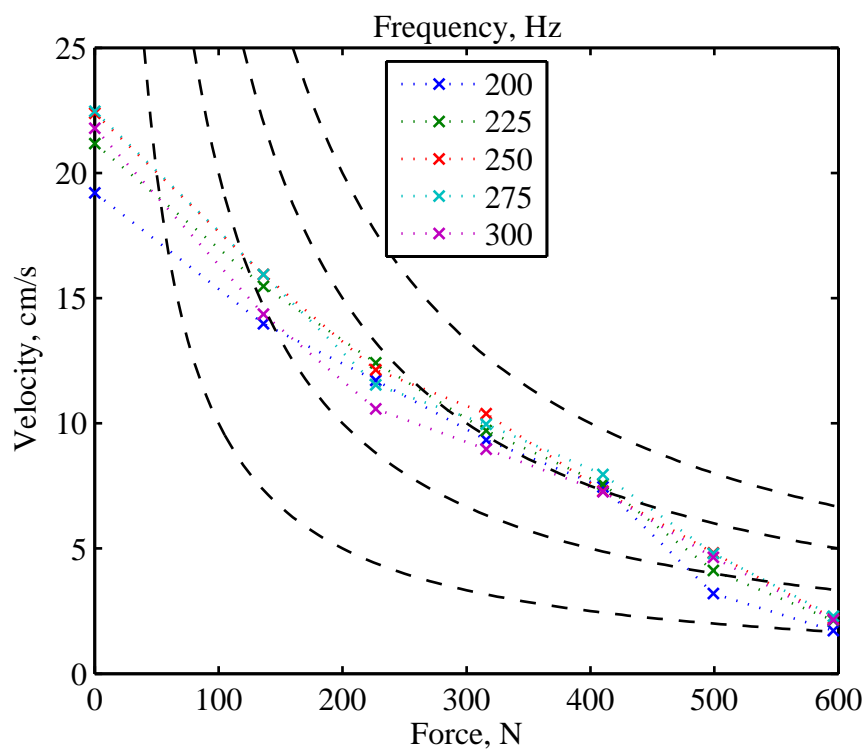


Figure 4.17: Force vs. velocity curves for a range of input frequencies ( $30 A_{\text{pk-pk}}$  sinusoidal input current applied over the frequency range).

## 4.6 Summary

A magnetostrictive EHA designed with a reduced-volume was evaluated over a range of experimental conditions. Using a manifold to reduce the size of the system by combining the output hydraulic cylinder and pump into one unit resulted in a large increase in the performance of the system. Additional testing conducted to identify other sources of loss within the system identified that deformation of the piston seal diaphragm and the extra fluid volume associated with a sensor had a harmful effect on the system performance.

The actuator was characterized over a range of input frequencies, applied loads, and currents (Table 4.2). Peak output performance was measured at 37 W based on a measured velocity of 17 cm/s with a 220 N mass load, using an input current of 12.4 A<sub>rms</sub> at 225 Hz. This output performance is significantly higher than other systems based on smart material drivers of similar size. For example, Chaudhuri, Yoo, and Wereley (2009) measured a power output of 2.7 W from a system utilizing a Terfenol-D rod of the same diameter (12 mm) and only 12 mm shorter at (102 mm) than the reduced-volume-manifold design [33].

In order to determine the effect of the single-reed valves used within the reduced-volume manifold EHA on the system operating bandwidth, the valves were characterized by additional experimental study to determine the steady state flow response and dynamic performance of the reeds (Chapter 5). The experimental results were correlated with both finite element modeling and analytical calculations. Experimental results from the reduced-volume-manifold actuator were used to validate a model of the overall system performance (Chapter 6).

Table 4.2: Summary of experimental tests applied to the reduced volume manifold EHA.

Figure	Test Description	Current
4.4	Comparison to EHA with external hydraulic cylinder	3.5 A <sub>rms</sub>
4.6	Consideration of the effect of a deformed seal diaphragm	3.5 A <sub>rms</sub>
4.9	Evaluation of shift in hydraulic resonances from sensor passage removal	3.5 A <sub>rms</sub>
4.10	Output power and efficiency evaluation using a range of mass loads	7.1 A <sub>rms</sub>
4.11	Force vs. velocity measurement at 225 Hz constant input current	7.1 A <sub>rms</sub>
4.12	Variation of applied input current at fixed 225 Hz input frequency and 220 N load	4 – 12.4 A <sub>rms</sub>
4.13	Input frequency sweep at higher current level with a range of applied loads	10.6 A <sub>rms</sub>

# Chapter 5

## Reed Valve Development

### 5.1 Introduction

The one-way valves used for rectification of hydraulic fluid are the key component that enables an electro-hydraulic actuator (EHA) to amplify the motion of a smart material. The frequency response of these valves has typically been cited as the factor limiting the peak operation of smart material EHAs to input frequencies of a few hundred hertz (Table 2.2) when the smart material drivers are capable of operation at much higher frequencies (over 2 kHz). However, experimental testing of a reduced-volume manifold EHA (Chapter 4) has demonstrated fluid rectification at very high frequencies, with a peak in the flow rate at 900 Hz and a significant flow rate measured at 1200 Hz. Additionally, testing of the system by replacing the reed valves with an array of miniature reed valves (designed for much higher resonance frequencies, 14.7 kHz) found no difference in the dynamic response of the system for the full range of frequencies tested (Figure 3.10).

In order to address the inconsistency between previously published reports on the behavior of reed valves within smart material EHA systems and the lack of a significant dynamic effect measured within an experimental system, modeling and

experimental study was conducted on the single-reed valves used within the reduced-volume manifold EHA. The reed valves were characterized in terms of both static and dynamic performance.

A 3-D finite-element fluid-structure interaction model was developed for the reed valves. The results from this model were compared with steady-state flow experiments conducted on the valves. Additionally, a simplified flow model based on the orifice flow equations was developed, which was shown to match well with the experimental results while remaining in a form suitable for integration within a model of the complete actuator system.

The dynamic response of the reed valves was characterized by experimentally measuring the natural frequencies of the valves. The measurements were conducted in a test fixture which includes the effect of the hydraulic fluid and the valve seat in order to accurately replicate the *in-situ* response of the valves within the EHA pump. The experimental results were reconciled with theoretical calculations of the natural frequency of a cantilever beam.

The static and dynamic modeling were combined to produce a model of the reed valve performance within the system. The position of the reed (i.e. the amount that it opens) is calculated according to a second-order system model, with parameters defined by the dynamic experiments. The effect on the EHA pump, which is the flow resistance over the reeds, can then be calculated for a given reed position based on the validated flow model. The model can also be used predictively to design improved reed valves for EHA systems or other hydraulic systems that require high-frequency valves.

## 5.2 Background

Owing to their relatively high frequency bandwidth and simple design, single, reed-style valves have been the rectification valve of choice for use within smart material hydraulic pumps. A detailed review of the different valve options for valve development is Section 3.2.

The concept for these valves is based on the reed valves typically found in other applications, such as two stroke engines and air compressors. However, the applicability of previous research in the literature from other applications is limited. Other applications typically use air which has a much lower density than hydraulic fluid, so the added mass effect of the working fluid is not considered in the analysis. Additionally, the frequencies of interest in other applications are typically much lower than the target input frequencies for an EHA; for instance, a typical operating speed for an engine may be 5,000 r.p.m. (less than 100 Hz). The analysis of reed valves has been the subject of much study within the literature on smart material pumps.

Previous efforts to model the flow resistance for a reed valve geometry include a 3-D computational fluid dynamics (CFD) model developed by Walters (2008) [55]. The flow through a series of static reed geometries was calculated, with the bending of the reed calculated from a separate analysis and specified to the CFD model as a boundary condition.

Chaudhuri, Yoo, and Wereley (2009) modeled included the coupling between fluid flow and valve displacement in a 2-D finite element analysis [33]. For a given pressure differential, the fluid flow and resulting reed deformation were solved together as a coupled problem (i.e. the pressure distribution was used to calculate the reed valve deformation and the reed valve flexure determined the flow path for the fluid). Several thickness of valves were considered, a typical example is reproduced in Figure 5.1. A shortcoming of this model is that the discontinuity in the results for the fluid flow

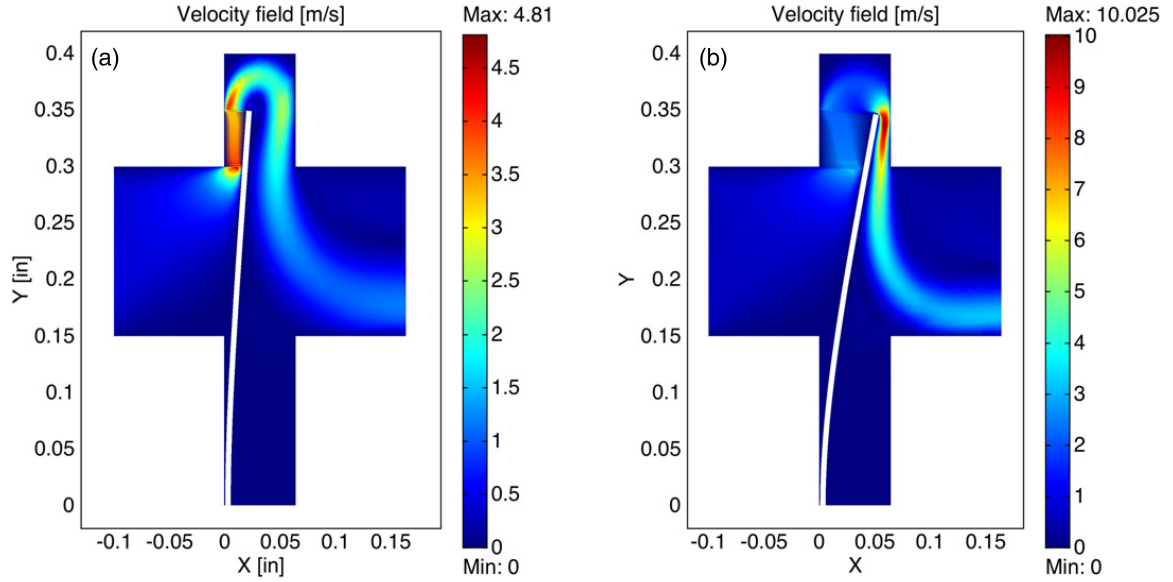


Figure 5.1: Velocity field for a 0.13 mm thick reed valve calculated by Chaudhuri, Yoo, and Wereley (2009): (a) Pressure = 28 kPa, (b) Pressure = 55 kPa (Reproduced from [33])

beneath the reed valves is clearly non-physical; the solution is calculated using a mesh-deformation algorithm and it appears that not enough elements were applied to give an accurate solution. Additionally, while the choice of a 2-D model is appropriate due to the flow of this particular reed valve, the way that the reed valve was designed limited the potential flow through the system. The reed valves open with pressure allowing for increased flow only up to a certain point, then further motion of the valve would reduce the available flow area as the reed approaches the other side of the chamber (refer to (b) of Figure 5.1). Similar valves were used in other systems designed by the authors [32, 33, 40].

The reed valves modeled in this chapter were designed by Rupinsky [67] and were used in the reduced volume manifold electro-hydraulic actuator (Chapter 4). The reeds were EDM cut from 301 F.H. stainless steel shim stock, 0.13 mm thickness; the dimensions of the reed is shown in Figure 5.2.



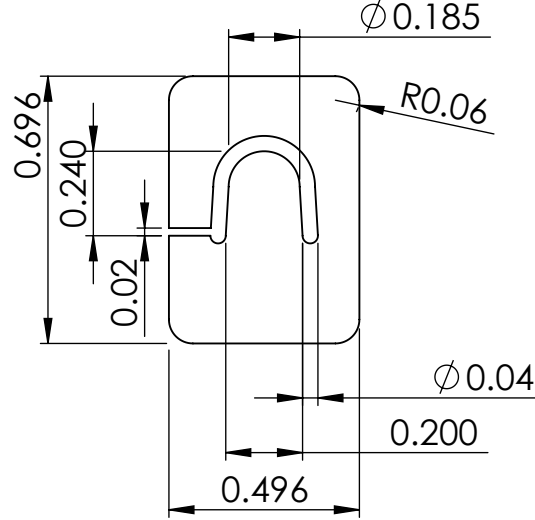


Figure 5.2: Single reed valve dimensions used within the reduced volume manifold EHA (Reproduced from [67]). All dimensions are given in inches. The thickness is 0.005" (0.13 mm).

### 5.3 Finite Element Modeling of Steady-State Flow

The flow through the reed valves was modeled using the finite-element software COMSOL. This 3-D multiphysics model incorporates the fluid-structure interaction between the reed valve and fluid flow. Figure 5.3 shows the geometry of the reed valve and flow chamber. A range of pressure differentials was applied between the inlet and outlet passages to the reeds, and the resulting flow rate and reed displacement were calculated (Figure 5.4). The model was validated experimentally by measurement of the steady-state flow through the valves over a range of applied pressures.

An arbitrary Lagrangian-Eulerian (ALE) finite element formulation was used to deform the mesh and track the motion of the valve with applied pressure. A difficulty for obtaining accurate results from the model is managing the deformation of the mesh, especially in the narrow region between the valve and the valve seat. The reed valve geometry is initially modeled with a small offset to maintain a continuous

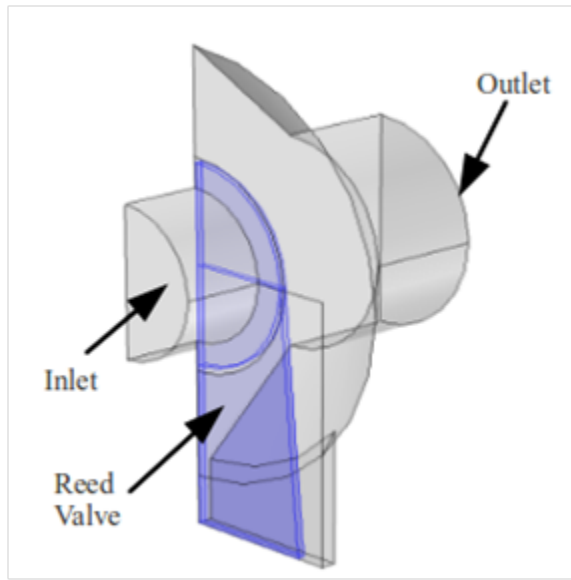


Figure 5.3: The geometry used for finite-element modeling of the reeds. The symmetry of the reed geometry was utilized to reduce the computational requirements by only modeling a cut-away section.

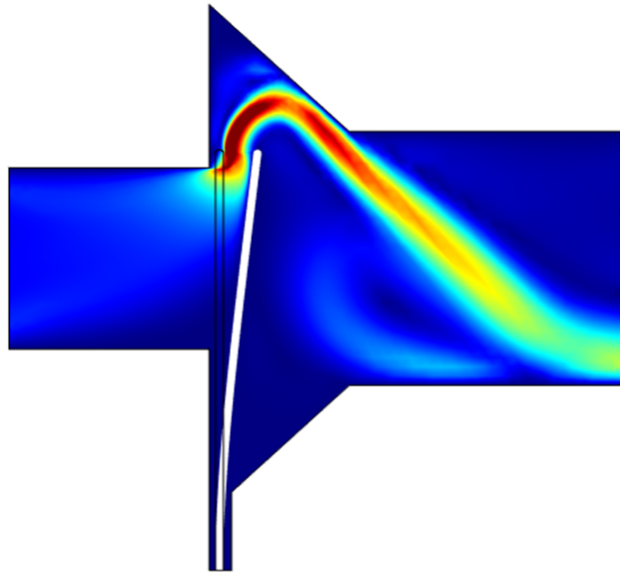


Figure 5.4: A typical velocity field calculated by applying a differential pressure across the inlet and outlet passages to the reed valves. The deformation of the reed (white) was calculated due to the applied pressure differential. The flow calculation is 3-D, a side view of the flow magnitude is shown.

volume for the fluid flow calculation. As pressure is applied and the reed valve opens, the mesh elements are stretched, resulting in a reduction in the resolution of the calculation of the flow at that location. The increased spacing between the calculation points can result in non-physical discontinuities in the results (Figure 5.1). The issue is illustrated in Figure 5.5, along with a solution of prescribing the lines on the finite element mesh to track the reed valve motion. (Note that the mesh shown in Figure 5.5 is exaggerated to help visualize the issue; the actual resolution used for simulation is much smaller.) Modifying the calculation used to define how mesh elements are deformed as the valve deflects is another way that the issue can be addressed.

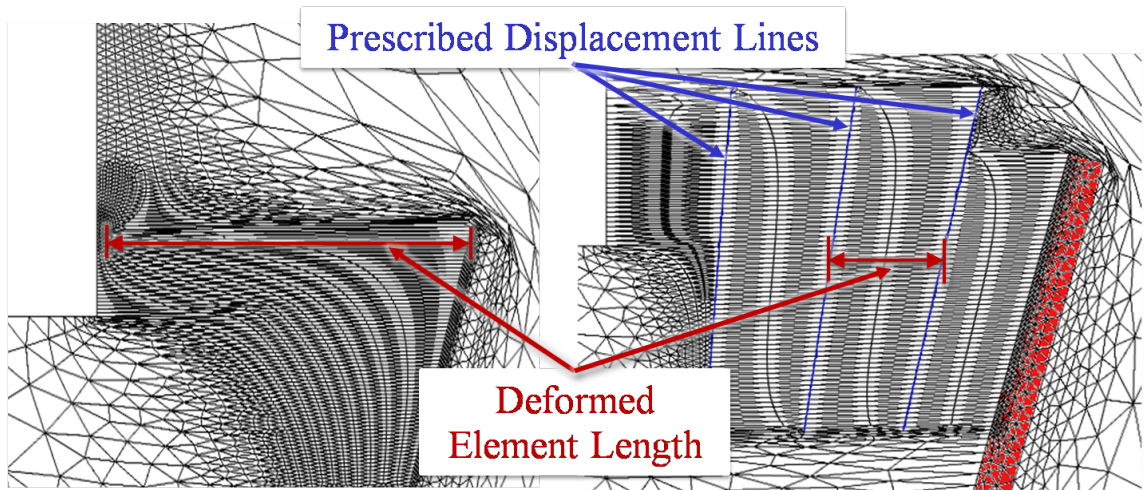


Figure 5.5: Two-dimensional representation of the reed valve solution geometry demonstrating improvement in element quality using a prescribed mesh displacement. (Deformations are exaggerated for illustration.)

The reed valves were tested with a static pressure to determine the flow resistance characteristics. To create conditions matching the CFD results, a valve holder was created to match the inlet and outlet passages and the valve port geometry of the pump. A fluid reservoir supplied Mobil DTE 24 hydraulic fluid at a constant pressure

maintained by a compressed nitrogen cylinder and regulator. The mass flow rate of the fluid was measured with a scale and the pressure differential across the valve was measured using two Sensotec 7351-02 pressure sensors. The tip displacement of the valves was also recorded during testing using a strain gage affixed to the root of the valve. A laser displacement sensor was used to calibrate the strain measurements to the displacement of the valve tip.

The measured flow resistance vs. valve tip displacement was compared with the finite-element calculation (Figure 5.6). Refining the resolution of the mesh elements between the valve and the valve seat improved the model results to correlate with the experimental data.

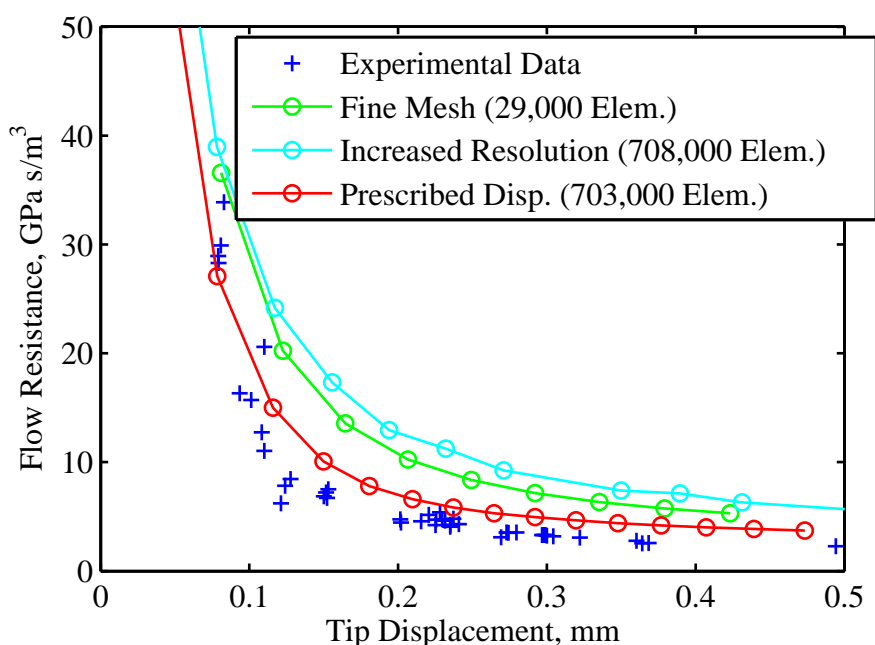


Figure 5.6: Reed valve flow resistance compared to tip displacement comparing experimental results with COMSOL calculations. The default “fine” mesh size is compared with a higher mesh resolution, with and without the prescribed mesh displacement surfaces.

## 5.4 Dynamic Response

### 5.4.1 Determination of Reed Valve Natural Frequency

Theoretical calculations of the reed frequency response by approximating the reed as a cantilever beam, indicate that the first resonance should occur at approximately 950 Hz; this calculation includes the effect of the fluid mass on the reed response by including an added mass term

$$m_{\text{add}} = \gamma \frac{\pi}{4} w_r^2 l_r \rho, \quad (5.1)$$

which is the mass of fluid contained in a cylinder swept by the reed width  $w_r$  and length  $l_r$  with a correction factor  $\gamma$  to account for the relatively short aspect ratio of the reed [66].

The calculated natural frequency of 950 Hz presents a discrepancy with the experimental data comparing the performance of the single-reed valves with the miniature reed valve array within an experimental magnetostrictive EHA (3.10). This frequency fell within the range of frequencies tested; however, the dynamic response of the system showed a similar trend in frequency response with both valve types.

The difference between the predicted reed frequency response and the observed response from the EHA velocity experiments is due the effect of the valve seat on the dynamic response of the valve. The theoretical frequency response assumes that the reed is free to vibrate as a cantilever beam; however, in the actual pump system the reed closes against a surface containing the flow path, the valve “seat”. Previous studies in the literature have considered the effect of a cantilever beam approaching a solid wall and found a significant decrease in natural frequency as the beam is placed closer to a surface [68]. Moving the beam close to a surface increased the added mass term (5.1) by a factor of as much as 8 [68]. However, the “wall” in the EHA pump

valve seat is not solid because of the flow path for the fluid, so these results are not applicable to the case of a fluid rectification valve.

In order to test the effect of the valve seat on the frequency response, a test holder was fabricated to clamp the reed against a valve seat containing a flow path with the same dimensions used in the experimental pump (Figure 5.7). Figure 5.8 shows the

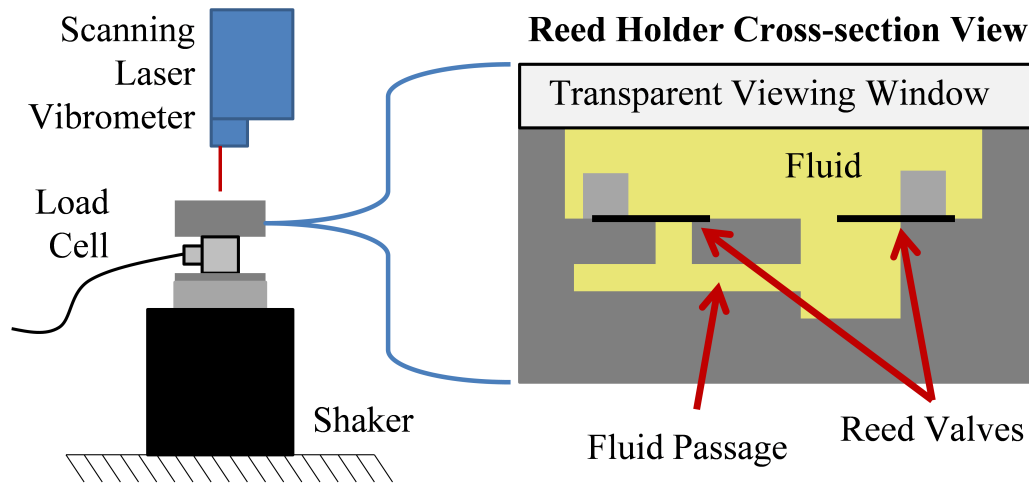


Figure 5.7: Illustration of reed valve dynamic test configuration. The reed frequency response was measured with a scanning laser vibrometer. The valves were tested in both a cantilever beam condition and with a simulated valve seat matching the reduced volume manifold EHA geometry.

test holder used to evaluate the reed dynamic response. An additional valve was tested in a clamped-free cantilever condition for reference and to compare the test results with the theoretical calculations. The test fixture with the reed valves was excited using a shaker and the natural frequencies and mode shapes were measured using a Polytec PSV-400-M scanning laser vibrometer. The results show that the effect of the valve seat is to approximately double the natural frequency of the rod to 2040 Hz (Table 5.1).

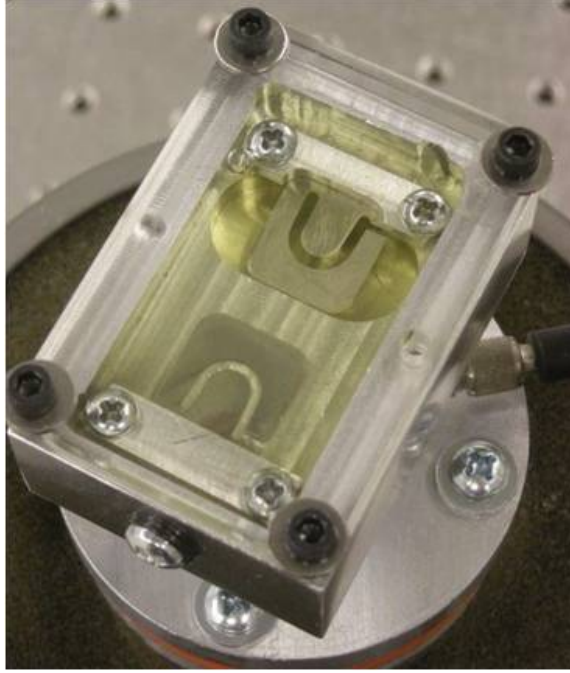


Figure 5.8: Test setup for evaluating the natural frequency of the reed valves; the valves are tested in the pump configuration (with valve seat, top reed) and as a cantilever beam for reference (bottom reed).

Table 5.1: Reed natural frequency testing results.

Test Condition	First Natural Frequency (Hz)	Damping Ratio
No-seat in air	1820	0.05
No-seat in fluid	940	0.2
With-seat in air	3450	0.55
With-seat in fluid	2020	0.55

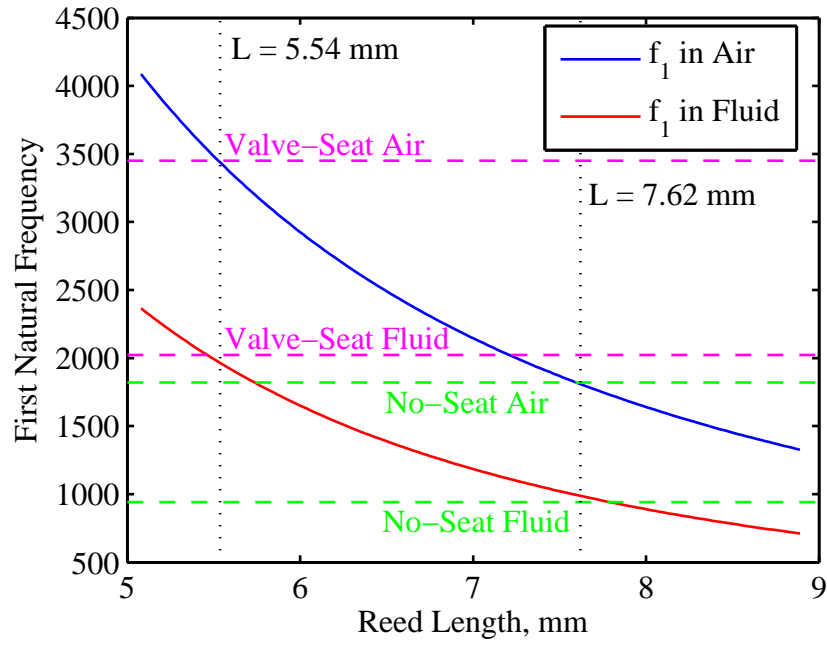


Figure 5.9: Reed valve dynamic experimental results compared with theoretical calculation of the natural frequency based on the length of the valve; the test results show that the effect of the reed valve seat is similar to shortening the valve from 7.62 mm to 5.53 mm.



Adding the seat to the reed valve is found to effectively shorten the length of the reed valve from 7.62 mm long to 5.53 mm (Figure 5.9). Using this equivalent length is found to correlate well with the measured natural frequency of the reed when tested in both air and in fluid. Additionally, considering the reeds to be effectively be made shorter by how the valves are restrained by the valve seat correlates with the scanning laser vibrometer, which indicated that the measurement points near the valve base were being held stationary relative to the test fixture and not vibrating with the rest of the length of the valve. The natural frequency of the reed in the free-cantilever condition was found to match well to the theoretical values using the actual reed length.

## 5.5 Simplified Flow Model

The opening positions of the reed tip for the output ( $x_{ro}$ ) and input ( $x_{ri}$ ) reeds are calculated by modeling the reeds as cantilever beams with equivalent mass  $m_r$ , stiffness  $k_r$ , and damping  $b_r$

$$m_r \ddot{x}_{ro} + b_r \dot{x}_{ro} + k_r x_{ro} = A_r (P_{ch} - P_{E1}), \quad (5.2)$$

$$m_r \ddot{x}_{ri} + b_r \dot{x}_{ri} + k_r x_{ri} = A_r (P_{D2} - P_{ch}). \quad (5.3)$$

The pressures  $P_{E2}$  and  $P_{D1}$  are the pressures in the manifold passages adjacent to the pumping chamber. The opening of the reed valve is determined by the stiffness, which was calculated using a finite element model based on the reed geometry as  $k_r = 2.3$  kN/m (Figure 5.11). This value is equal to the stiffness of a rectangular cantilever beam of similar size to the reed (5 mm x 6 mm x 0.127 mm).

A key factor in calculating how much the reed valve opens is determining the amount area upon which a pressure differential acts. The area was calculated from a linear fit of the static-testing results for the reed, although similar results were

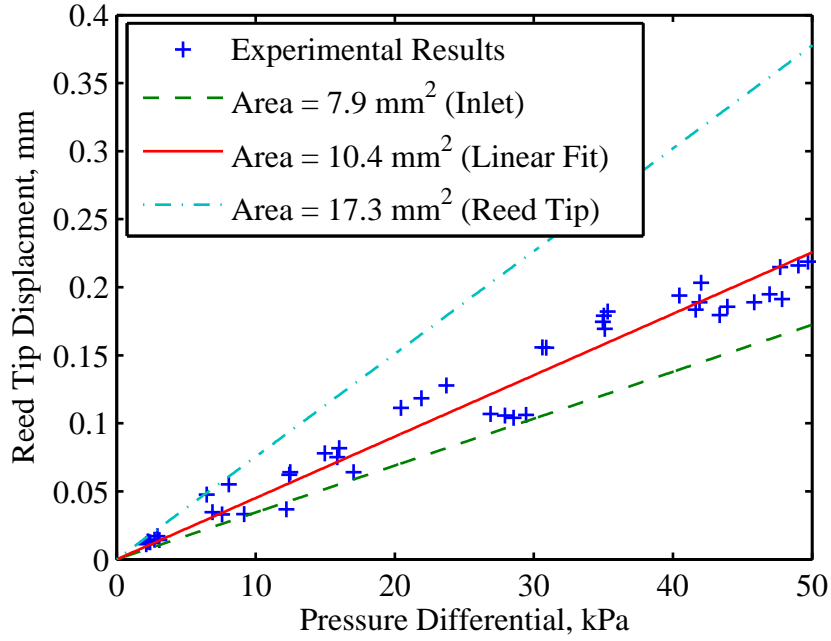


Figure 5.10: The tip displacement of the reed valve is determined by its stiffness and the amount of area that the fluid pressure is applied; the applied pressure area is bounded by the size of the inlet and the size of reed itself.

determined from a finite-element model of the flow over the reeds [69]. The pressure acts on an area slightly larger than the inlet area but smaller than the size of the reed tip (Figure 5.10).

The reed valve positions defined by (5.2) and (5.3) determine the opening area  $A_v$  of each reed valve, which has been calculated as a linear function of the tip opening  $A_v = \lambda_r x$  by integrating the opening area around the reed, assuming the first mode of a cantilever beam as the reed opening profile (Appendix B). This results in an area of  $8.5 \text{ mm}^2$  for every mm of tip displacement. The shape of the opening reed is illustrated in Figure 5.11. The pressure drop across the reeds can then be modeled according to the orifice flow equation

$$\Delta P = \frac{\rho Q^2}{2C_d^2 A_v^2} \quad (5.4)$$

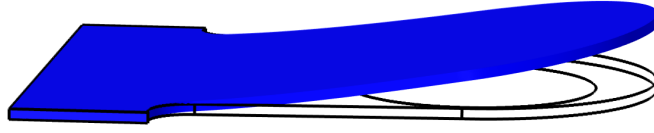


Figure 5.11: First bending mode of the reed valve, calculated using COMSOL.

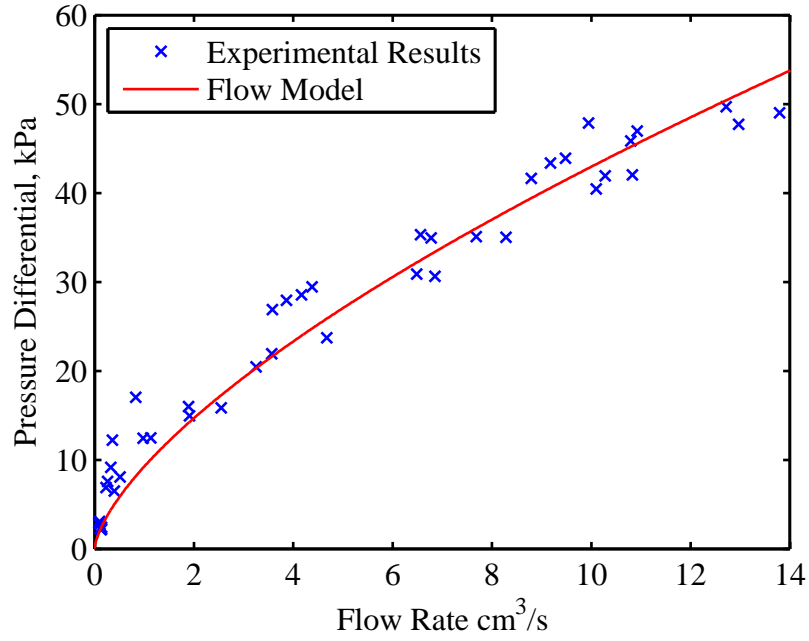


Figure 5.12: Comparison between the steady-state flow measurements and calculating the of the flow rate using the orifice flow equation.

with discharge coefficient  $C_d = 0.61$ .

Applying (5.4) and (5.2) to the case an applied static pressure matches well with the steady state flow experiments conducted on the reed valves (Figure 5.12). This demonstrates that a set of simplified equations based on the well-known orifice flow relationship can accurately describe the pressure drop across the reed valve for a range of flow conditions.

### 5.5.1 Effect of Natural Frequency on Fluid Rectification

To demonstrate the effect of the reed's natural frequency on the ability of the reeds to rectify fluid flow over a range of input frequencies, the average flow rate from an applied sinusoidal pressure differential was calculated using (5.3) and (5.4). The calculated average flow rate decreases as the pressure oscillation frequency approaches the natural frequency of the reed (Figure 5.13). The results are normalized according to the first natural frequency  $f_1$  of the valves and the average flow rate at low frequencies ( $<5\%$  of  $f_1$ , which was the same for all damping ratios  $\zeta$  shown). The decrease in

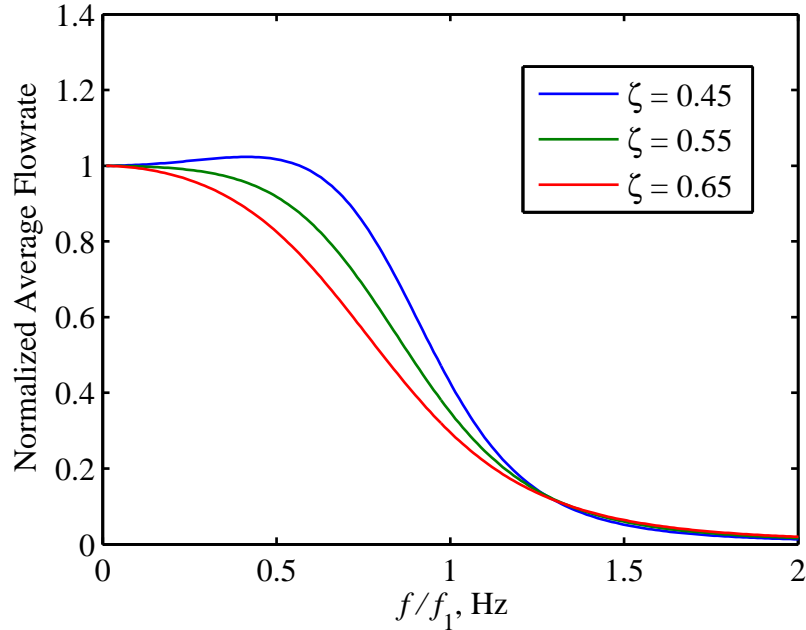


Figure 5.13: Normalized flow response over the reed valves for a sinusoidal pressure distribution over a range of frequencies; the flow rate decreases as the input frequency approaches the natural frequency of the reed.

flow with increasing frequency is expected as the response for a second-order system vibrating at its first natural frequency is 90 degrees out of phase with the input. Thus

at the reed natural frequency, the valves will open and close out of phase with the fluid pressure differential resulting in a low net flow through the valves.

The calculated flow rate is nearly flat at frequencies well-below ( $<40\%$ ) the first natural frequency. This means that the reeds will have little effect on the variation in system performance with input frequency as long as the reeds are designed to have a first natural frequency well-above the operating frequency of the system.

The measured experimental results comparing effects of the single-reed valves and the miniature valve arrays on the frequency response of the reduced-volume-manifold system (Figure 3.10). The shape of the velocity curves, including the location of the peak frequencies, was the same for both types of valves because the pump was operating below the valve first natural frequency in both cases.

## 5.6 Summary

The single-reed valves used within the reduced-volume-manifold EHA were evaluated in terms of their static and dynamic performance. The steady-state flow through the valves over a range of constant pressures was measured experimentally and compared with a 3-D finite-element model. Additionally, a simplified model based on the orifice flow equation, applied to the calculated opening area from the reed deflection with applied pressure, was used to characterize the pressure drop for a given flow through the reeds.

The high computational cost of performing a 3-D finite element model (FEM) of the flow through the valves limits how FEM simulations can be applied to reed valves in smart material EHAs [37]. The orifice-flow based model addresses this concern by allowing for the calculation of the flow performance of the reed without the computational cost of running a 3-D finite-element fluid-structure interaction model for every possible flow condition. The model can also be used to predict the

flow and pressure relationships for new valve designs. The only parameter which was determined experimentally was the area over which the opening pressure is considered to apply a force to the valve. This area is bounded between valve inlet passage and the size of the valve, so the valve performance can be predicted within a specified range. If greater accuracy is desired, the flow area can be calculated using FEM analysis and then the orifice flow model can be applied to extend the results to other input conditions.

The dynamic response of the reed valves was characterized by measuring the natural frequency of the reed using a scanning laser vibrometer. The test results indicate that while the hydraulic fluid adds mass to the valve, lowering the natural frequency, the valve seat of the pump restrains the reed to effectively shorten and stiffen it, increasing the bandwidth for test conditions within the EHA. A model of the valve motion as a second-order system demonstrates that the frequency range tested in the reduced-volume-manifold EHA fall below the range where valve dynamics have an effect on the system response. This result explains why the miniature reed valves, which were designed to have a frequency bandwidth much higher than the single-reed valves, did not have an effect on the system operating bandwidth (Chapter 3). In both cases, other factors limited the response of the system before the input frequencies reached a level where the reed valves would be expected to have reduced performance.

# Chapter 6

## Performance Modeling

### 6.1 Introduction

This chapter presents a framework for modeling a magnetostrictive electro-hydraulic actuator (EHA). A summary of established modeling approaches for smart material EHA systems from the literature is presented. Building on these previous studies, a lumped parameter approach is used to model the system. Component-level models are developed for the various fluid and mechanical parts of the system. These models are combined to form a set of differential equations, which can be used to predict the dynamic response of the system.

Compared to previous works, this model considers several nonlinear effects in order to accurately describe the dynamic behavior of a magnetostrictive EHA, including nonlinear fluid flow losses, a pressure-dependent bulk modulus, and a nonlinear Jiles-Atherton magnetostrictive model. Where appropriate, experimental testing at the component-level has been used to validate the individual model components, such as the testing of the static flow through the reeds shown in Figure 5.12.

The model is validated using experimental results from testing of the reduced-manifold-volume EHA, presented in Chapter 4. Several experimental configurations were studied, such as testing the pump with no reeds installed and selectively closing off the output passages, which highlight the capability of the modeling approach. The

model presented here is used to predict and optimize the frequency bandwidth of the compact aircraft EHA design (Chapter 7).

## 6.2 Background

Models of smart material electro-hydraulic systems developed in the literature typically take a lumped-parameter approach to model the flow losses within the hydraulic components (output cylinder and associated fluid passages), and couple this with a linear model of the material behavior. A summary of these modeling efforts is shown in Table 6.1. This type of modeling generally correlates well with experimental data at low frequencies. However, at higher frequencies, effects not typically included in the models such as the inertia of the hydraulic fluid and the dynamic response of the reed valves cause large discrepancies between model predictions and experimental performance. In addition, to maximize the performance of the smart materials it is necessary to drive them at high frequencies and field levels, which causes significant nonlinearities in the response that is typically not considered in the modeling approaches.



Table 6.1: Performance comparison of smart material electro-hydraulic actuators. The fluid model heading describes whether resistance (R), inertia (L), and compliance (C) terms are included in the model. The Valve model heading specifies if a static (S) or dynamic (D) valve model is applied to the system.

Author	Year	Fluid Model	Minor Losses	Valve Model	Cylinder Friction	CFD
Oates and Lynch [21]	2001	R-C	Y	S	N	Y
Nasser et al. [70]	2001	R-L-C	N	S	N	N
Cadou and Zhang [71]	2003	R	N	S	N	N
Tan and Leo [38]	2005	R-C	N	S	N	N
Rupinsky & Dapino [27]	2006	R	N	S	N	N
Kim and Wang [3]	2009	R-C	N	S	N	N
Chaudhuri et al. [33]	2009	R-L-C	Y	D	Y	Y

### 6.3 Ideal Flow Model

The approximately linear force-velocity relationship that was demonstrated experimentally (Figure 4.11) is a direct result of the force-displacement behavior of the material, which can be approximated using the linear piezomagnetic equation

$$\epsilon = s^H \sigma + qH, \quad (6.1)$$

where the strain  $\epsilon$  is the result of the applied stress  $\sigma$  and magnetic field  $H$ . The coefficient  $s^H$  is the compliance at constant field and  $q$  is the magneto-elastic coupling coefficient. The ideal (loss-less) flow rate  $Q$  as a result of the strain calculated in (6.1) is simply product of volume resulting from each strain cycle  $\Delta V$  and the input frequency  $f$

$$Q_{\text{ideal}} = \Delta V f = (\epsilon l_{\text{TD}} A_{\text{ch}}) f, \quad (6.2)$$

where  $l_{\text{TD}}$  and  $A_{\text{ch}}$  respectively denote the length of the Terfenol-D driver and the area of the pumping chamber. The reduction of the flow velocity due to applied load is calculated by the model by reducing the strain per cycle by the applied stress times the material compliance (6.1).

The results of (6.2) are compared to the average output velocity measured for the experimental reduced volume manifold EHA with an applied input current of 7.1 A<sub>rms</sub> in Figure 6.1. The linear increase in output velocity with increasing input frequency holds for frequencies below the first resonance peak of the system, approximately 200 Hz.

### 6.4 Lumped-Parameter Modeling

A lumped parameter approach is used to develop a model to predict the overall system performance. In this approach, the system is divided up into discrete lumps

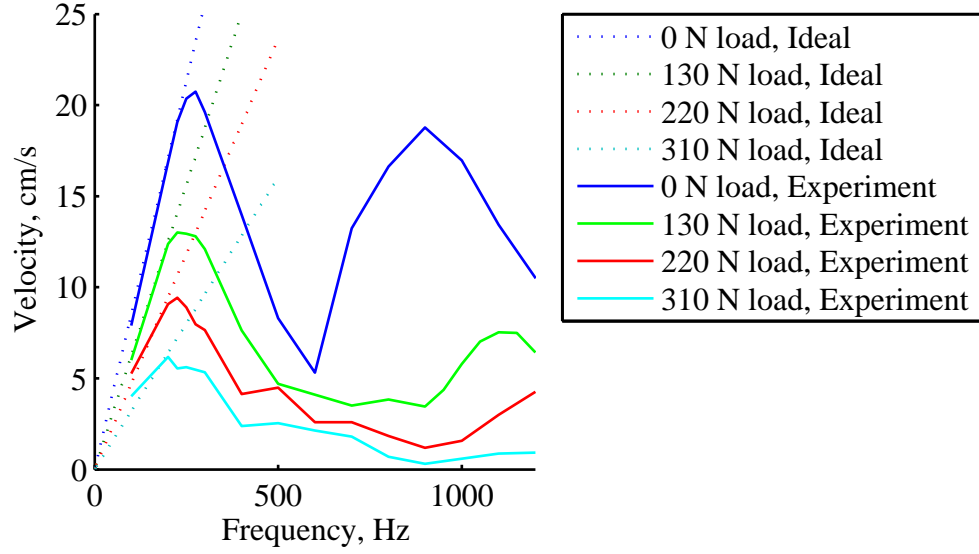


Figure 6.1: Ideal (loss-less) flow estimate from the linear piezomagnetic equations compared to the experimental results; this linear relationship holds for low frequencies (below  $\sim 200$  Hz). The ideal model is compared to the average output velocity measured at each frequency with an applied input current of  $7.1 A_{rms}$  (Figure 4.10).

which are assigned variables to calculate the behavior of the system at discrete points. Model equations are developed for the mechanical and fluid components of the system, which form a set of ordinary differential equations that can be integrated to model the system response to a given set of input and loading conditions.

While the basic equations for the fluid system model can be understood in terms of constant values for the bulk modulus of the fluid  $\beta$  and flow resistance  $R$ , nonlinearities in the fluid system response were including in the model by considering the pressure-dependent fluid bulk modulus (due to entrained air) and a flow-dependent fluid resistance (due to end effects in short passages).

The dynamic response of the reed valves in the system was modeled using the equations developed in the previous chapter (5.2), (5.3) and (5.4), which have been validated using steady-state flow experiments on the valves.

### 6.4.1 Mechanical Subsystem

The response of Terfenol-D depends on many factors including the amount of preload, the temperature, and the operating frequency. For low drive levels, the response can be approximated by linearizing the stiffness (Young's modulus) and piezomagnetic coupling terms about the operating point. For higher drive levels, the response is very nonlinear as the output strain approaches saturation (Figure 2.5). For the linearized Terfenol-D model, piston position ( $x_p$ ) is given by

$$m_p \ddot{x}_p + b_p \dot{x}_p + k_p x_p = \alpha I - A_{ch} P_{ch}, \quad (6.3)$$

where  $m_p$ ,  $b_p$ , and  $k_p$  represent the effective mass, stiffness, and damping of the piston, metal diaphragm, and Terfenol-D driver. A magnetostrictive coupling coefficient,  $\alpha$  relates the force response of the Terfenol-D driver to the applied current  $I$ , a result of (6.1) [27].

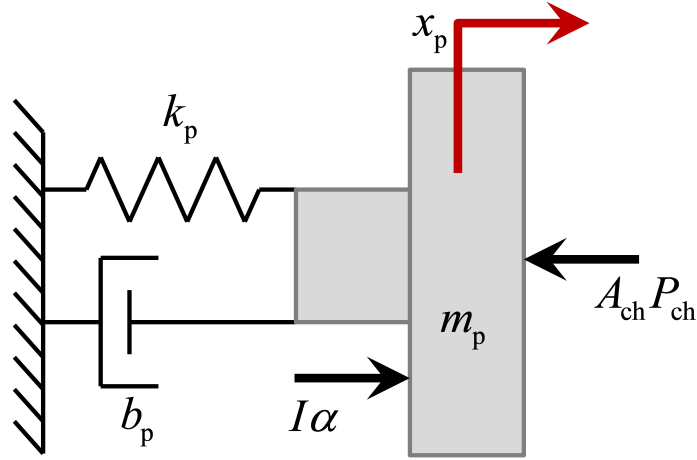


Figure 6.2: Mechanical model of the pumping piston.

The output cylinder position ( $x_{\text{out}}$ ) is defined by the differential equation

$$m_1 \ddot{x}_{\text{out}} + b_1 \dot{x}_{\text{out}} + k_1 x_{\text{out}} = A_{\text{out}} (P_{\text{hs}} - P_{\text{ls}}) - F_{\text{f}} - F_{\text{ext}}, \quad (6.4)$$

where the mass, stiffness, and damping of the piston rod are accounted with the load properties  $m_1$ ,  $b_1$ , and  $k_1$ . The external force  $F_{\text{ext}}$  represents the weight of the load. Friction in the cylinder is modeled with a Karnopp model [33, 72]. Letting  $F_e$  be the net force on the cylinder,  $F_e = A_{\text{out}} (P_{\text{hs}} - P_{\text{ls}}) - F_{\text{ext}}$ , the friction force is given by

$$F_{\text{f}} = \begin{cases} F_{\text{d}} & \text{if } |v| > v_{\text{min}} \\ F_{\text{e}} & \text{if } |v| \leq v_{\text{min}} \text{ and } |F_{\text{e}}| < F_{\text{s}} \\ F_{\text{s}} \text{sgn}(F_{\text{e}}) & \text{if } |v| \leq v_{\text{min}} \text{ and } |F_{\text{e}}| \geq F_{\text{s}} \end{cases} \quad (6.5)$$

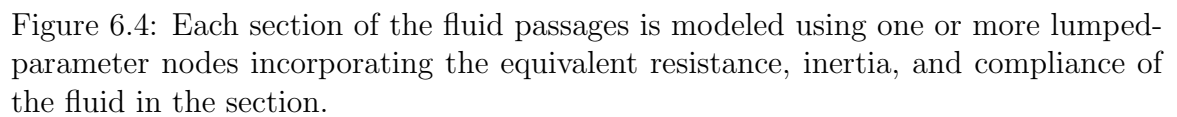
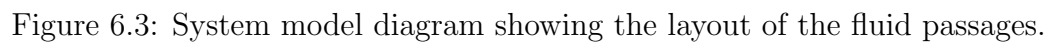
where  $F_{\text{s}}$  and  $F_{\text{d}}$  are the static and dynamic friction,  $v$  is the cylinder velocity, and  $v_{\text{min}}$  is the value used for the numerical simulation to consider the cylinder motion stopped.

### 6.4.2 Fluid Subsystem

Figure 6.3 shows the layout of the internal passages within the hydraulic manifold of the system. The fluid system passages are modeled using a lumped-parameter approach; each section of fluid passage (labeled A-H) is represented by one or more nodes which represent the passage with an equivalent resistance  $R$ , inertia  $L$ , and compliance  $C$  (Figure 6.4).

In developing the fluid system equations, laminar flow is assumed. The Reynold's number was calculated using  $N_R = \frac{\rho D v}{\mu}$  and was found to be less than 2000, indicating that the flow in the system is laminar [73]. The resistance term is defined by

$$R = \frac{128 \mu l}{\pi d^4} \left( 1 + \frac{2.78 d}{64 l} N_R \right), \quad (6.6)$$



which combines the Hagen-Poiseuille law for fully-developed laminar flow (first term) with a nonlinear correction factor (second term) accounting for end-effects [74]. This equation can be simplified to [73],

$$R = \frac{128\mu l}{\pi d^4} \left( 1 + \frac{0.1736}{\pi} \frac{\rho}{l\mu} Q \right). \quad (6.7)$$

The inertia ( $L$ ) and compliance ( $C$ ) terms account for the mass and stiffness of fluid contained in each lump of fluid

$$L = \frac{4\rho l}{3A}, \quad C = \frac{lA}{\beta}, \quad (6.8)$$

where  $\rho$  is the density of the fluid,  $l$  is the length of the fluid lump,  $A$  is the area. The bulk modulus  $\beta$  is considered to be a function of the pressure  $P$  and volume fraction of entrained air  $x$ ; this results in an effective bulk modulus

$$\beta = \left( \frac{1-x}{\beta_1} + \frac{x}{\beta_a} \right)^{-1} = \left( \frac{1-x}{\beta_1} + \frac{x}{P} \right)^{-1} \quad (6.9)$$

where  $\beta_1$  is the bulk modulus of the hydraulic fluid with no air. Even a small amount of entrained air is shown to have a large effect on the effective bulk modulus in the system (Figure 6.5); an important consequence of the pressure-dependence of bulk modulus is that the stiffness of the fluid in the hydraulic cylinder increases with applied load, as higher loads require higher pressures to produce output motions. This results in two differential equations for the pressure  $P$  and flow  $Q$  at each node (Figure 6.4),

$$Q_1 - Q_2 = C \frac{dP_1}{dt}, \quad (6.10)$$

$$P_1 - P_2 = RQ_2 + L \frac{dQ_2}{dt}. \quad (6.11)$$

The larger volumes of fluid in the system, including the pumping chamber  $P_{\text{ch}}$ , high-pressure side of the output cylinder  $P_{\text{hs}}$ , and low-pressure side of the pumping

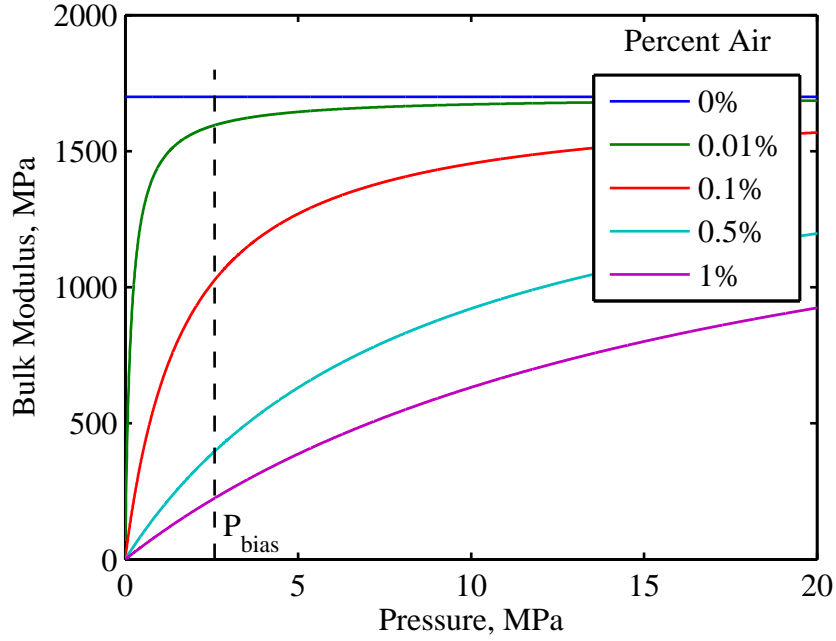


Figure 6.5: Variation of the effective bulk modulus of the fluid within the pump due to pressure changes and entrained air based on (6.9).

chamber  $P_{ls}$ , are modeled using the fluid compliance given by the bulk modulus  $\beta$  and flow in and out of each volume:

$$\left(\frac{V_{ch}}{\beta}\right) \dot{P}_{ch} = A_p \dot{x}_p - Q_{out} + Q_{in}, \quad (6.12)$$

$$\left(\frac{V_{hs}}{\beta}\right) \dot{P}_{hs} = Q_G - Q_H - A_{out} \dot{x}_{out}, \quad (6.13)$$

$$\left(\frac{V_{ls}}{\beta}\right) \dot{P}_{ls} = Q_A - Q_B + A_{out} \dot{x}_{out}. \quad (6.14)$$

The inclusion of velocity terms in the fluid system equations for the hydraulic cylinder and pumping chamber and pressure terms in the mechanical equations for these components link the mechanical and fluid system equations together. Thus the smart material EHA is modeled with a single system of equations that must be solved simultaneously.



### 6.4.3 Passage Compliance

Compliance of the connecting passages within the EHA is not included within the calculation of effective bulk modulus because the effect is insignificant compared to the decrease in bulk modulus due to entrained air. Figure 6.6 compares the fluid compliance of a unit volume for different levels of entrained air, with and without tubing losses. Compliance including tubing effects is calculated according to

$$C_{\text{tubing}} = \frac{V}{\beta} = V \left( \frac{D}{tE_{\text{steel}}} + \frac{1-x}{\beta_1} + \frac{x}{P} \right), \quad (6.15)$$

where  $E_{\text{steel}}$  is the Young's modulus of the steel passages used and  $\frac{D}{t}$  is the diameter to thickness ratio. Figure 6.6 assumes a ratio  $\frac{D}{t}$  of 10; the actual thickness of the hydraulic passages used within the EHA is significantly higher. The compliance from the entrained air itself is calculated using (6.9).

## 6.5 Nonlinear Terfenol-D Model Equations

Previous modeling of the magnetostrictive EHA system used a linear model to calculate the strain within the Terfenol-D drive rod due to applied currents and stress. This model does not accurately reflect the actual behavior of magnetostrictive materials, which display saturation and hysteresis effects in their response to applied magnetic fields, especially at high frequencies and drive levels (Figure 2.5). Despite these nonlinearities, the linear model was found to give a reasonable calculation of the output velocity of the EHA in many cases. This is because the hydraulic rectification process reduces the effect of Terfenol-D nonlinearities. Since the large output motions of the hydraulic cylinder are made up of hundreds to thousands of pumping cycles, the only characteristics of the Terfenol-D motion reflected in the system response are the actuation frequency and the stroke at each cycle.

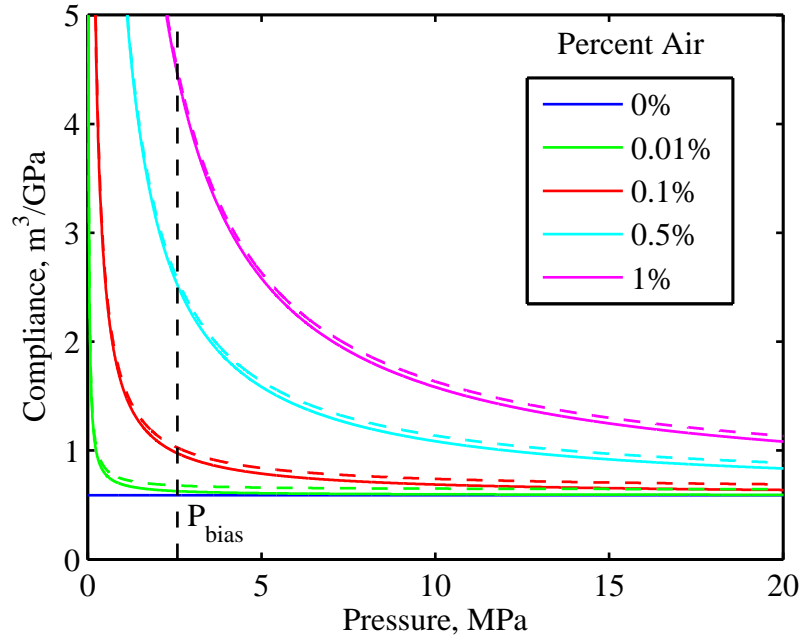


Figure 6.6: Effect of mechanical stiffness on the effective compliance of a fluid passage. Inclusion of the mechanical compliance of the fluid passage (dashed line) has a small effect on the compliance compared to the effect of entrained air only (solid line).

To more accurately calculate the response of the Terfenol-D rod used to drive the EHA system, the Jiles-Atherton equations to calculate magnetization are combined with Maxwell's equations for magnetic field diffusion, according to the method developed by Chakrabarti and Dapino [75]. The magnetostriction is calculated as a single-valued function of magnetization, which is calculated from a volume averaged sum over the radius of the rod. The force resulting from the magnetostriction strain replaces the value previously used in the lumped parameter model equations for the system, which was a linear function of the applied current.

## Magnetic field equations

Maxwell's Equations are used to calculate the magnetic field with the rod, and account for losses due to eddy currents,

$$\Delta \times H = J + \epsilon_0 \frac{\partial E}{\partial t}, \quad (6.16)$$

$$\Delta \times E = \frac{\partial B}{\partial t} \quad (6.17)$$

where  $H$  and  $E$  represent the magnetic and electric fields,  $B$  represents the magnetic flux density, and  $\epsilon_0$  is the permittivity of free space. The current density  $J$  is related to the electric field by the resistivity  $\sigma$ , according to Ohm's law ( $J = \sigma E$ ). For the frequency range considered, the second term on the right hand side of (6.17) can be neglected. Combining (6.16) and (6.17) and applying the result for cylindrical geometries gives the diffusion equation for magnetic field

$$\left( \frac{\partial^2 H}{\partial r^2} \right) + \frac{1}{r} \frac{\partial H}{\partial r} = -\sigma \mu \frac{\partial H}{\partial t} \quad (6.18)$$

where  $\mu$  is the magnetic permeability of the material,  $r$  is the radial coordinate, and  $t$  is time. The boundary condition for the applied field at the outer radius of the rod  $R$  can be taken as a harmonically applied field of amplitude  $H_0$  and frequency  $\omega$ ,

$$H(R, t) = H_0 e^{i\omega t}. \quad (6.19)$$

Assuming a solution of the form

$$H(r, t) = H_0 \tilde{h}(r) e^{i\omega t}, \quad (6.20)$$

where  $\tilde{h}$  is a complex function of the radius, reduces the diffusion equation to

$$\left( \frac{d^2 \tilde{h}}{dr^2} \right) + \frac{1}{r} \frac{d\tilde{h}}{dr} - i\sigma \mu \omega \tilde{h} = 0. \quad (6.21)$$

The solution to (6.21) can be written as

$$\tilde{h}(r) = \frac{I_0(q(r))}{I_0(q(R))}, \quad (6.22)$$

where  $I_0$  is the modified Bessel function of order zero and

$$q(r) = \left( \sqrt{i\sigma\mu\omega} \right) r. \quad (6.23)$$

### Jiles-Atherton Equations

The magnetization of the material due to the applied magnetic field was calculated using the Jiles-Atherton model. A summary of the basic equations of the model is given here, for a detailed derivation of the equations refer to [75, 76]. Magnetization  $M$  of the material at any point in time is considered to be sum of an anhysteretic component  $M_{\text{an}}$  and an irreversible component  $M_{\text{irr}}$

$$M = cM_{\text{an}} + (1 - c)M_{\text{irr}}, \quad (6.24)$$

where  $c$  is a reversibility parameter that accounts for reversible deflection of the walls of the magnetic domains within the material. (The value of  $c$  is considered as a material parameter, which falls between the range of 0 and 1.) The anhysteretic component of magnetization is defined by the Langevin function

$$M_{\text{an}} = M_s \left( \coth \left( \frac{H_e}{a} \right) \left( \frac{a}{H_e} \right) \right), \quad (6.25)$$

for the saturation magnetization  $M_s$  and shape parameter  $a$  controlling the shape of the curve. The effective field causing the magnetization  $H_e$  is calculated from

$$H_e = H + \left( \alpha + \frac{9}{2} \frac{\sigma_{\text{bias}} \lambda_s}{\mu_0 M_s^2} \right) M = H + \tilde{\alpha} M \quad (6.26)$$

where  $\alpha$  a parameter that quantifies magnetic domain interactions,  $\sigma_{\text{bias}}$  is the bias stress applied to the rod, and  $\lambda_s$  is the saturation magnetostriction; the parameters

can be combined into  $\tilde{\alpha}$  as shown to simplify the equations. A law of approach to the anhysteretic magnetization is used to calculate the irreversible component

$$\frac{dM_{\text{irr}}}{dH_e} = \frac{M_{\text{an}} - M_{\text{irr}}}{\delta k} \quad (6.27)$$

where  $\delta$  has a value of +1 for increasing fields and -1 for decreasing fields, and  $k$  is a parameter to quantify the energy required to break pinning sites for magnetic domain motion. Assuming that the field is radially dependent, the derivative of the magnetization with respect to the applied field can be expressed as

$$\frac{dM}{dH} = \left[ c \frac{dM_{\text{an}}}{dH_e}(r) + \frac{M_{\text{an}}(r) - M(r)}{\delta(r)k} \right] \left[ 1 + \tilde{\alpha} \frac{dM}{dH}(r) \right] = \Phi_{(M(r))} \left[ 1 + \tilde{\alpha} \frac{dM}{dH}(r) \right], \quad (6.28)$$

which can be reduced to

$$\frac{dM}{dH} = \left( \frac{\Phi_{(M(r))}}{1 - \tilde{\alpha}\Phi_{(M(r))}} \right) \quad (6.29)$$

Assuming a relatively large pre-stress, the magnetostriction  $\lambda$  calculated as a single-valued function of the magnetization

$$\lambda(r) = \frac{3}{2} \frac{\lambda_s}{M_s^2} M(r)^2. \quad (6.30)$$

To calculate the average magnetostriction within the rod  $\lambda_{\text{avg}}$ , the applied field, magnetization, and magnetostriction are calculated over a set of a 10 discrete radii,  $r_i$ . The average magnetostriction is obtained by taking an weighted average of the magnetostriction at each point, using the weighting parameters  $N(r_i)$  proportional to the cross-sectional area represented by each radius.

$$\lambda_{\text{avg}} = \frac{1}{\sum_{i=1}^n N(r_i)} \sum_{i=1}^n \lambda(r_i) N(r_i) \quad (6.31)$$

The nonlinear calculation of the average magnetostriction of the material was incorporated into the overall system model by replacing the previous calculation for

the magnetostrictive force using a term proportional to the input current  $F = \alpha I$ , with a value based on the calculated magnetostriction and the modulus and area of the Terfenol-D rod

$$F = E_{TD}A_{TD}\lambda_{avg}. \quad (6.32)$$

## 6.6 Model Results

The model equations developed result in a set of ordinary differential equations representing the smart material EHA system. These equations were solved using the MATLAB ordinary differential equation solver `ode45`. The components of the model were applied progressively. An initial no-valve model considered the pressure response that would be measured by testing the system without the reed valves installed. Then, the full system model, including the reed valve dynamics was evaluated using the linear and nonlinear versions of the Terfenol-D model. Additionally, a version of the model was implemented a commercial, 1-D modeling package called AMESim.

### 6.6.1 No-Valve Modeling

In order to characterize the effect of the hydraulic manifold on the frequency response of the system separate from the valve dynamic effects, experimental testing and modeling were conducted on the system without the valves installed. The linear model for the Terfenol-D rod was used. A schematic of the test configuration is shown in Figure 6.7.

The system was tested experimentally without the reed valves installed; a constant sinusoidal current was applied over a range of frequencies and the pressure response was measured (Figure 6.8). Large weights were used to hold the output cylinder fixed. The model results showed a good correlation between the locations of the peaks in the response to an applied current (Figure 6.9).

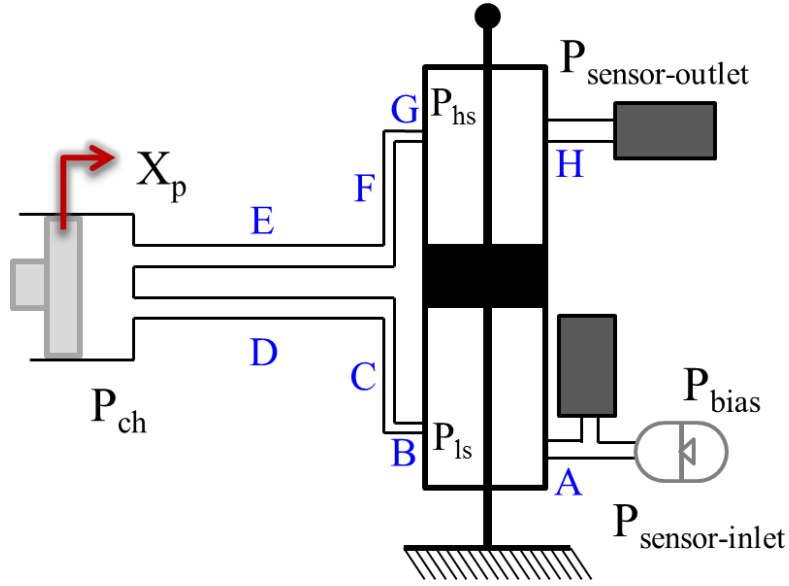


Figure 6.7: Layout of the hydraulic system model for the experimental system without the reed valves installed.

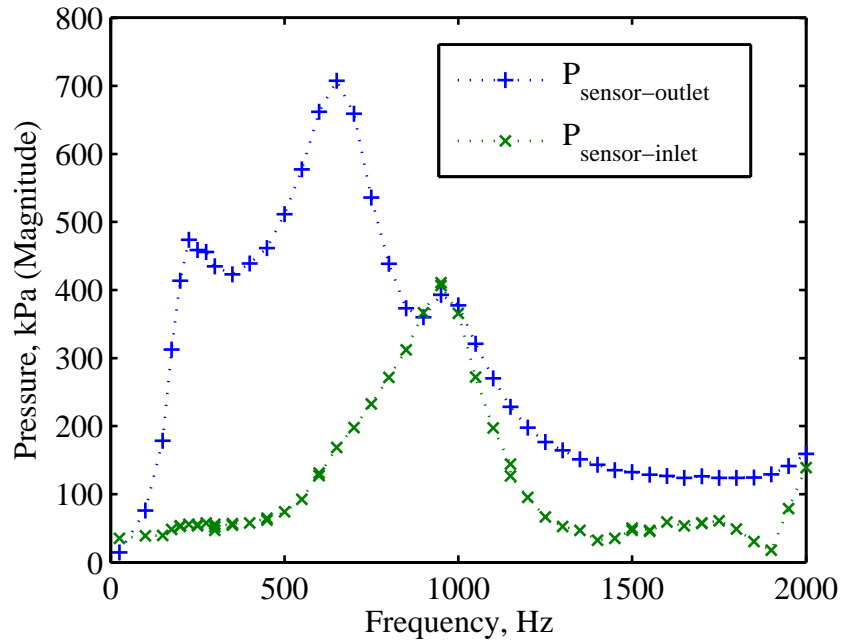


Figure 6.8: Experimental results of measuring the pressure amplitude generated within the system for a constant current input over the frequency range. The pressures correspond to the high-pressure at low-pressure sides of the output hydraulic cylinder.

The magnitude of the pressure response was much higher in the model results than in the experimental data. This discrepancy was likely due to the laminar flow assumption used to develop the model. Without the relatively large fluid resistance that the valves provide in the system, the high flow rates could shift the system to a turbulent flow regime. Also, the large pressure oscillations may have been limited by cavitation.

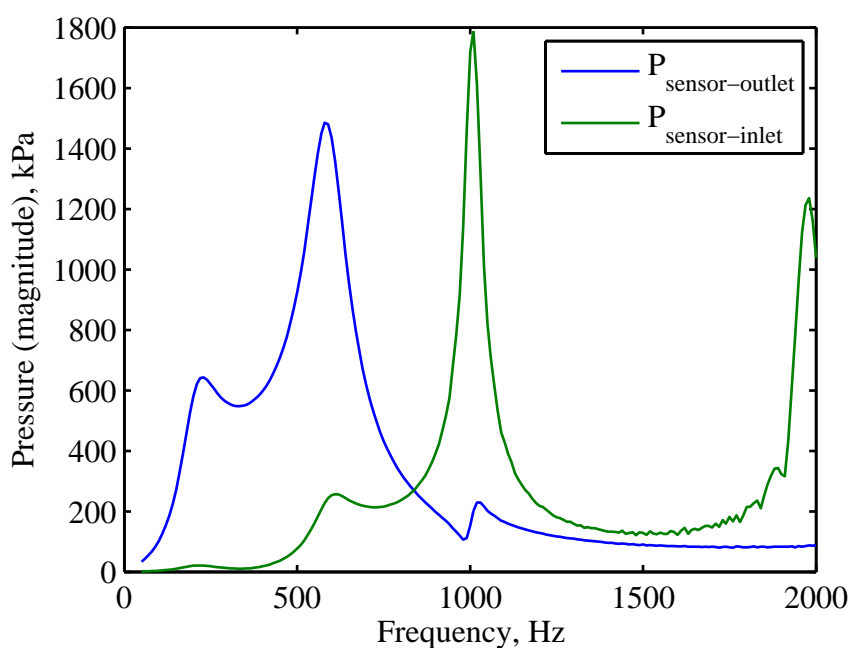


Figure 6.9: Model results of for the pressure amplitude generated within the system for a constant current input over the frequency range. The pressures correspond to the high-pressure at low-pressure sides of the output hydraulic cylinder.

After comparing the model results to the experimental performance, various fluid, pump, and measurement parameters were varied to determine the effect on the response of the system. Table 6.2 summarizes the results. Of the parameters considered, the largest effect on frequency response is from adjusting the side passage diameter



(C and F, Figure 6.7). Additionally, this model was used to predict the shift in frequency response from removing the extra volume associated with the high-side pressure sensor (Figure 4.9).

Table 6.2: Summary of the no-reed model results for various fluid, pump, and measurement parameters.

	Change	Frequency Bandwidth	Pressure
Fluid Bulk Modulus	+	+	+
	-	-	-
Pumping Chamber Height	+	=	=
	-	=	+
Piston Diameter	+	-	-
	-	+	-
Input Level	+	=	+
Terfenol-D Rod Length	+	-	+
Side Passage Diameter	+	+	+
Viscosity	-	=	+
Sensor Volume	-	+	+

## 6.7 Full System Modeling Results with Reeds Installed

### 6.7.1 Linear Terfenol-D Model

The linear Terfenol-D model was applied to the full system with the valves included, simulating an applied current of  $7.1 A_{\text{rms}}$  and a series of applied loads. The model calculations show a similar double-peaked response as the experimental data (Figure 4.10). As the applied load is increased, the trend of the second frequency peak

increasing with applied load is demonstrated in the model due to the increased bulk modulus as a higher pressure is used to move the load.

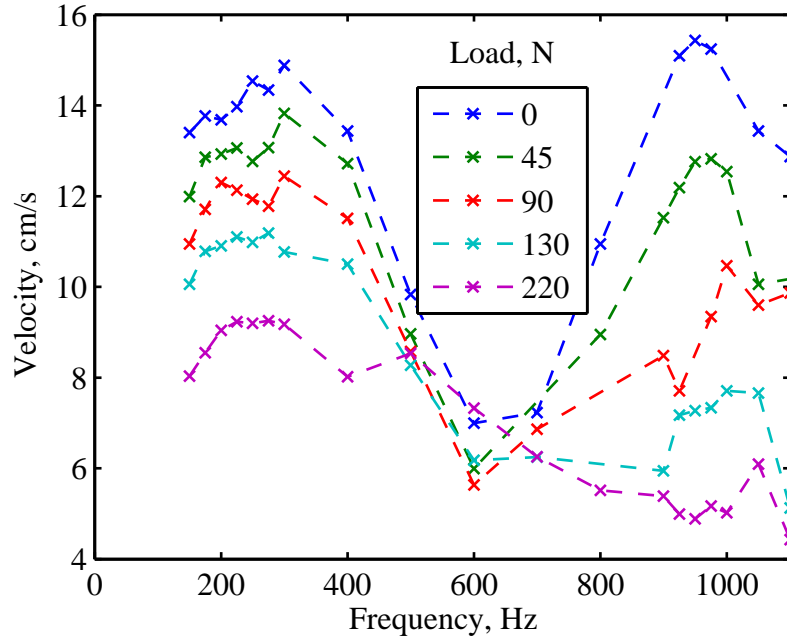


Figure 6.10: Model results for applying the linear Terfenol-D model for a 7.1  $A_{rms}$  input current over the frequency range.

There is some discrepancy between the magnitude of the response from the model results and the experimental data, which is most likely due to the linear model that was used for the magnetostrictive driver. The actual response of Terfenol-D varies nonlinearly with frequency and applied stress. Additionally, the input to the system over the frequency range was controlled to be a constant current. The effective magnetic field seen by the rod would be expected to decrease at higher frequencies due to losses such as eddy currents. The linear model represents an approximation of the overall behavior, which under-predicts the material response at low frequencies and over-predicts the response at high frequencies

### 6.7.2 AMESim Model

The system model was also implemented using LMS Imagine.Lab AMESim. AMESim is a commercial simulation software used for 1-D or lumped-parameter analysis. The same set of equations used for the linear Terfenol-D full system model was used in the AMESim implementation. However, in this case, the software compiled and solved the system of equations based on input of the a diagram of the system and the parameters of each component 6.11. Valve inertia was not included in the model

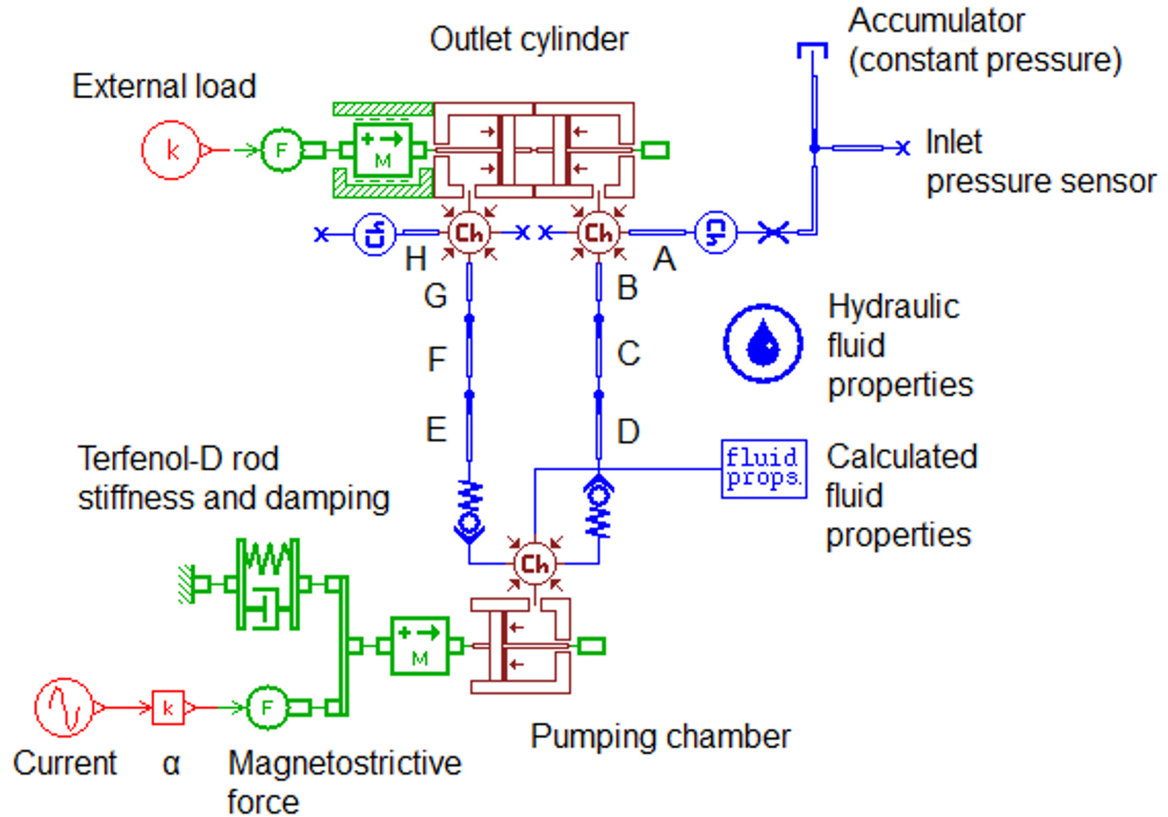


Figure 6.11: AMESim implementation of lumped parameter model utilizing the linear magnetostrictive model

solution. Additional components could have been added to the model to implement

valve inertia, but it was not necessary for obtaining a reasonable correlation to the experimental data.

The AMESim model was compared to experimental data using a  $3.5 A_{\text{rms}}$  input current over the frequency range. The model results show a very good correlation to the experimental data up a 400 Hz input frequency. The match is not as good at higher frequencies, but the model accurately predicts the second velocity peak at 900 Hz. The difference between the model and experimental results at high frequencies is likely due to the increasingly nonlinear response of Terfenol-D as the input frequency is increased. Additionally, at higher frequencies the response of the valves may start to have some influence on the system response, or there may have been differences in the physical system geometry compared to the simplified dimensions entered in the model. The approximation of the seal friction of the output hydraulic cylinder may also affect the system response.

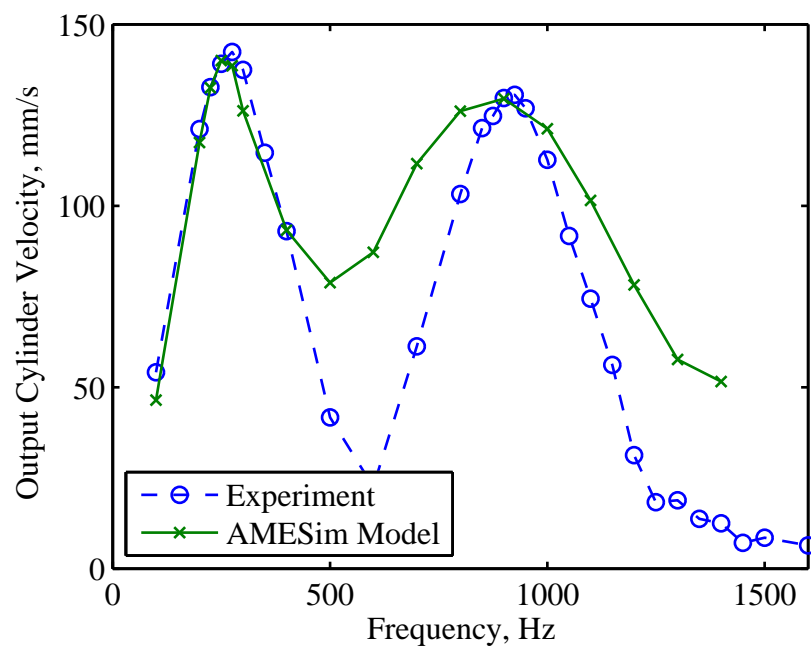


Figure 6.12: Comparison of the system response calculated with AMESim with experimental data.

### 6.7.3 Nonlinear Terfenol-D Model

Applying the nonlinear Jiles-Atherton model equations to the system produced a more accurate calculation of the output velocity for the 7.1 A<sub>rms</sub> input current level experiments (Figure 6.13). While the model correlation is more accurate at low frequencies, the model follows the experimental data closely up to 500 Hz. The second peak of the velocity data is also represented although the model underestimates the velocity by 2-3 cm/s at frequencies of 600 Hz and above.

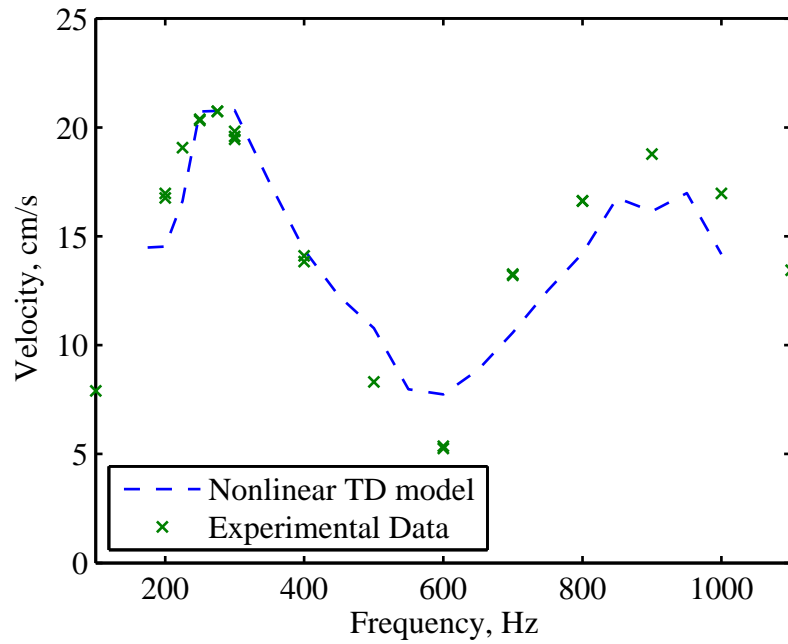


Figure 6.13: Comparison of the measured unloaded velocity with the calculation using the nonlinear Jiles-Atherton model for the Terfenol-D rod for a 7.1 A<sub>rms</sub> constant input current over the frequency range.

## 6.8 Summary

A modeling framework for predicting the response of a magnetostrictive EHA is presented, which uses a lumped-parameter approach to develop models of the fluid and mechanical components of the system. The component-level models are validated using experimental results to form a set of differential equations, which can be used to predict the overall dynamic response of a magnetostrictive EHA system.

The model is applied to the reduced-volume-manifold EHA system (Chapter 4), and the results show good agreement with the predicted output and experimental results. This validated model can thus be applied to the design of magnetostrictive EHAs for other applications. Chapter 7 uses the model to predict the response of a high-power EHA system for aerospace applications and to determine the effect of varying the passage diameter of the hydraulic components on the overall response.

While the model is developed for designing pumps driven by magnetostrictive materials, the general framework can be utilized for other types of systems, such as actuators developed with piezoelectric pumps. One could simply replace the stiffness and magnetostrictive force terms in (6.3) with the corresponding voltage dependent terms for the material used. The equations modeling the fluid, reed valves, and output hydraulic cylinder would remain the same. A nonlinear model could also be utilized in a similar fashion as the Jiles-Atherton model was applied in Section 6.5; however, this may not be necessary as piezoelectric materials generally have a more linear response than magnetostrictive materials.

Implementation of the system model was also demonstrated using AMESim, a commercial 1-D simulation software package. A reasonable correlation with the measured system performance was achieved, even though a linear magnetostrictive model was used along with a valve model neglecting valve inertia. Showing how a smart

material EHA can be modeled using general simulation tools is an important result for enabling the actuators to be applied in broader applications.



# Chapter 7

## Design of a Compact Aircraft EHA

### 7.1 Introduction

This chapter presents the methodology used to scale up a smart material electrohydraulic actuator (EHA) design for aircraft applications. A set of design goals are identified, which are used to define a preliminary set of design parameters based on a quasi-static analysis of the system. A dynamic model of the full system is developed based on the initial design geometry based on the model equations presented in Chapter 6. The results of the dynamic model are used to improve the overall frequency bandwidth of the system. Additional finite element modeling of the mechanical components of the system and computational fluid dynamics modeling of the fluid components of the system are conducted to ensure that the design performs according to the assumptions used within the overall system modeling framework.

Based on the model results, an overall design for the system is presented that meets the design goals identified for the design of a compact magnetostrictive EHA for aerospace applications. The model predictions show a dramatic increase both the frequency bandwidth and output power of the system compared to previous smart material EHA designs.

## 7.2 Design Requirements

For aerospace applications, an output power level range of at least a few hundred watts is needed [2, 10, 77]. This is approximately 10-20x higher than the output of previously published smart material EHA designs (Table 2.2). Based on discussions with industry partners, design goals for the blocked force and no-load velocity were established (Table 7.1). These requirements correspond to a maximum power output

Table 7.1: Performance goals for the high-power smart material EHA design.

Feature	Goal
No-Load Actuator Velocity	5 cm/s (2 in/s)
Blocked Force (Stall Load)	22 kN (5,000 lb <sub>f</sub> )
Cylinder Stroke	8 cm (3 in)

goal of 280 W, estimated using the formula

$$P_{\text{out}} = \frac{1}{4} F_{\text{blocked}} V_{\text{no-load}}, \quad (7.1)$$

which has been shown to correspond well with the actual performance of these types of actuators (Figures 4.11 and 4.17).

After considering several options for the type of hydraulic cylinder to be used for EHA design, it was decided to use a commercially-available hydraulic cylinder. An aircraft actuator centerline from a business-jet application was provided by Moog, Inc. (Figure 7.1). The hydraulic cylinder has an internal pressure area of 12.64 cm<sup>2</sup> (1.96 sq. in.) and a stroke of 6.3 cm (2.5 in). The hydraulic centerline-style



Figure 7.1: Commercial hydraulic actuator (Moog, Inc.) used for the design of a high-power magnetostrictive EHA.

cylinder is designed to bolt into a custom manifold, which is ideal for design of a compact actuator. An integrated LVDT is provided for sensing the cylinder displacement (G.W. Lisk Co. CA62723).

Based on the dimensions of the hydraulic cylinder, the actuator design force and velocity targets are converted to the flow rate and pressure requirements (Table 7.1). Expressing the design parameters in terms of flow and pressure allows for direct

Table 7.2: Design requirements applying the hydraulic cylinder area to the overall actuator performance goals.

Feature	Design Requirement
No-load Flow Rate	64 cm <sup>3</sup> /s (3.9 cu in/s)
Blocked Pressure	17.6 MPa (2,500 psi)
Cylinder Stroke	6.3 cm (2.5 in)
Output Power (7.1)	280 W

comparison to other published smart material EHA designs (Table 2.2).

### 7.3 Preliminary Design

An initial design for a magnetostrictive EHA can be calculated from quasi-static considerations based on the design requirements. The key design parameters that need to be identified are the diameter and length of the Terfenol-D driver and the diameter of the pumping piston.

The performance of a Terfenol-D rod can be evaluated on a quasi-static basis by its blocked force and free strain capability. The potential blocked force of a Terfenol-D,  $F_{\text{blocked}}$ , can be calculated from the rod area  $A_{\text{TD}}$ , Young's modulus  $E_{\text{TD}}$ , and free strain  $\epsilon_{\text{free}}$  according to

$$F_{\text{blocked}} = A_{\text{TD}} E_{\text{TD}} \epsilon_{\text{free}} = \left( \frac{\pi}{4} D_{\text{TD}}^2 \right) E_{\text{TD}} \epsilon_{\text{free}}. \quad (7.2)$$

Typical values for these properties considered for the design are given in Table 7.3. The available diameters and Young's modulus information is based on information from the manufacturer, Etrema Products [1]. The free strain is based on the experimental data, from the reduced-volume-manifold EHA, which is described in Chapter 4.

Table 7.3: Terfenol-D properties used for initial design of magnetostrictive EHA [1]

Property	Value
Diameters Available, $D_{\text{TD}}$	13, 20, 25, 40, or 65 mm
Young's Modulus, $E_{\text{TD}}$	25 – 35 GPa
Free Strain, $\epsilon_{\text{free}}$	1600 ppm

Applying (7.2), the amount of force that can be generated from each available Terfenol-D rod diameter can be calculated. The force required from the Terfenol-D driver to meet the pressure requirement, 17.6 MPa, depends on the piston diameter,  $D_p$ ,

$$F_{\text{required}} = \frac{\pi}{4} D_p^2 P_{\text{required}}. \quad (7.3)$$

By equating (7.2) and (7.3), the maximum allowable piston diameter,  $D_{p,\text{max}}$  can be calculated as

$$D_{p,\text{max}} = D_{\text{TD}} \sqrt{\frac{E_{\text{TD}} \epsilon_{\text{free}}}{P_{\text{required}}}}. \quad (7.4)$$

The allowable piston diameter for each available size Terfenol-D rod is shown in Figure 7.2; a rod diameter of 20 mm was selected to give a maximum allowable piston size of 30 mm.

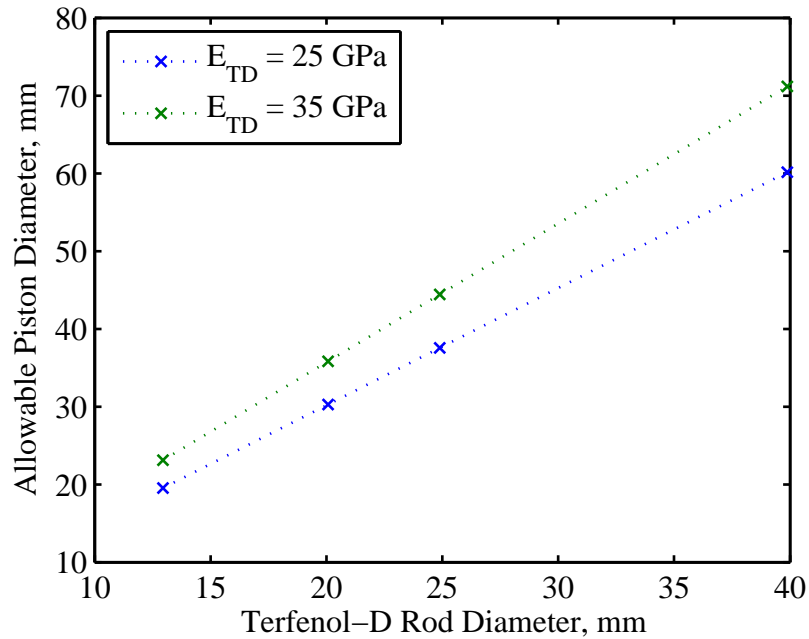


Figure 7.2: Allowable piston diameter for each available size Terfenol-D rod. The selected rod diameter of 20 mm can supply the required force to generate 17.6 MPa for a pump piston with diameter up to 30 mm.

The flow rate required for the system determines the length the Terfenol-D rod needed. The periodic motion of the pumping piston at frequency  $f$  gives a flow rate of  $Q = f\Delta V$ , where the volume of fluid moved in each pumping cycle,  $\Delta V$  is given by

$$\Delta V = A_p \delta = A_p L_{TD} \epsilon, \quad (7.5)$$

with piston area  $A_p$  and displacement of the Terfenol-D rod  $\delta$ . Potential combinations of driver length and piston diameter were evaluated (Figure 7.3), and a piston diameter of 28 mm and driver length of 152 mm was selected, which is predicted to generate the required no-load flow rate at a frequency of 425 Hz.

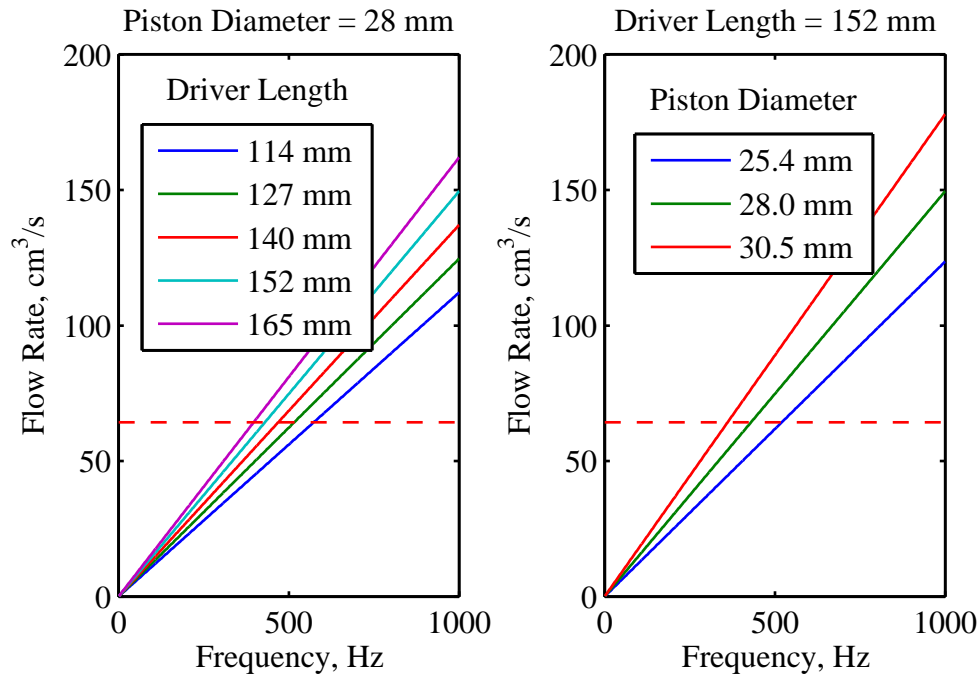


Figure 7.3: Unloaded flow rate vs. frequency for a combination of driver lengths and piston diameters. Neglecting losses, the selected piston diameter of 28 mm and driver length of 152 mm would be capable of reaching the desired no-load flow rate (red dashed line) at 425 Hz.

### 7.3.1 Power Analysis and Losses

Another quasi-static method to estimate the performance of a EHA design is to consider the maximum amount of work that can be performed by the actuator per cycle. Calculating the energy transfer within the system allows for the inclusion of loss terms to produce a more accurate estimation of the system output. This approach was proposed by Lindler, Anderson, and Regelbrugge and has been expanded here to include potential losses from compliance of the pump structure [18]. The calculation of the volume flow loss due to compression within the pumping chamber has also been corrected.

The maximum amount of work  $W_{\max}$  that can be performed actuation cycle is given by

$$W_{\max} = \frac{F_b \delta_{\max}}{4}, \quad (7.6)$$

where  $F_b$  is the blocked force of the the actuator and  $\delta_{\max}$  is the free displacement. Equation (7.6) represents the work cycle with the largest area that can be drawn from the force-velocity diagram, which describes the general behavior of a magnetostrictive (or piezoelectric) actuator. This approximately linear force velocity relationship is a consequence of (6.1) and is reflected in the measured performance of smart material EHA actuators, even at relatively high drive levels (Figure 4.17).

Equation (7.6) can be converted in terms of the blocked pressure  $P_b$  and maximum flow volume per cycle  $\Delta V_{\max}$  using the piston area  $A_p$

$$W_{\max} = \frac{1}{4} (P_b A_p) \left( \frac{V_{\max}}{A_p} \right) = \frac{P_b \Delta V_{\max}}{4}. \quad (7.7)$$

From the definition of bulk modulus  $\left( \beta = -V \frac{\Delta P}{\Delta V} \right)$ , the flow volume lost to compression of the fluid within the pumping chamber can be calculated as

$$\Delta V_\beta = P_b \frac{V_{ch}}{A_p^2}, \quad (7.8)$$

where  $V_{\text{ch}}$  is the initial volume of the pumping chamber. Subtracting the lost volume due to fluid compression (7.8) from (7.7) results in an equation for the work output per cycle, accounting for fluid losses

$$W_{\text{o,fluid}} = \frac{(P_{\text{b}} - \Delta P_{\text{v}})}{4} \left[ V_{\text{max}} - \frac{P_{\text{b}} V_{\text{ch}}}{\beta A_{\text{p}}^2} \right], \quad (7.9)$$

where  $\Delta P_{\text{v}}$  is an additional term estimating the pressure drop from the rectification valves and the fluid passages pumping chamber to the output hydraulic cylinder. Additionally, this term ( $\Delta P_{\text{v}}$ ) could be interpreted as including an estimate for the work done to overcome the output hydraulic cylinder friction.

Structural compliance losses, i.e. motion of the smart material being lost to compliance of the pump structure rather than moving a volume of fluid, is a design concern. For a practical estimate, these losses can be included in the initial calculations of system output power by assuming that the stiffness of the pump structure is 10x the stiffness of the magnetostrictive rod,  $k_{\text{TD}}$ , [10]

$$\delta_{\text{struct}} = \frac{F_{\text{b}}}{10k_{\text{TD}}} = \frac{P_{\text{b}} A_{\text{p}} L_{\text{TD}}}{10E_{\text{TD}} A_{\text{TD}}}. \quad (7.10)$$

Applying this additional loss term to (7.9),

$$W_{\text{o,total}} = \frac{(P_{\text{b}} - \Delta P_{\text{v}}) A_{\text{p}}}{4} \left[ \delta_{\text{max}} - \frac{P_{\text{b}} V_{\text{ch}}}{\beta A_{\text{p}}} - \delta_{\text{struct}} \right]. \quad (7.11)$$

The work output per cycle times the frequency (number of cycles per second) gives an estimate of the power output of the actuator at a given input frequency. Applying design parameters for the compact aerospace actuator from the initial design calculations ( $D_{\text{p}} = 28$  mm,  $D_{\text{TD}} = 20$  mm,  $L_{\text{TD}} = 152$  mm) shows that the actuator is expected to reach the output power target at a frequency of 540 Hz (Figure 7.4). A pressure loss estimate of  $\Delta P_{\text{v}} = 700$  kPa was used for the analysis.



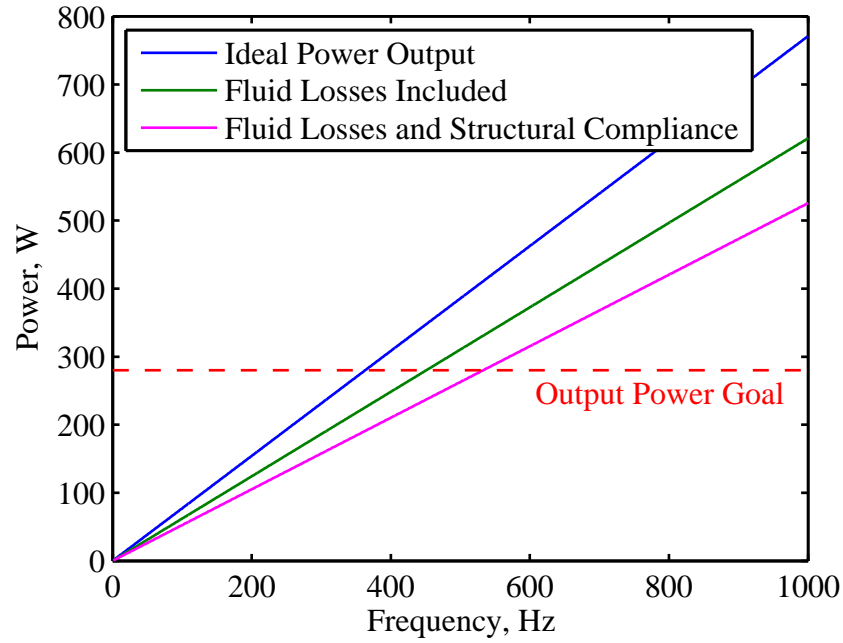


Figure 7.4: Estimated output power based on a quasi-static analysis for the preliminary pump design; output power goal of 280 W is achieved at an input frequency of 540 Hz. The calculation is based on calculating the work per cycle performed by the magnetostrictive actuator and subtracting out fluid pumping and compliance losses along with the loss in motion due to the structural compliance of the system.

For comparison, the calculated output power for the reduced-volume-manifold EHA is shown on Figure 7.5. The estimated power output of 37.5 W at 225 Hz is within 5% of the measured power output of the system (Figure 4.12).

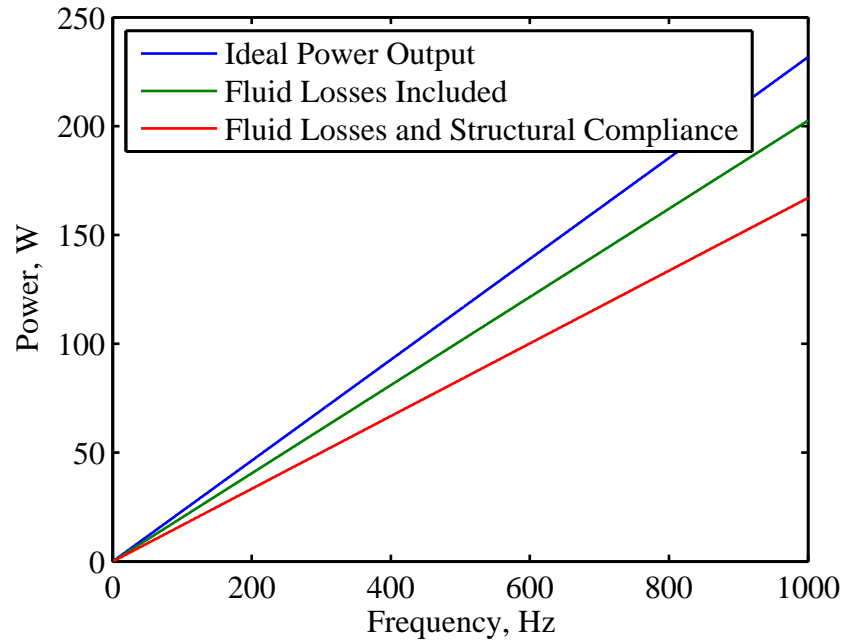


Figure 7.5: Results of applying the quasi-static power calculation to the previous, reduced-volume-manifold EHA. The predicted power output of 37.5 W at 225 Hz is similar to the peak performance of 37 W measured experimentally with the system (Figure 4.12).

## 7.4 Detailed Design

Section 7.3 described the preliminary design of a smart material system. The design requirements for a compact aircraft EHA were identified, and the key parameters for a design to meet these requirements were calculated (Table 7.4). These design

Table 7.4: Preliminary Design Parameters

Feature	Value
Terfenol-D Rod Diameter, $D_{TD}$	20 mm (0.79 in.)
Terfenol-D Rod Length, $D_{TD}$	152 mm (6 in.)
Pump Piston Diameter, $D_p$	28 mm (1.1 in.)
Hydraulic Cylinder Area, $A_{cyl}$	12.64 cm <sup>2</sup> (1.96 sq. in.)
Hydraulic Cylinder Stroke	6.3 cm (2.5 in.)

parameters are the basis for more detailed calculations to establish the design of the remaining aspects of the system: a magnetic circuit, rectification valves, and fluid passages. The magnetic circuit consists of the coil and flux return path used to supply the magnetic field to drive the Terfenol-D rod. The rectification valves perform the critical function of converting the bidirectional pumping motion of the magnetostrictive rod into unidirectional flow of hydraulic fluid. The fluid flow is carried to the hydraulic cylinder by fluid passages, which also play a role in determining the overall frequency response of the system.

### 7.4.1 Magnetic Circuit Design

The magnetic circuit supplies the field necessary to create magnetostriction within the Terfenol-D rod. For the compact aircraft magnetostrictive EHA, the circuit consisted

of a magnetostrictive rod, solenoid coil, and a low-carbon steel magnetic return path. The magnetic flux return path also serves as the support structure to keep the non-moving end of the Terfenol-D rod fixed. The the initial design of the coil is established by calculating the current and number of turns required to supply the necessary magnetic field [78]. The design is then refined using finite element analysis to improve the uniformity of the field within the coil and to ensure that the materials in the flux return are not saturated by the applied field.

The magnetic circuit is designed to supply a field of 140 kA/m (1800 Oe), which should result in a magnetostrictive strain of 1400 ppm according to data supplied by the manufacturer (Figure 2.5). The field will be supplied by a solenoid coil, using a sinusoidal current with a DC bias (i.e. an 70 kA/m amplitude and 70 kA/m DC bias).

For the purposes of design, the magnetomotive, mmf, force required can be given by

$$\text{mmf} = NI = 1.05H_{\text{req}}L_{\text{TD}}, \quad (7.12)$$

where  $N$  is the number of turns in the coil,  $I$  is the current,  $H_{\text{req}}$  is the required field, and  $L_{\text{TD}}$  is the length of the Terfenol-D rod [78]. This calculation assumes that the reluctance of the flux return is much less than the reluctance of the Terfenol-D rod (5%), which is reasonable since the permeability of the steel magnetic circuit components is much higher than that of Terfenol-D.

The number of turns that is in the coil is determined by the coil geometry and size of the wire. The number of turns in each layer of the coil  $N_t$  is given by

$$N_t = \frac{L_{\text{coil}}}{D_w}, \quad (7.13)$$

where  $L_{\text{coil}}$  is the length of the coil and  $D_w$  is the diameter of the wire. The number of layers that can be included  $N_l$  is calculated from the inner and outer diameters

( $D_1$  and  $D_2$ ) of the coil by

$$N_1 = \frac{D_2 - D_1}{2D_w}. \quad (7.14)$$

The inner diameter of the coil  $D_1$  is typically set to be close to the diameter of the magnetostrictive rod. The total number of turns for the coil is thus

$$N_{\text{tot}} = N_t N_1. \quad (7.15)$$

For a given number of turns, the required current can be calculated from *eqn : mmf*. The required voltage can then be calculated by the inductance  $L$  and resistance  $R$  of the coil. The inductance is given by

$$L = \frac{\mu_0 \mu_{\text{TD}} N_{\text{tot}}^2 A}{L_{\text{coil}}} = \frac{\mu_0 \mu_{\text{TD}} A}{L_{\text{coil}}} \left( \frac{L_{\text{coil}} (D_2 - D_1)}{2D_w^2} \right)^2, \quad (7.16)$$

where  $\mu_{\text{TD}}$  is the relative permeability of Terfenol-D,  $\mu_0$  is the permeability of free space, and  $A_{\text{coil}}$  is the area of the coil ( $A_{\text{coil}} = \frac{\pi}{4} D_1^2$ ). The length of the wire,  $L_w$ , can be calculated as

$$L_w = \pi \frac{D_1 + D_2}{2} N_{\text{tot}}, \quad (7.17)$$

and the resistance of the wire can be calculated on the basis of the resistivity  $\rho_w$  of the copper wire copper and the wire length and area

$$R = \frac{\rho_w L_w}{A_w} = \frac{\rho_w L_c (D_2^2 - D_1^2)}{D_w^4}. \quad (7.18)$$

Thus, the required voltage at a particular frequency  $\omega$  can be calculated from the current using

$$V = I \sqrt{R^2 + \omega^2 L^2}. \quad (7.19)$$

Similarly, the power applied to the coil can be calculated as

$$P = I^2 \sqrt{R^2 + \omega^2 L^2}. \quad (7.20)$$

An important implication of these equations is that it can be shown that the required power for the coil does not depend on the wire diameter, only the size of the coil itself [78]. However, the required voltage and current to supply that power does depend on wire diameter, so the capacity of the power supply must be taken into account when designing the coil.

### FE Modeling of Magnetic Circuit

In order to refine the design, an axi-symmetric finite element model of the magnetic circuit was used to calculate the resulting field from an applied current to the coil. The model includes the magnetostrictive rod, coil, flux return, and surrounding air (Figure 7.6).

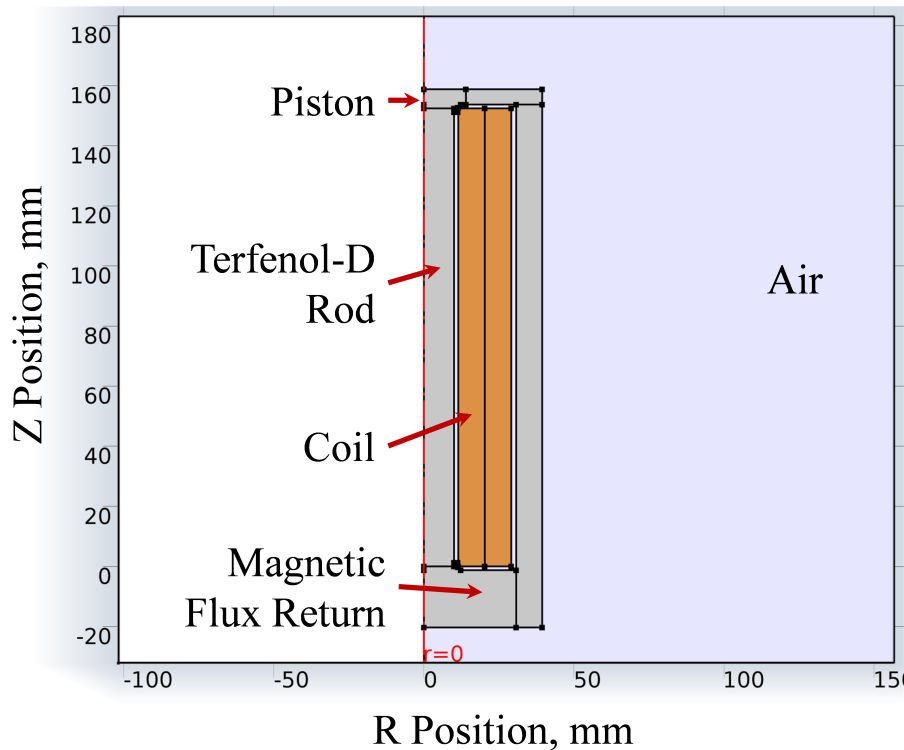


Figure 7.6: Geometry of magnetic circuit FE model, including the rod, flux return, coil, and surrounding air.

One feature of the system that was studied was the length of the coil. The previous, reduced-volume-manifold EHA, used a coil that was approximately 2.5 cm (1 inch) longer than the Terfenol-D driver. This design was chosen in order to avoid a drop-off in magnetic field at the ends of the rod [67]. Results from considering different coil lengths showed that a significantly more uniform field was generated when the coil length was the same as the length of the magnetostrictive rod (Figure 7.7).

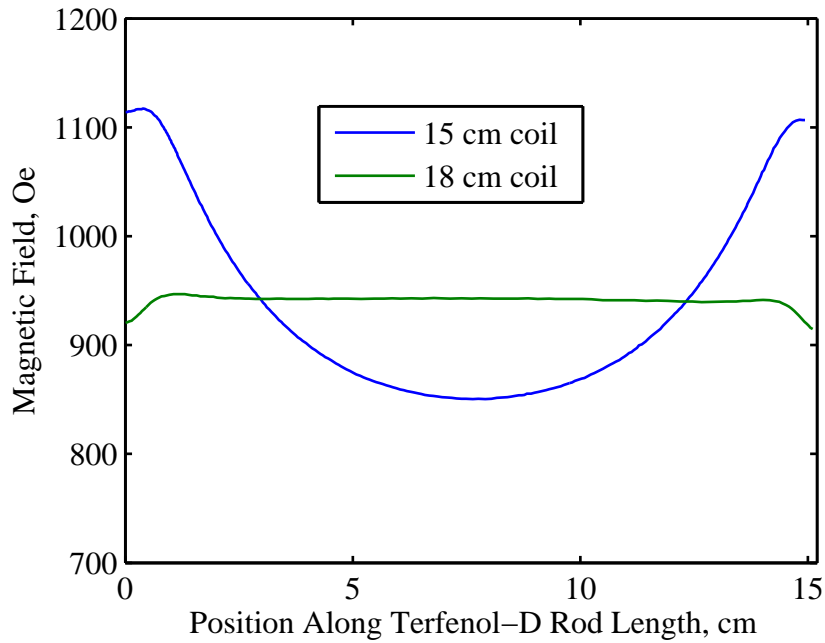


Figure 7.7: Comparison of the field distribution (Oe) using a 18 cm [7 in] (blue) and a 15 cm [6 in] (green) long coil. The shorter coil, which is equal to the length of the Terfenol-D driving rod was found to produce a more uniform field distribution.

Another change to the system that was made was to increase the thickness of some of the return path components (the pump piston and guide ring) in order to prevent saturation.

The final design for the magnetic circuit geometry is shown in figure 7.8. An applied field of 75 kA/m (940 Oe) was calculated for an applied current of 20.2 A. The coil was designed to utilize 568 turns of 12 AWG magnet wire.

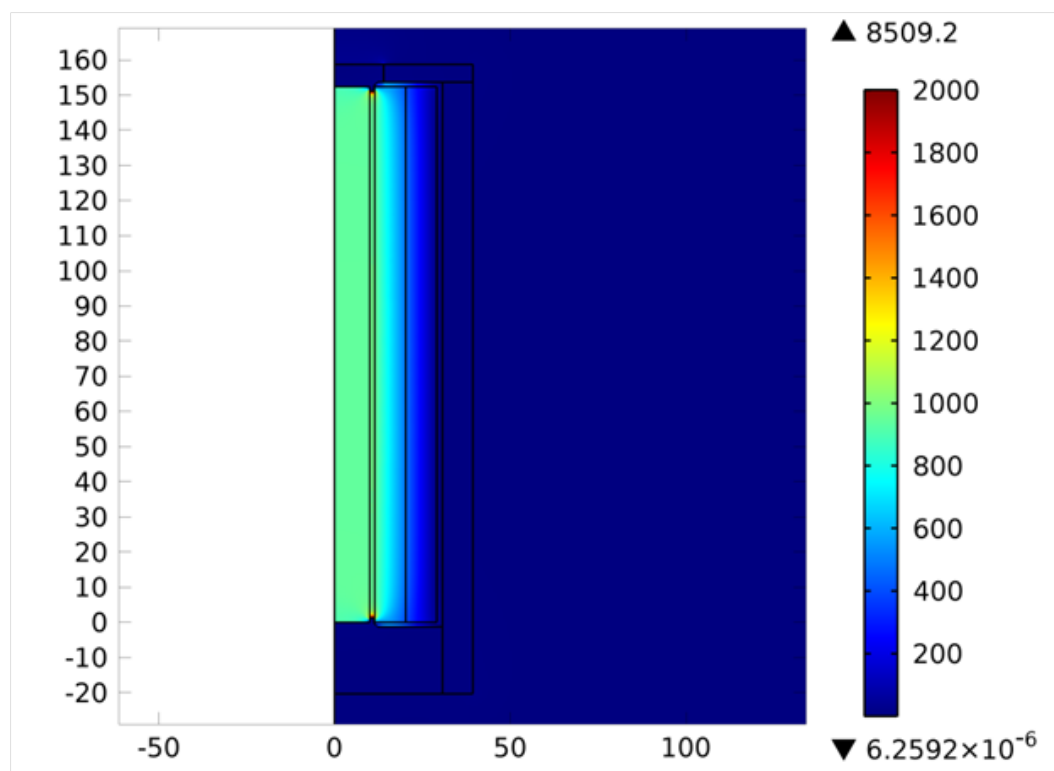


Figure 7.8: Magnetic field distribution (Oe) for FE model of final magnetic circuit design. The average applied field was calculated as 940 Oe (75 kA/m) for an applied current of 20.2 A.

### 7.4.2 Solid Model

A detailed solid model of the system was developed based on the preliminary design parameters (Figure 7.9). This model was used to determine how all of the different components of the system (magnetostrictive pump, valves, return valve, hydraulic cylinder, accumulator, and sensors) would fit together, which determines the



remaining parameters needed for detailed system modeling such as the length and configuration of the fluid passages.

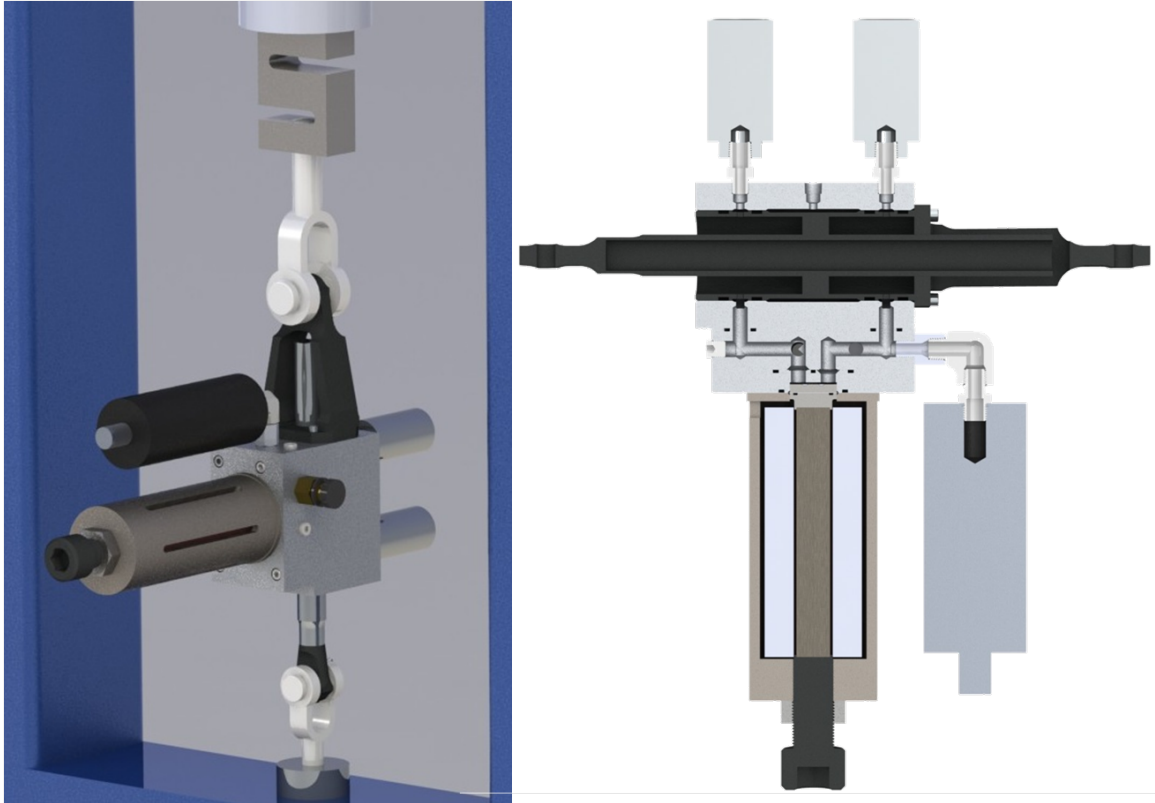


Figure 7.9: CAD rendering of high-power magnetostrictive EHA design with cross-section.

The final drawings of the complete system are reproduced in Appendix D. The system uses the same Sensotec TJE-5000 pressure sensors utilized previously in the reduced-volume-manifold EHA. A piston-type, 0.16 L capacity, nitrogen-charged accumulator is used to supply the bias pressure on the system (Parker ACP05AA016E1-KTB). The system is capable of operation in only one direction, a cartridge-style needle valve is provided for manually resetting the position of the output cylinder after test runs (Parker NVH081).

### 7.4.3 Finite-Element Modeling

Finite element modeling was used to evaluate and refine the compact aircraft EHA design. Structural modeling was used to calculate the stiffness of the flux return, and evaluate the stress on the hydraulic cylinder manifold under blocked-pressure conditions. Computational fluid dynamics modeling was applied to the pump piston to ensure that flow losses were at an acceptable level. The design of reed valves was evaluated for flow performance, frequency response, and durability.

#### Flux Return

The flux return was designed to have a stiffness much higher than the stiffness of the Terfenol-D rod (50 MN/m—70 MN/m). A 2-D axisymmetric structural model was developed using COMSOL, and the stiffness was calculated as 860 MN/m (Figure 7.10). Additionally, the stress within the flux return based on a 22 MPa (3100 psi) applied pressure was calculated and found to be within acceptable limits (Figure 7.11).

#### Manifold Blocked Pressure

Additional modeling was conducted to determine the stress within the manifold which houses the hydraulic cylinder. The manifold contains grooves to direct flow to the ports of the hydraulic cylinder centerline (Figure 7.12). A simulated pressure of 22 MPa (3100 psi) was applied to the flow areas, which resulted in a maximum stress of 90 MPa (Figure 7.13).

### 7.4.4 Pumping Chamber Modeling

One aspect of the lumped-parameter modeling approach used to develop a model for the overall system is that the pressure drop for the fluid flow within the pumping

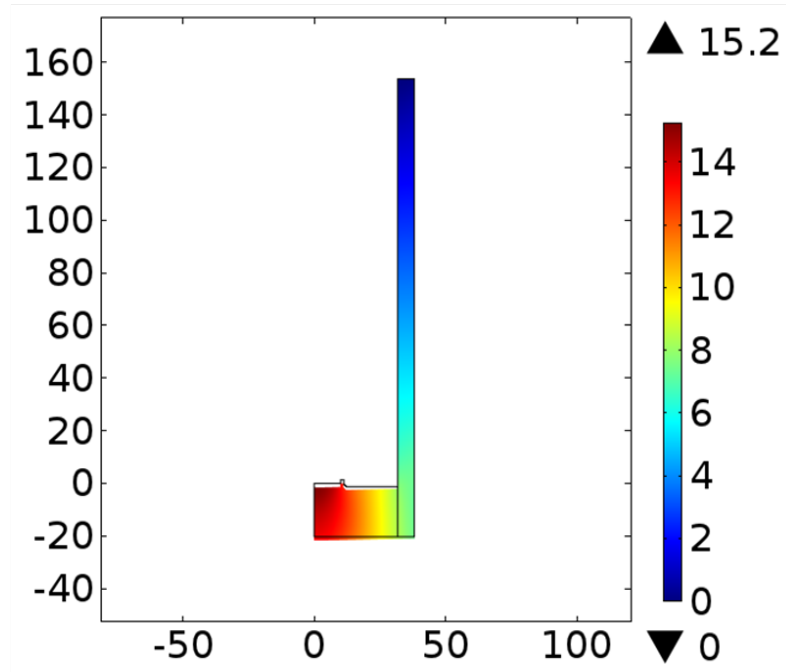


Figure 7.10: Displacement ( $\mu\text{m}$ ) of the pump flux return when subject to a 13 kN (3000  $\text{lb}_f$ ) load. The design's stiffness of the return, which holds the base of the Terfenol-D rod is designed to be approximately 20 times stiffer than the rod itself.

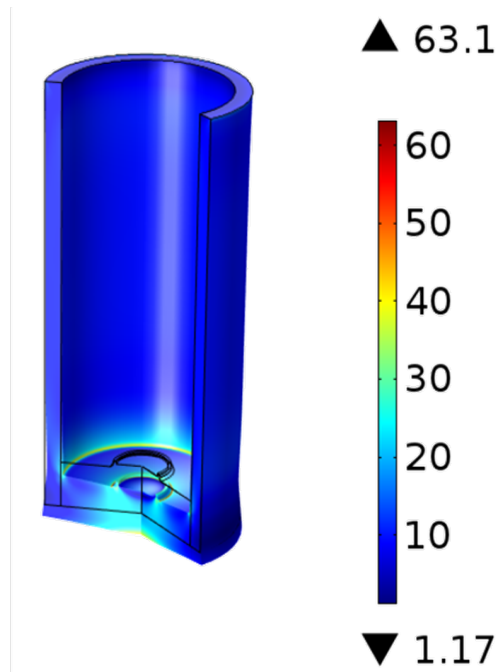


Figure 7.11: Calculated stress in MPa on the flux return when subjected to a 13 kN load (3000  $\text{lb}_f$ ), which corresponds to a pump pressure of 22 MPa (3100 psi).

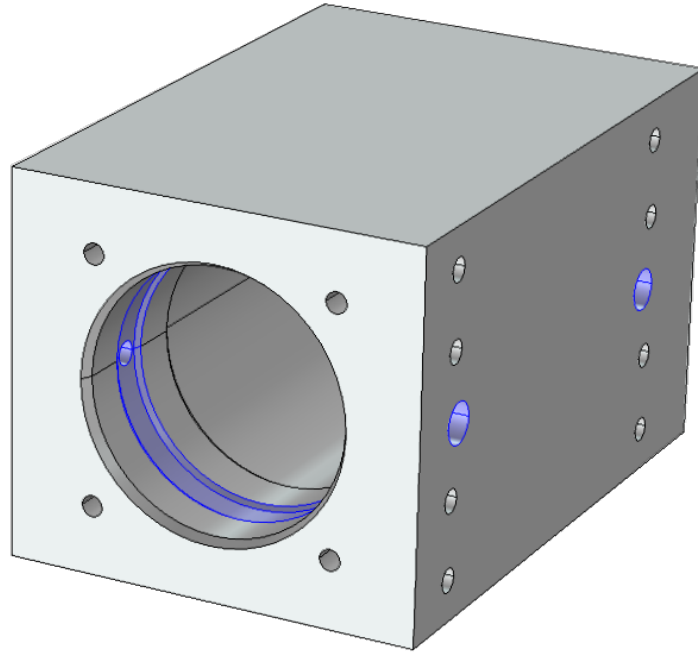


Figure 7.12: Geometry of the finite element model used to evaluate the stress due to the applied pressure within the hydraulic manifold. The highlighted (blue) areas are the pressure channels that interface with the hydraulic cylinder.

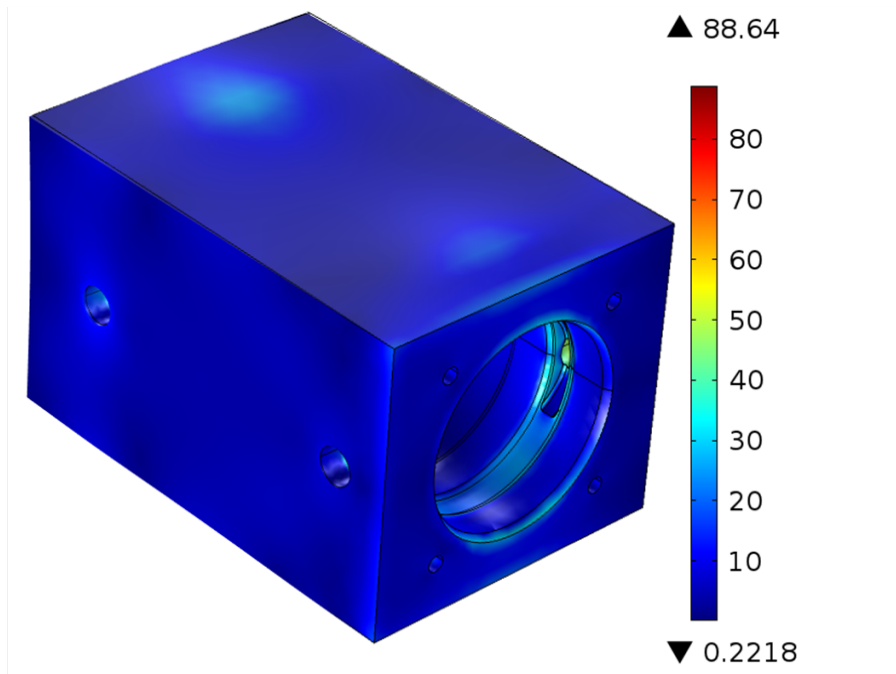


Figure 7.13: Stress from a 22 MPa (3100 psi) applied pressure on the internal flow passages of the hydraulic cylinder manifold.

chamber is neglected. It is assumed that the reed valve will have a much higher resistance to flow, making the chamber losses negligible.

A computational fluid dynamics model was applied to the pumping chamber to solve the velocity and pressure distribution within the pumping chamber. The model solve the laminar version of the Navier-Stokes equations for a 2-D axi-symmetric geometry. To simulate the flow induced by the motion of the pumping piston, a 120 mm/s velocity was applied to the piston surface as a boundary condition, which corresponds to the expected maximum velocity 1600 ppm Terfenol-D rod strain at 500 Hz, assuming a sinusoidal piston motion [35]. A zero pressure condition was applied at the end of the outlet passage and a no-slip condition was applied to the remaining boundaries. The resulting maximum pressure drop due to the motion of

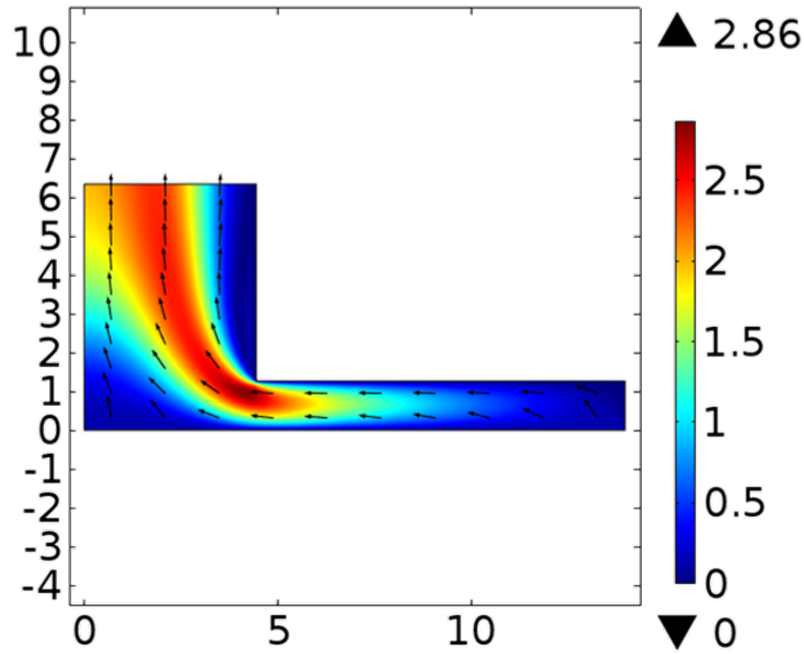


Figure 7.14: Velocity field calculated within the pumping chamber from an axi-symmetric model (m/s).

the fluid within the pumping chamber was calculated as 30 kPa (4 psi), which is small compared to the expected pressure losses in the valves and the blocked pressure capacity of the system.

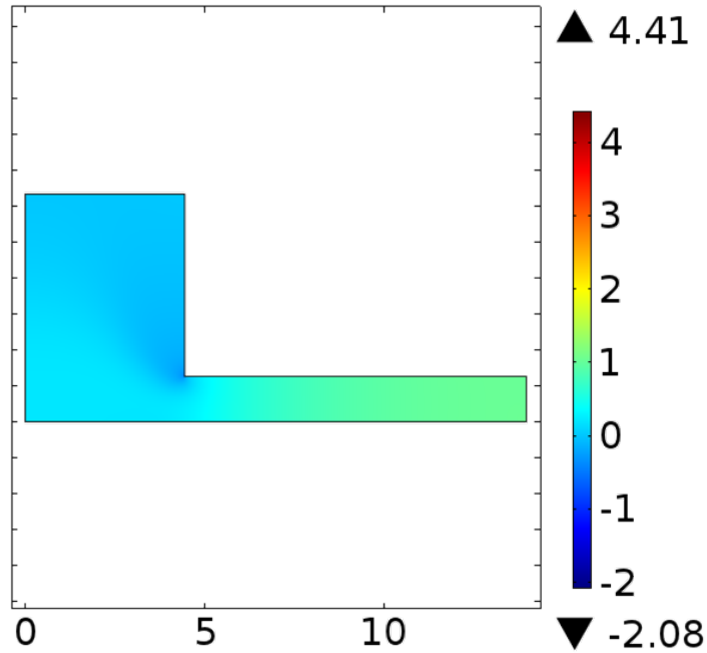


Figure 7.15: Pressure distribution within the pumping chamber (psi).

#### 7.4.5 Reed Valve Modeling

The stress withing the reed valve design was calculated for both opening (Figure 7.16) and closed (Figure 7.17) conditions. The closed-valve condition for a blocked-pressure was found have significantly higher stress than the valve opening case. A valve thickness of 0.51 mm (0.020") was used to keep the stress within the valve below the fatigue limit (Appendix A).

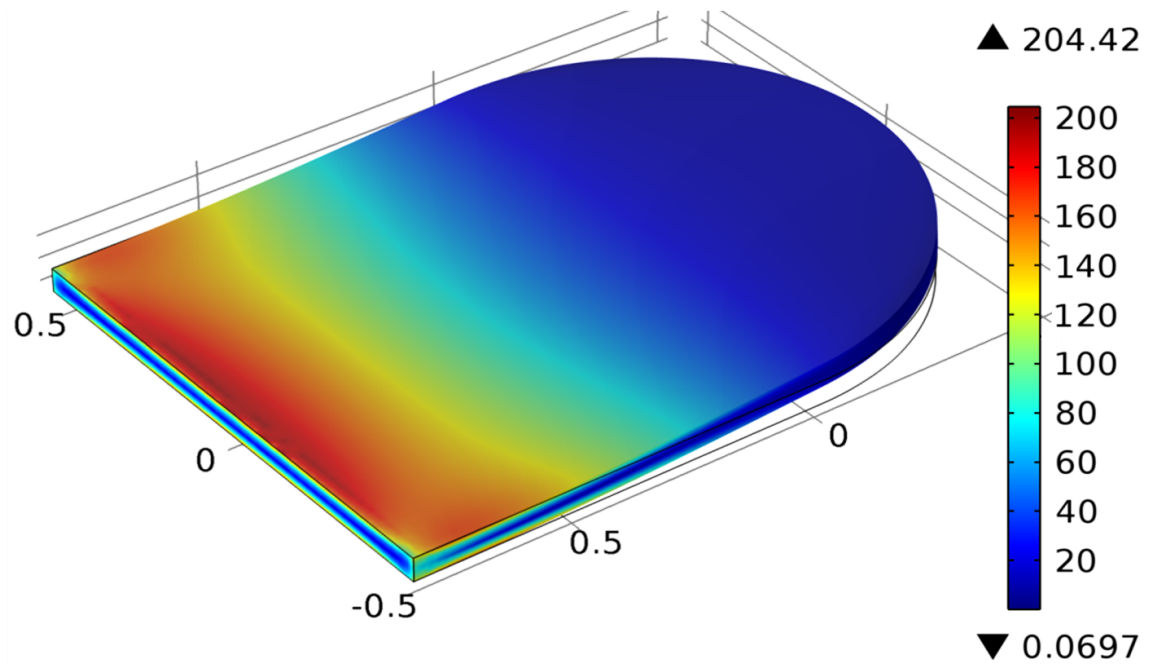


Figure 7.16: Bending stress (MPa) calculated for the reed valve in the while opening.

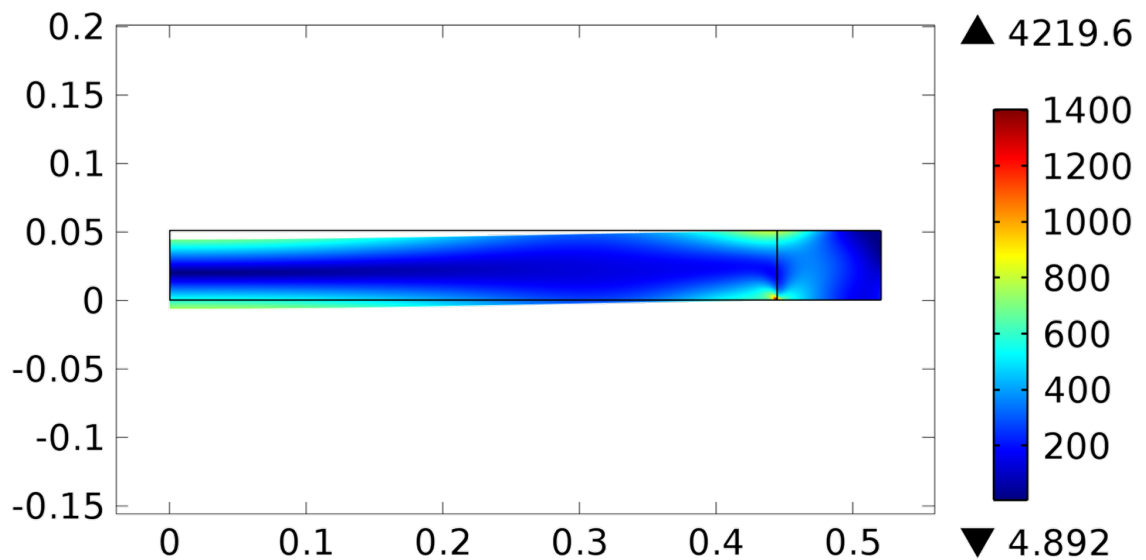


Figure 7.17: Axi-symmetric calculation of the stress (MPa) in the portion of the valve covering the inlet hole for a blocked pressure of 22 MPa (3100 psi).

## 7.5 System-Level Modeling

With a full set of design parameters for the compact aircraft electro-hydraulic actuator design established, the lumped-parameter modeling framework developed in Chapter 6 can be applied to predict the performance of the design. A no-valve model is applied to determine and optimize the bandwidth of the fluid components of the system. Then, the full-system model, including the valves is applied to determine the output velocity response over a range of input frequencies. Since the frequency bandwidth of the new design was predicted to be significantly higher than previous magnetostrictive EHAs, a nonlinear model for Terfenol-D was also applied to the system to determine the effect of transducer nonlinearities on the output performance.

### 7.5.1 No-Reed Dynamic Model

The frequency bandwidth of the previous, reduced-volume-manifold EHA design was shown to be limited by the response of the fluid-system components. To isolate the effect of the fluid-system components (i.e. the pumping chamber, hydraulic cylinder, and connecting passages), a lumped-parameter modeling approach was applied to simulate the response of the system without reed valves installed, using the approach developed in Section 6.6.1.

A schematic representation of the modeled components is shown in Figure 7.18. While the layout is similar to the reduced-volume-manifold EHA, a key difference in the design is the location of the accumulator. In the previous design the accumulator was connected to the low-pressure side of the hydraulic cylinder, but in the compact aircraft EHA the accumulator feeds directly into the pump inlet passage.

A sinusoidal input signal to the actuator was simulated and the amplitude of the pressure response at the high-pressure and low-pressure sides of the hydraulic



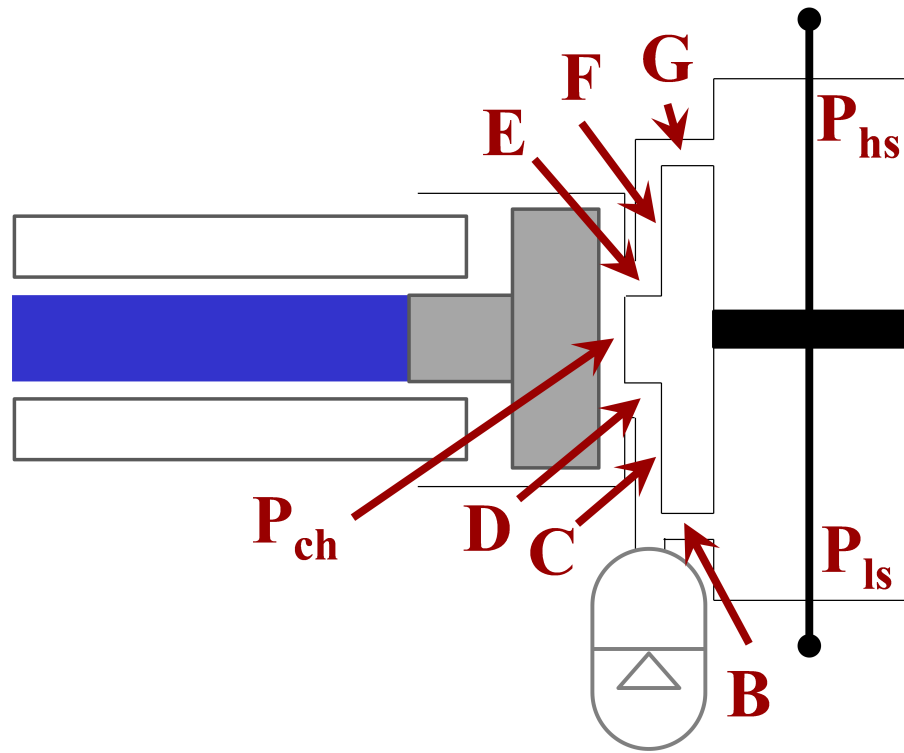


Figure 7.18: Schematic representation of the no-reed dynamic model used to determine the response of the fluid system components of the high-power EHA actuator design.

cylinder was calculated over a range of input frequencies. The response showed two peaks in the magnitude of the pressure response, similar to the response observed for the reduced-volume-manifold design (Figure 7.19). A section of the flow results

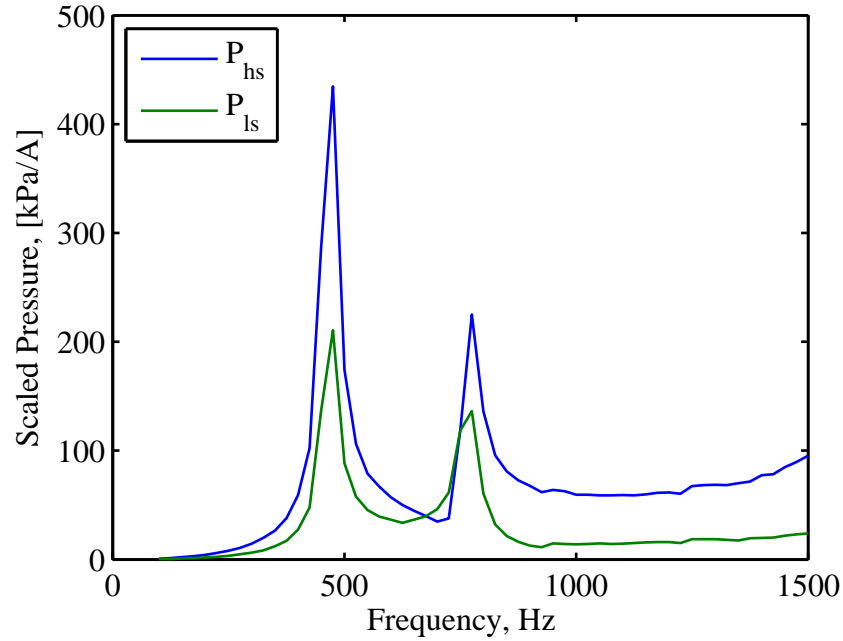


Figure 7.19: Modeled pressure amplitude response for a sinusoidal input current for a passage diameter of 0.89 mm (0.35 in.). A constant sinusoidal current was applied at each frequency and the pressure results were scaled accordingly.

for at the peak frequencies plotted in the time domain is shown in Figure 7.20; the results show repeating, synchronized pattern of flows equivalent to mode shapes in a vibrating system (illustrated by the arrows in Figure 7.20). The flow pattern changes at the second peak frequency with the flow from the low-pressure side of the hydraulic cylinder to the accumulator reversing with respect to the flow in the high-pressure side of the system.

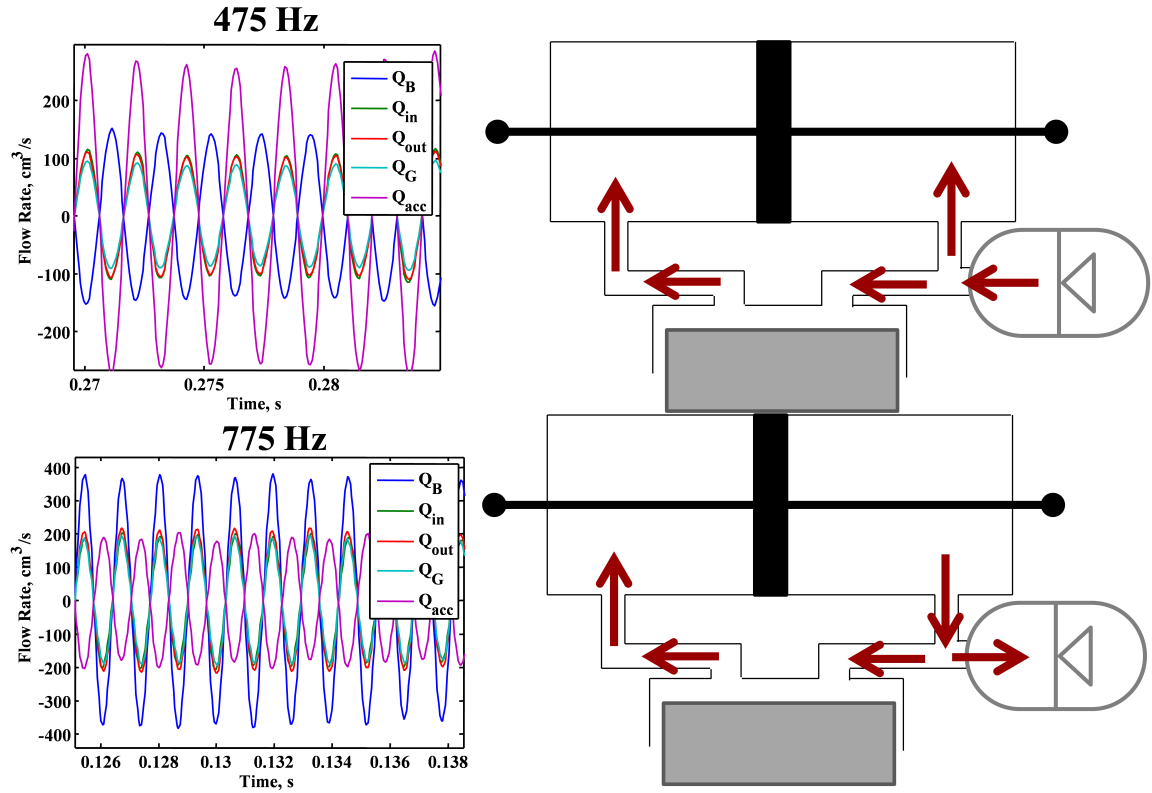


Figure 7.20: Time traces of the pressure amplitudes for the no-reed model at the frequency peaks; the arrows indicate the direction of the flows at the time of peak outlet flow from the pumping chamber  $Q_{out}$ .

Potential adjustments to the EHA design to improve the frequency response of the fluid components are limited. The length of the passages is determined mostly by the stroke of the output hydraulic cylinder; the passages should be made as short as possible to reduce flow losses, but the distance between the hydraulic cylinder ports sets a minimum length. The volume of the pumping chamber and output cylinder were determined by their respective areas, which were calculated using blocked force considerations (Section 7.3). The main parameter of the fluid system components that can be adjusted is the diameter of the passages connecting the pumping chamber to the output hydraulic cylinder.

There is a design trade-off for increasing the fluid passage area. An increased area reduces the flow inertia for the passage ( $L \propto \frac{\rho L}{A}$ ), but increases the compliance ( $C \propto \frac{LA}{\beta}$ ), from Equation (6.8). Several passage diameters were analyzed, and a passage diameter of 0.89 mm (0.35 in.) was selected (Figure 7.19). This is an approximately 5.5x increase from the passage diameter used for the reduced-volume-manifold system, which has fluid passage diameters as small as 0.16 cm (Appendix C). A limit for increasing the frequency at which the first frequency peak occurred was not reached, but the selected diameter was determined to be a reasonable limit for both designing a reed valve to seal the passage size and fitting the flow passages and valves within the pumping chamber area. A single diameter was chosen for all of the machined fluid passages within the system to avoid minor losses from flow area changes within the system.

### 7.5.2 Full System Model

While the no-reed model is useful for evaluating the effect of the fluid passage dimensions on the system bandwidth, including the rectification valves is necessary to predict the velocity performance of the EHA system. Two different lumped-parameter

full-system models were applied to calculate the unloaded velocity response over a range of input frequencies. The first model utilized the linear piezo-magnetic equations to calculate the magnetostriction of the Terfenol-D drive rod with applied current, as developed in Chapter 6. A refined model using a Jiles-Atherton magnetostriction model to account for nonlinearities in the magnetostrictive response was also applied. Using two different magnetostrictive models demonstrates a strength the overall system modeling approach in that the same valve and fluid system model could be applied in both cases.

### 7.5.3 Linear Terfenol-D Model

The magnetostrictive electro-hydraulic pump model developed in Chapter 6 was applied to the compact aircraft actuator design by changing the model parameter to reflect the dimensions of the new design. Additionally, the fluid passage equations were updated to reflect the change of the accumulator location in the system layout (Figure 7.18). The system equations were solved in the time domain, and a typical calculation for the calculated displacement of the hydraulic cylinder is shown in Figure 7.21. Although the net motion of hydraulic cylinder is approximately linear over time, the model predicts small back-and-forth motions corresponding with the motions of the pumping piston. These small motions superimposed on the overall response are typically observed in experimental results for smart material EHA systems and correspond to small amounts of back-flow through the valves or compression of the hydraulic fluid within the hydraulic cylinder.

The velocity response for a constant, bias sinusoidal current of  $7.1 A_{\text{rms}}$  was calculated over a range of input frequencies up to 1000 Hz (Figure 7.22). The results show a peak in the unloaded cylinder velocity of 7.2 cm/s (2.8 in/s) at 450 Hz, which corresponds to the first peak predicted by the no-valve model. The target unloaded

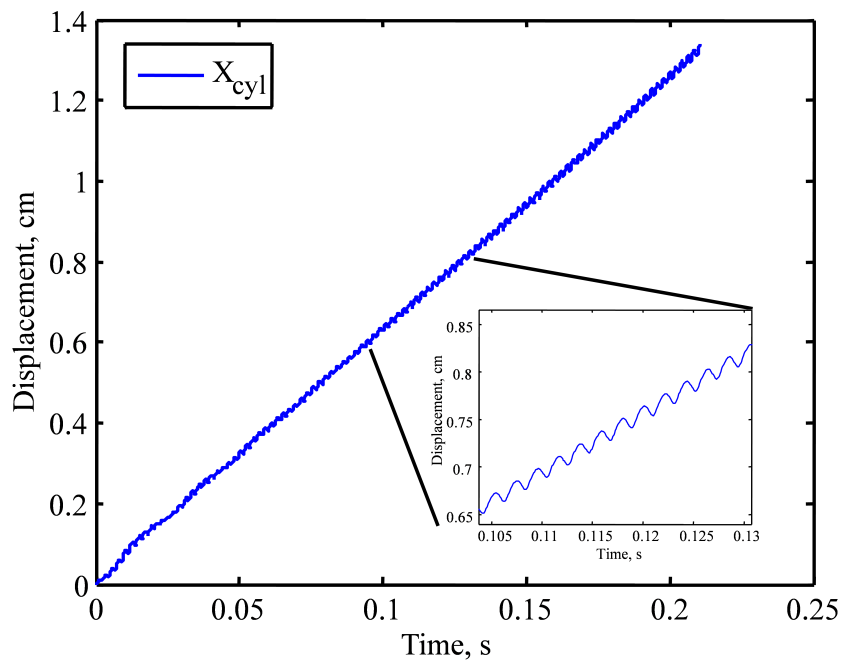


Figure 7.21: Typical unloaded displacement results for the full system model.

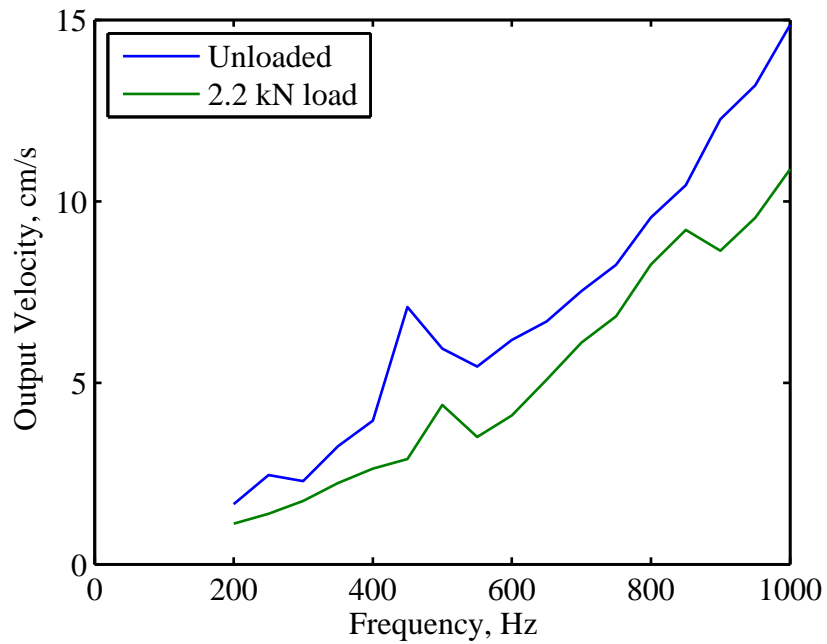


Figure 7.22: Predicted output velocity for a range of input frequencies with a constant current applied at each frequency.

velocity is reached at a frequency of approximately 400 Hz. However, the velocity is predicted to continue to increase almost linearly throughout the modeled frequency range. This increase would allow for the performance targets to be achieved utilizing the higher frequency performance with a lower drive level.

The response does not correspond to the response of the previous, reduced-volume manifold system, which had a drop-off in performance after the first frequency peak. The difference is likely due to the change in the configuration of the hydraulic circuit. Locating the accumulator closer to the pump inlet changes how the no-valve fluid system peaks relate to the performance of the system with the valves installed.

### 7.5.4 Nonlinear Terfenol-D Model

To form a better prediction of the system response at high frequencies, the nonlinear Terfenol-D model presented in Section 6.5 was applied to include the effect of eddy currents, saturation, and hysteresis on the system response. Maxwell's equations were used to calculate the field in the Terfenol-D rod resulting from the sinusoidal current input to the coil (Figure 7.23). As the input frequency is increased, eddy currents are shown to reduce the field within the rod, which reduces the potential magnetostriction. Figure 7.24 shows the strain vs. applied field relationship over

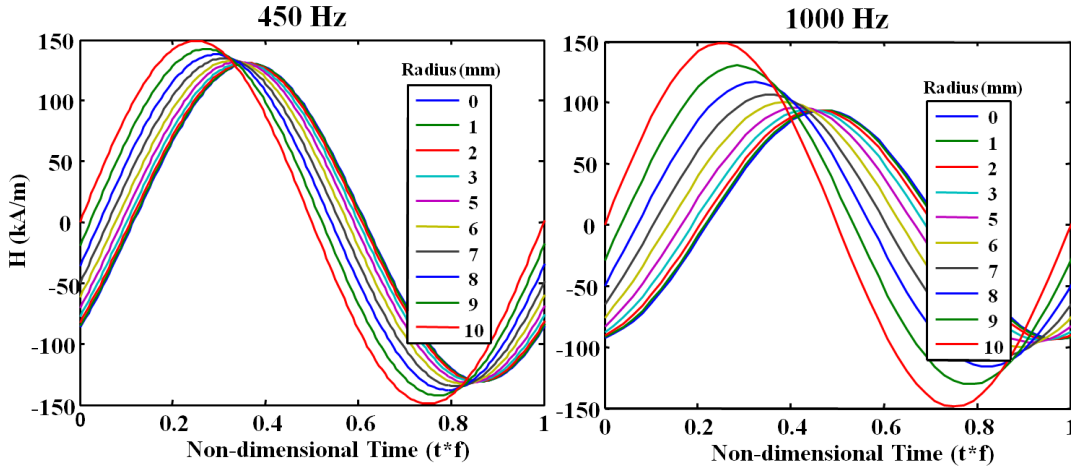


Figure 7.23: Eddy currents reduce the field in the Terfenol-D rod at high currents.

several pumping cycles. The model predicts the expected saturation behavior of the Terfenol-D rod since the applied field to the system is relatively high in order to utilize the full strain available from the material.

The time domain predictions for the displacement of the output cylinder have a similar behavior for both models, with the same generally linear pattern (Figure 7.25). The system performance over a range of input frequencies was calculated using the



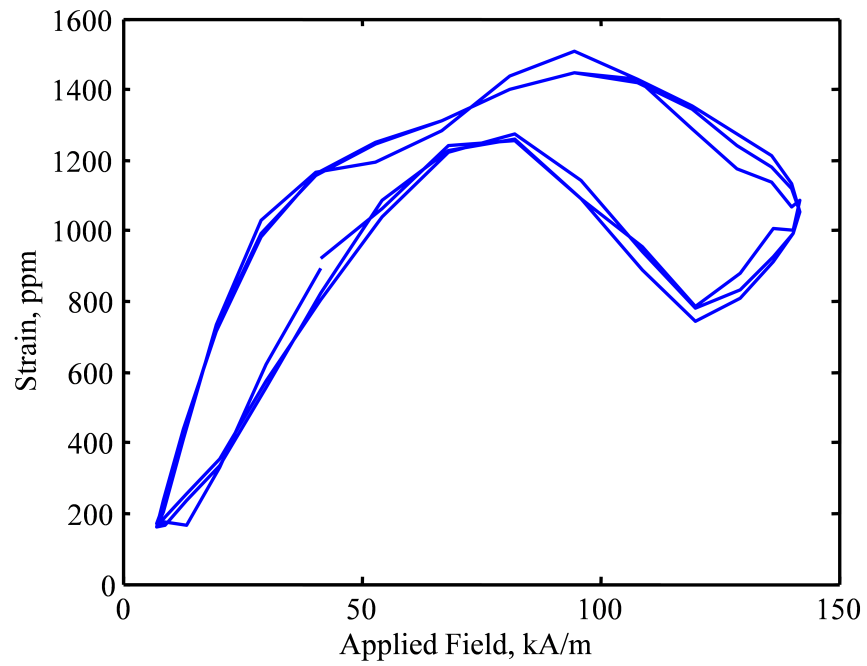


Figure 7.24: Nonlinear strain vs. field model results at 450 Hz.

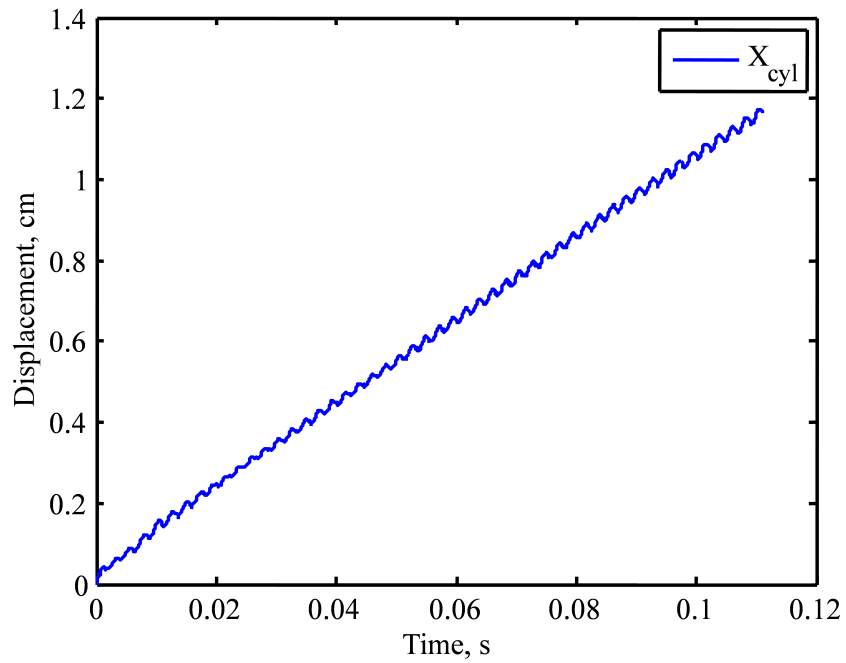


Figure 7.25: Typical unloaded displacement results for the system model including nonlinear Terfenol-D effects.

nonlinear Jiles-Atherton magnetostrictive model (Figure 7.26). The results show a generally linear increase in the output velocity of the EHA up to a frequency of 800 Hz, above which the performance decreases. This result is expected because the effective field within the Terfenol-D rod would decrease as the input frequency was increased. At some point, the system would have difficulty generating the pressure required to open the reed valves and overcome the output cylinder friction to produce motion.

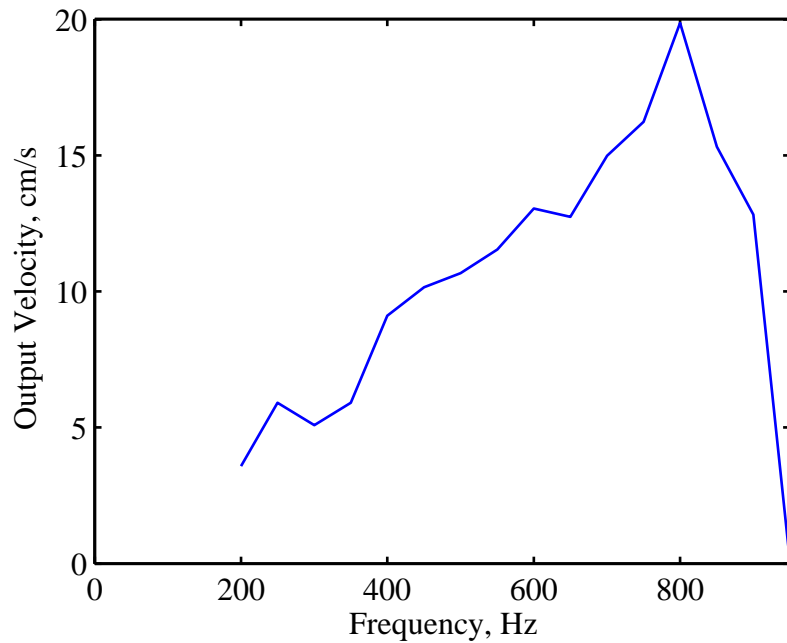


Figure 7.26: Predicted velocity response for a constant current amplitude frequency sweep using a nonlinear magnetostrictive model.

## 7.6 Summary

This chapter presents the detailed design and predictive modeling required to scale-up a smart material electro-hydraulic actuator for aircraft actuation applications.

Performance goals for the system are identified and translated into specific design requirements. Quasi-static calculations based on the blocked-force and free-strain of Terfenol-D are used to form a preliminary design outlining the size of the magnetostrictive drive rod, pump piston diameter, and output hydraulic cylinder area and stroke. Based on this initial design, a detailed design for the system is created including 3-D CAD models of the various components.

The design is evaluated using the lumped-parameter system model developed in Chapter 6. Modeling of the frequency response of the fluid-components of the system without reed valves installed is used to size the diameter of the flow passages connecting the pumping chamber with the output hydraulic cylinder. Modeling of the performance of the system including the valves predicts a large increase in the operating bandwidth over previous designs. The increase in operating bandwidth is due to the change in the configuration of the hydraulic passages. By changing the location of the accumulator, the output velocity now continues to increase at frequencies above the first fluid system resonance (the pressure peak calculated for the system without the reed valves installed).

In the previous reduced-volume-manifold system, this peak output at an input frequency of approximately 225 Hz, but in the compact aircraft actuator design, the velocity was predicted to continue to increase with input frequency up to and above 1000 Hz. Using a Jiles-Atherton model to consider the nonlinear Terfenol-D response at high-frequencies indicated that the system response could be expected to peak at a lower value of 800 Hz; however, this value is still significantly higher than the peak performance frequency of previous smart material EHA systems, which had been previously limited to a few hundred hertz (Table 2.2).

# Chapter 8

## Compact Aircraft EHA Testing

### 8.1 Introduction

This chapter presents the assembly and testing of the compact aircraft electro-hydraulic actuator (EHA). This system was designed to scale-up the performance of a magnetostrictive EHA in order to achieve a power output level that is relevant for aerospace applications. The system was designed to achieve a target output power of 280 W which is a 650% increase in output power compared to the previous actuator, the reduced-volume-manifold EHA (Chapter 4).

The design of the system, including the model calculations required to size the Terfenol-D driver and other components are presented in Chapter 7. Detailed design drawings used to fabricate the system are reproduced in Appendix D. The system utilizes a commercial aircraft hydraulic cylinder (Moog, Inc.) connected to a magnetostrictive hydraulic pump via a custom manifold. Figure 8.1 shows the assembled EHA.

### 8.2 Coil Fabrication

The coil to drive the Terfenol-D rod for the system was fabricated with 321 turns of 10 AWG enamel-coated magnet wire. The coil used for design modeling had been

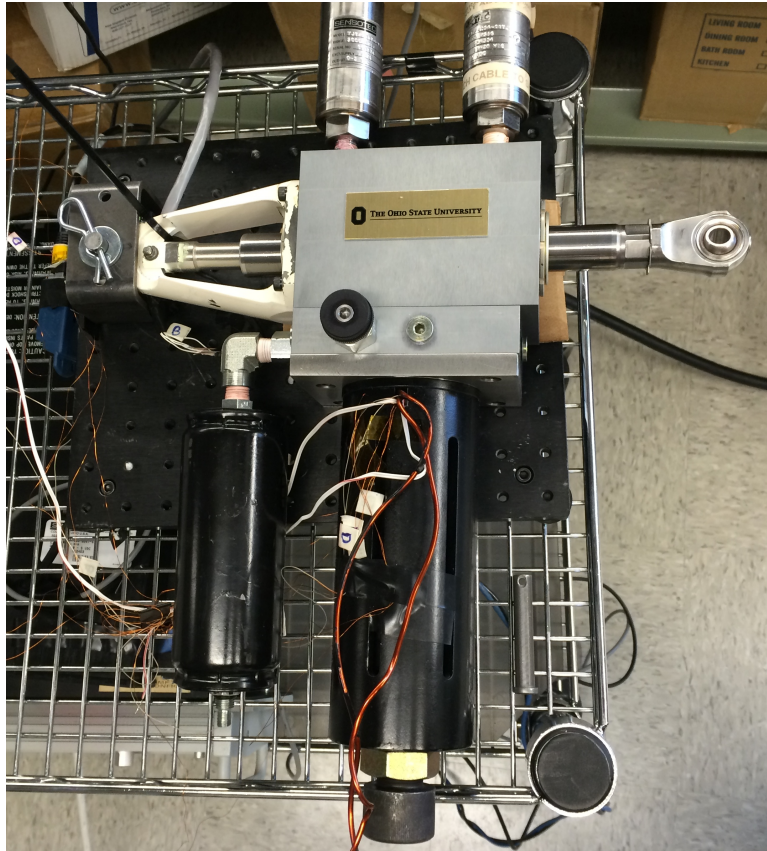


Figure 8.1: Assembled compact aircraft electro-hydraulic actuator.

specified using 12 AWG wire and a higher number of turns 568. Additionally, the reduced-volume-manifold EHA used a coil with 860 turns. The lower number of turns was used to reduce the impedance of the coil to better match the capabilities of the available drive amplifiers (Techron LVC 5050). The difference in number of turns needs to be taken into account when comparing experimental and modeling results since the field applied to the magnetostrictive material is proportional to both current and number of turns.

The coil is coated with Duralco 4525 epoxy resin, which holds the wires together and helps to dissipate heat from the coil. Additionally, the Terfenol-D rod used for testing contains 5-laminations which serve to reduce the effect of eddy currents (Figure 8.2).

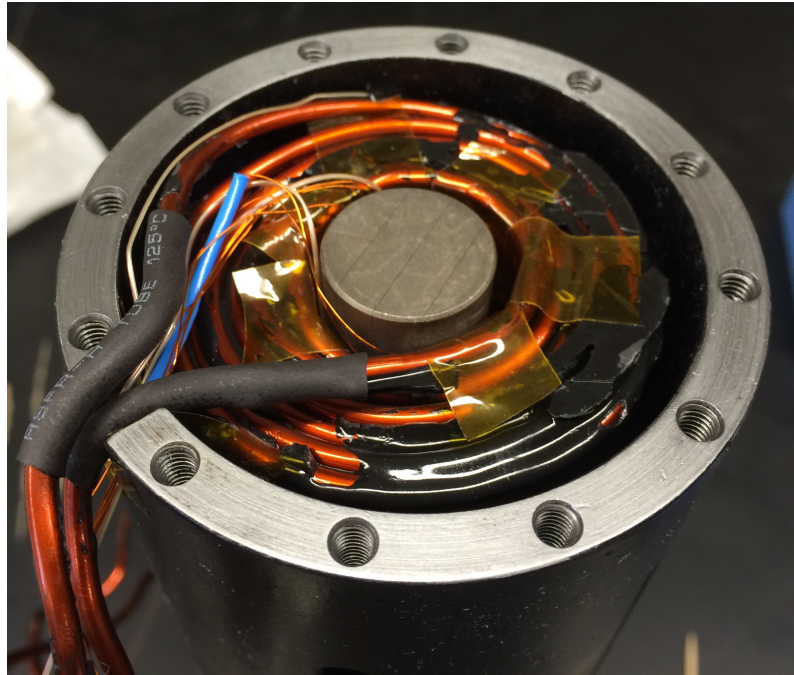


Figure 8.2: View of the partially assembled magnetostrictive pump showing the coil and laminated Terfenol-D rod.

### 8.3 Experimental Setup

The experimental test setup for unloaded velocity and blocked-pressure testing is shown in Figure 8.3. A Labview cDAQ-1798 USB-connected data acquisition system

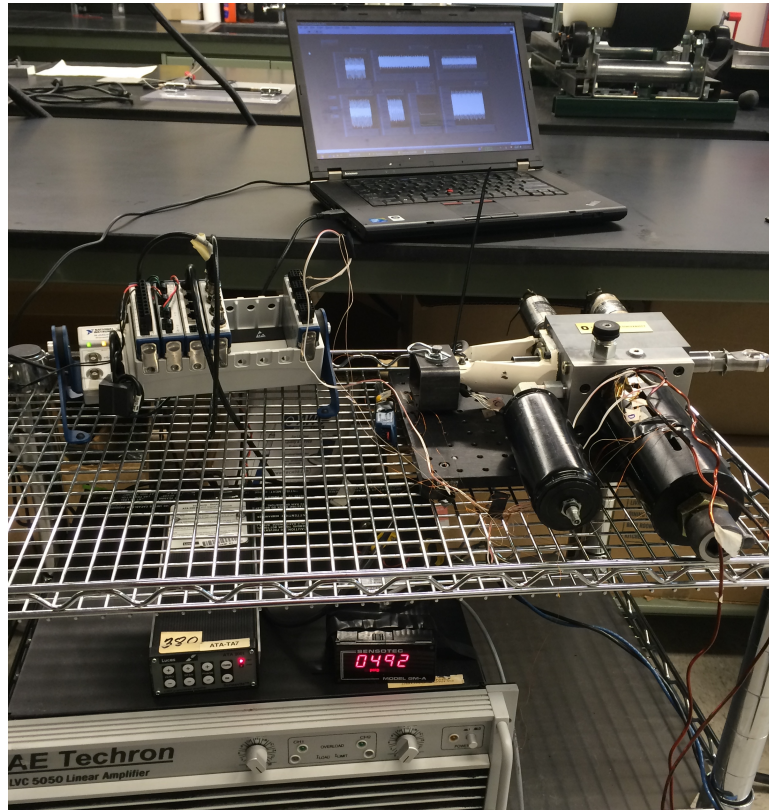


Figure 8.3: Experimental test setup for unloaded and blocked force testing of the high-power EHA system.

was used to generate the biased sinusoidal input to the system and to record test data from the various sensors installed in the system. The position of the output hydraulic cylinder was measured from an integral LVDT (G.W. Lisk Co., Inc. Model CA62723); an LVDT signal conditioner was used to provide the excitation current

to the LVDT and demodulate the output signal into a  $\pm 10$  V output signal proportional to the cylinder position. Two Sensotec TJE-5000, 34 MPa capacity pressure transducers were used to measure the pressure at the high-pressure and low-pressure sides of the output hydraulic cylinder. A strain gage was provided to measure the magnetostriction of the Terfenol-D rod, and several thermocouples were installed to record the temperature of the rod and coil. A bias pressure of 3.4 MPa (500 psi) was used for all tests on the system, which results in a bias stress of 6.7 MPa (970 psi) at the Terfenol-D rod (due to differences in the pump piston and magnetostrictive rod diameters).

## 8.4 Performance

The performance of the system was evaluated in terms of the unloaded velocity (flow rate) and blocked (stall) pressure output. A constant  $8.8 A_{\text{rms}}$  sinusoidal current was applied at each point over a range of input frequencies. A DC bias current was applied with the input sinusoid to provide a biased magnetic field to the Terfenol-D rod to prevent frequency doubling and to increase the total strain generated by the material. The measured output velocity of the actuator increased nearly linearly over the frequency range, up to a peak output value of 8.2 cm/s (3.2 in/s) at 1200 Hz (Figure 8.4). This corresponds to a flow rate of 100 cm<sup>3</sup>/s (6.4 cu in/s). The compact aircraft EHA achieved the target velocity of 5.1 cm/s at a frequency of 900 Hz.

The input power applied to the actuator was significantly lower than the value used for modeling of the system because a coil with a lower number of turns was used for experimental testing. The input voltage and current applied to the system is shown in Figure 8.5. The design model assumed an input current of  $7.1 A_{\text{rms}}$  with a 568 turn coil; this means that a  $12.6 A_{\text{rms}}$  input current would need to be applied to create the same magnetic field using the 321 turn coil in the system. Additionally,



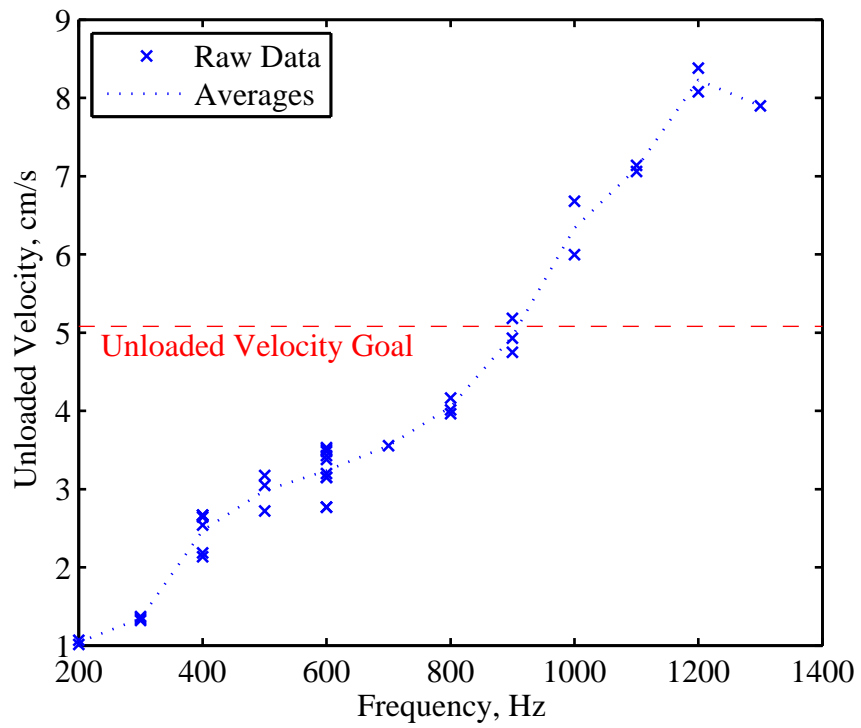


Figure 8.4: Unloaded velocity vs. frequency test results for the high power EHA design, with a  $8.8 A_{\text{rms}}$  sinusoidal current applied over the frequency range.

the  $8.8 \text{ A}_{\text{rms}}$  input current applied to the system would be equivalent to a  $3.3 \text{ A}_{\text{rms}}$  input applied to the reduced-volume-manifold system (Chapter 4). The expected peak in performance at approximately 425 Hz predicted by modeling of the system does appear to be present, but is significantly less pronounced in the experimental results compared to the model predictions. This may indicate that there is more damping in the system than predicted in the model, sources of this damping could include a higher than predicted losses in the reed valves or higher cylinder friction values than predicted.

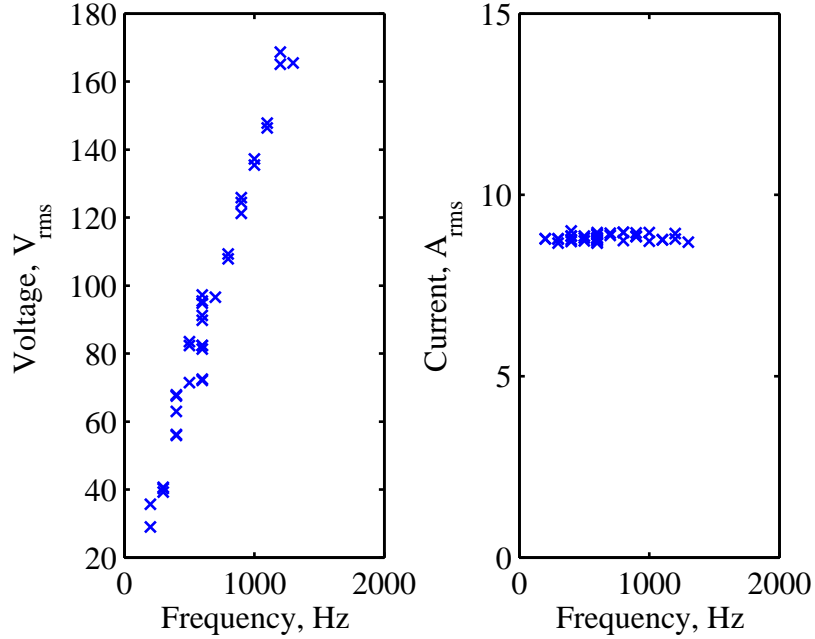


Figure 8.5: Input current and voltage for the unloaded velocity tests conducted at a  $8.8 \text{ A}_{\text{rms}}$  input current over the frequency range.

The peak performance recorded at 1200 Hz was higher than the peak of 800 Hz predicted by modeling of the system including a nonlinear, Jiles-Atherton magnetostrictive model (Figure 7.26). One difference between the model and experiment is

that a laminated Terfenol-D rod was used in the experimental system, while a solid rod was considered for the modeling results. This would explain the difference in test results as a laminated rod has lower eddy current losses at high frequencies, which allows for a higher effective field to be realized in the material.

The blocked pressure was evaluated within the system by measuring the pressure at the high-pressure side of the output cylinder with the cylinder extended to the end of its range, holding it fixed. A blocked pressure differential of 6.3 MPa (920 psi) was measured at 1200 Hz using the 8.8  $A_{\text{rms}}$  input current used for unloaded velocity testing. This corresponds to a blocked force value of 8 kN (1800 lb) based on the area of the hydraulic cylinder. The resulting potential output power for the actuator based on the measured unloaded velocity and blocked force can be estimated as 164 W (7.1) for an input current of 8.8  $A_{\text{rms}}$ .

The average (real) input power for an 8.8  $A_{\text{rms}}$  input current at 1200 Hz is 1000 W. This gives an estimated efficiency of 16%. Since the power output was measured according to the blocked pressure and unloaded flow rate; the efficiency when moving a load may be lower (due to output hydraulic cylinder friction, for example). This efficiency calculation is similar to the up to 12% efficiency value measured for the reduced volume manifold system (Figure 4.12). The input power required for the DC bias field was a small portion (4%) of the overall input power (Figure 8.6); the DC resistance of the drive coil was approximately 0.45  $\Omega$ , which resulted in a DC power of 37 W required to supply the DC bias current of 9.1 A used for testing at the 8.8  $A_{\text{rms}}$  drive level.

Amplifier limitations restricted the input current level that could be applied at 1200 Hz, but additional testing to measure the blocked force with a higher level of input current was conducted at a 200 Hz input frequency. Applying an input current of 23  $A_{\text{rms}}$  resulted in a blocked differential pressure of 12.1 MPa (1750 psi). Based on

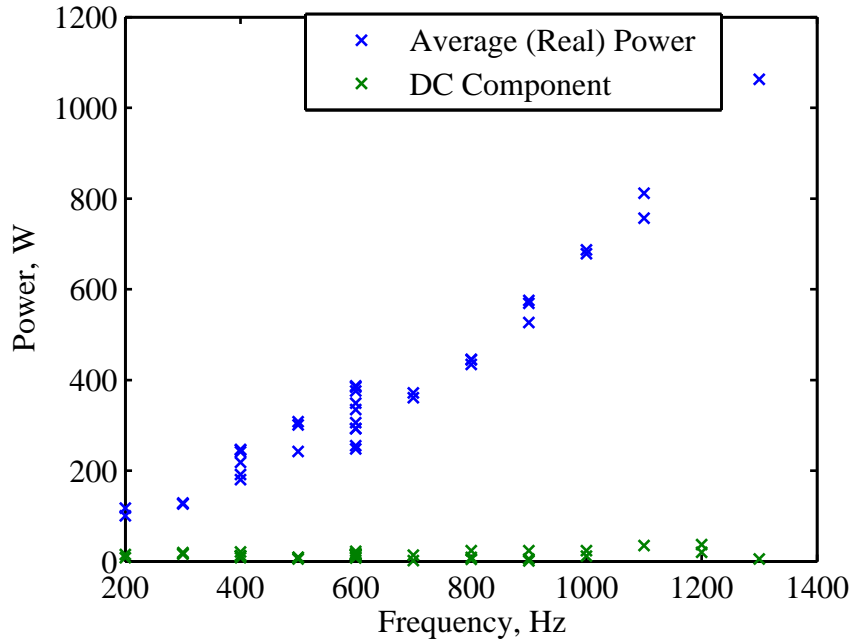


Figure 8.6: Input power applied over the frequency range tested for the 8.8  $A_{\text{rms}}$  input current input tests with the 0.51 mm (0.02") reed valves installed.

the output cylinder area, the resulting blocked force is 15.3 kN (3,430 lb). This blocked force value with the 8.2 cm/s unloaded velocity gives an output power estimate for the compact aircraft EHA of 310 W. This exceeds the target output power of 280 W by approximately 10%. It would be expected that applying this higher current level at the peak performance frequency of 1200 Hz would increase unloaded flow rate and thus the available output power.

The measured blocked force of 15.3 kN (3,430 lb) is still below the target value for blocked force of 22 kN (5000 lb). There is potential for increasing blocked force by increasing the applied current further. The reduced-volume-manifold system was shown to have a measured increase in output power up to a equivalent applied current of 32  $A_{\text{rms}}$  (Figure 4.12), so there is still remaining potential for increasing the measured output performance by increasing the current. Disassembly of the system after testing

showed that the diaphragm used to seal the pumping chamber had been deformed, likely while adding or removing the bias pressure from the system (Figure 8.7). Plastic

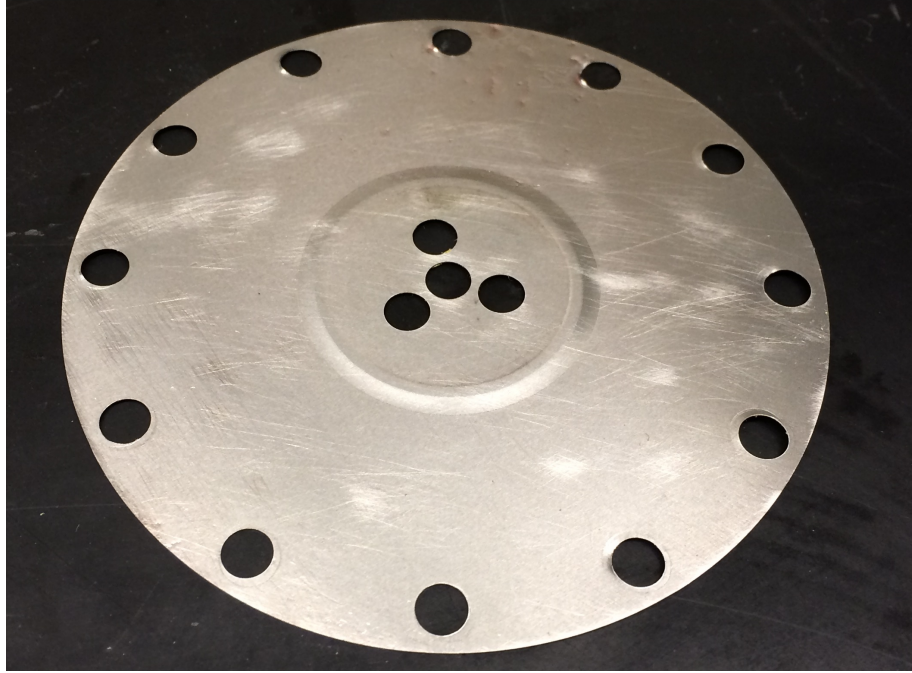


Figure 8.7: The piston seal diaphragm in the compact aircraft EHA was found to be deformed when the actuator was disassembled after testing.

deformation of this seal diaphragm has been shown to reduce the measured output performance of a magnetostrictive EHA system (Figure 4.6). Additional sources of loss, which could also be addressed to increase the blocked pressure performance of the system include improving air removal from the system and increasing the bias pressure to reduce the effect of any air which may be remaining. Exceeding the output power target demonstrates that a magnetostrictive electro-hydraulic actuator is capable of producing power output levels that are relevant for aircraft actuation applications. Since the flow rate target was exceeded by 60%, the system could also be

modified to produce a higher blocked force by either increasing the output cylinder area or decreasing the pumping piston area.

Additional testing was conducted using a thinner reed (Figure 8.8). A 0.25 mm (0.010") reed, which is half the thickness of the reed designed for the system. This reed has a lower resistance to flow than the thicker reed since the decreasing the thickness by one-half decreases the stiffness of the reed by approximately 8x; a decreased stiffness allows for more opening area and less resistance to flow. However, the decreased reed stiffness also reduces the bandwidth over which the reed can successfully rectify flow. This behavior was reflected in the experimental results. At low frequencies (up to 300 Hz), a higher flow rate was observed for the thinner reeds, with approximately doubling of the flow at 200 Hz. However, the flow for the thinner reeds peaked at 300 Hz and leveled off at higher frequencies. The thicker reeds showed an approximately linear increase in flow at frequencies up to 1200 Hz. These test results show that the system bandwidth may be limited by the reed valves. Additional testing could be conducted using thicker reeds than the design value to determine if the frequency bandwidth of the system could be increased further.

## 8.5 Summary

A magnetostrictive EHA, scaled-up from previous designs was assembled and tested. The target power level for the system was 280 W, which was determined to be a relevant output performance for aircraft actuation applications (Chapter 7). Measurement of the unloaded flow rate and blocked pressure produced by the system result in a calculated power output of 310 W, which exceeds the design goal for the output power of the system.

The unloaded velocity of the system was found to increase with the applied frequency, up to a value of 1200 Hz. This bandwidth, where the input frequency increases

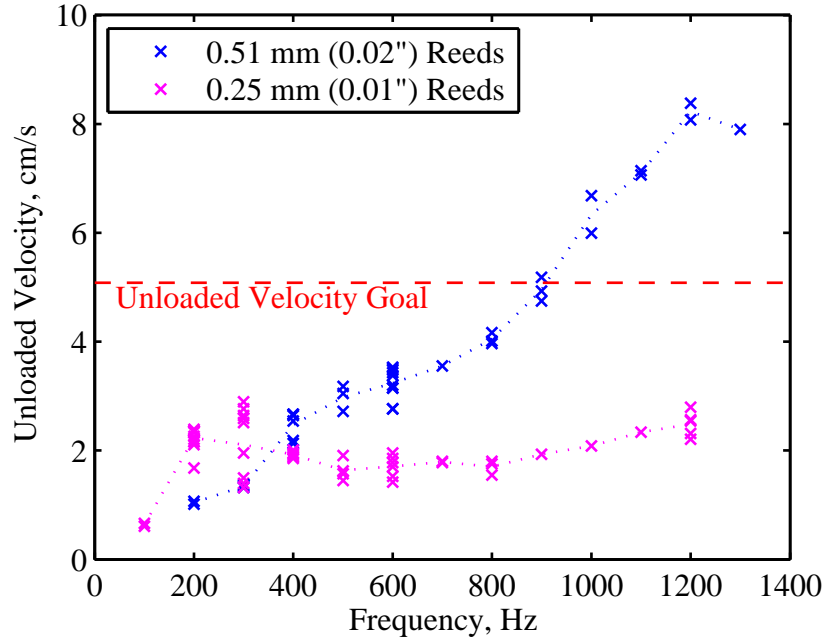


Figure 8.8: Unloaded velocity vs. frequency comparison between two different reed thicknesses. The thinner reed (0.25 mm) developed more flow at low frequencies, but the thicker reed (0.5 mm) had a higher frequency bandwidth.

the output of the system, is a significant improvement over previous smart material EHA systems where the performance leveled off at frequencies above a few hundred hertz, even though the power available to the system from the smart material driver motion continued to increase.

Applying a constant sinusoidal input current ( $8.8 A_{\text{rms}}$ ) over a range of input frequencies resulted in a peak output velocity of 8.2 cm/s (3.2 in/s) at 1200 Hz, corresponding to an unloaded flow rate of 100 cm<sup>3</sup>/s (6.4 cu in/s) since the output hydraulic cylinder had an area of 12.6 cm<sup>2</sup> (1.96 sq. in.). At this input current level, a blocked differential pressure of 6.3 MPa (920 psi) was measured, which corresponds to a power output for the system of 164 W (Equation 7.1). The input power to the system for these test values was 1000 W, so the estimated efficiency of the system was calculated at 16%.

Testing conducted at a higher input current level ( $23 A_{\text{rms}}$ ) resulted in an increase in the blocked differential pressure to 12.1 MPa (1750 psi). Combined with the measured unloaded flow rate value, this resulted in a calculated system power of 310 W. The blocked force capability of the system based on this pressure differential is 15.3 kN (3,430 lb), which is below the target value of 22 kN (5000 lb). Previous testing of a magnetostrictive hydraulic actuator at higher magnetic field levels has shown that the blocked force capability of the system may be higher than the recorded values. Additionally, since the target output power has been achieved and the unloaded flow rate goal was exceeded by 60%, future designs for this power level could utilize a larger output hydraulic cylinder to increase the blocked force.



# Chapter 9

## Contributions and Future Work

### 9.1 Summary of Findings

This work presents the development of a magnetostrictive electro-hydraulic actuator (EHA) with increased output power for aircraft actuation applications. The motivation for the work is to take advantage the high-energy density of smart materials, specifically Terfenol-D, to form a compact, lightweight system which uses hydraulic rectification to convert the small vibrations of the material into large, useful motions of a hydraulic cylinder.

A summary of previous work in the literature on smart material EHAs was presented in Chapter 2. While many authors have demonstrated working actuators, a limitation of past attempts has been the input frequency bandwidth. The bandwidth over which the applied smart materials can operate is relatively high (over 1 kHz). Utilizing as much of this bandwidth as possible is important for improving the system performance, since increasing the number of pumping cycles should result in more flow of hydraulic fluid and a higher power output. However, the peak performance of previous systems was only a few hundred hertz; output velocities were reduced at higher input frequencies.

One limitation on the system performance that has been identified is the reed valves used for fluid rectification. These one-way valves convert the small, high-frequency vibrations of the smart material driver into unidirectional flow of a hydraulic fluid. An array of miniature valves was developed (Chapter 3), which was designed to rectify fluid flow up to very high frequencies (approximately 10 kHz). While the valve array was demonstrated to successfully rectify flow and survive within the EHA pump, the novel valve design was shown not to affect the overall frequency response of the magnetostrictive EHA used for testing.

Further testing was conducted with a magnetostrictive pump designed with a reduced-volume manifold (Chapter 4). This manifold combines the output hydraulic cylinder and associated passages with the pump to form a compact EHA system. The system was shown to have an increase in performance over a previous configuration of the EHA pump with an external hydraulic cylinder connected by hydraulic tubing. Testing over a range of applied currents, loads, and input frequencies was used to establish the performance of the system. The peak output power for the system was measured at 37 W, which is significantly higher than the output power level reported for previous smart material EHA systems utilizing drive materials of a similar size (1 to 5 W, Table 2.2).

Experimental and computational studies were conducted on the single-reed valves used in the reduced-volume-manifold EHA in order to develop a better understanding of their flow performance and dynamic response (Chapter 5). The results were used to develop a simplified model of the reed valve dynamic behavior by applying the orifice flow equations along with a dynamic model of the valve opening area. A lumped-parameter model was developed to model the mechanical and fluid components of the system and was compared with experimental measurements of the overall performance (Chapter 6). A key finding of the experimental and modeling

results with the reduced volume manifold system was that dynamic response of the system (i.e. the input frequencies where peak performance occurred) was determined by the fluid system components. Therefore, the design, modeling, and characterization of smart material EHA systems must include the effects of these components (e.g. the hydraulic cylinder, pumping chamber, and the connecting passages).

A compact aircraft magnetostrictive EHA was designed with a target power output of 280 W (Chapter 7). This power level, which was determined to be relevant for aerospace applications, was significantly higher than the output of previous smart material EHA systems (approximately 1 to 40 W, Table 2.2) and was also higher than the power output of previously reported smart material pumps (180 W for a single pump, Table 2.3). A quasi-static analysis was applied to determine a preliminary design for the major system components. A lumped-parameter modeling approach was applied to refine the design parameters and to predict the performance of the system over a range of frequencies. The model included the application of a nonlinear Jiles-Atherton model for the Terfenol-D drive rod to predict the nonlinear response of the material at high frequencies and drive levels.

The actuator design was fabricated and tested to determine the overall performance of the system (Chapter 8). Test results demonstrated an improved bandwidth over which the output velocity increased with input frequency. The peak output velocity of 8.2 cm/s (3.2 in/s) was measured at 1200 Hz, a dramatic increase over previous state-of-the-art smart material actuator designs which were limited to input frequencies of a few hundred hertz. Based on the output hydraulic cylinder area, the output velocity corresponded with an unloaded flow rate of 100 cm<sup>3</sup>/s (6.4 cu in/s). A blocked differential pressure of 12.1 MPa (1750 psi) was measured for the system. The measured blocked power and unloaded flow rate resulted in an output power capacity of 310 W for the system, which exceeded the design target.

## 9.2 Research Contributions

1. Increased overall smart material EHA power output

The measured output capability of 310 W is a dramatic increase over previous smart material EHA actuator results (approximately 1 to 40 W, Table 2.2) and also higher than the output power reported for smart material pumps (180 W for a single pump, Table 2.3). This increase in the system performance expands the potential applications for smart material EHAs.

2. Developed nonlinear system model for magnetostrictive EHA

A general modeling framework was developed to predict the dynamic response of a smart material EHA. The framework uses a lumped-parameter approach to model the major components of the system: smart material driver, rectification valves, and fluid-system components. The model accounts for nonlinearities in the response of both the magnetostrictive material and the hydraulic fluid. Additionally, the frequency response and flow performance of the valves was included using a model of the valves which was also validated via experimental study.

3. Designed and tested a magnetostrictive EHA with improved frequency bandwidth

Using the model, a general design process for smart material EHAs was established and applied to create a high-power actuator suitable for aerospace applications. Design goals for the system were identified, and preliminary pump parameters were established based on a quasi-static analysis. Then the design was subsequently fine-tuned using the full-system modeling framework. The modeled performance was validated by experimental testing. While the design

process was established for scaling up the output of a magnetostrictive EHA, the approach can be used to improve performance at any power level, allowing the resulting system design to be smaller and lighter.

The Compact Aircraft Actuator magnetostrictive EHA design expands the range over which the performance of the pump increases proportional to input frequency over previous state-of-the-art designs, from 200-600 Hz to 1200 Hz. Operating the smart material driver for the EHA system at a higher input frequency increases the power output of the system. This higher energy density makes the smart material EHA concept more attractive as an alternative to conventional actuators.

4. Developed robust, miniature, high-frequency valves

A novel design for miniature reed valves was designed and tested, with each layer of the valve assembly fabricated separately using micro-machined stainless steel. The valves were demonstrated to reliably rectify fluid flow at frequencies above 1 kHz within the high-pressure EHA pump. This type of valves may be used in future smart material EHA designs to further improve the frequency response of the system (to 10 kHz and above), or they may have other applications, such as in high-frequency compressors or in microfluidic devices.

5. Used innovative experimental methods for dynamic characterization of reed valves

The difficulty in designing reed valves capable of rectifying fluid flow at frequencies above a few hundred hertz has limited the design of smart material EHAs. Novel experiments using a scanning laser vibrometer allowed for the *in situ* characterization reed valves by using a test holder that simulated the valve seat while including a transparent viewing window. This study demonstrated the

contributions of the added mass of the hydraulic fluid and the stiffening effect of the valve seat on the bandwidth of the valve. Based on the knowledge gained from the experimental study, reed valves for the compact aircraft EHA were then successfully used to rectify fluid flow in a system with peak performance above 1 kHz.

#### 6. Developed 3-D model of reed valve fluid-structure interaction

The flow resistance through the valves was modeled using a 3-D finite-element fluid-structure interaction model. The model results were validated by steady-state flow experiments, which included the measurement of the deflection of the reed valves over a range of input pressure differentials. Additionally, a simplified calculation for the reed valve resistance based on applying the orifice flow equations using the reed opening area was shown to accurately characterize the pressure loss across the reed valves in an analytic form suitable for the system-level modeling.

#### 7. Implemented model using AMESim

While the majority of the modeling results were computed using the MATLAB programming language, the modeling framework used to predict the response of a smart material EHA was also implemented in the commercial 1-D simulation software AMESim. One of the main drawbacks for applying smart materials in commercial products is the difficulty in modeling the system performance. The development of system-level models which can integrate with commercial analysis software will help enable more widespread adoption of these materials.

## 9.3 Future Work

1. Characterize system at higher input power levels

To fully characterize the performance of the compact aircraft EHA system, future testing could be conducted at higher levels of input current. Testing of the system presented in this dissertation was limited by the power supply amplifier used, so a higher capacity power amplifier would need to be applied (Chapter 8). Additionally, the magnetic circuit may need to be optimized by adjusting the number of turns in the coil according to power supply requirements. Previous testing applying higher magnetic field levels to the reduced volume manifold EHA indicate that the output performance capability of the system could be improved by increasing the input power (Chapter 4).

2. Consider additional reed valves thicknesses

Testing of the compact aircraft EHA with reed valves of one-half the design value demonstrated the trade-offs associated with adjusting the stiffness of the reeds. At low frequencies, the more compliant reed opened further, allowing for higher flow rates for a given input current level. However, at high frequencies, the system performance was reduced due to the decreased rectification bandwidth associated with the thinner valves. Additional modeling and testing is needed to identify the optimum reed valve stiffness for the system. Fatigue considerations may limit the potential for using thinner designs, especially for testing with increased input currents.

3. Test miniature reeds in the compact aircraft EHA

The expanded frequency bandwidth of the compact aircraft EHA makes the system more suitable for evaluating the performance of miniature reed valve

array designs than previous systems. Since the reed valve design has already been demonstrated to have an effect on the dynamic response of the system, applying a very high frequency bandwidth miniature valve design to the system has the potential to increase the useful input frequency. The modular design of the compact aircraft EHA would allow for testing of a larger array of miniature valves than were previously used, since the components that house the current rectification valves can be replaced to allow for a significantly larger valve array than previously tested. A larger array would allow for the higher frequency miniature valves to be utilized without adding an additional flow restriction to the system.

4. Apply model to scale system for lower output power applications

The same performance gain from expanding the usable input frequency bandwidth, which was demonstrated for the high-power, compact aircraft EHA system, would make actuators for lower power applications smaller and lighter. The modeling framework developed in this work can be applied to evaluate and improve designs for low power systems for a range of applications.

5. Apply improved magnetostrictive model

The magnetostrictive model used in the system currently does not take into account the effect of using a laminated Terfenol-D rod. Additionally, more advanced magnetostrictive models exist, which could be applied to more accurately characterize the behavior of the magnetostrictive material in order to predict the system response over a larger range of applied loads and drive levels.

6. Consider thermal effects in the design and model

Heating of the coil and the magnetostrictive material during system operation is a subject that requires more attention for the application of these systems



into commercial devices. The effect on the experimental system was limited by running the tests for short duration and allowing the system to cool between tests if necessary. There is a need to identify the duty cycle requirements and cooling availability for applying the system to specific applications, and then conduct testing with the actuator to determine how the actuator responds. The effect of temperature changes on the behavior of the Terfenol-D driver could also be added to the system model.

#### 7. Add bi-directional operation capability

Bidirectional operation is desired for application in aircraft actuation systems. The actuator was designed in a modular fashion, so the “adapter plate” component could be exchanged with a new component that includes a 4-way solenoid valve to enable testing with bidirectional motion of the output hydraulic cylinder (Figure D.1).

The modeling framework developed in this dissertation can be applied to these future research objectives to evaluate their feasibility and explore other research directions. Improvements achieved by following these research steps could be used to either expand the power capacity of the system or to redesign the device to achieve the application power requirements at with a lower size, weight, and cost.

# Appendix A

## Allowable Stress Calculation for Valve Design

The endurance limit for the stainless steel used in the miniature reed valve design was calculated using the method outlined by Hamrock et al. [64]. It was noted that the maximum stress in the reed occurs in torsion of the arms that extend from the reed flap, so the uncorrected endurance limit,  $S'_e$ , was calculated for torsion loading based on the ultimate strength of the material,  $S_u$

$$S'_e = 0.29S_u. \quad (\text{A.1})$$

The endurance limit,  $S_e$ , is then modified using correction factors for surface finish,  $k_f$ ; size,  $k_s$ ; reliability,  $k_r$ ; and temperature,  $k_t$

$$S_e = k_f k_s k_r k_t S'_e \quad (\text{A.2})$$

The allowable stress is then equal to twice the alternating stress, calculated from the modified Goodman criterion using a mean stress equal to the alternating stress [22]

$$\sigma_{\text{allow}} = 2\sigma_a = 2S_e \left(1 + \frac{S_e}{S_u}\right)^{-1}. \quad (\text{A.3})$$

To calculate the allowable stress for the valve design, an ultimate strength of 1280 MPa was assumed for fully hardened 301 stainless steel. The surface finish factor was

set to  $k_f = 0.75$  based on the expected surface roughness from discussion with the supplier. The reliability factor was set to  $k_r = 0.82$  based on 99% reliability. The size and temperature factors were set to 1 because the valves are small, and testing was conducted at room temperature. This resulted in an allowable stress of 390 MPa for the design of the miniature valves. The allowable stress value is conservative since the material actually used for fabrication was certified to have a higher ultimate strength than used for design,  $S_u = 1386$  MPa (fully-hardened 304 stainless steel from Trinity Brand Industries).

# Appendix B

## Calculation of Reed Valve Opening Area Factor

This appendix presents the calculation of the area factor  $\lambda_r$  used to calculate the opening area of the reed valves  $A_v$ , which is proportional to the tip displacement  $x_r$

$$A_v = \lambda_r x_r. \quad (\text{B.1})$$

To calculate the reed opening area, the valve is assumed to deflect according to the first bending mode shape for a clamped-free cantilever beam. Defining  $y$  as the position along the length of the reed valve measured from the base, the vertical displacement of the reed at any point is given as a function of  $y$  as

$$x(y) = \frac{x_r}{2} \left\{ \cosh \left( \lambda_1 \frac{y}{l} \right) - \cos \left( \lambda_1 \frac{y}{l} \right) - \sigma_1 \left[ \sinh \left( \lambda_1 \frac{y}{l} \right) - \sin \left( \lambda_1 \frac{y}{l} \right) \right] \right\} \quad (\text{B.2})$$

where  $l$  is the length of the reed [66]. The dimensionless natural frequency parameters  $\lambda_1$  and  $\sigma_1$  are calculated numerically as  $\lambda_1 = 1.8751$  and  $\sigma_1 = 0.7341$  from the transcendental equations [66]

$$\cos \lambda_i \cosh \lambda_i + 1 = 0, \text{ and} \quad (\text{B.3})$$

$$\sigma_i = \frac{\sinh \lambda_i - \sin \lambda_i}{\cosh \lambda_i + \cos \lambda_i}. \quad (\text{B.4})$$

The reed flow area  $A_v$  can then be calculated by integrating the transverse displacement  $x$  along the reed perimeter. The reed geometry is considered as a rectangle with a semi-circle on the end (Figures 5.3 & D.12); therefore,

$$A_v = A_{\text{side}} + A_{\text{tip}} = 2 \int_0^{l_{\text{side}}} x(y) dy + \int_0^\pi x(l_{\text{side}} + r_{\text{tip}} \sin \theta) r_{\text{tip}} d\theta \quad (\text{B.5})$$

where  $A_{\text{side}}$  is the area along the side of the valve and  $A_{\text{tip}}$  is the area at the rounded valve tip. The radius at the tip of the reed  $r_{\text{tip}}$  is defined as half of the reed width, and the length of the side of the reed is the length remaining after subtracting the tip length from the overall length of the reed

$$l_{\text{side}} = l - r_{\text{tip}}. \quad (\text{B.6})$$

The area factor for the reed valves  $\lambda_r$  is then given by substituting (B.2) into (B.5) and dividing out  $x_r$  according to (B.1)

$$\begin{aligned} \lambda_r = & \int_0^{l_{\text{side}}} \left\{ \cosh \left( \lambda_1 \frac{y}{l} \right) - \cos \left( \lambda_1 \frac{y}{l} \right) - \sigma_1 \left[ \sinh \left( \lambda_1 \frac{y}{l} \right) - \sin \left( \lambda_1 \frac{y}{l} \right) \right] \right\} dy \\ & + \int_0^\pi \left\{ \cosh \left( \frac{\lambda_1}{l} (l_{\text{side}} + r_{\text{tip}} \sin \theta) \right) - \cos \left( \frac{\lambda_1}{l} (l_{\text{side}} + r_{\text{tip}} \sin \theta) \right) \right. \\ & \left. - \sigma_1 \left[ \sinh \left( \frac{\lambda_1}{l} (l_{\text{side}} + r_{\text{tip}} \sin \theta) \right) - \sin \left( \frac{\lambda_1}{l} (l_{\text{side}} + r_{\text{tip}} \sin \theta) \right) \right] \right\} r_{\text{tip}} d\theta \quad (\text{B.7}) \end{aligned}$$

For each specific reed geometry, the area factor is a constant and has no dependence on the value of the reed tip displacement.

# Appendix C

## Actuator Parameters

This appendix summarizes the key parameters used to model the “Reduced Volume Manifold” and “Compact Aircraft” magnetostrictive electro-hydraulic actuators (EHAs).

### C.1 Reduced Volume EHA Parameters

Tables C.1 and C.2 list the parameters used to model the experimental magnetostrictive hydraulic actuator.

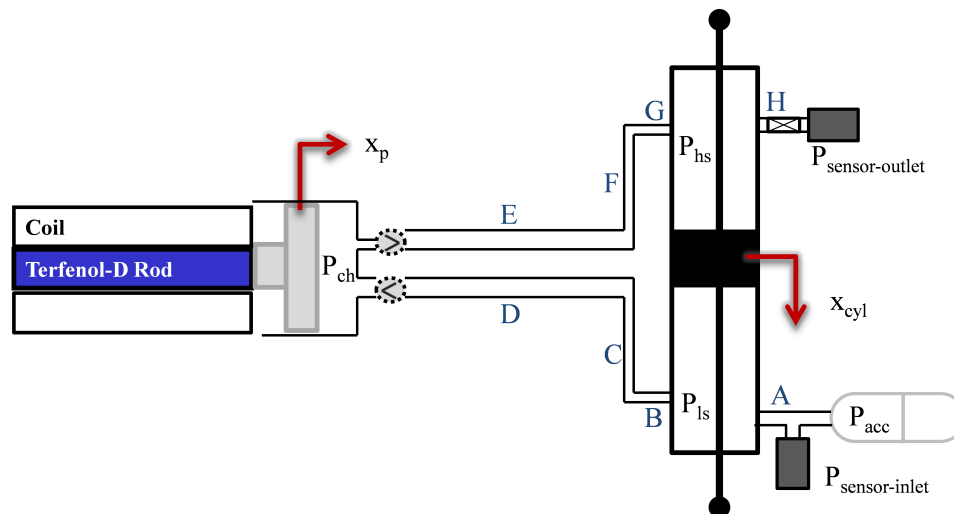


Figure C.1: System model diagram showing the layout of the fluid passages.

Table C.1: Fluid passage dimensions for the reduced-volume-manifold EHA.

<b>Fluid Passage</b>	<b>Diameter (cm)</b>	<b>Length (cm)</b>
A	0.24	0.70
B	0.24	0.87
C	0.16	2.76
D	0.32	5.72
E	0.44	5.72
F	0.16	2.76
G	0.24	0.87
H	0.24	0.95
Low-side Sensor Passage	0.70	4.57
Inlet from Accumulator	0.95	11.43

Table C.2: Magnetostrictive driver, piston, and output hydraulic cylinder properties for the reduced-volume-manifold EHA.

Parameter	Value	Units	Description
$x$	0.02	–	Air volume fraction
$\beta_l$	1.7	GPa	Hydraulic fluid bulk modulus
$\rho_f$	871	kg/m <sup>3</sup>	Hydraulic fluid density
$E_{TD}$	15	GPa	Terfenol-D modulus
$D_{TD}$	12.7	mm	Terfenol-D diameter
$L_{TD}$	114	mm	Terfenol-D rod length
$\alpha$	233	N/A	Coupling coefficient
$m_p$	124	g	Piston effective mass
$k_p$	24.3	MN/m	Piston effective stiffness
$\zeta_p$	0.09	–	Damping ratio for the piston and driver
$m_r$	0.0206	g	Reed effective mass
$k_r$	30	N/cm	Reed effective stiffness
$\zeta_r$	0.55	–	Reed damping ratio
$\lambda$	0.85	cm <sup>2</sup> /cm	Area factor for reed tip displacement
$A_r$	0.135	cm <sup>2</sup>	Reed valve area
$A_{ch}$	5.07	cm <sup>2</sup>	Pumping chamber area
$h_{ch}$	1.27	mm	Pumping chamber height
$A_{out}$	0.95	cm <sup>2</sup>	Output cylinder area
$L_{stroke}$	5.1	cm	Output cylinder stroke



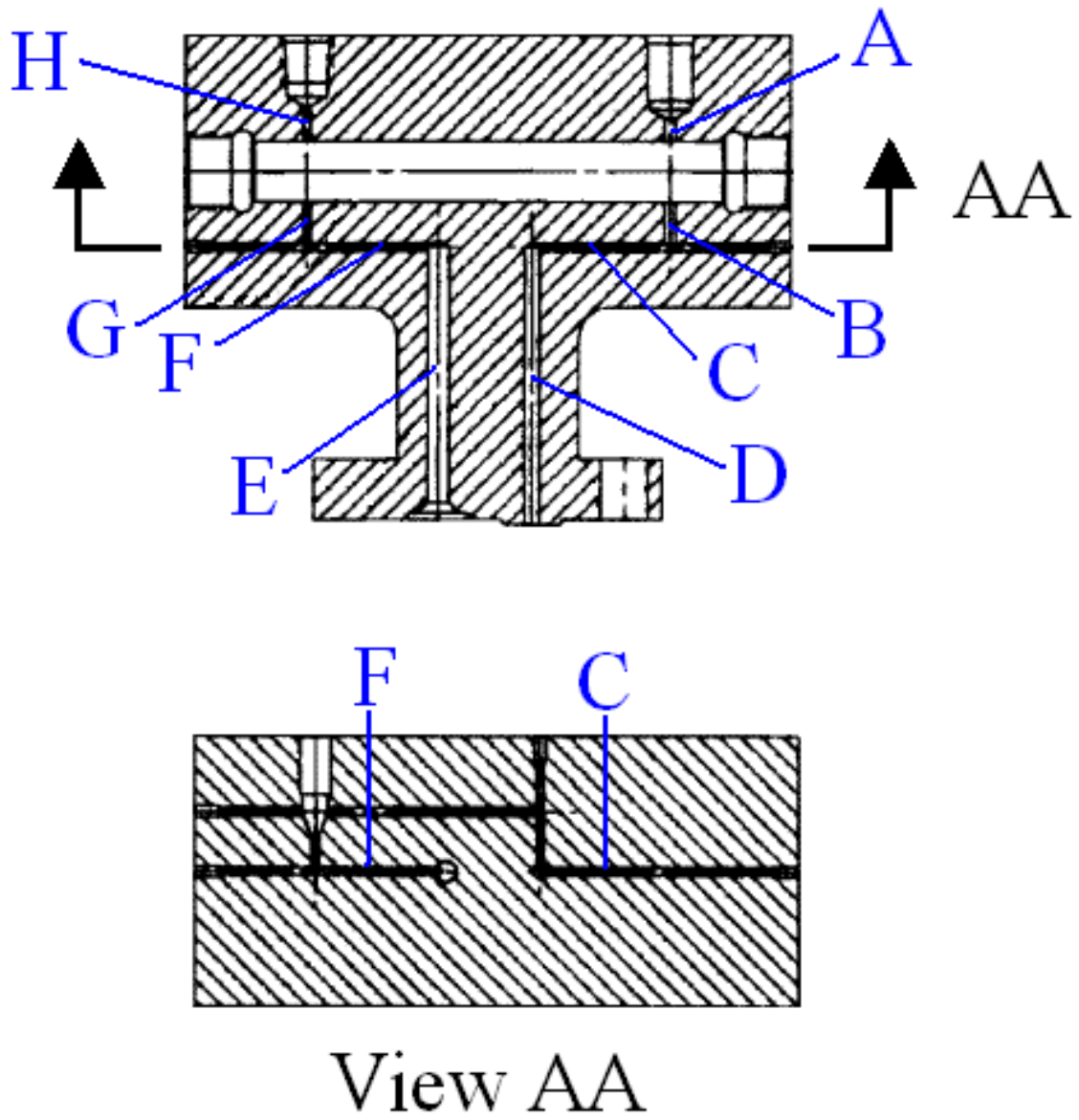


Figure C.2: Cut-away drawing of the reduced-volume manifold.

## C.2 Compact Aircraft EHA Parameters

Tables C.3 and C.4 summarize the parameters used to model the compact aircraft EHA design.

Table C.3: Fluid passage dimensions for the compact aircraft EHA.

Fluid Passage	Diameter (cm)	Length (cm)
A	0.89	1.27
B	0.89	1.27
C	0.89	3.47
D	0.89	1.91
E	0.89	1.91
F	0.89	3.47
G	0.89	1.27
H	0.89	1.27
Inlet from Accumulator	0.89	3.81

Table C.4: Magnetostrictive driver, piston, and output hydraulic cylinder properties for the compact aircraft EHA.

Parameter	Value	Units	Description
$x$	0.002	–	Air volume fraction
$\beta_l$	1.7	GPa	Hydraulic fluid bulk modulus
$\rho_f$	880	kg/m <sup>3</sup>	Hydraulic fluid density
$E_{TD}$	25	GPa	Terfenol-D modulus
$D_{TD}$	20.0	mm	Terfenol-D rod diameter
$L_{TD}$	152	mm	Terfenol-D rod length
$\alpha$	237	N/A	Coupling coefficient
$m_p$	191	g	Piston effective mass
$k_p$	54	MN/m	Piston effective stiffness
$\zeta_p$	0.03	–	Damping ratio for the piston and driver
$m_r$	0.033	g	Reed effective mass
$k_r$	23	N/cm	Reed effective stiffness
$\zeta_r$	0.1	–	Reed damping ratio
$\lambda$	0.85	cm <sup>2</sup> /cm	Area factor for reed tip displacement
$A_r$	0.62	cm <sup>2</sup>	Reed valve area
$A_{ch}$	6.13	cm <sup>2</sup>	Pumping chamber area
$h_{ch}$	1.27	mm	Pumping chamber height
$A_{out}$	12.65	cm <sup>2</sup>	Output cylinder area
$L_{stroke}$	6.30	cm	Output cylinder stroke

### C.3 Jiles-Atherton Model Parameters

Table C.5 summarizes the Jiles-Atherton model parameters used for considering nonlinear effects in the Terfenol-D driven EHA designs.

Table C.5: Parameter values used for the Jiles-Atherton model applied to model the nonlinear behavior of the Terfenol-D rod.

Parameter	Value	Units
$E$	32	GPa
$a$	6512	A/m
$c$	0.18	—
$\alpha$	0.046	—
$k$	3	kA/m
$\lambda_s$	1150	ppm
$\sigma_{\text{bias}}$	-6.9	MPa
$M_s$	765	kA/m
$\mu_{\text{TD}}$	5	—
$\rho_{\text{TD}}$	0.58	$\mu\Omega$ m
$N_{\text{tot}}$	568	turns

## C.4 Fluid Viscosity Comparison

Two types of hydraulic fluids were used in the experimental data presented in this thesis. The reduced-volume-manifold pump used Mobil DTE-24, a ISO-32 grade fluid. The high-power design used Royco 756, a Mil-H-5606 type fluid that is typically used for aircraft hydraulic applications. The main difference between the two oils is that the DTE-24 fluid is significantly more viscous. Using the ASTM method for extrapolation (D341), the DTE-24 fluid viscosity is 83 cSt compared to 27 cSt for the Mil-H-5606 fluid at room temperature (Figures C.3 and C.4).

Viscous fluid losses tend to be small compared to inertial fluid losses within the high-frequency flow environment of magnetostrictive hydraulic pumps, so the performance difference for the two fluids is expected to be small. However, the less viscous fluid is less likely to retain air during the filling process. Any amount of entrained air can have a significant impact on the fluid bulk modulus, which increases the compliance and decreases overall frequency response of the system.

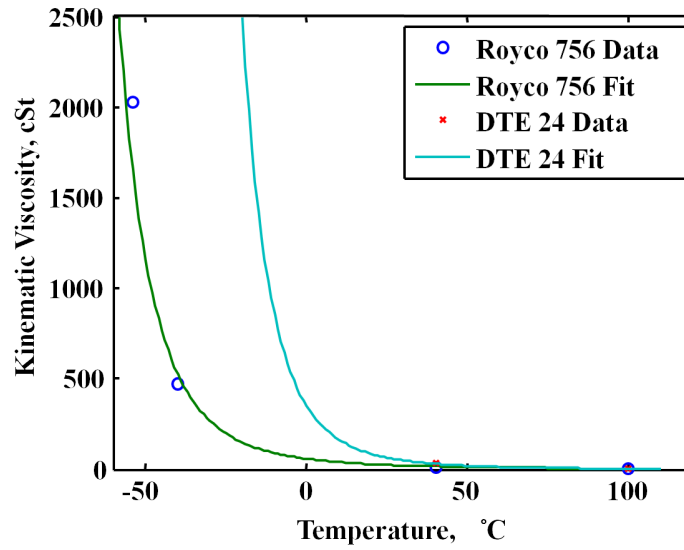


Figure C.3: Viscosity comparison between Royco 756 and Mobil DTE-24 hydraulic fluids. The extrapolation method given in ASTM D341 is used to extrapolate the data from the manufacturers' reported values.

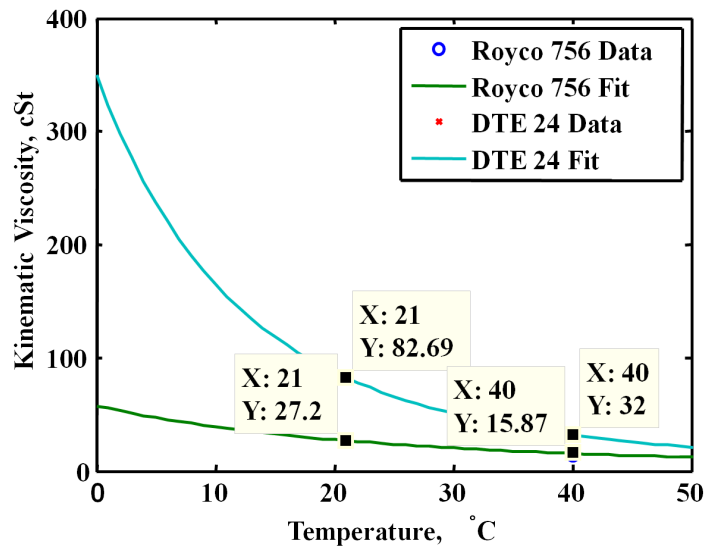


Figure C.4: Viscosity comparison between Royco 756 and Mobil DTE-24 hydraulic fluids using the ASTM D341 method. At room temperature, the viscosity of the DTE-24 is significantly higher than the Royco 756 (Mil-H-5606) fluid.

# Appendix D

## Design Drawings for Compact Aircraft EHA

### D.1 Solid Model Exploded Views

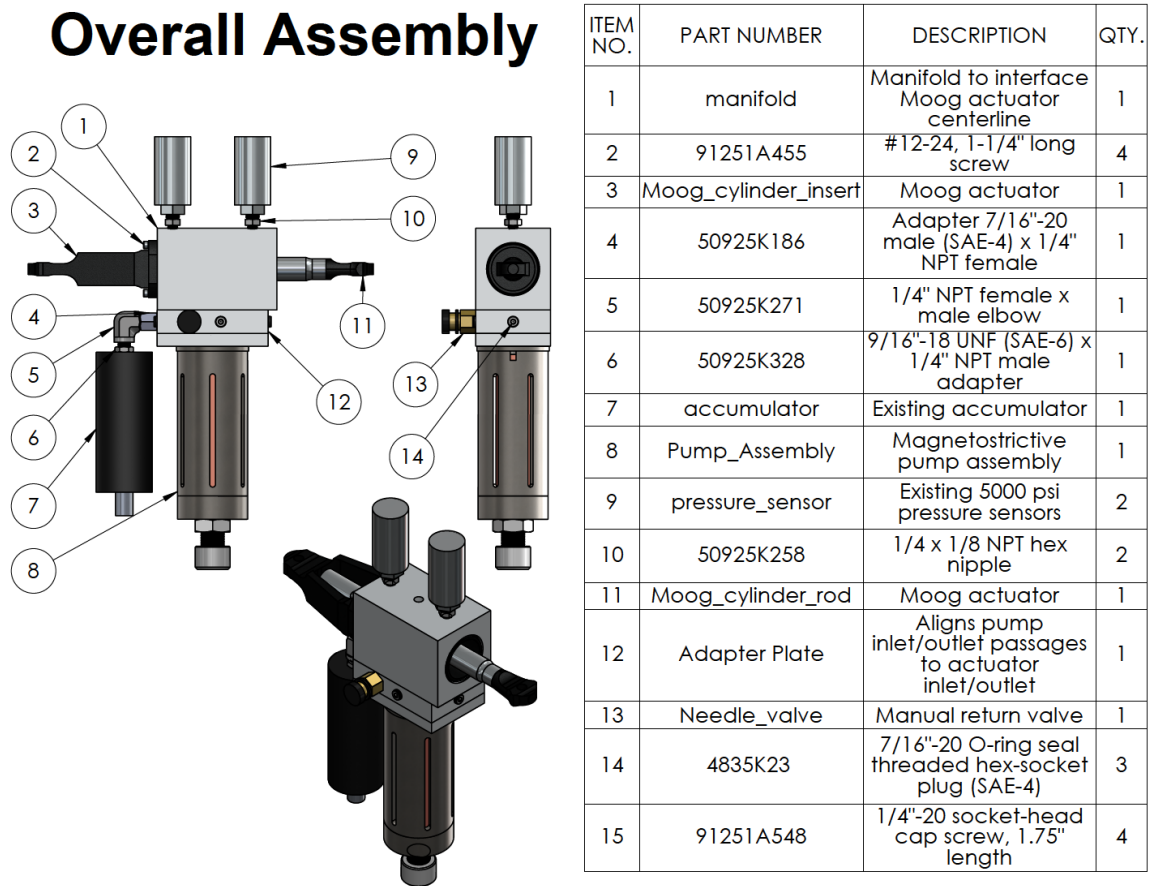


Figure D.1: Overall assembly for the high power EHA design.



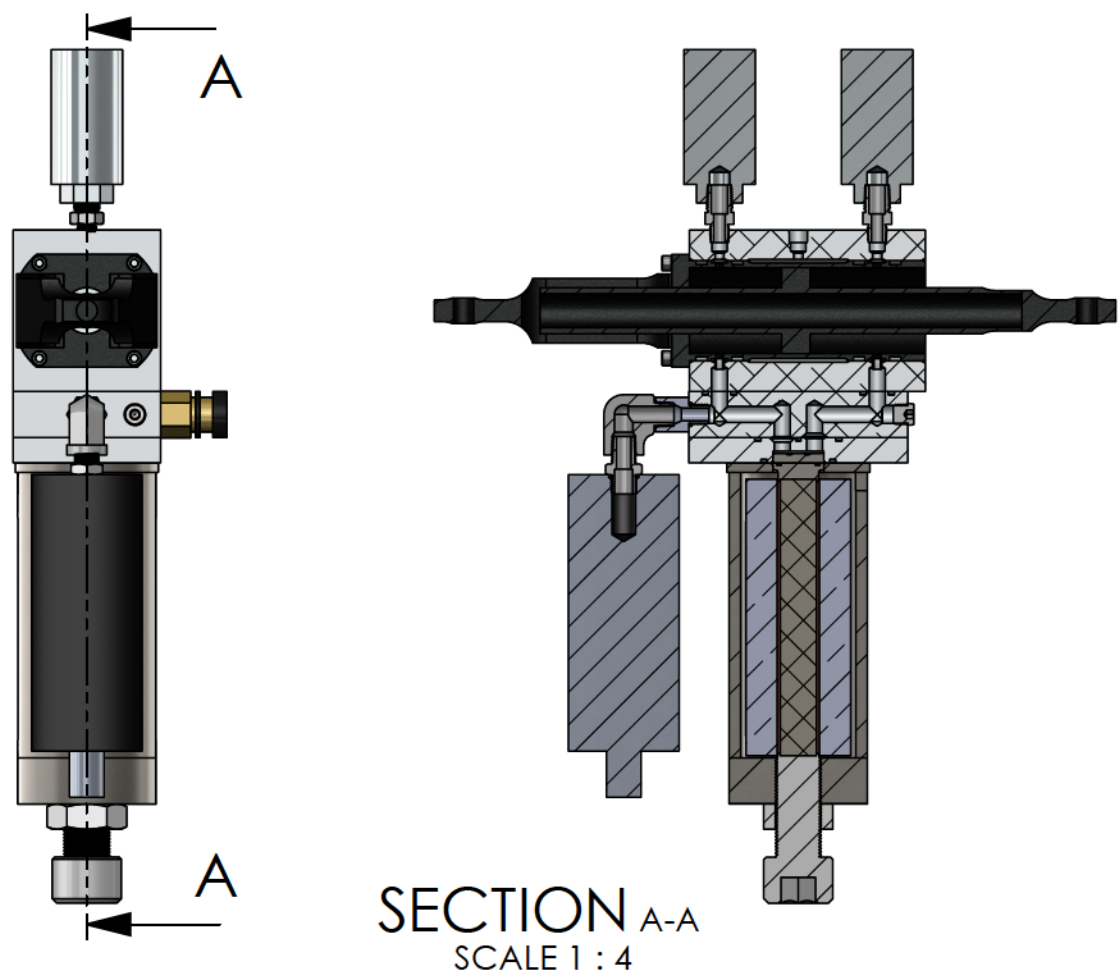


Figure D.2: Cross section view of the high-power EHA design.

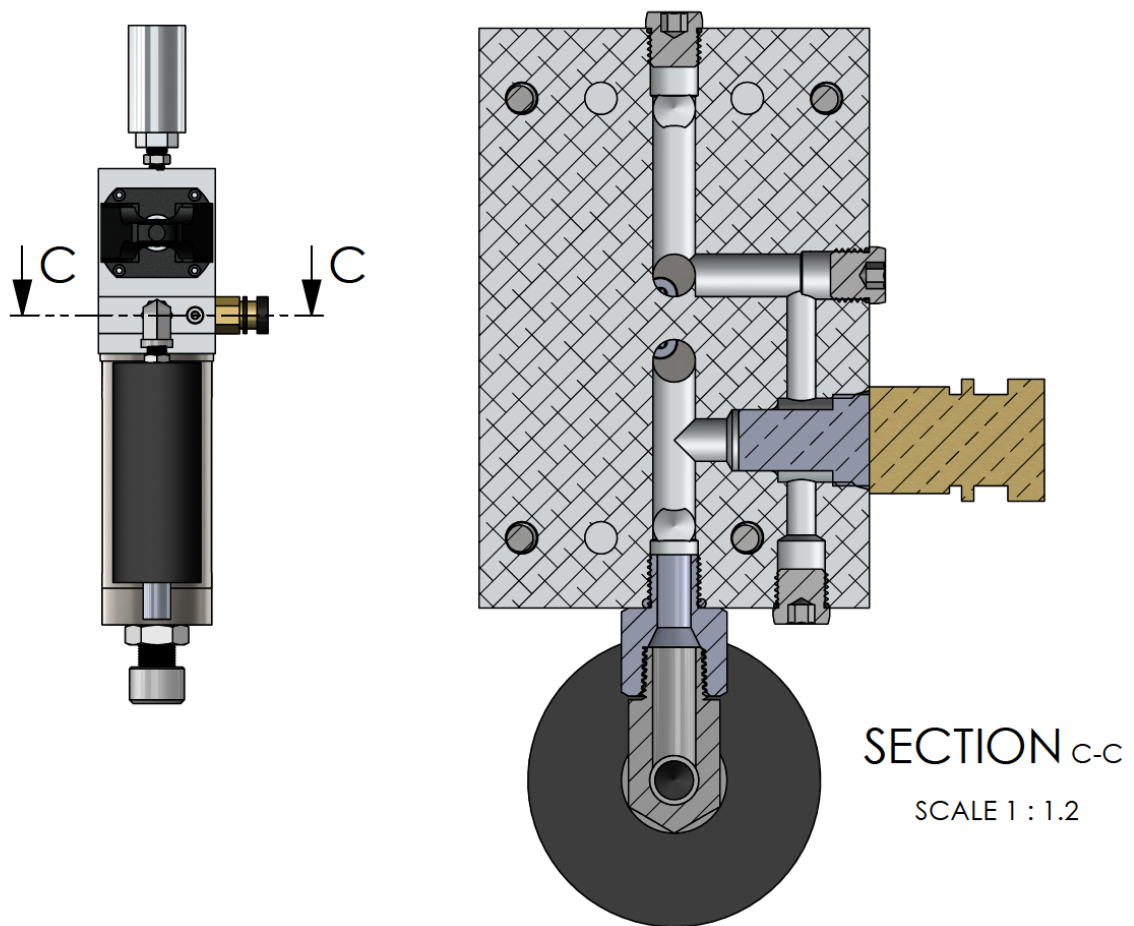


Figure D.3: Cross section of the adapter plate, which connects the magnetostriuctive pump with the hydraulic cylinder. A manual cartridge-style return valve is represented in bronze.

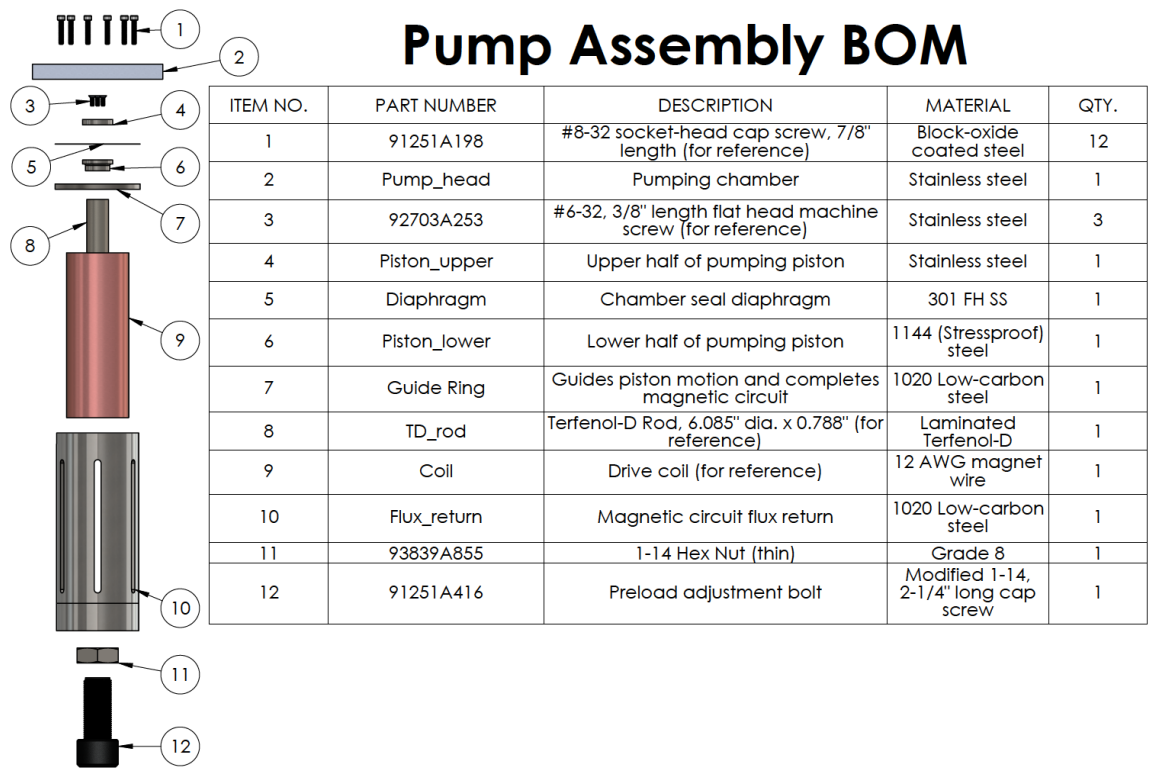


Figure D.4: Bill of material for the magnetostrictive pump portion of the high-power EHA design.

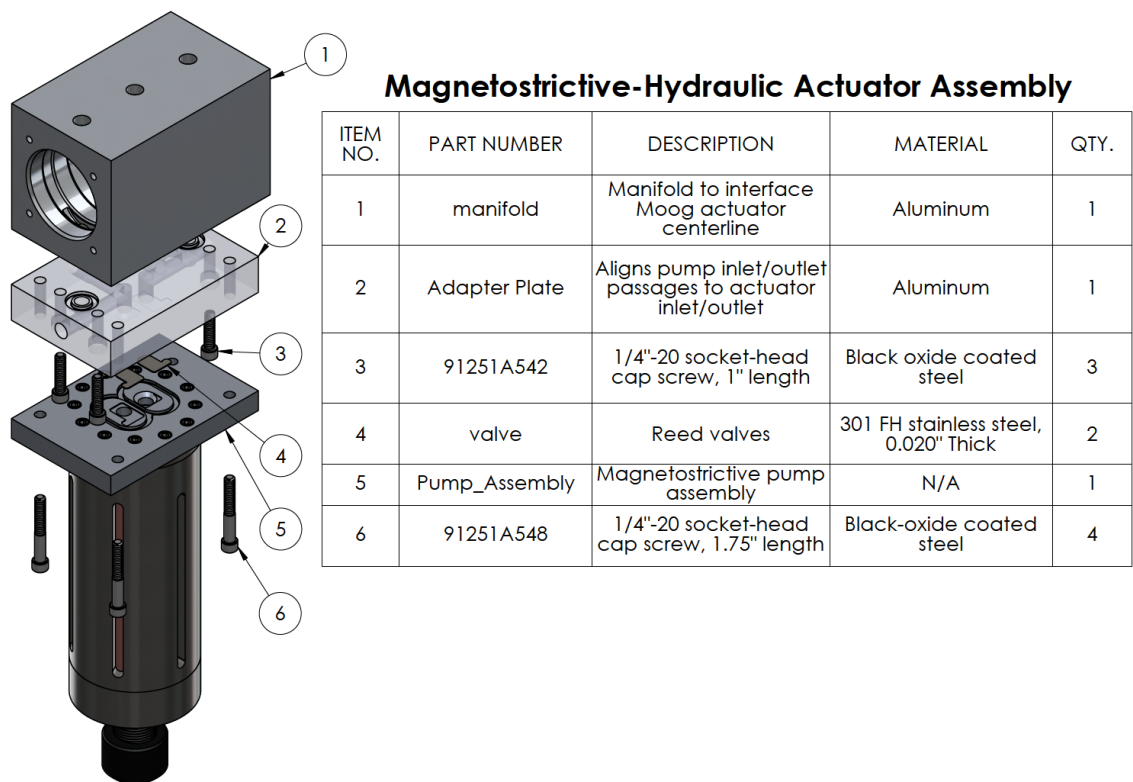


Figure D.5: Exploded view of the EHA actuator assembly, showing the placement of the rectification reed valves.

## D.2 Detailed Design Drawings

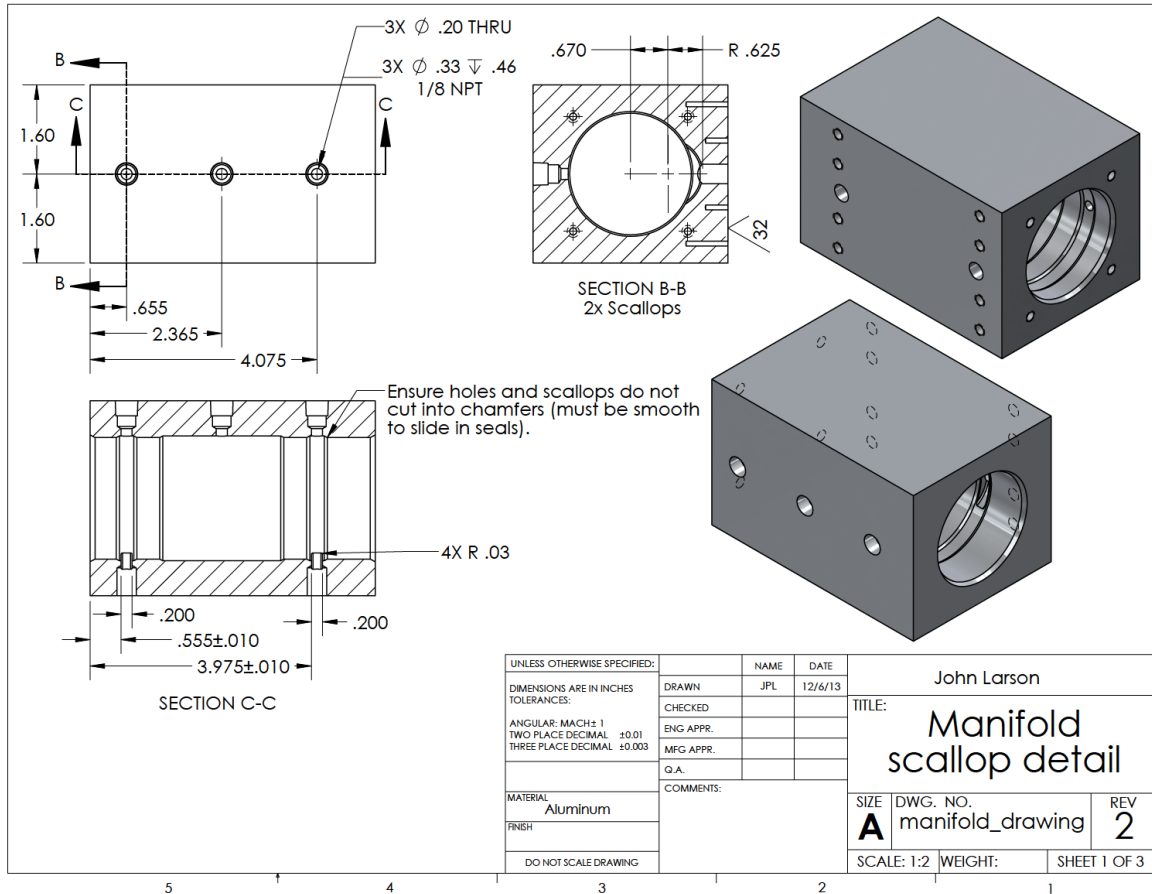


Figure D.6: Detailed drawing of the manifold to interface with the hydraulic actuator centerline.

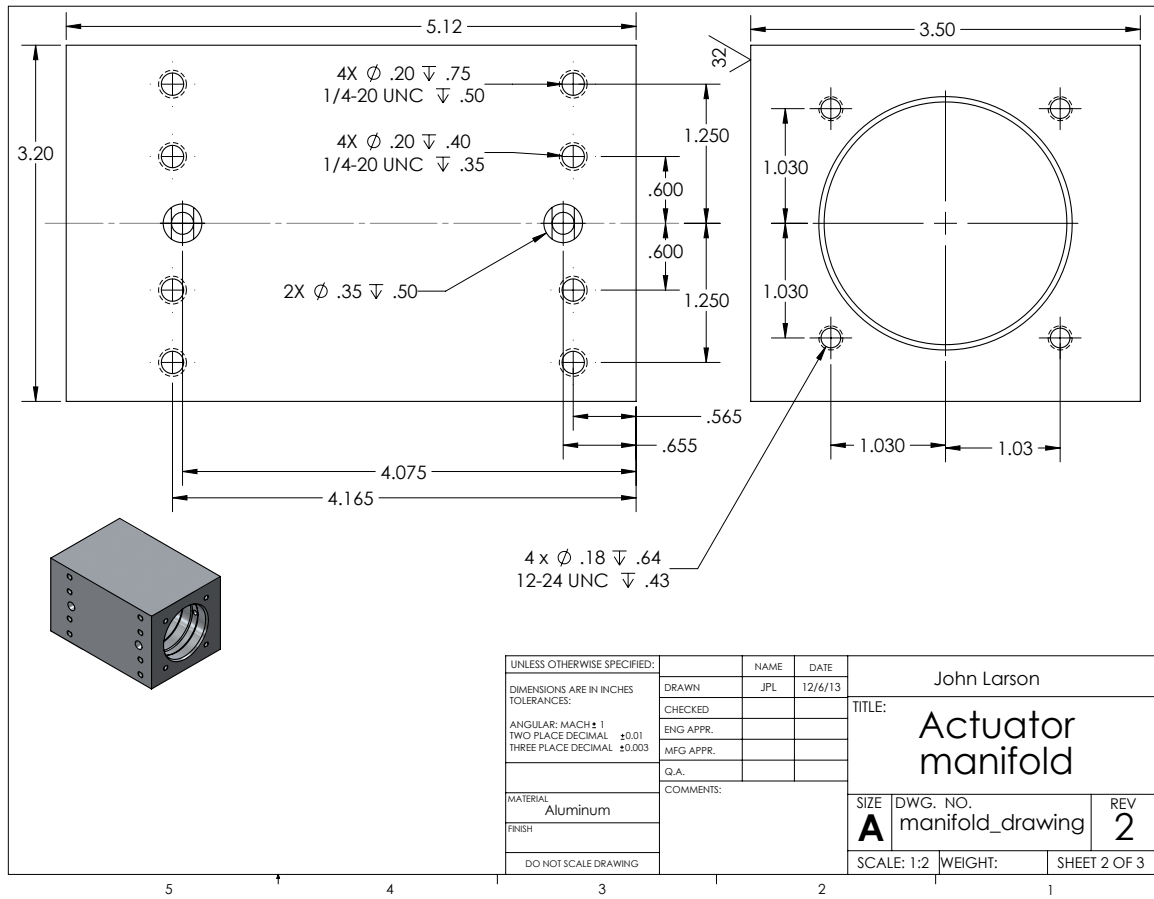


Figure D.7: Hole details for the actuator manifold.



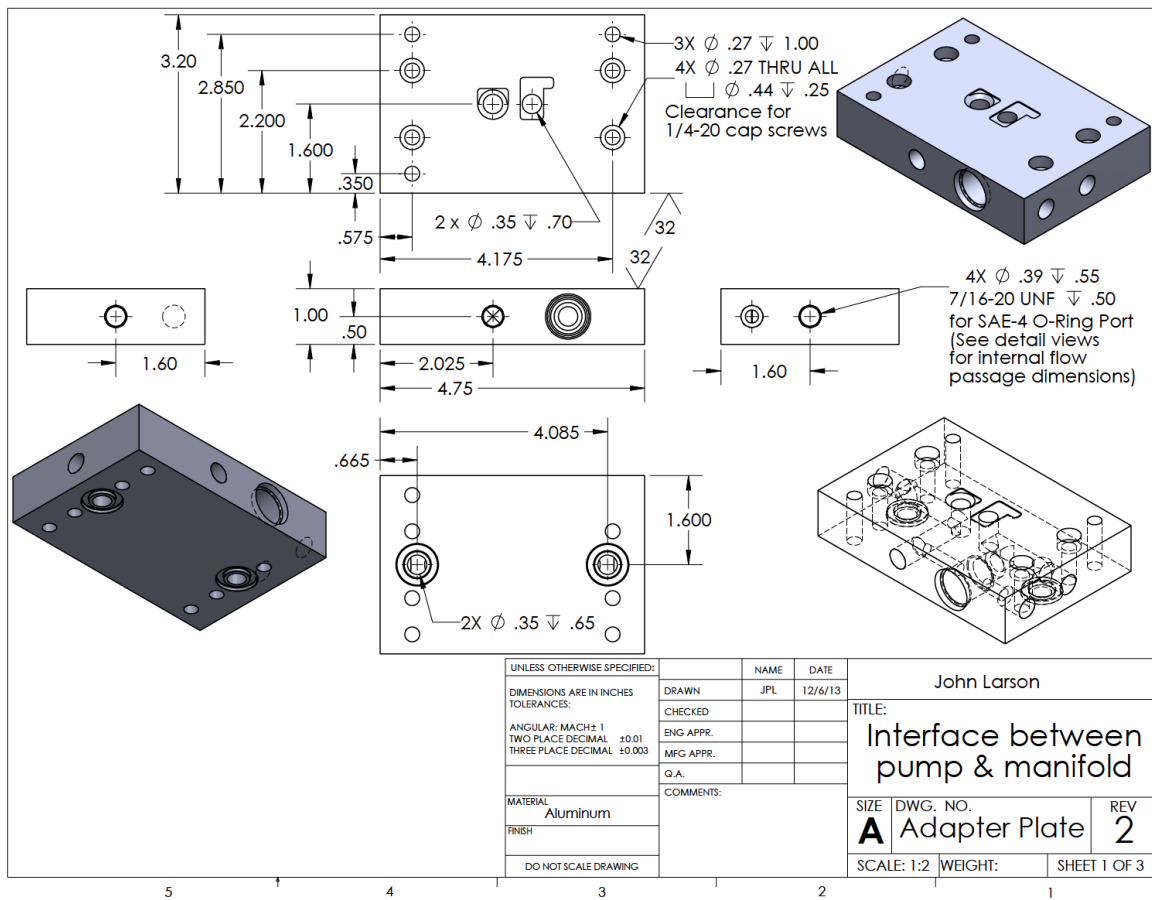


Figure D.9: Adapter plate used to connect the pump portion of the actuator with the hydraulic cylinder manifold.



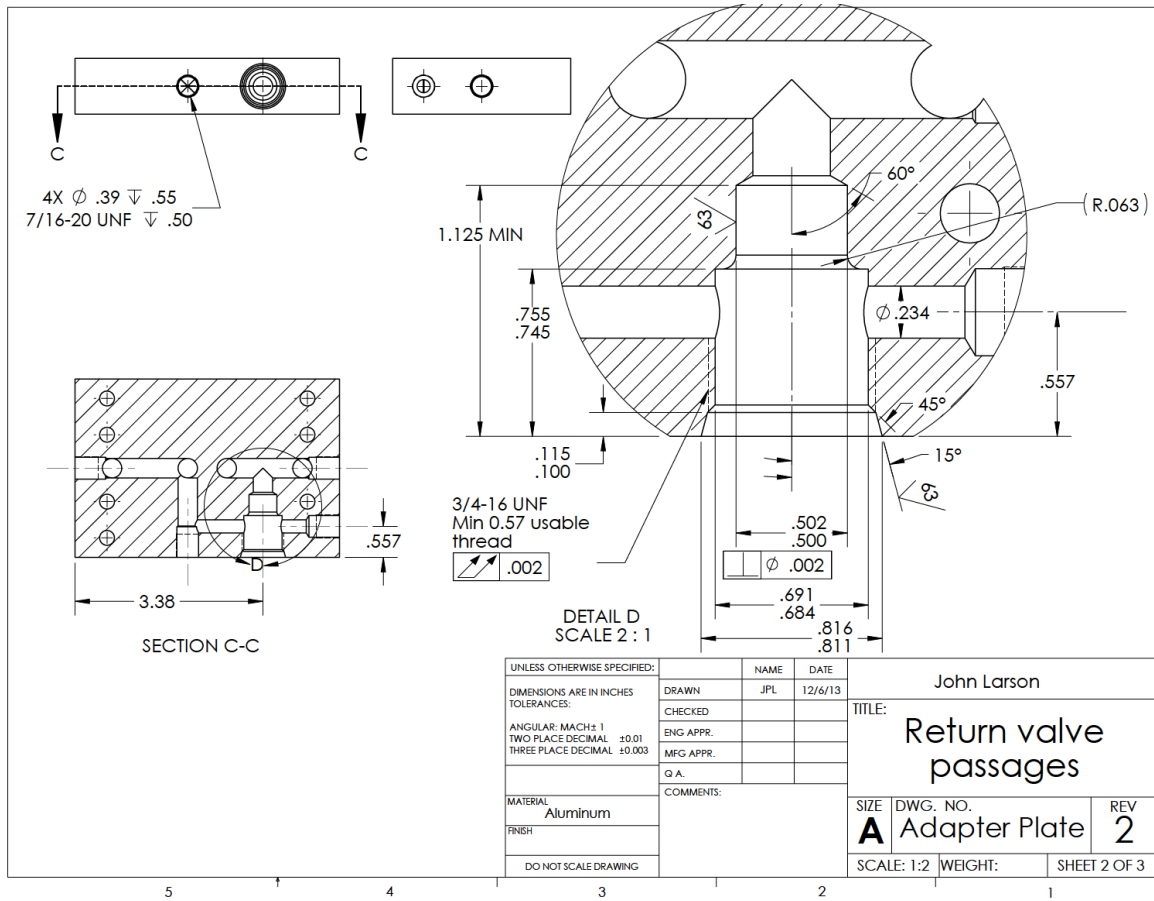


Figure D.10: Details for the return valve passages within the adapter plate.

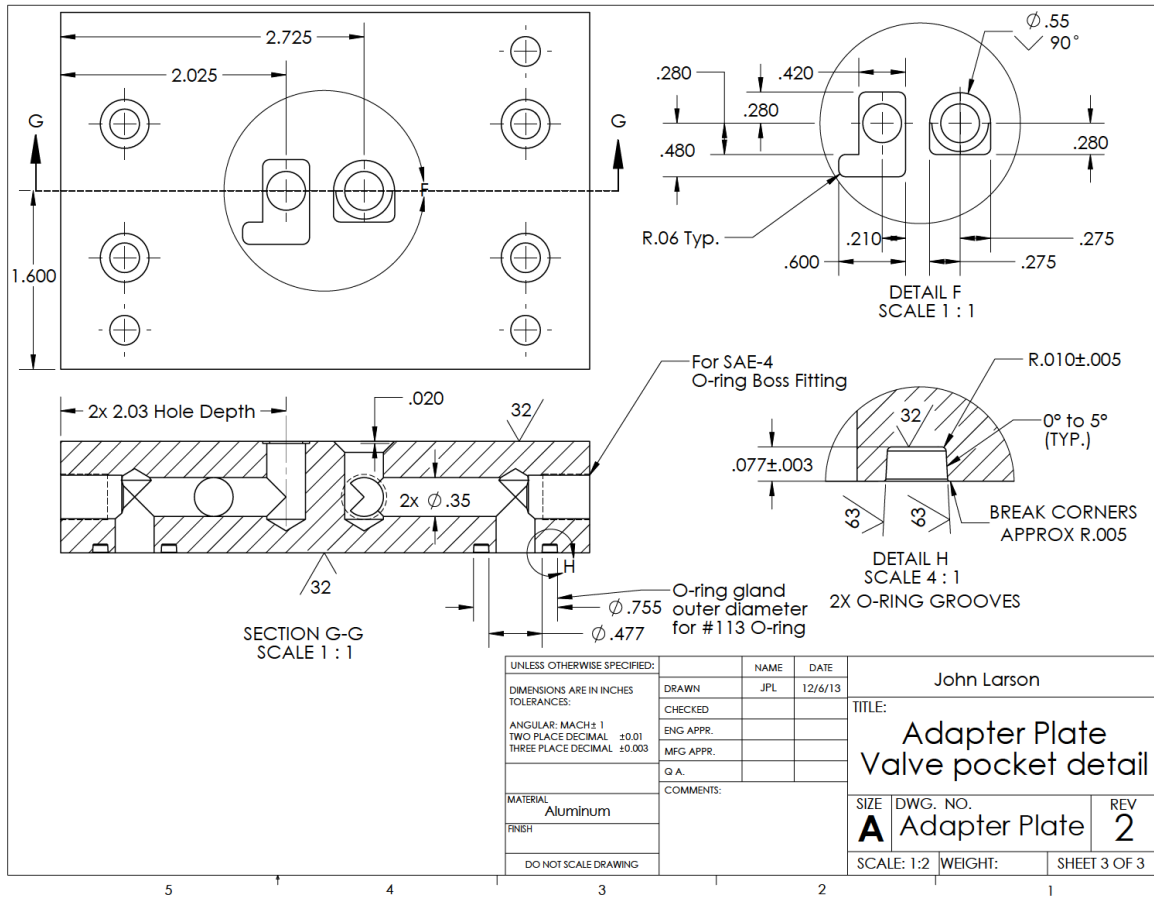


Figure D.11: Surface details for the adapter plate.

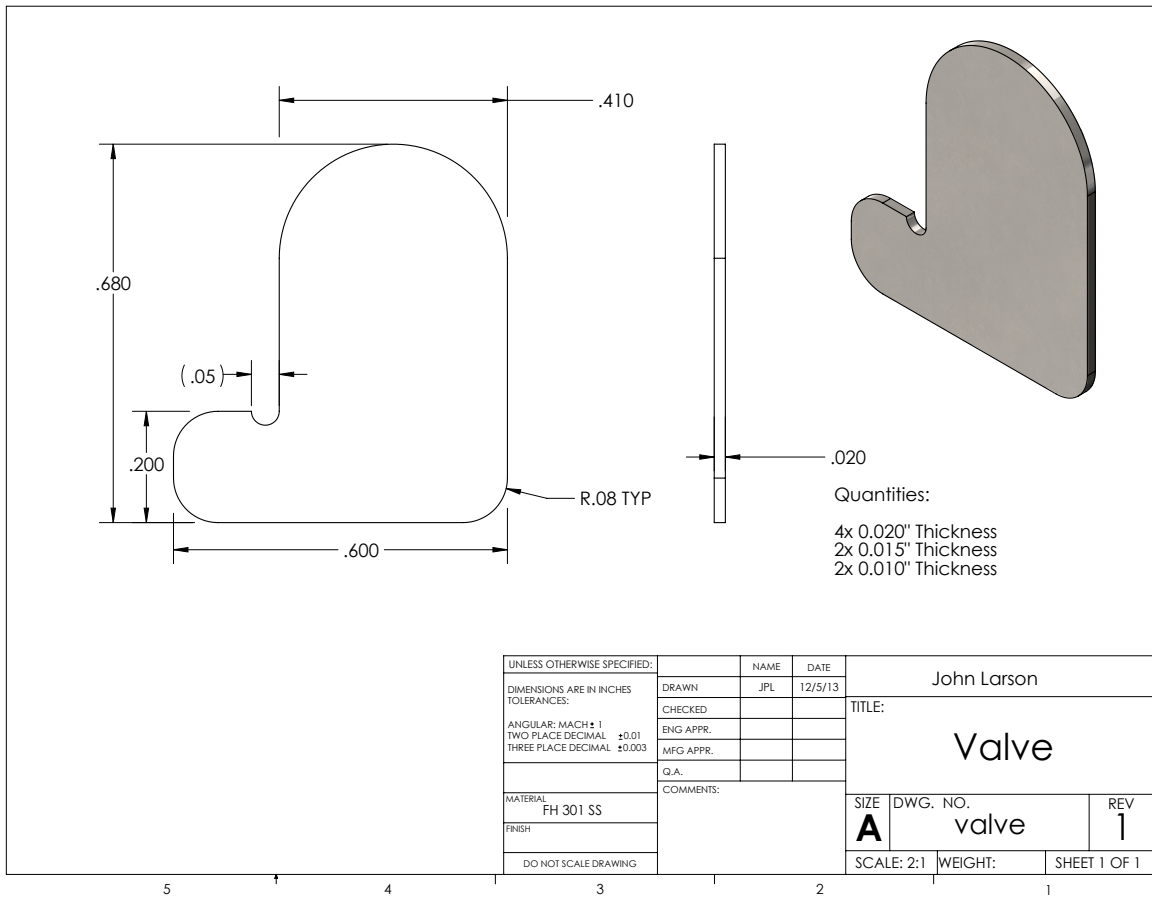


Figure D.12: Reed valve dimensional drawing.

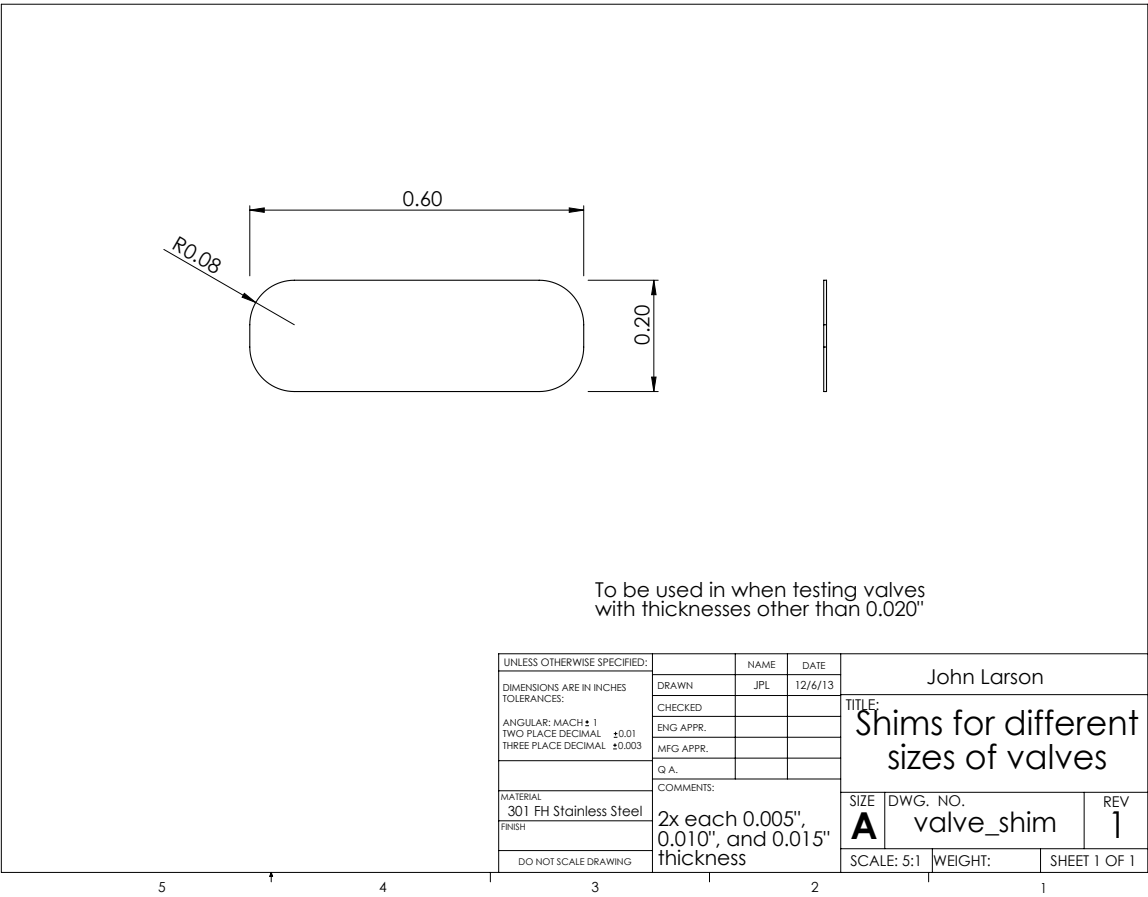


Figure D.13: Spacer dimensions used to clamp down valves thinner than 0.51 mm

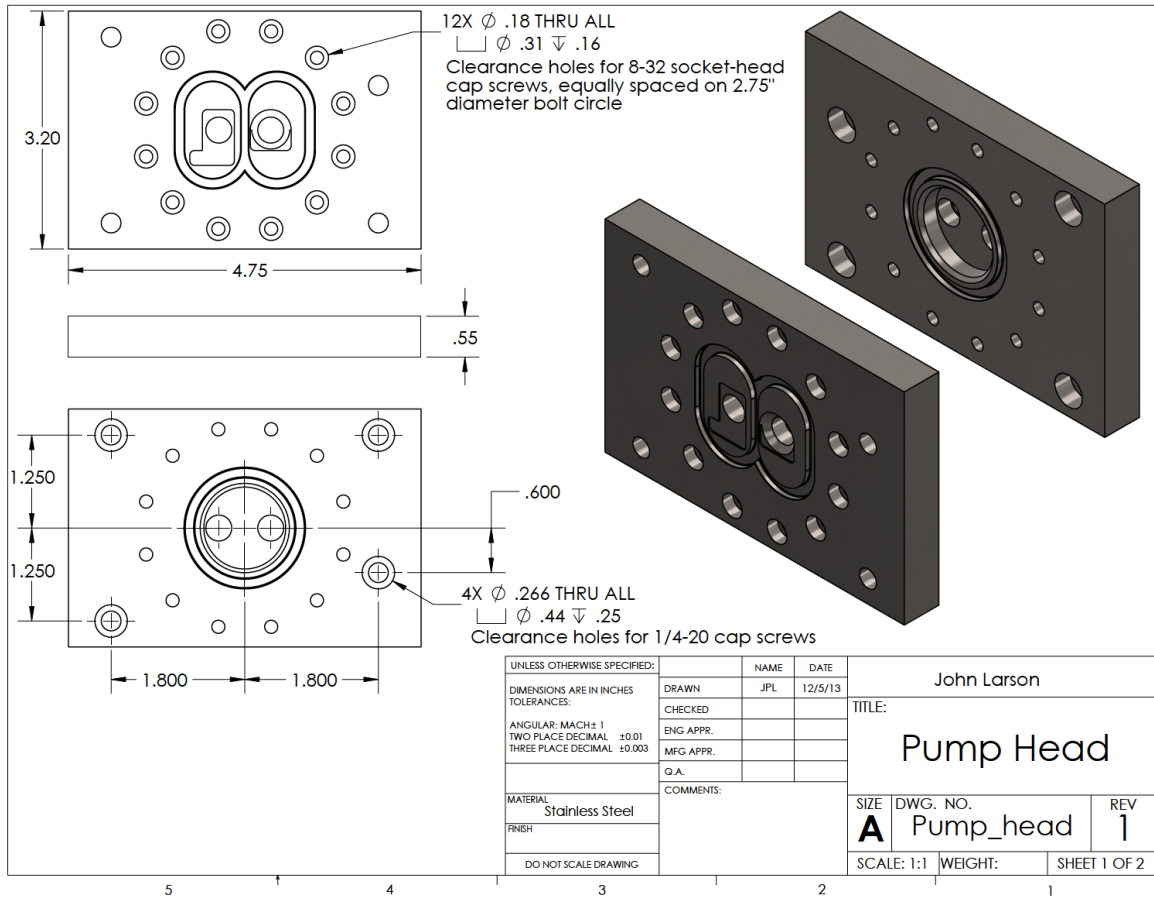


Figure D.14: Pump head design drawing.



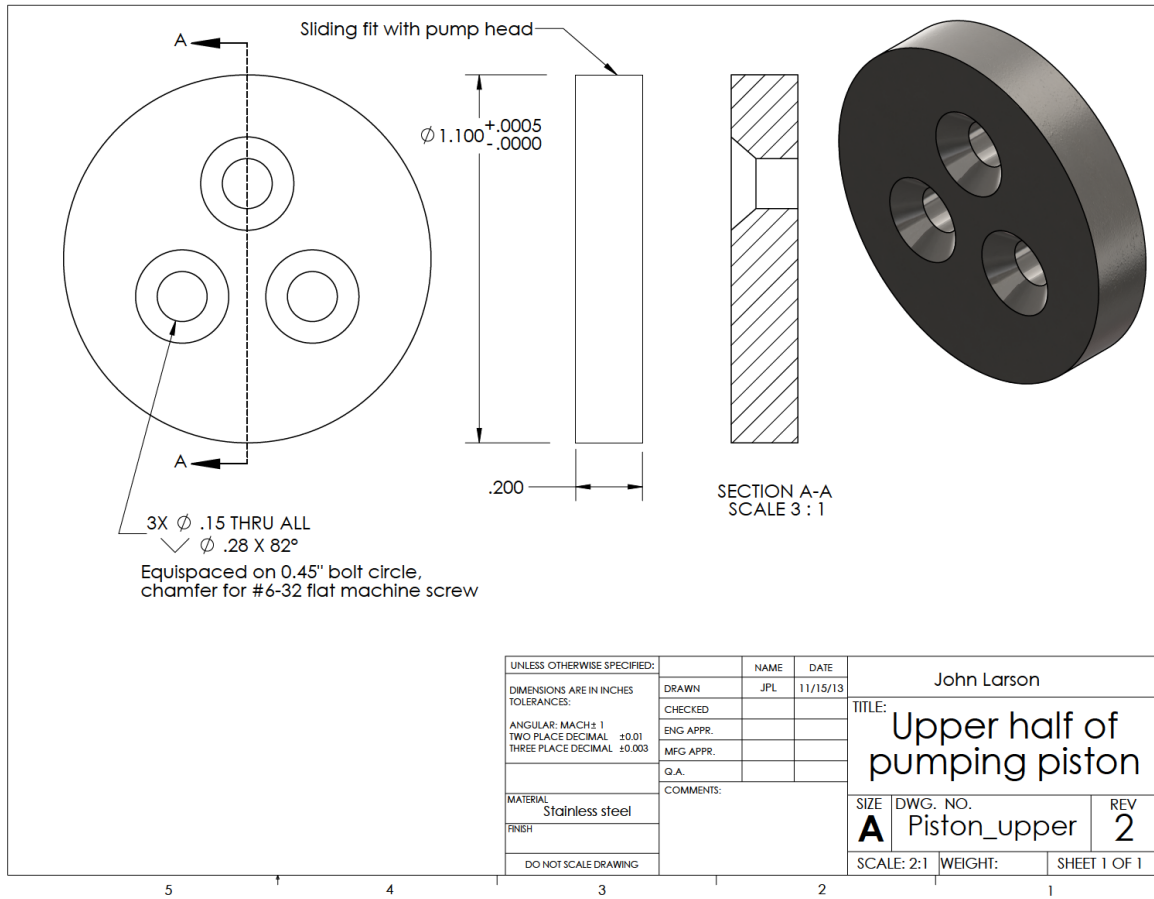


Figure D.16: Upper half of pumping piston.

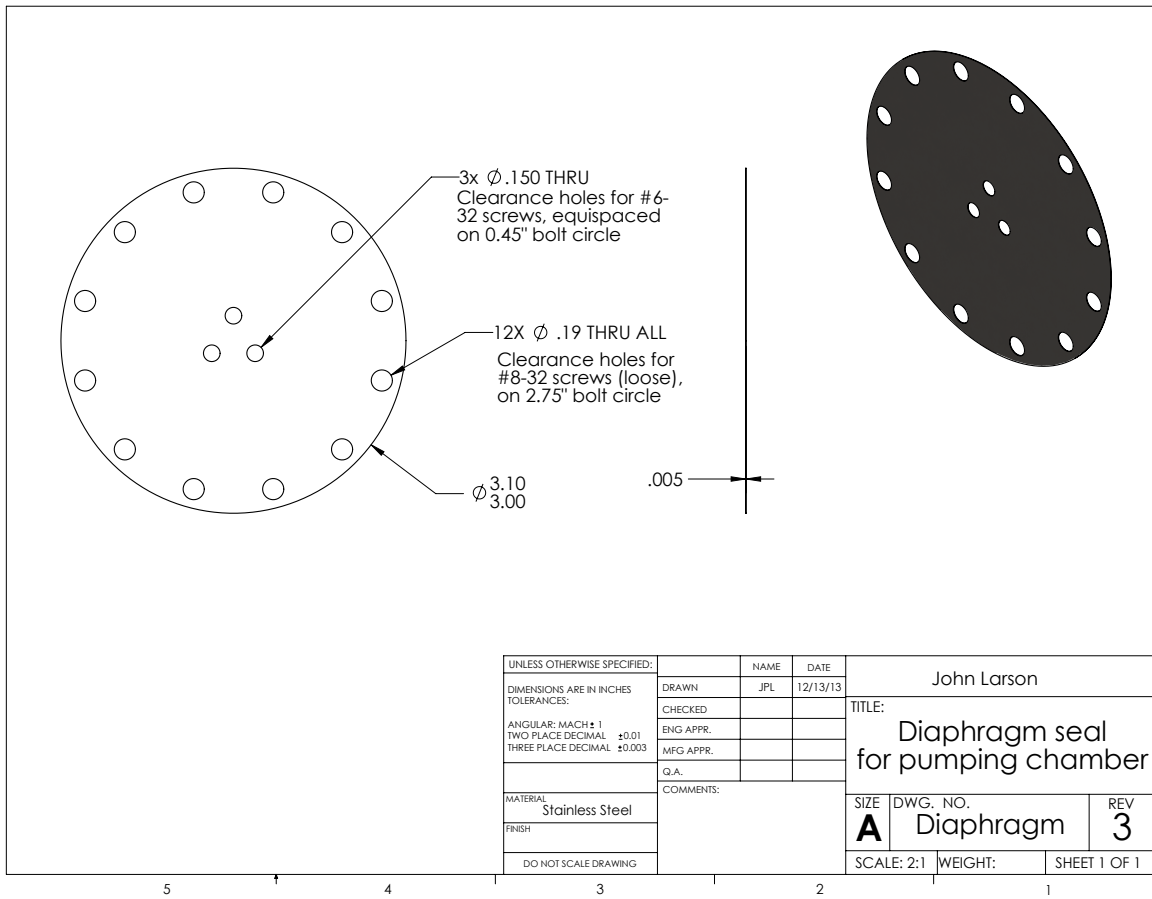


Figure D.17: Pumping chamber seal diaphragm design drawing.



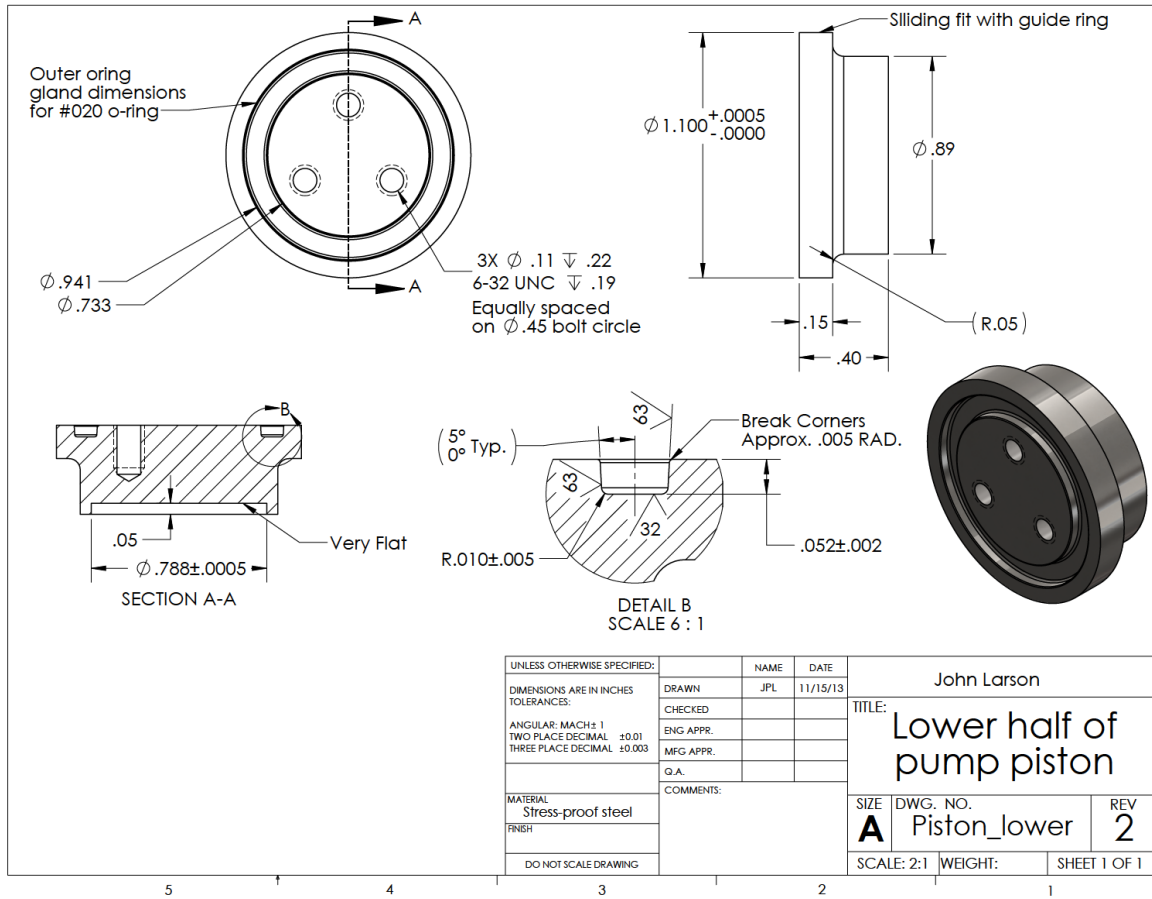


Figure D.18: Lower half of pumping chamber design.

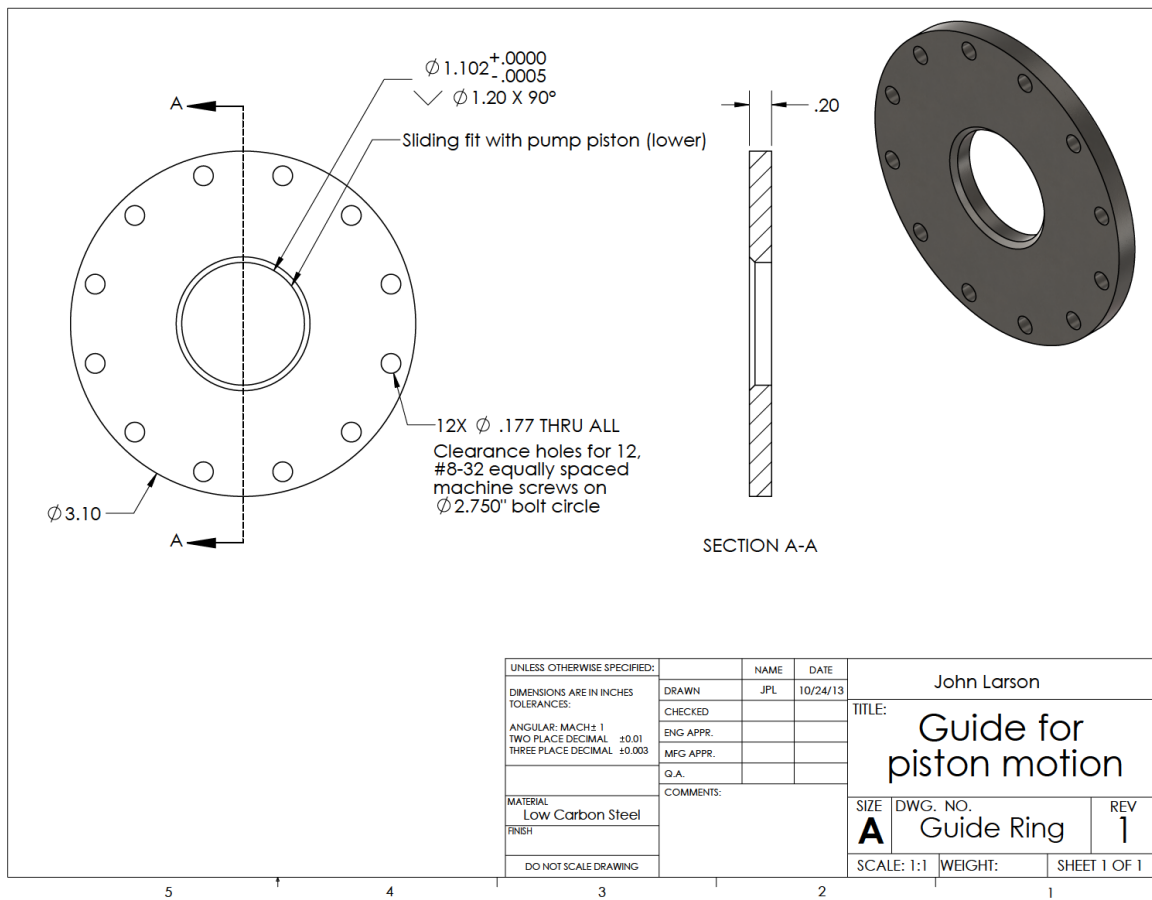


Figure D.19: Guide ring used to align flux return with pumping piston and to complete the magnetic circuit.

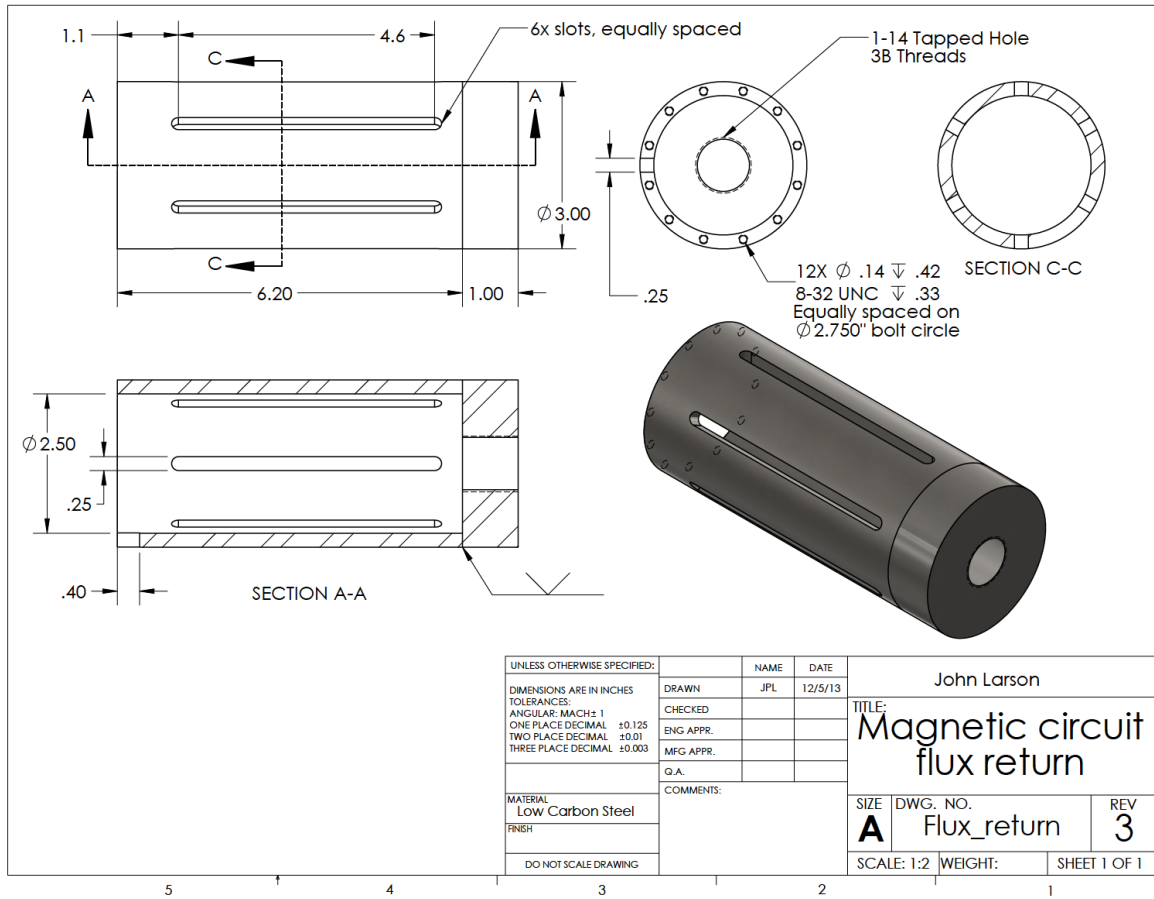


Figure D.20: Flux return and pump body.

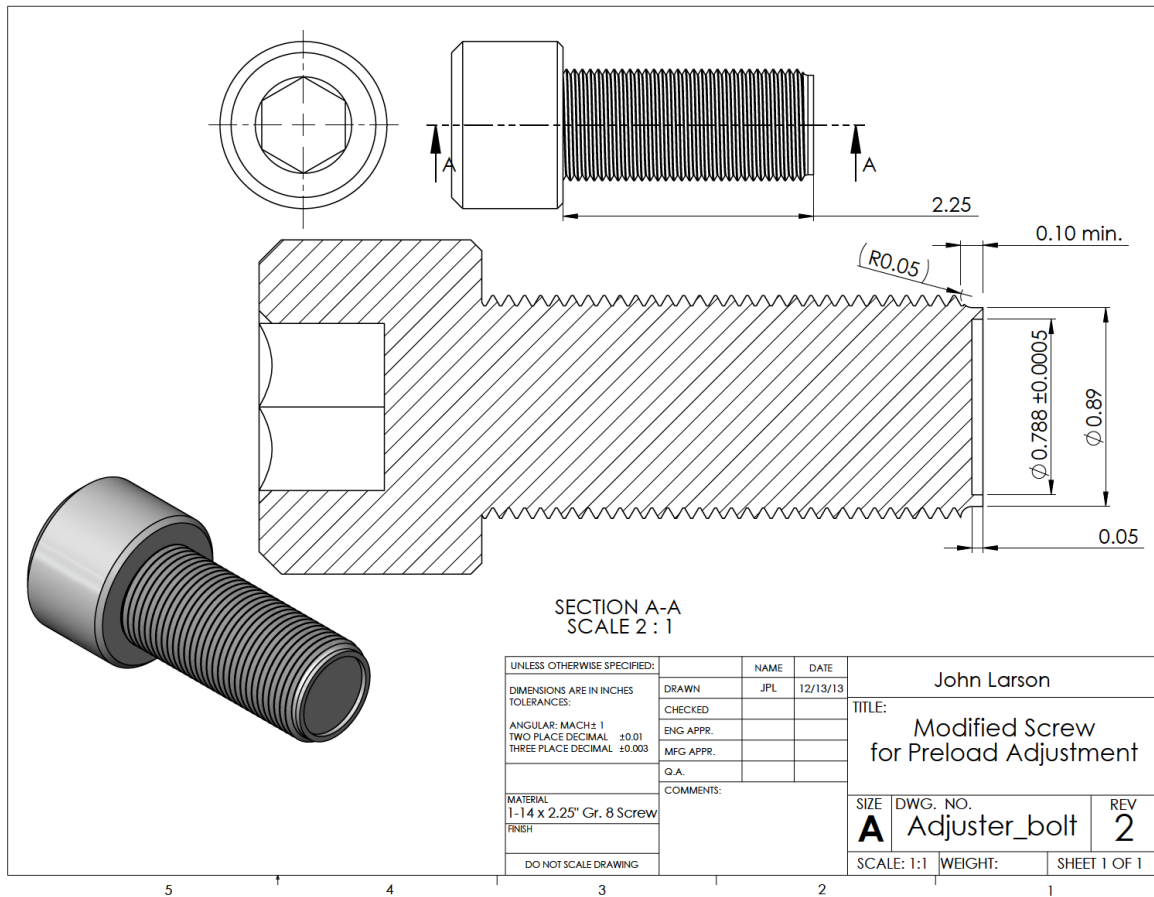


Figure D.21: A modified socket-head cap screw allows the position of the pumping piston to be adjusted while the preload bias pressure is applied to avoid plastic deformation of the seal diaphragm.

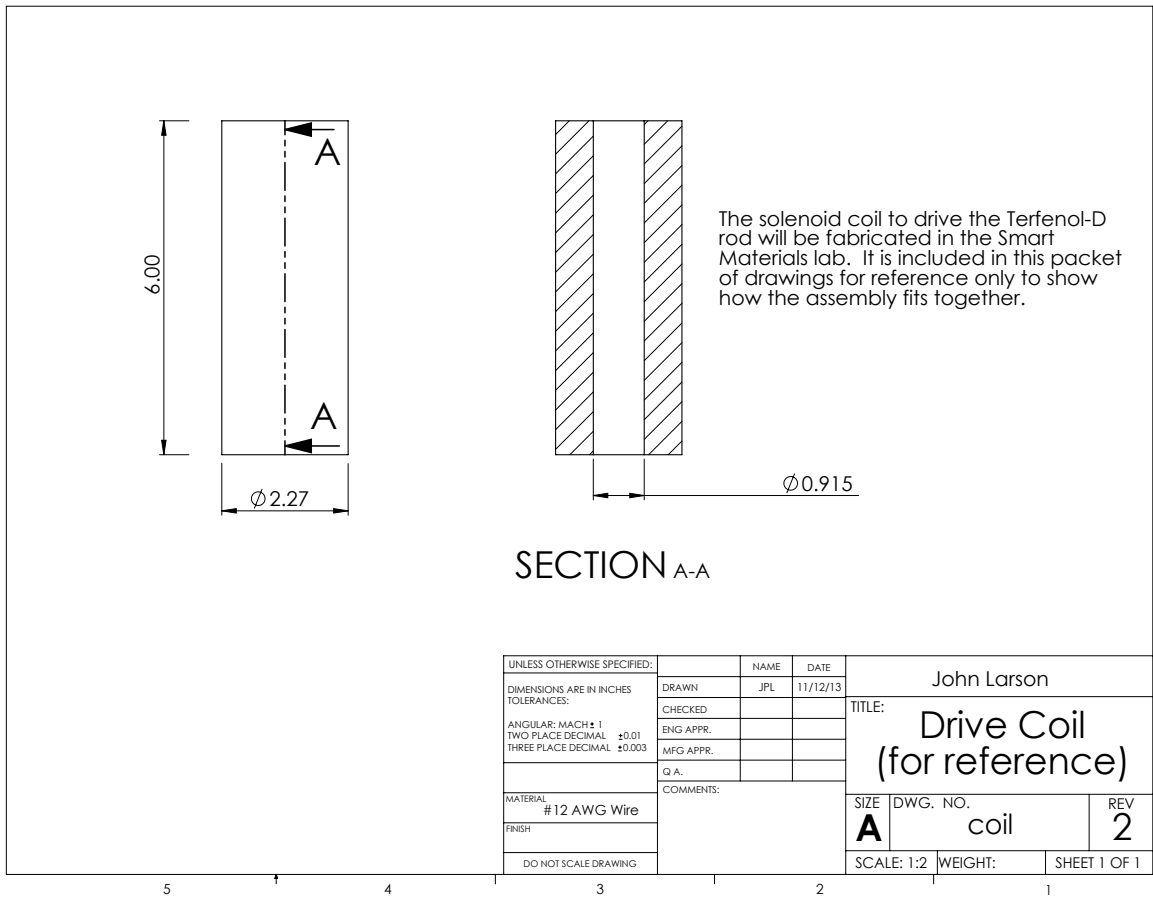


Figure D.22: Sketch of coil dimensions provided for reference.

# Bibliography

- [1] Etrema Products, Inc., “Terfenol-D data sheet.” [Online]. Available: <http://www.etrema-usa.com/documents/Terfenol.pdf>, 2012.
- [2] E. H. Anderson, G. L. Bales, and E. V. White, “Application of smart material-hydraulic actuators,” *Proceedings of SPIE*, vol. 5054, p. 73, 2003.
- [3] G. W. Kim and K. W. Wang, “Switching sliding mode force tracking control of piezoelectric-hydraulic pump-based friction element actuation systems for automotive transmissions,” *Smart Materials and Structures*, vol. 18, no. 8, p. 085004, 2009.
- [4] S. Alfayad, F. B. Ouezdou, F. Namoun, and G. Gheng, “High performance integrated electro-hydraulic actuator for robotics-Part I: Principle, prototype design & first experiments,” *Sensors and Actuators A: Physical*, vol. 169, no. 1, pp. 115–123, 2011.
- [5] J. S. Cloyd, “Status of the United States Air Force’s more electric aircraft initiative,” *Aerospace and Electronic Systems Magazine, IEEE*, vol. 13, no. 4, pp. 17–22, 1998.
- [6] M. J. Provost, “The more electric aero-engine: A general overview from an engine manufacturer,” in *International Conference on Power Electronics, Machines and Drives*, vol. 487, pp. 246–251, IET, 2002.

- [7] V. Giurgiutiu, “Actuators and smart structures,” in *Encyclopedia of Vibrations*, vol. 1, pp. 58–67, Academic Press, 2001.
- [8] K. Bridger, A. Cooke, F. Crowne, J. Lutian, J. Sewell, and G. Small III, “Compact hybrid actuator.” U.S. Patent 6 751 954, June 22, 2004.
- [9] D. Van den Bossche, “The A380 flight control electrohydrostatic actuators, achievements and lessons learnt,” in *International Conference of the Aeronautical Sciences*, 2006.
- [10] K. Bridger, J. M. Sewell, A. V. Cooke, J. L. Lutian, D. Kohlhafer, G. E. Small, and P. M. Kuhn, “High-pressure magnetostrictive pump development: A comparison of prototype and modeled performance,” *Proceedings of SPIE*, vol. 5388, p. 246, 2004.
- [11] Etrema Products, Inc., “Core technology: What is Galfenol?.” [Online]. Available: <http://www.etrema.com/core/galfenol/>, 2014.
- [12] A. Grunwald and A. Olabi, “Design of a magnetostrictive (MS) actuator,” *Sensors and Actuators A: Physical*, vol. 144, no. 1, pp. 161 – 175, 2008.
- [13] F. Claeysen, N. Lhermet, R. Le Letty, and P. Bouchilloux, “Actuators, transducers and motors based on giant magnetostrictive materials,” *Journal of Alloys and Compounds*, vol. 258, no. 1, pp. 61–73, 1997.
- [14] J. Lindler and E. Anderson, “Piezoelectric direct drive servovalve,” in *Proceedings of SPIE*, vol. 4698, p. 488, 2002.
- [15] S. Chakrabarti and M. Dapino, “Hydraulically amplified Terfenol-D actuator for adaptive powertrain mounts,” *Journal of Vibration and Acoustics*, vol. 133, p. 061015, 2011.

- [16] S. Wax, G. Fischer, and R. Sands, “The past, present, and future of DARPA’s investment strategy in smart materials,” *JOM*, vol. 55, no. 12, pp. 17–23, 2003.
- [17] M. J. Gerver, J. H. Goldie, J. R. Swenbeck, R. Shea, P. Jones, R. T. Ilmonen, D. M. Dozor, S. Armstrong, R. Roderick, F. E. Nimblett, *et al.*, “Magnetostrictive water pump,” *Proceedings of SPIE*, vol. 3329, pp. 694–705, March 1998.
- [18] J. E. Lindler, E. H. Anderson, and M. E. Regelbrugge, “Design and testing of piezoelectric-hydraulic actuators,” *Proceedings of SPIE*, vol. 5054, pp. 96–107, 2003.
- [19] L. D. Mauck and C. S. Lynch, “Piezoelectric hydraulic pump development,” *Journal of Intelligent Material Systems and Structures*, vol. 11, no. 10, p. 758, 2000.
- [20] D. Shin, D. Lee, K. Mohanchandra, and G. Carman, “Development of a SMA-based actuator for compact kinetic energy missile,” *Proceedings of SPIE*, vol. 4701, p. 237, 2002.
- [21] W. S. Oates and C. S. Lynch, “Piezoelectric hydraulic pump system dynamic model,” *Journal of Intelligent Material Systems and Structures*, vol. 12, no. 11, pp. 737–744, 2001.
- [22] C. A. Keller, “Novel concepts in piezohydraulic pump design,” Master’s thesis, Georgia Institute of Technology, Atlanta, Georgia, 2004.
- [23] D. G. Lee, S. W. Or, and G. P. Carman, “Design of a piezoelectric-hydraulic pump with active valves,” *Journal of Intelligent Material Systems and Structures*, vol. 15, no. 2, p. 107, 2004.
- [24] Kinetic Ceramics, Inc., “Piezoelectric fluid pumps.” [Online]. Available: [http://www.kineticceramics.com/piez\\_fluid.html](http://www.kineticceramics.com/piez_fluid.html), 2014.



- [25] J. Sirohi and I. Chopra, "Design and development of a high pumping frequency piezoelectric-hydraulic hybrid actuator," *Journal of Intelligent Material Systems and Structures*, vol. 14, no. 3, pp. 135–147, 2003.
- [26] E. Chapman, S. Herdic, C. Keller, and C. Lynch, "Development of miniaturized piezo-hydraulic pumps," *Proceedings of SPIE*, vol. 5762, pp. 299–310, 2005.
- [27] M. J. Rupinsky and M. J. Dapino, "Smart material electrohydrostatic actuator for intelligent transportation systems," *ASME Conference Proceedings*, vol. 2006, no. 47683, pp. 721–730, 2006.
- [28] D. T. Nosse and M. J. Dapino, "Magnetorheological valve for hybrid electrohydrostatic actuation," *Journal of Intelligent Material Systems and Structures*, vol. 18, no. 11, pp. 1121–1136, 2007.
- [29] D. T. Nosse, "Compact actuation through magnetorheological flow control and rectification of magnetostrictive vibrations," Master's thesis, The Ohio State University, 2005.
- [30] R. C. Sneed, R. R. Smith, M. F. Cash, G. L. Bales, and E. H. Anderson, "Development of smart material-hydraulic pumps and actuators," in *ASME 2006 International Mechanical Engineering Congress and Exposition*, pp. 435–443, American Society of Mechanical Engineers, 2006.
- [31] R. C. Sneed, R. R. Smith, M. F. Cash, and E. H. a. Anderson, "Smart-material based hydraulic pump system for actuation of a morphing wing," in *AIAA/ASME/AHS Adaptive Structures Conference*, (Honolulu, Hawaii), April 2007.

- [32] S. John, J. Sirohi, G. Wang, and N. M. Wereley, "Comparison of piezoelectric, magnetostrictive, and electrostrictive hybrid hydraulic actuators," *Journal of Intelligent Material Systems and Structures*, vol. 18, no. 10, p. 1035, 2007.
- [33] A. Chaudhuri, J. H. Yoo, and N. M. Wereley, "Design, test and model of a hybrid magnetostrictive hydraulic actuator," *Smart Materials and Structures*, vol. 18, p. 085019, 2009.
- [34] S. John, A. Chaudhuri, C. Cadou, and N. M. Wereley, "Unsteady fluid flow in hybrid hydraulic actuators," *Journal of Intelligent Material Systems and Structures*, vol. 20, pp. 2201–2214, Dec 2009.
- [35] S. John, C. Cadou, J. Yoo, and N. Wereley, "Application of CFD in the design and analysis of a piezoelectric hydraulic pump," *Journal of Intelligent Material Systems and Structures*, vol. 17, no. 11, p. 967, 2006.
- [36] S. John, N. Cadou, and N. M. Wereley, "Application of CFD in the design and analysis of a piezoelectric hydraulic pump," *Proceedings of SPIE*, vol. 5390, pp. 471–482, 2004.
- [37] A. Chaudhuri and N. Wereley, "Compact hybrid electrohydraulic actuators using smart materials: A review," *Journal of Intelligent Material Systems and Structures*, vol. 23, no. 6, pp. 597–634, 2012.
- [38] H. Tan, W. Hurst, and D. Leo, "Performance modeling of a piezohydraulic actuation system with active valves," *Smart materials and structures*, vol. 14, pp. 91–110, 2005.
- [39] G. W. Kim and K. W. Wang, "Enhanced control performance of a piezoelectric–hydraulic pump actuator for automotive transmission shift control," *Proceedings*

*of the Institution of Mechanical Engineers, Part D: Journal of Automobile Engineering*, vol. 224, no. 2, pp. 161–174, 2010.

- [40] A. Chaudhuri and N. M. Wereley, “Experimental validation of a hybrid electrostrictive hydraulic actuator analysis,” *Journal of Vibration and Acoustics*, vol. 132, no. 2, p. 021006, 2010.
- [41] J. P. Larson and M. J. Dapino, “Design of a smart material electro-hydraulic actuator with improved frequency bandwidth,” *Proceedings of SPIE*, vol. 8343, p. 83430K, 2012.
- [42] R. J. Stevens, “Pumps for fluids, more especially liquids.” U.S. Patent 2 842 067, July 8, 1958.
- [43] C. L. Stec, “Piezoelectric pump.” U.S. Patent 3 150 592, September 29, 1964.
- [44] J. B. Beckman and M. J. Blickstein, “Apparatus and method for piezoelectric pumping.” U.S. Patent 4 449 893, May 22, 1984.
- [45] J. B. Beckman and M. J. Blickstein, “Piezoelectric pump with internal load sensor.” U.S. Patent 4 519 751, May 28, 1985.
- [46] T. T. Hansen, R. R. Clifford, T. D. Pierce, C. B. Cartwright, B. G. Johnson, and G. D. Zunkel, “Compact actuator and controller and pumping apparatus for same.” WO Patent 98/11357, March 19, 1998.
- [47] F. E. Sager and C. J. Matice, “Piezoelectric pumps.” U.S. Patent 5 798 600, August 3, 1998.
- [48] R. P. Bishop, B. R. Face, S. A. Face, S. E. Clark, and N. S. Rose, “Piezoelectric actuated piston pump.” U.S. Patent 6 071 088, June 6, 2000.

- [49] R. F. Cusack, “Magnetostrictive pump.” U.S. Patent 4 795 318, January 3, 1989.
- [50] R. F. Cusack, “Magnetostrictive pump with reversible valves.” U.S. Patent 4 815 946, May 28, 1989.
- [51] R. F. Cusack, “Magnetostrictive pump with hydraulic cylinder.” U.S. Patent 4 726 741, February 23, 1988.
- [52] G. T. Engdahl and G. V. Molund, “Liquid pump driven by elements of a giant magnetostrictive material.” U.S. Patent 4 927 334, May 22, 1990.
- [53] R. Burkhart, G. Pietron, Y. Fujii, T. Snyder, and W. Tobler, “Hydraulic actuator for a vehicular power train.” U.S. Patent 7 654 377, February 2, 2010.
- [54] C. O’Neill, “Piezoelectric fluid pump.” U.S. Patent 7 484 940, February 3, 2009.
- [55] T. E. Walters, “Development of a smart material electrohydrostatic actuator considering rectification valve dynamics and in situ valve characterization,” Master’s thesis, The Ohio State University, 2008.
- [56] C. O’Neill and J. Burchfield, “Kinetic Ceramics piezoelectric hydraulic pumps,” *Proceedings of SPIE*, vol. 6527, p. 65270I, April 2007.
- [57] G. N. Weisensel, T. D. Pierce, and G. Zunkel, “High-authority smart material integrated electric actuator,” *Proceedings of SPIE*, vol. 3044, pp. 382–390, 1997.
- [58] D. G. Lee, D. D. Shin, and G. P. Carman, “Large flow rate/high frequency microvalve array for high performance actuators,” *Sensors & Actuators: A. Physical*, vol. 134, pp. 257–263, February 2007.
- [59] B. Li, Q. Chen, D. G. Lee, J. Woolman, and G. P. Carman, “Development of large flow rate, robust, passive micro check valves for compact piezoelectrically

- actuated pumps,” *Sensors & Actuators: A. Physical*, vol. 117, pp. 325–330, January 2005.
- [60] B. Li and Q. Chen, “Design and fabrication of in situ UV-LIGA assembled robust nickel micro check valves for compact hydraulic actuators,” *Journal of Micromechanics and Microengineering*, vol. 15, no. 10, p. 1864, 2005.
- [61] M. Seong, K. P. Mohanchandra, Y. Lin, and G. P. Carman, “Development of a ‘bi-layer lift-off’ method for high flow rate and high frequency Nitinol MEMS valve fabrication,” *Journal of Micromechanics and Microengineering*, vol. 18, p. 075034, 2008.
- [62] G. Eggeler, E. Hornbogen, A. Yawny, A. Heckmann, and M. Wagner, “Structural and functional fatigue of NiTi shape memory alloys,” *Materials Science and Engineering A*, vol. 378, pp. 24–33, July 2004.
- [63] J. P. Larson and M. J. Dapino, “Reliable, high-frequency miniature valves for smart material electro-hydraulic actuators,” *Journal of Intelligent Material Systems and Structures*, vol. 23, no. 7, pp. 801–809, 2012.
- [64] B. J. Hamrock, B. O. Jacobson, and S. R. Schmid, *Fundamentals of Machine Elements*. WCB/McGraw-Hill New York, USA, 1999.
- [65] C. Bathias, L. Drouillac, and P. Le Francois, “How and why the fatigue S–N curve does not approach a horizontal asymptote,” *International Journal of Fatigue*, vol. 23, pp. 143–151, 2001.
- [66] R. D. Blevins, *Formulas for Natural Frequency and Mode Shape*. Van Nostrand Reinhold Company, 1979.
- [67] M. J. Rupinsky, “Smart material electrohydrostatic actuator for intelligent transportation systems,” Master’s thesis, The Ohio State University, 2006.

- [68] T. Naik, E. K. Longmire, and S. C. Mantell, “Dynamic response of a cantilever in liquid near a solid wall,” *Sensors and Actuators A: Physical*, vol. 102, no. 3, p. 240254, 2003.
- [69] J. P. Larson and M. J. Dapino, “High-frequency valve development for smart material electro-hydraulic actuators,” *Proceedings of SPIE*, vol. 7979, p. 79790E, 2011.
- [70] K. Nasser, N. Vujic, D. J. Leo, and H. H. Cudney, “Modeling and testing of a piezohydraulic actuation system,” *Proceedings of SPIE*, vol. 4327, pp. 354–365, 2001.
- [71] C. Cadou and B. Zhang, “Performance modeling of a piezo-hydraulic actuator,” *Journal of Intelligent Material Systems and Structures*, vol. 14, pp. 149–160, March 2003.
- [72] H. Olsson, K. Åström, C. Canudas De Wit, M. Gäfvert, and P. Lischinsky, “Friction models and friction compensation,” *European Journal of Control*, vol. 4, pp. 176–195, 1998.
- [73] E. O. Doebelin, *System Dynamics: Modeling, Analysis, Simulation, Design*. New York: Marcel Dekker, Inc., 1998.
- [74] H. E. Merritt, *Hydraulic Control Systems*. Wiley New York, 1967.
- [75] S. Chakrabarti and M. J. Dapino, “A dynamic model for a displacement amplified magnetostrictive driver for active mounts,” *Smart Materials and Structures*, vol. 19, p. 055009, March 2010.
- [76] D. Jiles and D. Atherton, “Theory of ferromagnetic hysteresis,” *Journal of magnetism and magnetic materials*, vol. 61, no. 1-2, pp. 48–60, 1986.

- [77] N. Lhermet, O. Delas, and F. Claeysen, “Magnetostrictive pump with piezo active valves for more electrical aircraft,” in *ACTUATOR 2006, 10th International Conference on New Actuators*, (Bremen, Germany), pp. 964–967, June 2006.
- [78] J. Ellison, “Investigation of active materials as driving elements in a hydraulic-hybrid actuator,” Master’s thesis, University of Maryland, College Park, Maryland, 2004.